National Technical University of Athens
School of Mechanical Engineering
Fluids Section
Laboratory of Thermal Turbomachines

Integrated Processes for Turbocharger Design and Retrofitting

PhD Thesis

Konstantinos Ntonas
Dipl. Mechanical Engineer

Supervisor:

Nikolaos Aretakis
Associate Professor, NTUA

Athens, February 2022

National Technical University of Athens
School of Mechanical Engineering
Fluids Section
Laboratory of Thermal Turbomachines

Integrated Processes for Turbocharger Design and Retrofitting

PhD Thesis

Konstantinos Ntonas
Dipl. Mechanical Engineer

DOCTORAL SUPERVISORY COMMITTEE:

1 Nikolaos Aretakis(Supervisor)
Associate Professor NTUA,
School of Mechanical Engineering
2 Konstantinos Mathioudakis
Professor, NTUA,
School of Mechanical Engineering
3 Kyriakos Giannakoglou
Professor NTUA
School of Mechanical Engineering

DOCTORAL EXAMINATION COMMITTEE:

1 Nikolaos Aretakis(Supervisor)
Associate Professor NTUA,
School of Mechanical Engineering
2 Konstantinos Mathioudakis
Professor, NTUA,
School of Mechanical Engineering
3 Kyriakos Giannakoglou
Professor NTUA
School of Mechanical Engineering
4 Ioannis Anagnostopoulos
Professor, NTUA,
School of Mechanical Engineering
5 Evangelos Giakoumis
Professor, NTUA,
School of Mechanical Engineering
6 Athanasios Chasalevris
Assistant Professor NTUA
School of Mechanical Engineering
7 Ioannis Roumeliotis
Senior Lecturer
Cranfield University

Athens, February 2022

Part of the research study was supported from the Special Account for Research Funding (E.L.K.E.) of National Technical University of Athens (N.T.U.A.), providing to the author a one-year full scholarship (April. 2021 – 2022).

Τμήμα της διδακτορικής διατριβής υποστηρίχθηκε οικονομικά από τον Ειδικό Λογαριασμό Κονδυλίων Έρευνας (Ε.Λ.Κ.Ε.) του Εθνικού Μετσόβιου Πολυτεχνείου (Ε.Μ.Π), παρέχοντας στον συγγραφέα μονοετή πλήρη υποτροφία (Απρίλιος. 2021 – 2022).

Acknowledgements

At this point, I would like to thank all those who have contributed to the completion of this thesis. First of all, I would like to sincerely thank the supervisor of this thesis, Nikolaos Aretakis, Associate Professor NTUA, for giving me the opportunity to work on such a challenging field of research. His constant presence and investment in time and effort throughout the duration of my studies have been of paramount importance for the completion of this work.

I would also like to special thank Konstantinos Mathioudakis, Professor NTUA, for his valuable advice and guidance during these years, enabling me to successfully navigate difficult problems.

I would also like to thank Kyriakos Giannakoglou, Professor NTUA for his comments on the thesis presentation-manuscript and their participation in the advisory committee of my thesis. His immediate response in correcting the manuscript has been truly valuable.

I owe special thanks to Dr. Alexis Alexiou for his priceless advices during this PhD thesis. Also, I would like to express my acknowledgment to Dr. Ioannis Roumeliotis, Dr Efthimios Pariotis and Dr Theodoros Zannis for our cooperation during my first paper. Additionally, I would like to appreciate Mr Yiannis Paraskevopoulos and Turbomed SA for providing the turbocharger data used in this study.

I owe also special thanks to my colleague and friend Ioannis Kolias for his help, his useful suggestions and the pleasant time throughout my study. His assistance at every stage of my research was priceless

My sincere thanks goes to my colleagues and friends Georgios Athanasakos and Orestis-Anastasios Koskoletos for our cooperation and their enthusiastic support.

Last but not least, I would like to express my huge appreciation to my parents Nikolaos and Georgia and my brother Anargyros, for the priceless support at each level and their emotional encouragement from my difficult starting point till the end. The last words are for Helen, for her patience and support during this period.

Finally, I would like to thank the Special Account for Research Funding (E.L.K.E.) of National Technical University of Athens (N.T.U.A.) for providing one year financial support in the frame of the PhD research.

At this point, I would like to say a huge thank you to my late Professor Tassos Stamatis, who initiated me to the field of Turbomachinery as an

undergraduate student and inspiring me regarding the scientific research and Turbomachines.

Abstract

The thesis is concerned with the development of integrated processes for turbocharger(T/C) design and retrofitting. The processes, developed with three modes of operation, provide a fully automatic retrofit and design solution or the option for T/Ced Diesel Engine Simulation.

The first process which corresponds to turbocharged(T/Ced) diesel engine simulation, utilizes 1D meanline models for T/C components, a single-zone model for the diesel engine and a T/C-diesel engine matching analysis. The diesel engine model is adapted to engine-specific data and the overall integrated model is validated against shop trials data, obtained from a marine diesel auxiliary engine. A physically consistent, transparent, and fully automated procedure is integrated in each turbo-component meanline model, for producing the corresponding performance map. Additionally, turbine meanline model(axial and radial) is developed with the ability to compute turbine performance beyond choke limit, allowing the prediction of T/C operation with choked turbine.

The second process refers to T/C preliminary design. An optimization procedure is employed, to design both compressor and turbine to match the entire T/Ced system. The optimization process focuses on engine fuel consumption reduction in the engine range of operation, while ensuring appropriate matching between turbomachinery components and the diesel engine. Structural integrity of both turbo-components is ensured by using simplified static and modal analysis. Dimensionless parameters are used as optimization variables, for both compressor and turbine, providing a more general and automated design process since there is no need to redefine the range of optimization variables and the initial geometry for different T/C scales. It also produces four improved 1D geometries, of different possible centrifugal compressor diffuser and turbine combination. The combination that gives the best improvement to the diesel engine operation is identified.

Additionally, partial turbo-component design option is provided. Similar to the entire T/C design procedure, a 1D turbo-component multi-point design optimization process is carried out, aiming to provide a fast and reliable solution based on T/Ced diesel engine range of operation. Structural integrity is also ensured by using simplified structural analysis. For compressor design, a CFD compressor multi-point design optimization process is also provided, producing an improved 3D compressor geometry. It complies with the T/Ced diesel engine

range of operation, while structural integrity is ensured by using Finite Element analysis.

The last process corresponds to automatic T/C retrofitting. During this process, available turbo-components are examined, in order to select the one that best matches the entire engine system, aiming to retain or improve the diesel engine efficiency.

Then, the above procedures are then applied to two application test cases. In the first one, a T/C redesign-retrofit case study is presented, where four retrofitting options are analyzed (compressor replaced, T/C replaced, compressor redesign and entire T/C redesign). In the first and second option, T/C retrofitting is carried out, using available turbo-components. It is shown that initial performance cannot be reconstituted using off-the-self solutions.

In the third option, a T/C compressor redesign is carried out. First, a T/C 1D compressor design is performed, aiming to at least reconstituting the original diesel engine performance, providing a reliable compressor initial geometry for the 3D design procedure. Then, a fully 3D compressor design is then performed, using a CFD-FEA optimization process, in order to provide an improved retrofitting solution.

In the fourth option, where the entire T/C is redesigned, all four T/C configurations are designed and analyzed aiming to at least reconstituting the original diesel engine performance. All four improved T/C geometries are sorted based on the diesel engine annual fuel cost reduction. Finally, a techno-economical assessment is carried out, analyzing all four retrofit options economic performance.

In the second case, specific faults are simulated, utilizing physical consistent parameters such as blade roughness and thickness based on relevant literature data. Overall system simulation and operation analysis is carried out assessing operability and performance parameters. Analysis results show a significant reduction in engine performance, especially in case of both turbo components being fouled, in contrast with the heat exchanger fouling where the power reduction is less affected.

Περίληψη

Στο πλαίσιο της παρούσας διδακτορικής διατριβής έγινε ανάπτυξη διαδικασιών προσομοίωσης, στοχεύοντας στον σχεδιασμό και μετεξοπλισμό στροβιλοϋπερπληρωτών. Οι διαδικασίες αναπτύχθηκαν συνθέτοντας τρεις καταστάσεις λειτουργίας, παρέχοντας δηλαδή μια πλήρως αυτόματη λύση μετεξοπλισμού και σχεδιασμού στροβιλοϋπερπληρωτών ή τη δυνατότητα προσομοίωσης στροβιλοϋπερπληρούμενης μηχανής ντίζελ.

Η πρώτη λειτουργία στοχεύει στην προσομοίωση στροβιλοϋπερπληρούμενης μηχανής ντίζελ, χρησιμοποιώντας μονοδιάστατα μοντέλα μέσης γραμμής για κάθε στροβιλο-συνιστώσα, ένα μοντέλο ενιαίας ζώνης για τον κινητήρα ντίζελ και μια ανάλυση ταιριάσματος στροβιλοϋπερπληρωτή - ντίζελ μηχανής. Το μοντέλο της ντίζελ μηχανής έχει την δυνατότητα προσαρμογής των παραμέτρων του με βάση τα διαθέσιμα δεδομένα δοκιμών παραλαβής που παρέχει η κατασκευάστρια εταιρία, ενσωματώνοντας παράλληλα για πρώτη φορά, μια πλήρως αυτοματοποιημένη διαδικασία υπολογισμού χάρτη επιδόσεων σε κάθε μοντέλο στροβιλο-συνιστώσας. Επιπλέον, αναπτύχθηκε μοντέλο μέσης γραμμής στροβίλου (αξονικό και ακτινικό) με τη δυνατότητα υπολογισμού της απόδοσης του στροβίλου πέραν του ορίου στραγγαλισμού.

Η δεύτερη λειτουργία αναφέρεται στον προκαταρκτικό σχεδιασμό στροβιλοϋπερπληρωτών, χρησιμοποιώντας μια διαδικασία βελτιστοποίησης με γνώμονα το ταίριασμα με το υπόλοιπο σύστημα μηχανής ντίζελ. Η διαδικασία βελτιστοποίησης επικεντρώνεται στη μείωση της κατανάλωσης καυσίμου της ντίζελ μηχανης σε όλο το εύρος λειτουργίας της, διασφαλίζοντας παράλληλα το ταίριασμα μεταξύ των στροβιλο-συνιστωσών με το υπόλοιπο σύστημα της ντίζελ μηχανής. Η δομική ακεραιότητα και των δύο στροβιλο-συνιστωσών ελέγχεται με χρήση απλοποιημένης στατικής και δυναμικής ανάλυσης. Αδιάστατοι παράμετροι χρησιμοποιούνται ως μεταβλητές βελτιστοποίησης, τόσο για τον συμπιεστή όσο και για τον στρόβιλο, παρέχοντας πιο γενικευμένη και αυτοματοποιημένη διαδικασία σχεδιασμού, καθώς δεν απαιτείται ο επαναπροσδιορισμός τόσο του εύρους των μεταβλητών βελτιστοποίησης όσο και της αρχικής γεωμετρίας για διαφορετική κλίμακα στροβιλοϋπερπληρωτή. Παράλληλα, μέσω της ανάλυσης όλων των πιθανών διατάξεων στροβιλοϋπερπληρωτών, επιλέγεται η καλύτερη διάταξη με γνώμονα τη βελτίωση της λειτουργία του συστήματος ντίζελ μηχανής.

Επιπλέον, παρέχεται επιλογή μερικού σχεδιασμού στροβιλο-συνιστώσας. Παρόμοια με τη διαδικασία σχεδιασμού στροβιλοϋπερπληρωτή, πραγματοποιείται μονοδιάστατος σχεδιασμός πολλαπλών σημείων στροβιλο-συνιστώσας σε επίπεδο συστήματος ντιζελ μηχανής. Επίσης, διασφαλίζεται η δομική ακεραιότητα της λύσης με τη χρήση απλοποιημένης δομικής ανάλυσης. Για τον σχεδιασμό του συμπιεστή, παρέχεται επίσης μια διαδικασία σχεδιασμού πολλαπλών σημείων λειτουργίας, βασισμένη σε διαδικασία βελτιστοποίησης υπολογιστικής ρευστοδυναμικής(CFD), η οποία παράγει μια βελτιωμένη τρισδιάστατη γεωμετρία με βάση τις ανάγκες της μηχανής ντίζελ. Σχετικά με τη δομική ακεραιότητα της τριδιάστατης γεωμετρίας, η διασφάλιση επιτυγχάνεται μέσω εργαλείου τριδιάστατης στατικής ανάλυσης με πεπερασμένα στοιχεία.

Η τελευταία λειτουργία σχετίζεται με τον μετεξοπλισμό στροβιλοϋπερπληρωτών. Πραγματοποιείται εξέταση όλων των διαθέσιμων στροβιλο-συνιστωσών, αποσκοπώντας στην επιλογή του καλύτερου συνδυασμού. Η επιλογή γίνεται με γνώμονα την κατανάλωση καυσίμου της μηχανής ντίζελ, το ταίριασμα με το υπόλοιπο σύστημα και τη δομική ακεραιότητα.

Εν συνεχεία, πραγματοποιείται χρήση των διαδικασιών σε 2 είδη εφαρμογών με σκοπό την ανάδειξη των δυνατοτήτων τους. Στην πρώτη εφαρμογή, πραγματοποιείται μετεξοπλισμός στροβιλοϋπερπληρωτή, αναλύοντας τέσσερις επιλογές μετεξοπλισμού (αντικατάσταση συμπιεστή, αντικατάσταση στροβιλοϋπερπληρωτή, επανασχεδιασμός συμπιεστή και επανασχεδιασμός ολόκληρου του στροβιλοϋπερπληρωτή). Στην πρώτη και δεύτερη επιλογή, η διαδικασία του μετεξοπλισμού πραγματοποιείται με χρήση διαθέσιμων στροβιλο-συνιστωσών.

Στην τρίτη επιλογή, πραγματοποιείται μονοδιάστατος επανασχεδιασμός συμπιεστή, με στόχο την πλήρη επανασύσταση της αρχικής λειτουργείας του συστήματος μηχανής ντίζελ, παρέχοντας παράλληλα στο εργαλείο τριδιάστατου σχεδιασμού μια αξιόπιστη αρχική γεωμετρία. Εν συνεχεία, πραγματοποιείται η διαδικασία τριδιάστατου σχεδιασμού συμπιεστή, ακολουθώντας μια διαδικασία βελτιστοποίησης CFD-FEA, με στόχο την εύρεση μιας βελτιωμένης λύσης μετεξοπλισμού.

Στην τέταρτη επιλογή, πραγματοποιείται επανασχεδιασμός ολόκληρου του στροβιλοϋπερπληρωτή, αναλύοντας παράλληλα και τις τέσσερις πιθανές διατάξεις με στόχο την πλήρη επανασύσταση της αρχικής λειτουργίας του συστήματος μηχανής ντίζελ. Τα αποτελέσματα του σχεδιασμού των τεσσάρων διατάξεων ταξινομούνται με βάση την ετήσια μείωση του κόστους καυσίμου. Τέλος, πραγματοποιείται τεχνοοικονομική αποτίμηση των τεσσάρων επιλογών μετεξοπλισμού, αποσκοπώντας στην αξιολόγηση τους από οικονομική σκοπιά.

Η προσομοίωση βλαβών είναι ιδιαιτέρως σημαντική κατά τη διαδικασία του σχεδιασμού ή μετεξοπλισμου στροβιλοϋπερπληρωτών. Συνεπώς, στη δεύτερη εφαρμογή, πραγματοποιείται προσομοίωση συγκεκριμένων σφαλμάτων, χρησιμοποιώντας φυσικές συνεπείς παραμέτρους όπως η τραχύτητα και το πάχος πτερυγίου με βάση δεδομένα από την ανοιχτή βιβλιογραφία. Τα αποτελέσματα της προσομοίωσης δείχνουν σημαντική μείωση στην απόδοση της μηχανής, ειδικά σε περίπτωση επικαθίσεων και στις δύο

στροβιλο-συνιστώσες, σε αντίθεση με τη ρύπανση του εναλλάκτη θερμότητας όπου η μείωση της ισχύος επηρεάζεται λιγότερο.

Contents

Nomenclature

Abbreviations

ASA	Adaptive simulated annealing
AT	Axial Turbine
BTDC	Before top dead center
C.P	Charged Air Pressure
C.T	Charged Air Temperature
CC	Centrifugal Compressor
CFD	Computational Fluid Dynamics
CML	Compressor meanline analysis
FEA	Finite Element Analysis
GENSETs	Auxiliary power generator sets
GHG	Greenhouse gas
GUI	Graphical user interface
HFO	Heavy fuel oil
ICE	Internal combustion engine
KNN	K-nearest neighbor
kser	Turbine tip type Boolean variable
L/H SFO	High/Low Sulfur fuel oil
LHV	Lower Heating Value of Diesel fuel
MDO	Marine distillate oil:
MGO	Marine gasoil
OS	Operating System
OTE	Original Turbocharged Engine
RMS	Root mean square
RT	Radial Turbine
SSA	Simplified Structural Analysis
SST	Menter Shear Stress Transport/Simplified Structural Tool
SVM	Support Vector Machine
T/C	Turbocharger
T/Ced	Turbocharged
TML	Turbine meanline analysis
VGT	Variable geometry turbocharger

Symbols

A	Area	[m^2]
AR	Aspect Ratio	[-]
b	Width	[m]
B	Blockage Factor	[-]
c	Chord	[m]
C	Purchase Cost	[$]
CA	Crank Angle	[Deg]
C_f	Friction Coefficient	[-]
cl	Clearance	[m]
C_{man}	Manufacturing Cost	[$]
$C_{piston,mean}$	Mean piston speed	[m/s]
C_{red}	Redesign	[$]
D	Diameter	[m]
dP	Pressure Drop/Pressure difference	[Pa]
e	Roughness/Turbine Blade Camber line radius	[m]/[m]
F	Force	[N]
h	Height	[m]
h	Specific enthalpy	[J/kg]
hr	Hours	[hours]
I	Area moment of Inertia	[m^4]
$K_{x,y}$	Lateral stiffness coefficient	[N/m]
$K_{\theta_{x,y}}$	Circulant stiffness coefficient	[Nm/rad]
KE	Kinetic Energy	[J]
L	Length/ Turbine Kinetic Energy Loss Coefficient	[m]/[J/kg]
le_{spl}	Dimensionless splitter blade leading edge position	[-]
M	Mach number	[-]
m	Mass	[kg/s]
$\dot{m}$	Mass flow	[kg/s]
$\dot{m}_{cor}$	Corrected mass flow ($\dot{m}\sqrt{\theta}/\delta$)	[kg/s]
N	Diesel engine crankshaft speed, T/C speed	[Rpm]
n	Polytropic exponent	[-]
N_c	T/C Corrected speed ($N/\sqrt{\theta}$)	[Rpm]
Nu	Nusselt Number	[-]
o	Throat	[m]
p	Pressure	[Pa]
P	Profit	[$]
Pr	Prandlt number	[-]
pwr	Power	[W]
Q_{comb}	In-cylinder fuel combustion energy input	[J]
$Q_{comb,tot}$	Total heat of combustion	[J]
Q_W	Heat transfer through the boundaries of the engine cylinder	[J]

R	Radius	[m]
r	Curvature/Interest rate	[m]/[-]
Re	Reynolds number	[-]
R_{gas}	Air gas constant	[J/kg K]
RH	Relative Humidity	[-]
s	Blade-Vanes Pitch	[m]
s_f	Safety factor	[-]
SFC	Specific Fuel Consumption	[g/kWh]
T	Temperature	[K]
t	Thickness/Time	[m]/[s]
TC	Total investment cost	[$]
t_e	Trailing edge thickness	[m]
U	Overall Heat Transfer Coefficient/Rotational Speed	[J/(m^2 K]/[m/s]
U_{cyl}	Internal Energy of the engine cylinder content	[J]
V	Velocity/Volume	[m/s]/[m^3]
VR	Velocity Ratio	[-]
V_{SW}	Diesel engine Cylinder swept volume	[m^3]
V_u	Circumfferential Velocity	[m/s]
W	Engine work output/Relative Velocity	[J]/[m/s]
x	Blade maximum thickness position	[m]
Y	Turbine Pressure Loss Coefficient	[-]
y_G	Center of mass	[m]
Z	Number of Blades or Vanes	[-]
z	Objective function	[kg/s]
z´	Objective function	[-]
Z_{load}	Blade Load Coefficient	[-]

Greek Letters

α	Absolute flow angle/Decay rate	[Deg]/[Hz]
β	Relative flow angle	[Deg]
β_g	gauging angle = arc sin(o/s)	[Deg]
γ	Heat capacity ratio	[-]
δ	Deviation angle	[Deg]
$\Delta\varphi_c$	Duration of combustion	[Deg]
ε	Effectiveness	[-]
η	Efficiency	[-]
μ	Dynamic Viscosity	[kg/(m)]
ρ	Density	[kg/m^3]
σ	Slip factor/Stress	[-]/[Pa]
φ	Flow coefficient	[-]
$\varphi(T)$	Entropy function	[-]
χ	Component price reduction after usage	[%]
ω	Angular velocity/Eigenfrequency	[rad/s]/[Hz]
$\bar{\omega}$	Compressor pressure loss coefficient	[-]
Ω	Critical frequency	[Hz]

Subscripts

1	Compressor impeller inlet/Radial Turbine Volute Inlet/Axial Turbine Rotor - Stator Inlet
2	Radial Turbine Vaned Nozzle Inlet/Axial Turbine Rotor - Stator Outlet
3	Compressor impeller outlet/ Radial Turbine Vaneless Nozzle Inlet
4	Compressor Vaneless diffuser outlet/ Radial Turbine Impeller Inlet
5	Compressor vaned diffuser outlet
6	Compressor Volute outlet/ Radial Turbine Impeller Outlet
AD	Adiabatic
air	Air
amb	Ambient
axial	Axial
B	Blade Mid-Stream
b	Blades
calc	Calculated
ch	Choke
cmp	Compressor
cr	Critical
cyl	Cylinder
des	Design
e	Roughness
eff	Effective
EVO	Exhaust Valve Opening
exh	Diesel engine exhaust gas
exh,manif	Exhaust manifold
ext	External
FB	Full Blades
fuel	Diesel engine fuel
GV	Guide vanes
hyd	Hydraulic
id	Ideal
im	Inlet manifold
imp	Impeller
in	Inlet
int	Internal
is	Isentropic
IVC	Inlet valve closing
le	Leading edge
m	Mean Stream Meridional
m1	Mode 1
m2	Mode 2
m3	Mode 3

max	Maximum
MB	Main Blades
opt1	Option 1
opt2	Option 2
opt3	Option 3
opt4	Option 4
out	Outlet
r	Relative
R	Recirculation/Rotor
r	Relative Conditions
ref	Reference
S	Stator
s	Static Conditions/shaft
SC	Scaling
shopt	Shop trials data
stag	Stagger
t	Total Conditions
te	Trailing edge
th	throat
trb	Turbine
v	Vanes
vnd	Vaned Diffuser
vnless	Vaneless Diffuser
vol	Volumetric/Volute
w	Wall

List of Figures

List of Tables

Chapter

1 Introduction

Turbochargers(T/C) are mainly used as a part of a turbocharged(T/Ced) internal combustion engine(ICE) while lately have been used in other power generation units such as T/Ced fuel cells and micro gas turbines.

T/Ced ICEs have been widely used in vehicles, heavy duty trucks, ships, non-interconnected electric power systems and other energy applications. Specifically, they have a leading role in marine industry, used mainly as main propulsion engines and as auxiliary power generator sets (GENSETs). Naval vessels up to frigate class utilize four-stroke diesel engines for propulsion as well as GENSETs since they offer lower acquisition cost, better fuel economy and better response to load changes compared to gas turbines [Bricknell 2006].

1.1 Turbochargers

Various types of exhaust-driven T/C have been designed for charging thermal engines. Basically, a T/C consists of a compressor and a turbine, coupled on a common shaft. The exhaust gases from the engine are directed by the turbine inlet casing to the blades and subsequently discharged to the atmosphere. Exhaust gases are then used in the turbine to drive the compressor which compresses the air and directs it to the engine intake manifold, to supply, in turn the engine cylinders with air of higher density compared to a naturally aspirated engine.

There exists a number of different types of compressors and turbines (or expanders), but few of these are suitable to form the basis of an exhaust-gas driven supercharging system. The combination of a single stage centrifugal compressor and a single-stage axial or radial flow turbine is almost universally used in T/C. The former type with the axial flow turbine is used for most of medium and large size engines and its suitable for rail traction, industrial and marine purposes and the latter type for small engines of the automotive (truck and automobile) type (Figure 1-1). [Watson and Janota 1982]

(a)

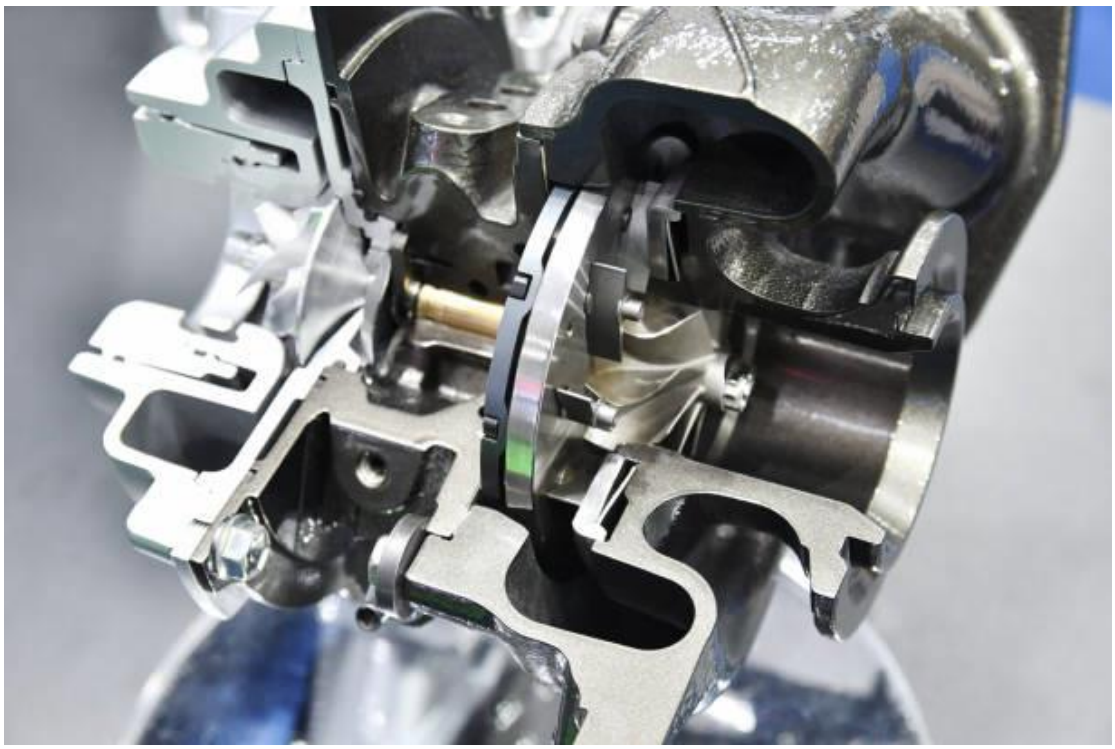

(b)

Figure 1-1: Turbocharger with: **(a)** Axial[1] and **(b)** Radial[2] Turbine.

[1] www.nauticexpo.com
[2] http://www.epi-eng.com

1.2 Historical background

In 1905, Swiss born Dr. Alfred Büchi received the first patent(Figure 1-2) on a T/C for a marine engine. However, the concept of turbocharging goes back to the end of the 19th century when both Gottlieb Daimler and Rudolf Diesel were doing research into forced intake. The first T/C were not applied to marine or automotive but to airplanes. Around 1918, the General Electric(GE) engineer, Sanford Alexander Moss, applied a T/C to a V12 Liberty airplane and subsequently turbocharging was applied to many American airplanes[1].

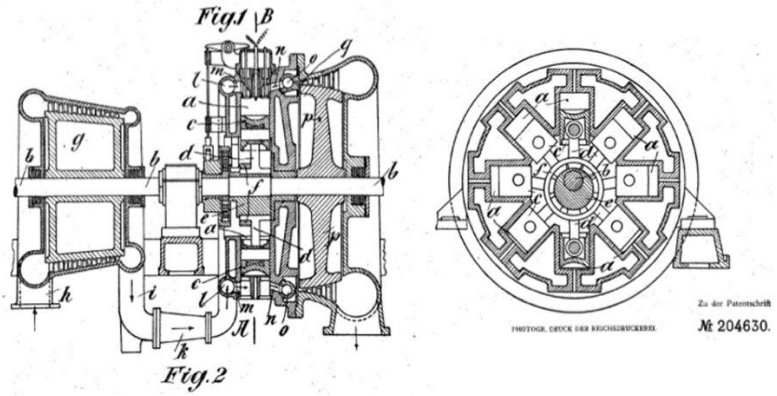

Figure 1-2: Highly supercharged compound engine[Buchi 1905].

The first T/C were nothing like the advanced today technology. Among other things, a lack of proper metal and bearing technology held back their advancement as the materials used were unable to withstand the high temperatures in the engines. With the improvement in engineering materials, T/C were gradually applied to smaller engines. By the 70s, T/C were standard on large marine diesel engines, in contrast to automotive engine turbocharging.

The first automotive T/C prototype was manufactured around 1938, the first T/Ced passenger cars did not appear until the 60s, and even then they were still very unreliable. In the 70s, turbocharging became very popular for Formula 1 racing, and even today this is still the image that many people have about T/C. However, the oil crisis in the 70s also brought on a new awareness for fuel reduction. "Downsizing" by the means of turbocharging provided a great opportunity for cleaner engines, without losing power.

In Germany, the breakthrough of T/Ced diesel cars led to the start of series production of the Mercedes Benz 300 SD in 1978 and VW Golf Turbo Diesel in 1981. With turbocharging diesel engines, their efficiency increased, leading to low emissions achievement. The combination of engines power increase and fuel consumption reduction showed over the world the advantages of turbocharging, while made Diesel engine more interesting for the passenger car industry. [Popular Science Magazine 1979].

Another great step forward for T/C was the introduction of the Variable geometry T/C (VGT). The first passenger car fitted with a VGT (Honda), came on

[1] https://www.ge.com/

the market in 1988[1]. VGT had clear advantages, as they could operate as both small and large T/C due to the rotating vane system in the turbine inlet, leading to turbo lag reduction while offering a high flow capacity at maximum power operation. Mitsubishi Heavy Industries began developing VGT in 1984 for truck applications and started mass production in 1994. MHI also launched VGT for passenger cars in 2001, and this new technology quickly spread to the European market.

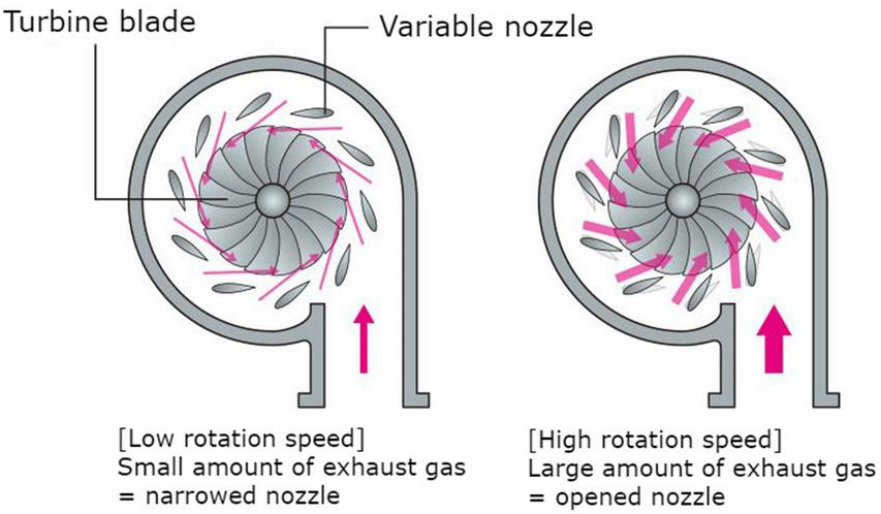

Figure 1-3: VGT mechanism.[Hu et al. 2019].

Applying two T/C to an engine has been a popular trend for maximizing power while reducing turbo lag. Maserati was the first to use this setup already in 1981 and Bugatti even used a set-up with four sequential T/C on a W16 engine. Concerning the two-stage concept, there are three different types parallel sequential and serial and are depicted in. Specifically, the parallel configuration refers to using two equally-sized turbochargers which each receive half of the exhaust gases. The sequential turbocharging refer to a set-up in which the engine uses one turbocharger for lower engine speeds, and a second or both turbochargers at higher engine speeds. The serial turbocharging is where the turbochargers are connected in series with the output of the first turbocharger then being further compressed by the second turbocharger and in some cases powering the larger turbine

[1] Dieselnet.com

1.3 Turbocharger as a Greenhouse gas emission reduction mechanism

As it is well known, T/C force air into an engine by using the wasted energy from the exhaust. Nowadays, with the hybrid T/C being developed, they can also contribute directly to the power generation in case of a hybrid electric system.

Even if a T/C is an auxiliary part of a road vehicle or maritime power generation unit, its development is important for GHG emission reduction, as they play a significant role in the engine downsizing, fuel consumption reduction and efficiency increase.

1.3.1 Greenhouse gas emission statement

Transport represents almost a quarter of Europe's greenhouse gas emissions and the main cause of air pollution around the globe, as it is shown in Figure 1-4. The transport sector has not seen the same gradual decline in emissions as other sectors as emissions only started to decrease in 2007 and still remain higher than in 1990 (Figure 1-4).

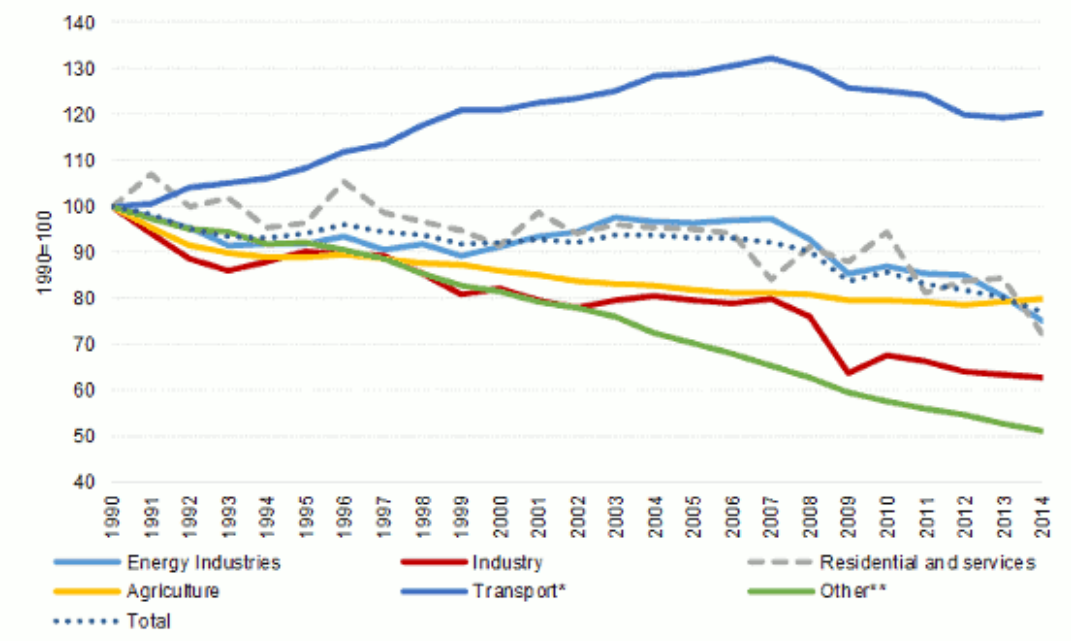

Figure 1-4: Europe Greenhouse gas emissions[1].

Transport is by far the biggest emitter accounting for more than 70% of all greenhouse gas (GHG) emissions in 2014. With the global shift towards a low-carbon, circular economy already underway, the Commission low-emission mobility strategy, adopted in July 2016, aims to ensure Europe stays competitive and able to respond to the increasing mobility needs of people and goods.

[1] https://ec.europa.eu/clima/policies/transport_en

1.3.2 Current Energy Use in Road Transportation

A vast majority of road vehicles are powered by ICE either as an entire energy unit or as a part of a hybrid system(coupled with electric unit) while only a small percentage is based on all-electric system. The ICE will remain the primary road transportation power generation mode for at least the next decade, even if the electric systems have made acceptable progress and achieve zero emissions(not including the electricity generation units emissions). The reason is that a fully electric vehicle requires further research and development in the following fields:

- Local workshops: Require further familiarization with the electric engines field.
- Low autonomy: Due to limited batteries capacity, electric vehicles are suitable only for city transportation. Efforts must be made in developing charging controllers to manage the technical, environmental and economic factors, in order to supervise the critical task of battery status charge. Current technologies can only provide energy storage in a very limited extent.
- Mass government investment in charging points: Public policies development for the structured implementation of charging stations in public places and in common use areas within large shared spaces, such as parking and residential areas, all with the objective of implementing electric vehicles on a larger scale.
- Time consuming recharging: In contrast to a conventional ICE vehicle, the electric ones recharge time(fast recharging) may exceed the one hour, making them less attractive for being purchased.

Nowadays, electric vehicles are presented as the key for facing both economic crisis and global warming. Although, the mass usage of electric vehicles has a negative impact on both issues, as it requires efficient recharging(Figure 1-5) during off-peak hours which may not be accomplished. Thus, the inevitable increase in power demand during peak hours may lead to:

- Overall electricity price increase in all costumers (independent of having purchased electric vehicles).
- GHG emissions increase due to the power generation demand which in case of efficient recharge can be generated by renewable energy systems.
- Risk of local black outs/flickering due to obsolete electrical network or inability to cover the power demand.

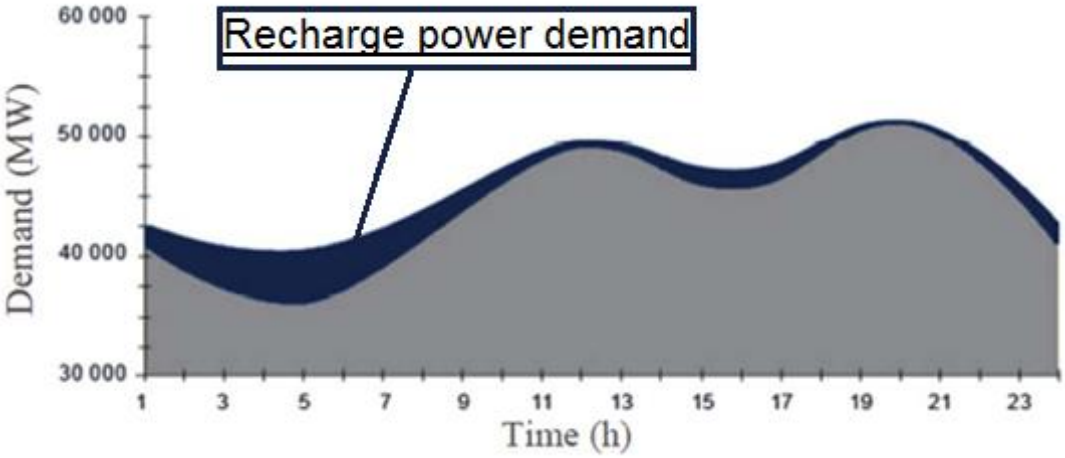

(a)

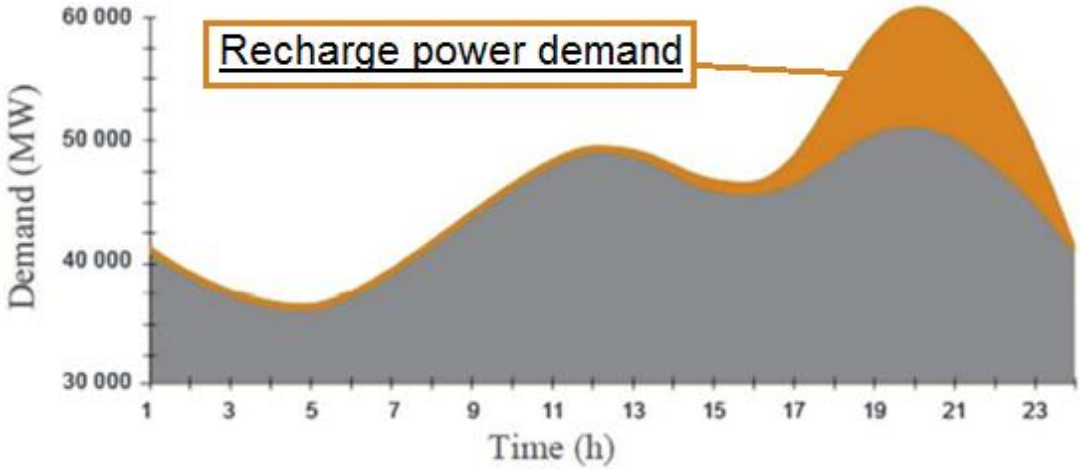

(b)

Figure 1-5: Recharge during off-peak hours for Spain: **(a)** Efficient **(b)** Inefficient [Martínez-Lao et al. 2017]

The compressed natural gas (CNG) engines, namely ICE with CNG fuel type, represent a promising solution for road transportation vehicles, concerning low GHG emissions. Landersheim et al. (2021) perform series of simulations, comparing both diesel and CNG powertrains. They conclude that a CNG powertrain even if it is bigger than a diesel one with higher investment cost, leads to lower fuel consumption, hence both operating cost and emissions reduction.

Additionally, taking advantage from the zero-sulfur CNG (no SO_x in combustion derivatives), the exhaust gas energy absorption beyond the dew point can be accomplished, allowing further engine downsizing(higher e-Turbocharger) or possible coupling with an organic Rankine cycle [Mariani et al. 2020],hence leading to further fuel consumption, operating cost and GHG emissions reduction.

1.3.3 Current Energy Use in Maritime Transportation

Maritime transportation is the backbone of the international trade and the global economy. Around 80% of global trade by volume and over 70% of global trade by value are carried by sea and are handled by ports worldwide [Barki and Deleze-Black 2017]. While shipping enjoys low costs, serious environmental pollutions (such as CO_2, SO_x, NO_x, and HC) are caused by marine fuel(Bunker[1]).

Similarly to road vehicles, the ICE will remain the primary power generation mode for at least the next decade, even if electric engines have made some progress in maritime transportation. In maritime, the fundamental aspects of an electric engine are the same with that used for powering road vehicles (on a much larger scale). Note that the first all-electric ship was built in 2017 by Guangzhou Shipyard International and has a range of 40 nautical miles [Schnurr and Walker 2019].

As depicted in Figure 1-6, most of the global shipping fleet relies on heavy fuel oil which contributes significant amounts of GHG, sulfur, and other emissions that contribute negatively to climate change and have negative impact on environment and human health. As Tian et al. (2020) point out, the liquified natural gas (LNG) is viewed as the most suitable fuel for ships, depicted as the most promising solution for GHG emissions reduction. LNG engines, compared to heavy oil ones, succeed reduction in CO_2, NO_X and SO_X emissions by about 20%, 90% and 100% respectively.

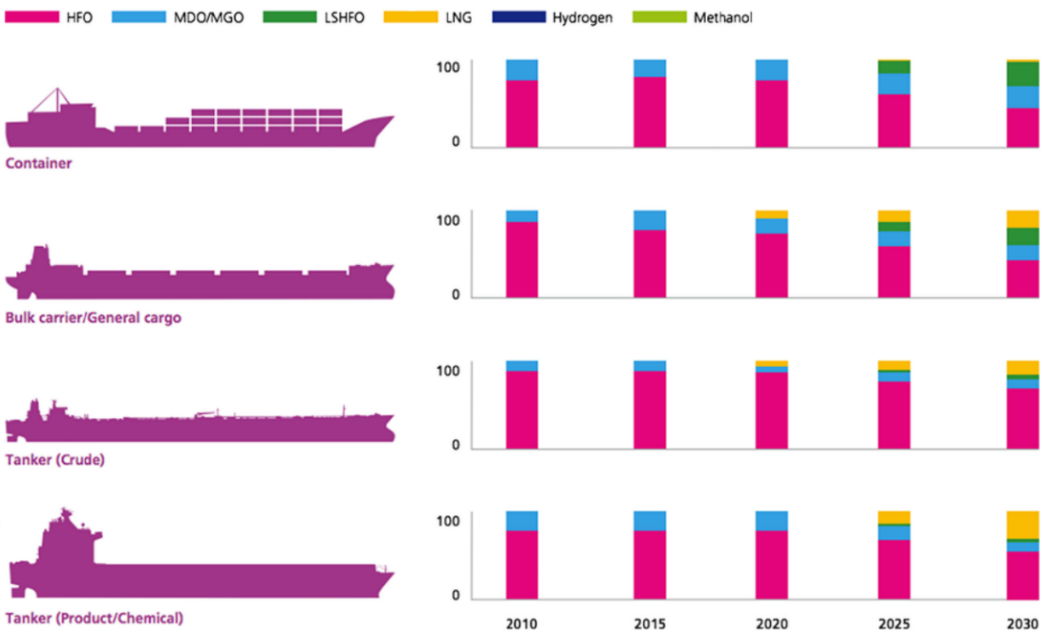

Figure 1-6: Maritime fuel usage. [Olmer et al. 2017]

[1] **Bunker**: Marine fuel, typically for international shipping. The term is adapted from the days of coal-fired steam boilers; fuel was stored aboard ship in coal bunkers and was shoveled into the boiler; when oil replaced coal, the bunkers became fuel tanks, but the name was retained.

1.3.4 Turbocharged Reciprocating Internal Combustion Engine

According to the greenhouse gas emissions analysis, described in the previous section, the ICE improvement and emissions reduction is important as it will remain primary power generation mode for both the road and the maritime transportation.

Ricardo et al. (2011) point out that the most capable ICE(Spark-ignition and compression-ignition) emissions reduction mechanism today is the engine downsizing, combined with boosting technology. This can be seen by studying the T/Ced ICE penetration in the global road vehicle market (Figure 1-7).

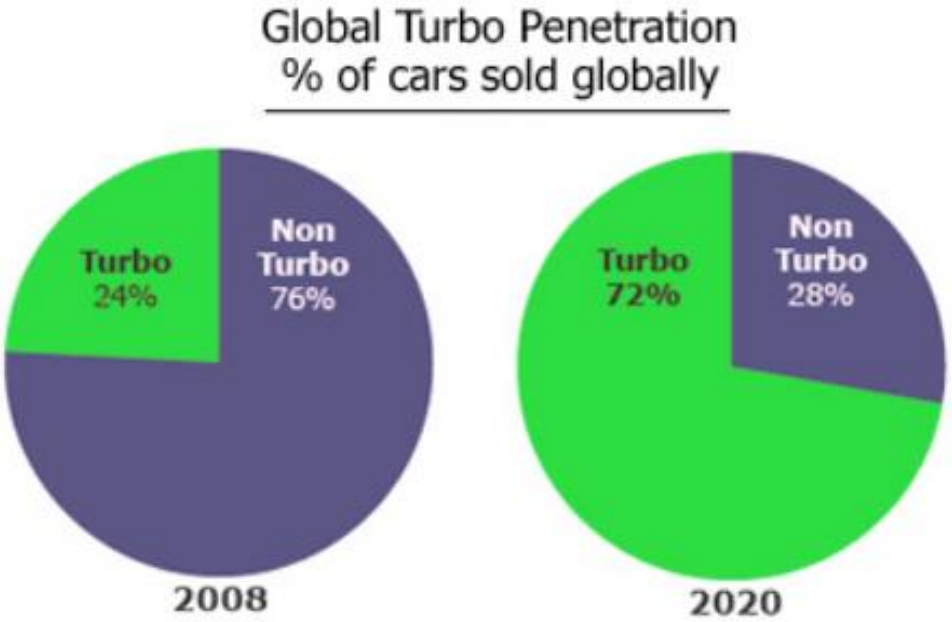

Figure 1-7: Turbocharged internal combustion engine penetration in the global car market.[1]

Boosting systems are essential features of engines downsizing. Turbocharging (and, to a lesser extent, in terms of efficiency, supercharging) is an inherent downsizing technology, as it increases boost levels above ambient, hence forcing more power out of a given size engine. Most vehicle manufacturers downsize engines from 2 liters to 1.3 - 1.4 liters focusing on both fuel economy and emissions reduction, according to Shahed (2003). He points out that engine downsizing(Figure 1-8) is the most cost-effective method of emissions reduction.

[1] www.turbodynamics.co.uk

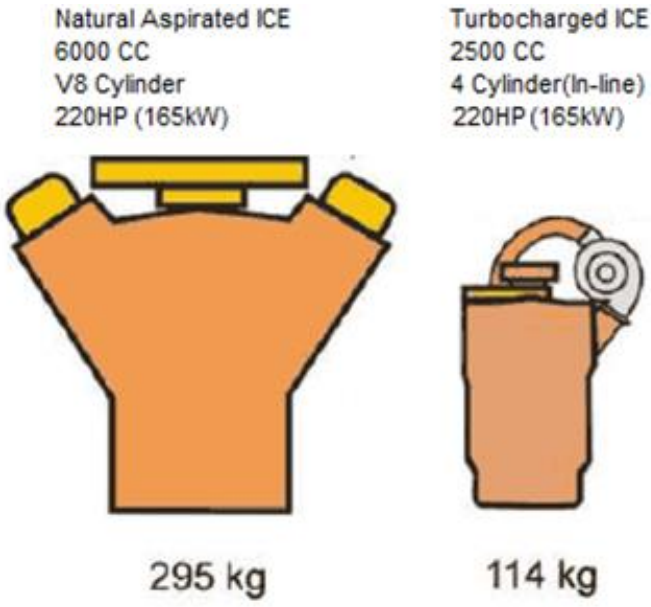

Figure 1-8: Comparison between Natural Aspirated and Turbocharged Internal combustion engine[1].

Apart from the exhaust gas emissions, the noise pollution also negatively affects both flora and fauna. By turbocharging an ICE, both air and noise pollutions are reduced as depicted in Figure 1-9.

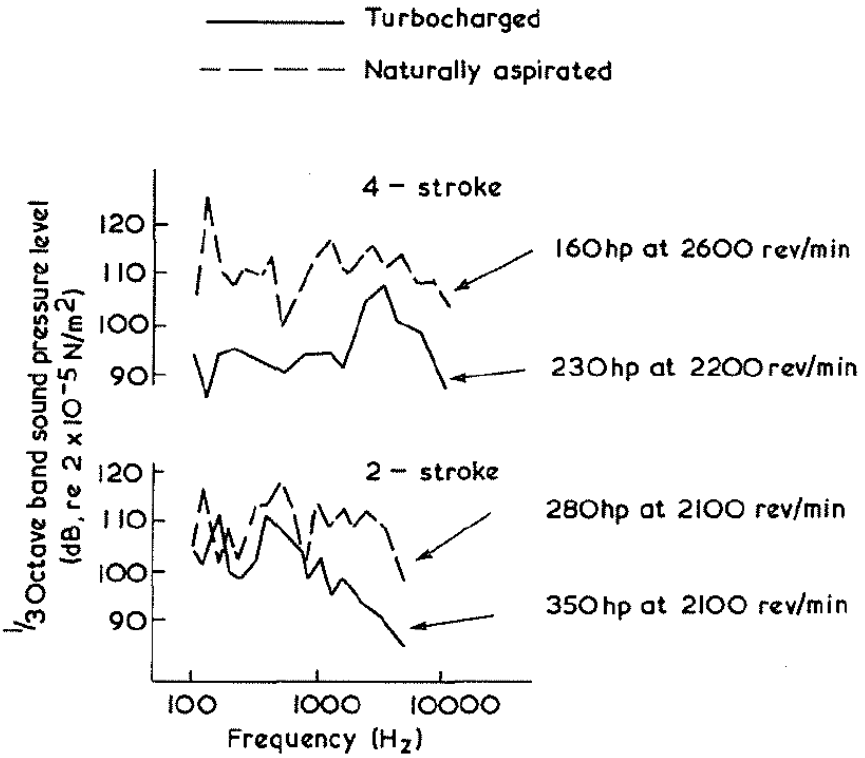

Figure 1-9: The effect of turbocharging on noise from an unsilenced exhaust. [Watson and Janota 1982]

[1] www.autoportal.com

Concluding, T/C plays a significant role in ICE emission reduction. Its further research and development can provide both further engine efficiency increase and downsizing, especially in case of LNG or CNG engines, where exhaust gas energy can further be absorbed beyond the dew point.

1.3.5 Turbocharged four-stroke rotating Internal Combustion Engine

One of the specific features of the four-stroke rotating ICE are that as the rotor completes a full rotation, the output shaft accomplishes three revolutions. In terms of the rotating angle of the output shaft, the time required to complete one stroke is 270 degrees, that is 1.5 times more than that of a four-stroke reciprocating engine [Sher 1998].

Among rotary engines, the Wankel engine is the only one that has been employed on mass production vehicles. The Wankel engine has been designed and studied by the German Felix Wankel. A comparison between Wankel and reciprocating ICE in terms of working principle is given in Figure 1-10.

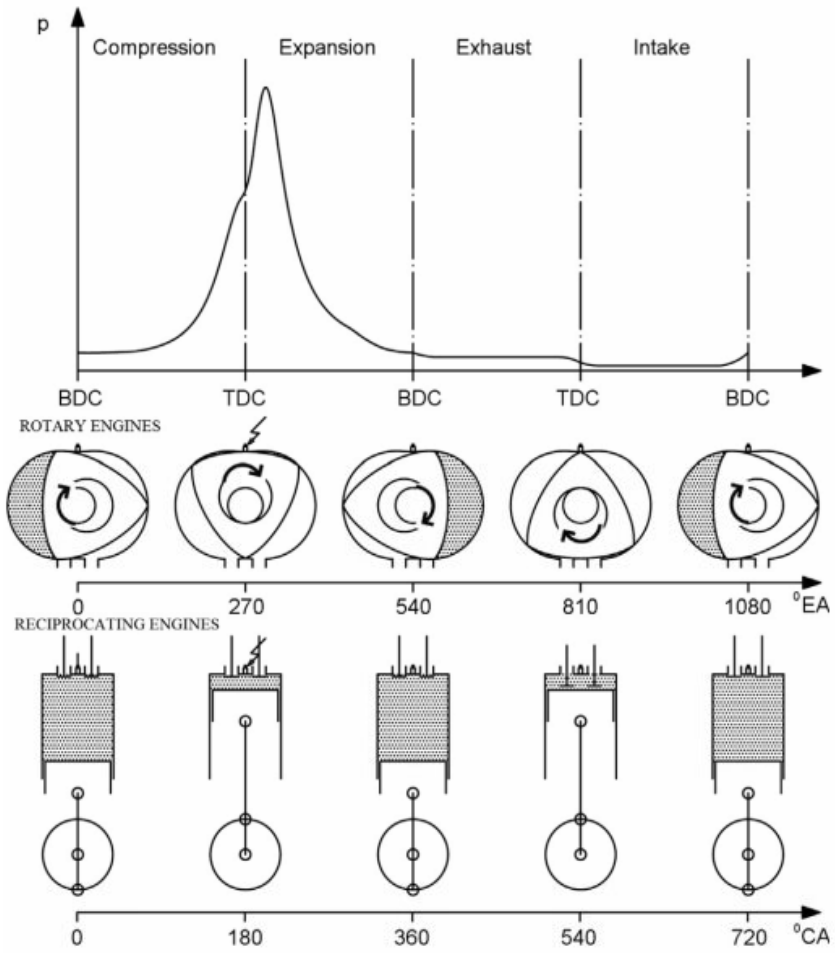

Figure 1-10: Comparison of reciprocating engine and rotary engine in terms of operating principle. [Cihan 2020]

It is well known that the Wankel engine is basically composed of a rotary piston that rotates inside an epitrochoidal statoric housing. The rotor has the form of an equilateral triangle with convex sides placed on an eccentric part of the output shaft. The different pressure conditions in the three chambers of the Wankel engine during the four-stroke cycle produce the driving torque. Another well promising four-stroke rotating ICE is the opposed rotary piston(ORP) engine with similar operation mechanism.

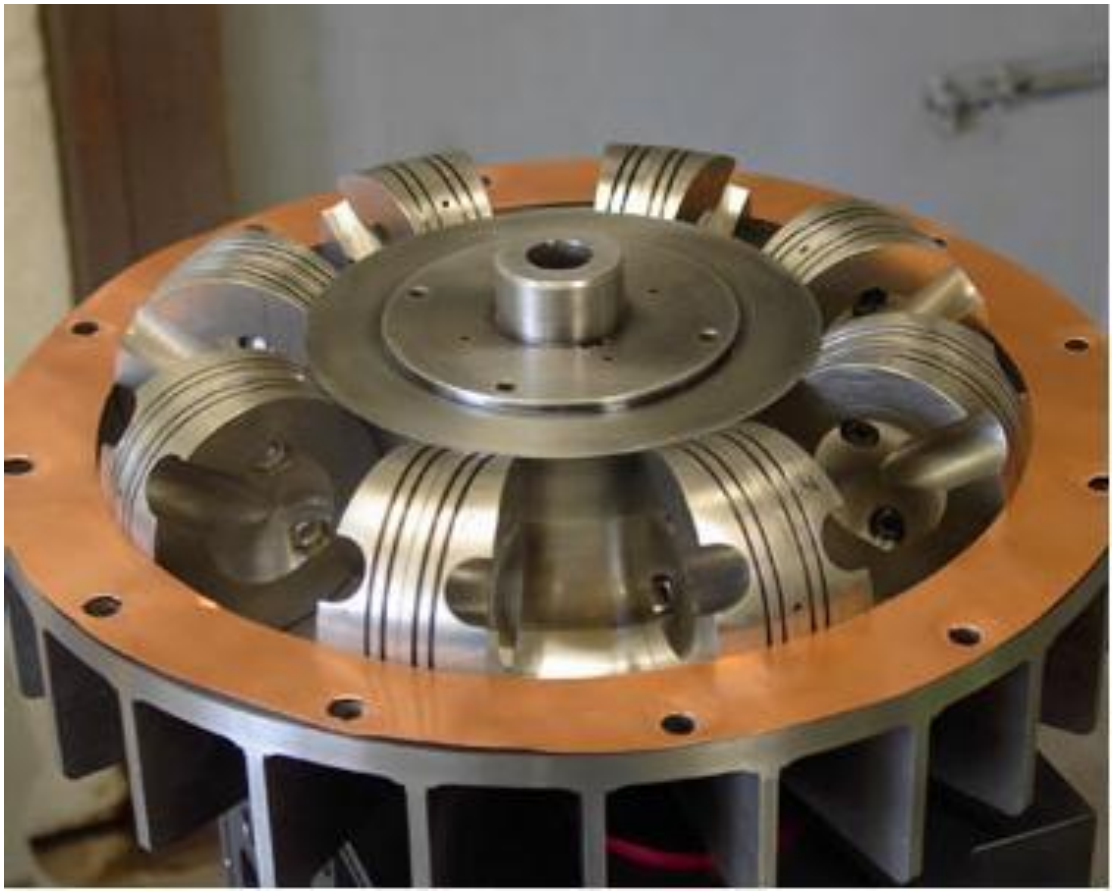

Figure 1-11: Opposed rotary piston(ORP) engine[1].

The main advantages of these engines compared to reciprocating ones are the higher power density and the lower number of components. Also, lower fuel octane number is required and due to the lower maximum temperature in combustion chamber a reduction in NO_x generation is succeed. However, because of the low reliability and the short longwearing of some components(especially labyrinth seals), the irregular torque supply at low and medium engine speeds, the high specific fuel consumption and the high unburned hydrocarbons (HC) emissions (Figure 1-12) the four stroke rotating ICEs development rate drops.

[1] www.douglas-self.com

Due to global warming recrudescence, clean fuels such as hydrogen and natural gas are attracting much attention as the combustion process of hydrogen is free of the formations in particulate matters (PM), greenhouse gas (CO2), CO and HC. Additionally, flam propagation speed of hydrogen combustion is much higher than other types of fuels.

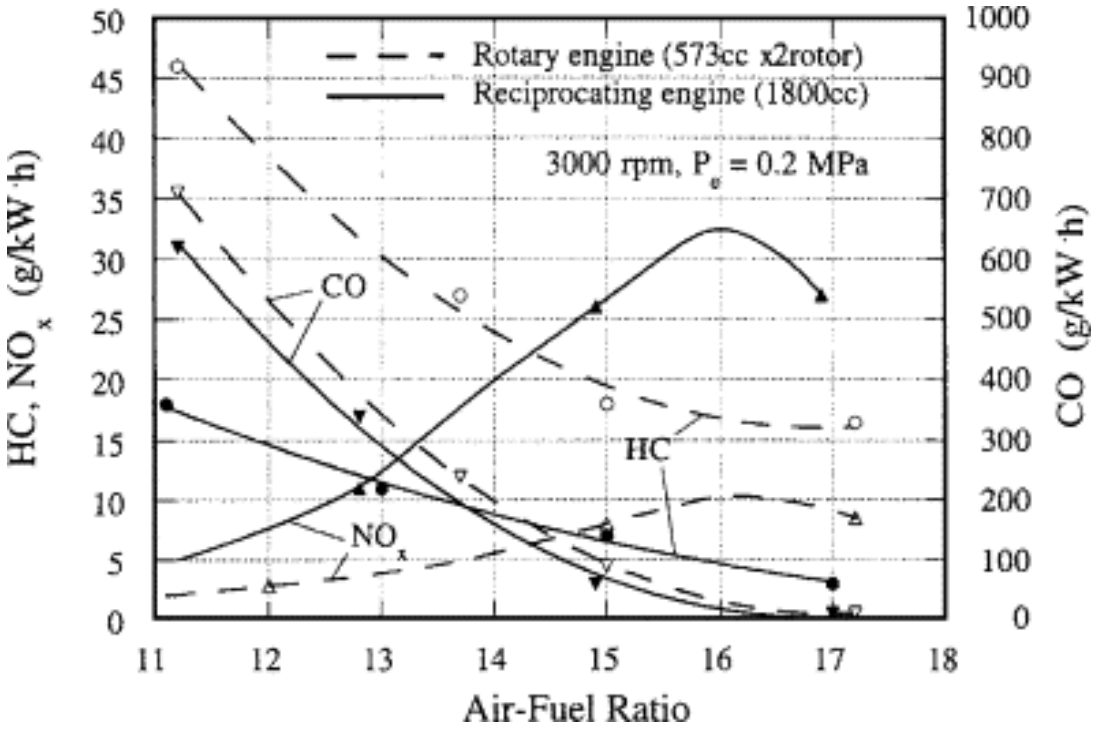

Figure 1-12: Rotary and Reciprocating engines emissions comparison. [Sher 1998]

According to Gao et al (2021), who compare both T/Ced hydrogen reciprocating and four stroke rotating engines, they conclude that hydrogen fuel will be more beneficial for Wankel engines and ORP engines. The reason is that hydrogen fuel can ease many disadvantages caused by narrow and long combustion chambers of Wankel engines. Also, it will be very useful for the ORP engines due to their short cyclic period.

1.3.6 Turbocharged Fuel Cells

The fuel cells are a promising sustainable efficiently energy option due to their low environmental impact in terms of GHG emissions and noise pollution. The most prominent configurations are described in the Table 1-1.

Similarly to the ICEs, a boosting system can be used with a fuel cell stack to increase its efficient while downsizing it. Depending of the fuel cell type, the boosting system can be either a T/C or a supercharger (Turbo-compressor[1]). Even if the fuel cell turbocharging is an efficient solution as Kerviel et al. (2018)

[1] https://www.garrettmotion.com/electric-hybrid/twostage-electric-compressor-for-fuel-cells/

point out, it cannot be accomplished in all fuel cell types due to the exhaust gas temperature being too low (to recover enough power to drive the compressor).

The fuel cells are well placed in the panorama of sustainable energy options owing to some of their important characteristics, such as low environmental impact, in terms of both polluting gases emissions and noise pollution, and the high- energy conversion efficiency.

Table 1-1: Summary of most prominent fuel cells. [Abdelkareem et al. 2021]

Fuel Cell Type	Membrane electrolyte	Fuel	Electrical Efficiency	Power range
Polymer electrolyte membrane (PEM)	Nafion	Hydrogen	30-50%	1W-500kW
Alkaline (AFC)	Alkaline	Hydrogen	62%	10W-200kW
Phosphoric acid (PAFC)	Phosphoric Acid	Hydrogen	40%	50 kW-1 MW
Molten carbonate (MCFC)	Molten Carbonate	Hydrocarbon Fuel	45-55%	1 kW-1 MW
Solid oxide (SOFC)	Yttria Stabilized Zirconia	Hydrocarbon Fuel	55-60%	5kW-3 MW

The most suitable for turbocharging fuel cells are the molten carbonate fuel cell (exhaust gas temperature = 400 °C) and the Solid Oxide Fuel Cell Systems (exhaust gas temperature = 297.6 °C) based on Xing et al. (2021) study. Typical T/Ced MCFC and SOFC layouts are depicted in the Figure 1-13. In most cases, a hybrid T/C is chosen aiming to contribute in overall electrical power generation.

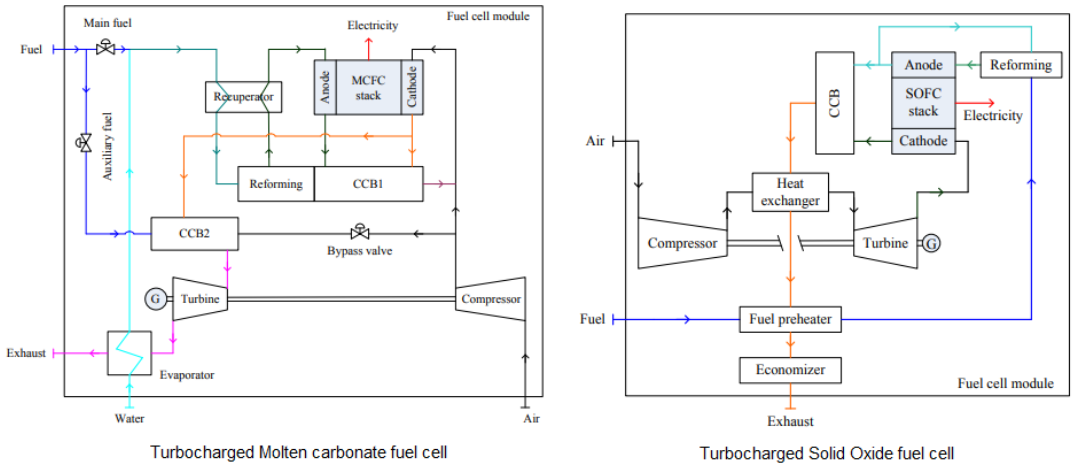

Figure 1-13: Turbocharged Fuel Cells typical lay outs. [Xing et al. 2021]

Pomfret et al. (2011) conclude that solid oxide fuel cells (SOFCs) in comparison with other fuel cells have several advantages, including the ability to operate using complex, carbon containing fuels via internal fuel reforming, increased poison tolerance, and fabrication from relatively inexpensive materials.

1.3.7 Solar micro gas turbines based on Turbocharger

A solar micro gas turbine, based on a T/C (Figure 1-14), is another promising sustainable efficiently energy option due to their low environmental impact in terms of GHG emissions. It is materialized using a T/C, a receiver, inlet and outlet ducts, a generator and a burner in the case of the hybrid configuration. The generator is coupled on the T/C shaft on the compressor side. A high-speed generator, equipped with the relevant electronics for connection to the network is envisaged. Alternatively, a gear box can be used to match (reduce) high T/C speed with that of a generator, if the two rotational speeds cannot be directly matched. In the solar-only configuration operation exploits only the available solar energy, while in hybrid configuration, solar energy substitutes (partially or entirely) the fossil fuel energy. Solar energy is captured by the receiver, which heats the air after it exits the compressor. Solar beams are concentrated on the receiver by a heliostat field. (Kalathakis et al. 2018).

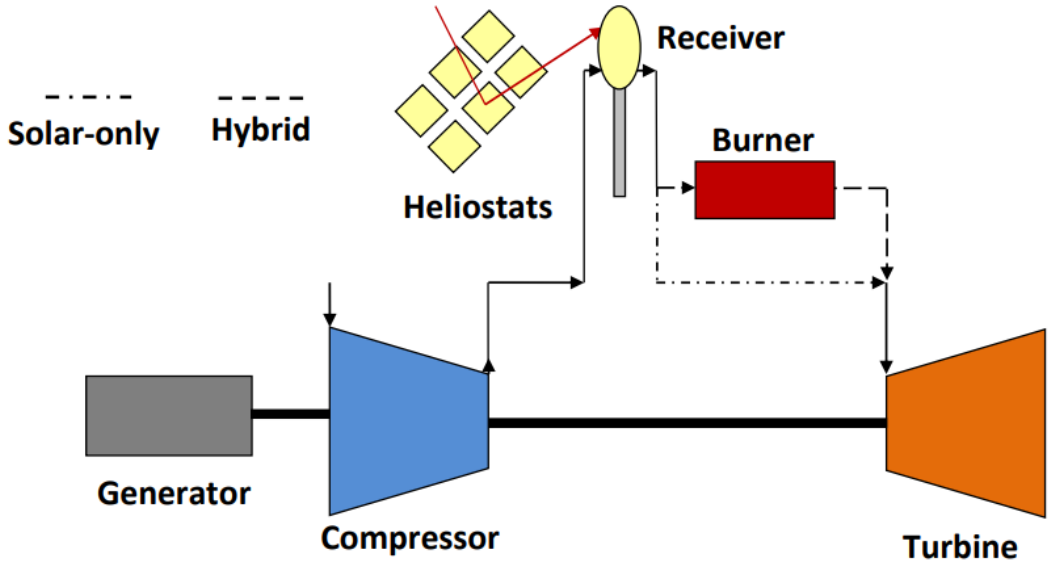

Figure 1-14: Solar micro gas turbine based on a T/C configuration.
[Kalathakis et al. 2018]

1.4 Motivation

As discussed, the T/C development is the key for GHG emissions reduction in transportation sector, as it plays significant role in a power generation unit efficiency enhancement, contributing to the fuel consumption reduction, independent of the type of engine or fuel. Due to the above-mentioned benefits in relation to GHG emissions, the research on T/C field is continuously increasing.

Motivating by the cooperation with a T/C manufacturer company[1] during PhD research, the current study focuses on two basic pillars of interest, as they are both academically and commercially attractive. The first one refers to T/C preliminary design, aiming to provide a more efficient design solution while the second one on T/C retrofit process for improved performance reconstitution.

For illustrating the impact of T/C efficient improvement as a GHG emission reduction mechanism, a simplified approach, presented by Sui et. al (2020), is followed for predicting global CO_2, NO_x, and HC daily emissions based on fuel consumption. Both NO_x, and HC are responsible for the annually premature death of 400000[2] people in the European region. Based on the marine traffic website[2,] the average number of Vessels track in daily base is about 250000 (Figure 1-15).

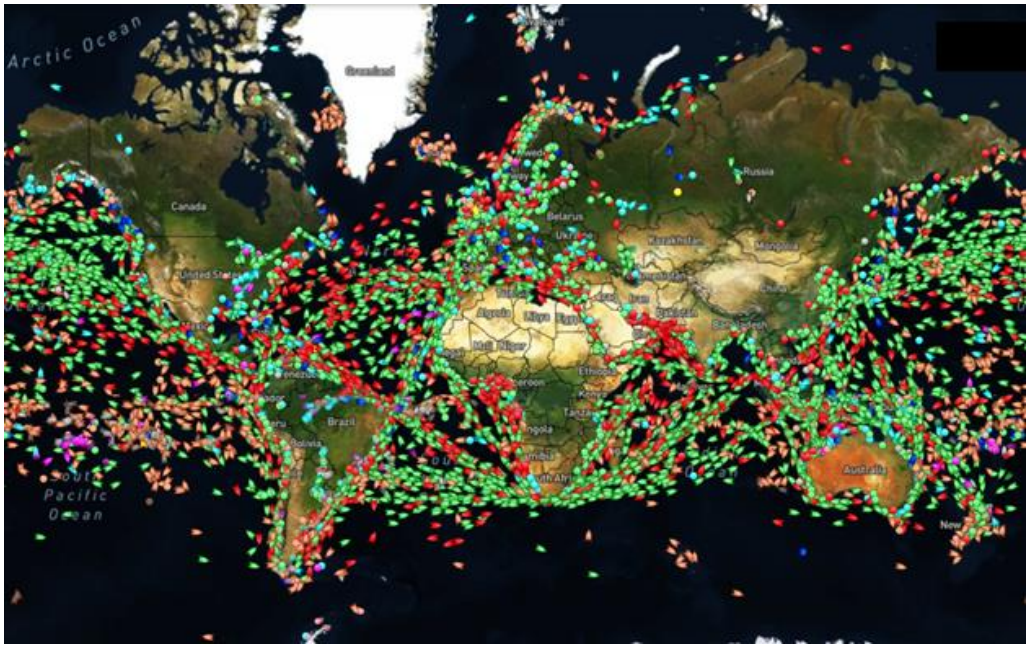

Figure 1-15: Vessel track live map.[3]

Thus, a mass marine engine fuel consumption reduction of about 0.1% can lead to a global daily reduction of about 18500, 432 and 24 emitted tons for CO_2, NO_x and HC respectively, showing the importance of T/C as a field of research.

[1] https://turbomed.gr/
[2] https://www.europarl.europa.eu/news/el/press-room/20161117IPR51548/nea-ethnika-oria-gia-tis-ekpompes-atmosphairikon-rupon
[3] https://www.marinetraffic.com

1.4.1 T/Ced Diesel Engine literature survey

T/C consists of two components, namely centrifugal compressor (CC) and radial turbine (RT) or axial turbine (AT) depending on diesel engine size. The impact of T/C modeling on diesel engine combustion mechanism and performance characteristics have been thoroughly examined in the past by Giakoumis and Tziolas (2018) and by Giakoumis et al. (2017). Also the influence of turbocharger heat transfer modeling both for diesel and gasolines engine performance parameters have been investigated using neural networks by Huang et al. (2018). Various types of models have been proposed and used in the literature for the simulation of performance and emissions of turbocharged diesel engines, depending on the application and configuration examined [Watson and Janota, 1982].

Concerning the diesel engine modeling, three are the main categories: zero-dimensional thermodynamic models, quasi-dimensional phenomenological models and multi-dimensional CFD models. In zero-dimensional thermodynamic models [Baldi et al. 2015 and Catania et al. 2011] the heat release is simulated in a simplified way, using empirical / mathematical expressions, without detailed study of physical and chemical sub-processes that actually take place in the combustion chamber, because these are strongly dependent on the spatial distribution of temperature and composition which are not taken into account. This approach is advantageous in applications where limited data are available regarding the design configuration and the operating parameters of the engine, while computational power is limited, and computational time is a critical parameter. In the field of phenomenological simulation models, quite important are the multi-zone combustion models, which provide a temporal and spatial distribution of combustion temperature and mixture composition based on the concept of fuel jet distribution into zones. A fair compromise between more detailed multi-zone and single-zone combustion models is provided by two-zone combustion models, which offer reasonable accuracy at economic computer runtime [Rakopoulos et al., 2003]. Two-zone models have been used very effectively for examining the effect of exhaust gas recirculation (EGR) rate and temperature on diesel engine combustion characteristics and pollutant emissions as demonstrated by Rakopoulos et al. (2018). Phenomenological models along with experimental campaigns have been used by Rakopoulos et al. (2015) and Rakopoulos et al. (2019) to examine the effect of various alternative fuels on HDDI turbocharged diesel engine performance characteristics and pollutant emissions under both steady-state and transient conditions.

On the other hand, the multidimensional CFD models [Petranović et al. 2018, Reitz and Rutland 1995 and Liang et al. 2010] are based on locally resolved solution of conservation of mass, energy and momentum and include detailed sub-models for spray and combustion phenomena. With this approach it is possible to obtain detailed results regarding the gas flow pattern and the spatial distribution of temperature and composition inside the combustion chamber. However, these models are very demanding in terms of detailed design data,

computational power and expertise to be applied making its use appropriate only for specific applications.

The intermediate category is the quasi-dimensional phenomenological models, which allows to execute efficient, fast and economic preliminary calculations of heat release models and exhaust emissions as a function of important engine parameters like injection pressure, injection timing, swirl ratio and boost pressure. These models are based on physical and chemical sub-models for fuel spray formation, air fuel mixing, combustion and emission formation, offering a fair compromise between the detailed CFD ones and the zero-dimensional models, being appropriate as predictive tools conducting parametric studies during engine development [Pagán Rubio et al. 2018, Pariotis and Hountalas 2003 and 2004, Pariotis et al. 2005].

Focusing on models applied to investigate the matching between diesel engine and a turbocharger system, Charlton (1992) proposed the SPICE modeling software, which is a quasi-dimensional model, based on the filling and emptying method and is particularly suited for turbocharged diesel engine systems. The system of components is modeled as a combination of thermodynamic volumes, flow junctions and shafts. The intake and exhaust valves are represented by junctions, each having a schedule of effective flow area versus crankshaft position. One dimensional compressible flow equations are used to obtain flow rates for given pressures in the neighboring volumes. The performance of the turbocharger compressor and turbine is represented by tabulated data taken from performance maps published by the manufacturers.

An alternative approach has been proposed by Ledger et al. (1971 and 1973), focusing on the transient simulation of turbocharged engines, by linking steady speed experimental data (regarding engine performance and gas flow) with dynamic models of the mechanical components of the system. However, the weakness of this approach is that it is heavily dependent on experimental data and it oversimplifies the simulation of combustion. A more comprehensive transient model (extended from the filling and emptying model) was developed by Watson and Marzouk (1977). Their model was used to investigate turbocharger response problems at a fundamental level. It takes into account the non-linear influence of combustion on the torque developed and the exhaust-gas energy available at the turbine, the pulsating nature of gas flow (including reverse flow) and also the influence of manifold pressure on pumping work.

The importance of the turbomachinery component maps used as part of a turbocharged engine model has been highlighted by Pesiridis et al. (2012). As discussed, suitable fitting and extrapolation methods should be applied for accurately predicting the engine performance.

Considering T/C components 1D analysis, the flow through the impeller is assumed uniform and the off-design performance is calculated using mean streamline single zone models [Wasserbauer and Glassman 1975, Aungier 2000, 2005]. A significant aspect for the compressor map is the prediction of surge line. Rodgers (1963) set the surge and choke limits for a wide range of centrifugal compressors using experimental data. Another approach was made by Japikse (1996), who assumed that a jet-wake structure exists in the impeller passage.

Stuart et al. (2017) made a new approach in CC 1D analysis using a three-zone model assuming that impeller exit recirculation influences compressor work input. For the turbine performance, 1D models have been extensively applied, as for example described by Romagnoli and Martinez–Botas (2011) utilizing mean line analysis method well described in the past (e.g. Wasserbauer and Glassman 1975).

The increasing need for marine engine system downsizing, combined with the harsh working conditions, leads to frequent engine components failure, especially for the T/C. To ensure T/Ced engine safe operation, by preventing those failures, a fault diagnosis system must be developed.

The development of an integrated simulation framework for simulating fault effects on turbocharged diesel engines is expected to contribute towards quantifying the degradation effect on operational cost by providing information on the increased fuel consumption and decreased load [Murphy et al., 2015]. At the same time, it may provide information on maintenance cost and operability concerning compressor surge margin reduction along with temperature and rotational speed changes that affect bearings life. Additionally, it can be used for providing suitable fault signatures, as discussed by Pagán Rubio et al. (2018).

For T/C fault diagnosis, slight improvement has been made, comparing with the rest of turbomachines (e.g., industrial and aircraft gas turbines), relying in most cases on engineers personal experience. Barelli et al. (2009) presents a T/C diagnosis methodology based on artificial neural network (ANN) and proposed a frequent data gathering campaign every six–nine months to ensure the proper operation of such a system. Sakellaridis and Hountalas (2013) also develop a radial turbine mean-line model as part of a T/C diagnostic tool with the ability of adapting to available measured data. Additionally, Cui et al. (2018) model a gas-path diagnosis for diesel engine T/C, using health factors (flow capacity and isentropic efficiency), hence monitoring the T/C health status. In this way, the fault effect on the stall margin and therefore on operability is predicted, which is usually neglected in the literature where analysis do not include CFD simulation.

T/C fouling, which is the main system degradation and fault reason, can be caused due to compressor fouling, turbine fouling, or a combination of both, leading to inefficient operation and a shift of the operating and stall margin as depicted in Figure 1-16. All compressors are susceptible to fouling as a result of the ingestion of air impurities that accumulate on and stick to gas path free surfaces, blades, and shrouds, modifying airfoil geometry [Diakunchak, 1992]. A typical T/C fouled compressor is shown in Figure 1-17.

Additionally, oil leaks from compressor seals and bearings mix with some of the ingested particles and deposit on the blade surfaces (Landersheim et al. 2021). The result will be the deterioration of airfoil aerodynamic behavior and reduction of flow area leading to the compressor and engine performance degradation.

Turbine fouling is primarily dependent on type and quality of the operating fuel as discussed by (Meher-Homji 1987). When heavy fuel oil or crude oil is used, the turbine degradation is expected to be significant due to low melting point of ashes, metals, and unburned hydrocarbons. The contaminant deposition

will have an impact over blade, by changing the airfoil shape, the inlet angle, and increasing the surface roughness. These effects will result in reducing the airfoil throat area and apparently reducing the performance characteristics and the service life of the component. Also, especially in marine gas turbines, sulfidation may occur resulting in turbine corrosion. As a result, fouling rate will increase, as discussed by [Basendwah 2006].

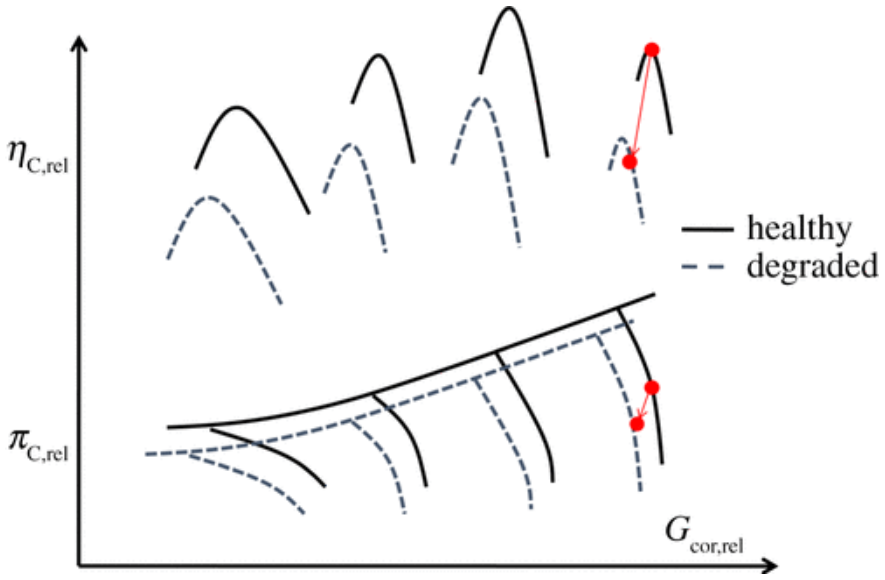

Figure 1-16: Turbocharger Compressor healthy and fouled operation comparison. [Cui et al. 2018]

Figure 1-17: Typical T/C fouled compressor[1].

[1] www.turbomed.gr

1.4.2 Preliminary Turbocharger design literature survey

Preliminary 1D design is the key for a successful component manufacturing. With a comprehensive design review being carried out, an efficient, operable, manufacturable and structurally safe 1D design solution should be provided. The detailed design is always a time-consuming process, hence by developing an efficient preliminary design procedure, both overall design process time and cost can be reduced.

1D Geometry optimization is always sought in T/C design process. The design of the turbo-components is conducted separately and not at engine level. Qiu et al. (2013) describe the importance of T/C design on engine system level, nevertheless their work is limited to centrifugal compressor (without volute).

Ebel et al. (2021) propose a preliminary design method following the well known reverse model process, presented by Japikse and Baines (1997), for both turbo-components. Such a process does not ensure that the design geometry is optimum as no optimization process is followed. Catalani et al. (2021) present a 3D T/C design method, skipping the preliminary design part as an initial 3D T/C geometry is given. Both works, even though they are focused on T/C design for specific ICE, they are not performed in engine system level, as the engine model is utilized once for both calculating the T/C demanding operating conditions and evaluating the designed T/C new operation. Thus, there is no interaction between engine and T/C design process. Also, the fully unchoked forced designed turbine operation in combination with the highly small stall margin in both works shows the importance of further research in the field of T/C design.

For 1D centrifugal compressor design, Japikse and Baines (1997) present a 1D procedure in their book by following a reverse model approach. Rossetti et al. (2009) on the other hand, focus on vaned diffuser with incompressible flow optimization, trying to achieve the best compromise between flow deflection, static pressure recovery and total pressure loss. Li et al. (2012) create an optimization design method for the entire centrifugal compressor (without the volute), using 1D single zone model. The second part of his work is focused on impeller and vaned diffuser matching optimization.

For 1D radial turbine design, Japikse and Baines (1997) present a 1D design process similar to the compressor one. Alshammari et al. (2021) propose a radial inflow turbine optimization method, combining meanline and CFD approaches, focusing only on turbine performance and neglecting the part of structural analysis. At the end of their work, they highlight the importance of the 3D CFD turbine stage optimization. Lv et al. (2018), following an integrated approach, combine a 1D design model with a sequential quadratic programming optimization algorithm, aiming to design a high efficiency sCO_2 radial inflow turbine. In the same way, Pini et al. (2013), Casati et al. (2014) and Wang et al. (2019) combine a genetic algorithm with a meanline design tool.

Concerning 1D axial turbine design, Japikse and Baines (1997) propose a 1D turbine design process, similar to centrifugal compressor and radial turbine ones. Turcotte et al. (2004) present a two-stage turbine multidisciplinary design optimization, utilizing both 0-D performance and 1D aerodynamic models while ensuring rotor disc structural integrity with a simplified stress analysis tool.

Similar to previous study, Kolias et al. (2018) propose an entire turbofan engine multidisciplinary design process. Sathish et al. (2019) work fulfills the stated objective of sCO_2 axial turbine design for Waste Heat Recovery application.

From all the above 1D design processes the following conclusions are drawn:

- 1D T/C compressor and turbine have not been designed in engine system level.
- 1D T/C design process including different possible configurations has not been performed, hence not ensuring the optimal performance improvement.
- The above design processes focus on 1D performance improvement without ensuring structural integrity.
- 1D axial turbine design focuses in most cases on other applications (turbofan, turboprop, etc.) rather than turbocharging.
- In 1D T/C optimization, dimensional geometrical parameters(hub radius, impeller tip radius, etc.) are selected as optimization variables. Such an approach makes the design process not general, since for different components scales, both the range of variables and the initial geometry must be redefined, hence making the process difficult to be automated in terms of a more general component design process.

The modal analysis plays significant role in T/C design process. In most cases modal analysis is performed during detailed and not preliminary (1D) design, hence, utilizing high-fidelity modal analysis tools (e.g. Zhang et al. 2012, Zhai et al. 2014). For ensuring modal structural integrity during preliminary design, a more simplified tool is sufficient as it provides accurate results in reasonable time. A conventional simplified approach for analyzing the turbo spool dynamic behavior is the usage of the equivalent Jeffcott rotor [Nguyen-Schäfer 2015]. Additionally, Yang et al. (2016) propose a simplified model, consisting of two rigid massive disks (compressor and turbine), two journal bearings and a compact shaft separated into three equivalent springs (flexible shaft) and two equivalent disks. Note that in this analysis the gyroscopic effect is not taken into account.

Serrano et al. (2020) for improving their T/C model meanline accuracy, they calibrate both compressor and turbine meanline models against measured data. Such a calibration may be useful for 1D modelling, although it cannot be used for a wide-used T/C design tool. No T/C volute CFD-based surrogate or artificial neural network loss models have been proposed in the open literature, in order to improve loss prediction accuracy while avoiding geometries with intensive 3D effects during preliminary design.

1.4.3 Turbocharger retrofit literature survey

Retrofitting an existing engine with newer T/C technology is an effective method of extending its useful life while improving its operation from both

economic and environmental point of view. The T/C retrofit is a complicated and time-consuming process, as each turbo-component must be chosen carefully in order to match the engine while retaining or improving the overall system efficiency. The Figure 1-18 illustrates a typical retrofitting process.

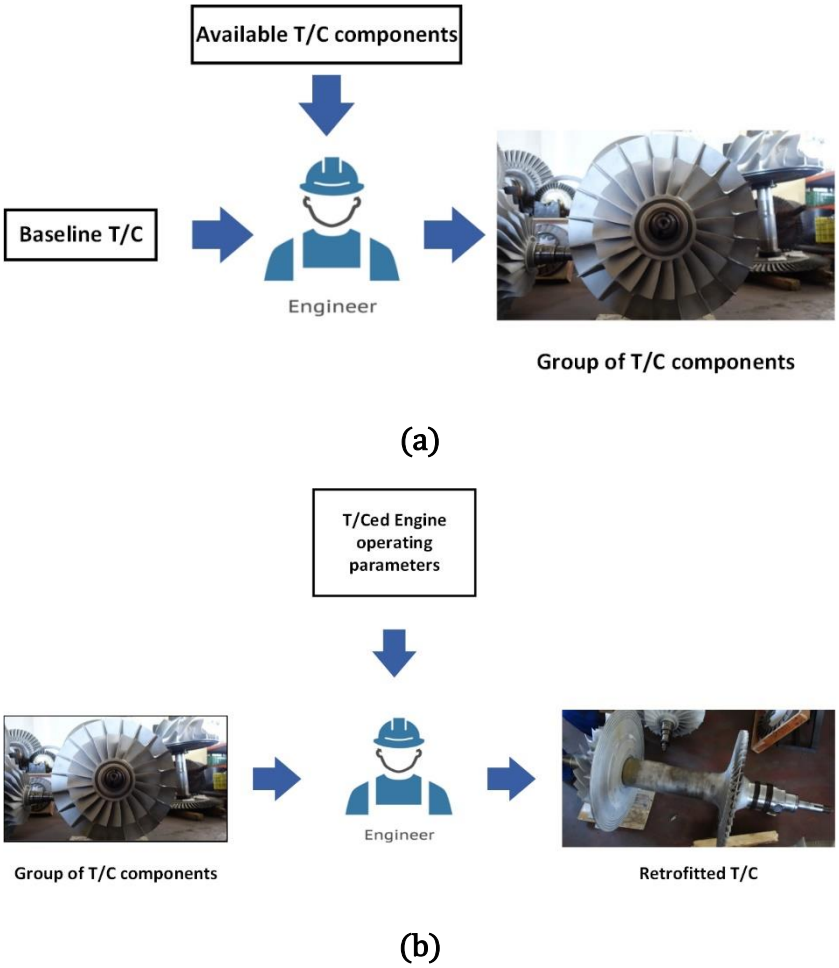

Figure 1-18: Typical retrofitting process: (a) Selecting available T/C component with similar size to baseline ones (b) Selecting the best fitted T/C components based on T/Ced diesel engine operation.

Generally, in a T/C retrofitting procedure, the engineer first selects a group of available T/C components with the same configuration as the baseline one. For example, in case of a baseline T/C with radial turbine, the bank of possible T/C components to select from is shown in the left part of Figure 1-19. Next, according to the T/Ced engine operating parameters which are specified by the customer, the engineer selects the one that best matches the overall system performance, as shown in Figure 1-19. Thus, assuming that the baseline T/C has a nominal volumetric flow rate and a nominal pressure ratio of about 0.8 m^3/s and 3, respectively, the most obvious selection is the circled one.

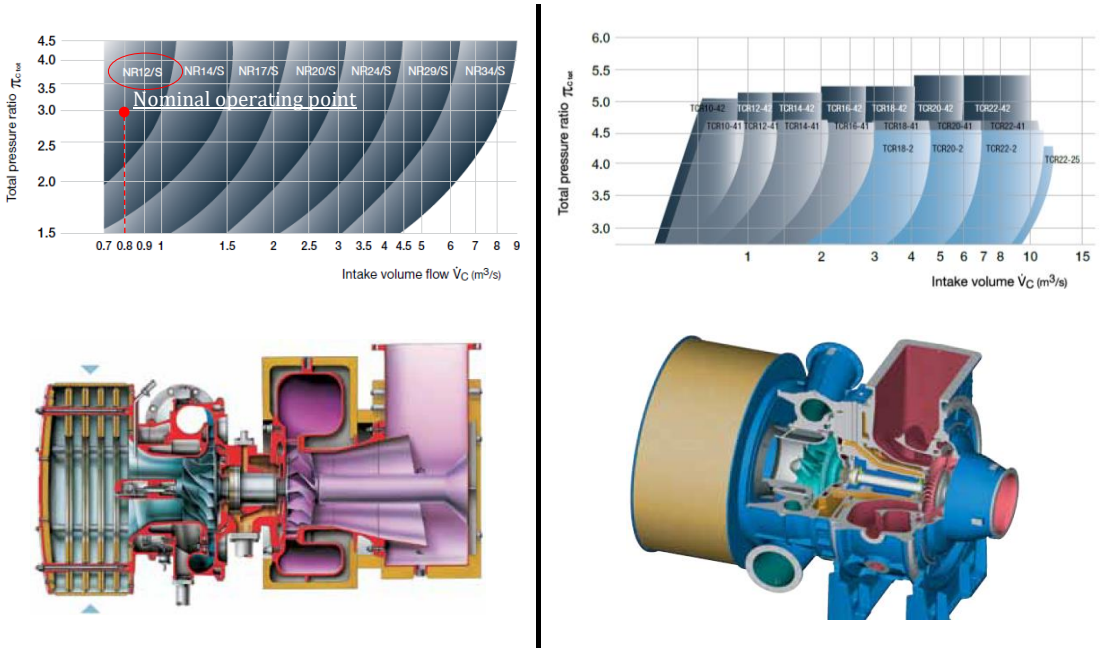

Figure 1-19: Typical retrofitting process: Selecting the best fitted T/C components based on T/Ced diesel engine operation[1].

The retrofit process, relying on the engineer's personal judgment, may not always match in an optimal way the system performance and, thus, a T/Ced engine unnecessary degradation occurs. This degradation leads to an engine fuel consumption increase and to a subsequent NO_x and CO_2 increase. Both gases are responsible for climate change and global warming.

The development of a retrofit tool can benefit both the T/C manufacturer and the marine company, by decreasing the retrofitting process time, hence leading to lower process cost, productivity improvement and anchored ship time reduction. For the majority of retrofitting cases, the most obvious approach is to use market available turbo-components, because of the high cost for designing and manufacturing new tubro-components. In case there are no available components that could match the ICE, a possible solution is to redesign a new component aiming at matching the diesel engine performance.

1.5 Goals and Objectives

The goal of this thesis is to investigate the aforementioned pillars of interest, proposing more efficient and novel approaches.

A number of simulation tools are developed, encompassing three specific processes, hence providing a fully automatic retrofit-design solution or the option for simulating a T/Ced diesel engine.

[1] library.e.abb.com

The methodology applied in order to meet the objectives are to:

- Develop each turbo-component meanline model and verify it against available measured data.
- Develop an T/Ced Diesel engine model and verify it against available measured data.
- Develop static and modal structural analysis tools and verify them against commercial high-fidelity software numerical results.
- Propose a multi-point preliminary T/C design process based on T/Ced diesel engine operating line, while ensuring that the solution is both structurally safe and manufacturable.
- Propose a retrofitting process, examining all the available turbo-components and selects the one that best matches the entire engine system, aiming to retain or improve the diesel engine efficiency.
- Develop and fill an "available turbo-components" database.
- Perform a retrofitting process for a specific T/C, examining the best retrofit solution. In this process, both turbo-components and entire T/C replacement are investigated.
- Perform a re-design process in engine system level for a specific T/C, analyzing all possible configurations. In this process, both turbo-components and entire T/C re-design are investigated.
- Quantify the impact of all retrofit and re-design solutions in terms of techno-economic assessment.

The T/C fault simulation is an important part of the T/C design-retrofit process as the engine components are led to frequent failure, due to the increasing need for engine system downsizing, combined with the harsh working conditions. Additionally, as the stall margin reduction due to the fault effect is predicted, the T/C compressor can be designed with a sufficient stall margin, hence ensuring the stable operation even under faulty operation. Thus, the following methodology are also applied:

- Perform both T/C and intercooler fouling analyses, investigating their effect on both T/Ced diesel system degradation and compressor stable operation regime.

For applying the above methodology, the following tools-models are developed in order to encompass these three specific processes, namely T/Ced diesel engine simulation, T/C design and T/C retrofit. These tools are:

- CC meanline model.
- RT meanline model.
- AT meanline model.
- Intercooler model.
- T/C Matching analysis model.
- CFD-based CC volute surrogate loss model.
- CFD-based RT volute surrogate loss model.

- T/Ced simulation process development.
- CC preprocessor(reverse model).
- RT preprocessor(reverse model).
- AT preprocessor(reverse model).
- Static structural analysis tools for CC, RT, AT
- 1D to 3D transformation tool: automatically 3D blade geometry generation having meanline model geometrical parameters as input data.
- T/C modal structural analysis tools.
- Utility function development for 3D CFD-FEA simulation.
- T/C design process development and integration in a commercial optimization tool.
- T/C retrofitting process development.
- Turbo-components trimming tool.

These processes can be applied on any type of T/Ced reciprocating engine and in every T/Ced engine system (e.g. T/Ced Wankel, T/Ced SOFC, etc.), by replacing the reciprocating engine model.

1.6 Organization of the Thesis

The remaining text is organized in the following chapters. In Chapter 2 a presentation of the processes is performed. Specifically, a technical detailed description of each process is carried out, including sub-tools, their development environments and how they are coupled with each other. In Chapters 3, 4 and 5, an extensive description of the corresponding processes is also performed.

In Chapter 3, the T/Ced diesel engine simulation process is analyzed. All the integrated sub-models are presented, focusing on their theory-correlations and each other coupling. Additionally, both the centrifugal compressor and the radial turbine volutes loss models enhancement via CFD-based surrogate loss models are analyzed, including a presentation of the corresponding learning chosen methods and processes. Finally, a validation of the model of each individual component, as well as the entire T/Ced diesel engine, is performed.

In Chapter 4, the automatic T/C preliminary design process follows. It is basically a 1D T/C multi-point design optimization process, aiming to provide a fast and reliable solution based on T/Ced diesel engine range of operation. Additionally, the turbo-component/entire T/C static and modal structural integrity is ensured by using a simplified structural analysis tool. Dimensionless parameters are used as optimization variables, for given nominal mass flow, speed and power. A CFD compressor multi-point design optimization option is provided, producing an optimized 3D compressor geometry. It complies with the T/Ced diesel engine range of operation, while structural integrity is ensured by using Finite Element Analysis.

In Chapter 5, the automatic T/C retrofit process is analyzed, while presenting all possible T/C retrofit options. Then, a more detailed description is

followed for each retrofit option, showing how the tool examines all available turbo-components in order to select the one that best matches the entire engine system, aiming to retain or improve the diesel engine efficiency.

In Chapter 6 and 7, the use of the developed tools and processes is demonstrated through several application test cases. In Chapter 6, the tools are applied in a retrofitting case study, where four retrofitting options are analyzed (compressor retrofit, T/C retrofit, compressor redesign and entire T/C redesign).

In the first and second option, T/C retrofitting, using existed turbo-components, is carried out. In the third option, a compressor designing is performed, following a weighted single-objective optimization procedure, in order to provide an improved retrofitting solution, aiming to at least reconstituting the original diesel engine performance, while ensuring compressor structural integrity. In the fourth option, a weighted single-objective optimization procedure is also employed to design both compressor and turbine to match the entire T/Ced system in an improved way. The optimization process focuses on engine fuel consumption reduction in the engine range of operation, while ensuring appropriate matching between turbomachinery components and the diesel engine. Both turbo-components structural integrity (static-modal) is ensured by using simplified structural and modal analysis. Dimensionless parameters are used as optimization variables, for both compressor and turbine, providing a more general and automated design process independent of the T/C scale.

Additionally, volute loss surrogate models, trained with CFD simulated data, are also provided for both centrifugal compressor and radial turbine as option, allowing for a more detailed design process. The process produces four T/C (compressor and turbine) optimal 1D geometries (if it is possible), of different configurations, namely vaneless diffuser centrifugal compressor – axial turbine, vaned diffuser centrifugal compressor – axial turbine, vaneless diffuser centrifugal compressor – radial turbine, vaned diffuser centrifugal compressor – radial turbine. The combination that gives the best improvement to the diesel engine operation is identified. Finally, a techno-economical assessment is performed aiming to present the best fitted retrofit option from an economic aspect.

In chapter 7, the tools are applied in a T/Ced engine fouling analysis for both T/C and intercooler as fault effect on engine system degradation is an important part of both T/C design and retrofit process. The T/C component faults simulation is materialized using physical consistent parameters such as roughness.

In the last Chapter the conclusions of the thesis, the contributions to science and technology and the future work suggestions are discussed, including a list of publications.

1.7 References

Abdelkareem, M. A., Elsaid, K., Wilberforce, T., Kamil, M., Sayed, E. T. and Olabi, A. (2021). Environmental aspects of fuel cells: A review. Science of the Total Environment 141803 (752).

Aungier, R.H. (2000). Centrifugal Compressors, A Strategy for Aerodynamic Design and Analysis. ASME PRESS.

Aungier, R. H. (2005). TurbineAerodynamics Axial Flow And Radial Inflow Turbine Design And Analysis. ASME PRESS, New York.

Alshammari, F., Pesyridis, A. and Elashmawy,. M. (2021). Turbine optimization potential to improve automotive Rankine cycle performance. Elsevier Applied Thermal Engineering 186(2021) 116559.

Baldi, F., Theotokatos, G, and Andersson, K. (2015). "Development of a combined mean value-zero dimensional model and application for a large marine four-stroke Diesel engine simulation." *Applied Energy* 154, 402-415.

Barelli, L., G. Bidini and F. Bonucci. (2009). Diagnosis methodology for the turbocharger groups installed on a 1 MW internal combustion engine. Applied Energy 86 (2009) 2721–2730.

Barki, D. and Deleze-Black, L. (2017). Review of Maritime Transport 2017. United Nations Conference on trade and development.

Basendwah, A., Pilidis, P. and Li, Y. G. (2006). Turbine Off- Line Water Wash Optimization Approach for Power Generation. Proceeding of ASME Turbo expo, GT2006-90244, Barcelona, Spain.

Buchi, A., (1905). Highly supercharged compound engine(Patent No. 204630) Imperial Patent Office of the German Reich.

Bricknell, D. (May 8-11, 2006.). Marine Gas Turbine Propulsion System Application. Proceeding of ASME Turbo Expo. GT2006-90751, Barcelona, Spain.

Casati, E., Vitale, S., Pini, M., Persico, G., and Colonna, P. (2014). Centrifugal Turbines for Mini-Organic Rankine Cycle Power Systems. Journal of Engineering for Gas Turbines and Power, 136, p. 122607.

Catalani, I., Agnolucci, A., Balduzzi, F., Bianchini., A., Arnone, A., Ferrara, G., Vichi, G., Bellissima, A., Minamino, R., and Asai, G. (2021). Aerodynamic optimization of a turbocharger unit based on the overall efficiency enhancement of an internal combustion engine for stationary power production. Proceedings of ASME Turbo Expo, GT2021-58843, Virtual, Online, June 7-11.

Catania, A.E., Finesso, R., and Spessa, E. (2011). "Predictive Zero-Dimensional Combustion Model for DI Diesel Engine Feed-Forward Control." *Energy Conv. Manageme.* 52(10), 3159-3175.

Charlton, S.J. (1992). “SPICE - Simulation program for internal combustion engines.” User Manual (University of Bath).

Cihan, Ö., Doğan, H., Kutlar, O.A., Demirci, A. and Javadzadehkalkhoran, M. (2020). Evaluation of heat release and combustion analysis in spark ignition Wankel and reciprocating engine. Fuel, 261, 116479.

Cui ,X., C Yang ,J. Serrano and M. Shi. (2018). A performance degradation evaluation method for a turbocharger in a diesel engine. R. Soc. open sci. 5: 181093.

Diakunchak, I. S. (1992). Performance Deterioration in Industrial Gas Turbines. ASME J. Eng. Gas Turbines Power, 114(2): 161-168.

Ebel, T., Anderson, M., Pandya., P., Perchanok, M., Tiney, N., Gravante, S. P. (2021). Use of an integrated approach for analysis and design of turbocharged internal combustion engine. Proceedings of ASME Turbo Expo, GT2021-60326, Virtual, Online, June 7-11.

Gao, J., Xing, S, Tian, G, Ma, C, Zhao, M, and Jenner, P. (2021). Numerical simulation on the combustion and NOx emission characteristics of a turbocharged opposed rotary piston engine fuelled with hydrogen under wide open throttle conditions. ELSEVIER Fuel 285 118210.

Giakoumis, E.G., and Tziolas, V. (2018) “Modeling a variable-geometry turbocharged diesel engine under steady-state and transient conditions”, *J. Energy Engineering, ASCE,* 144(3), 04018017, DOI: 10.1061/(ASCE)EY.1943-7897.0000537.

Hu, B., Yang, J., Li, J., Li, S. and Bai, H. (2019).Intelligent Control Strategy for Transient Response of a Variable Geometry Turbocharger System Based on Deep Reinforcement Learning. MDPI Processes, 7(9), 601.

Huang, L., Ma, C., Li, Y., Gao, J., and Qi, M. (2018) “Applying neural networks (NN) to the improvement of gasoline turbocharger heat transfer modeling”, Applied Thermal Engineering, 141, 1080-1091

Japikse, D., N. C. Baines. (1997). Introduction to Turbomachinery. Concepts ETI Inc and Oxford University Press.

Japikse, D. (1996). Centrifugal Compressor Design and Performane. 3rd ed., Concepts ETI Inc.: Wilder,TN, USA, pp. 2.26–2.81.

Kalathakis, C., Aretakis, N., and Mathioudakis, K. (2018). Solar Hybrid Micro Gas Turbine Based On Turbocharger. Appl. Syst. Innov. 1(3), 27.

Kerviel, A., Pesyridis, A., Mohammed, A. and Chalet, D. (2018). An Evaluation of Turbocharging and Supercharging Options for High-Efficiency Fuel Cell Electric Vehicles. MDPI Applied Sciences. 8(12):2474.

Kolias, I., Alexiou, A., Aretakis, N. and Mathioudakis, K. (2018). Direct integration of axial turbomachinery preliminary aerodynamic design calculations in engine performance component models. Proceedings of ASME Turbo Expo 2018, GT2018-76494, Oslo, Norway, June 11-15.

Lakshminarasimha A. N., Boyce, M. P. and Meher-Homji, C. B. . (1994). Modelling and Analysis of Gas Turbine Performance Detrerioration. ASME J. Eng. Gas Turbines Power,, 116, 46-52.

Lakshminarasimha, A.N., Boyce, M.P., and Meher-Homji, C.P. (1994). "Modelling and Analysis of Gas Turbine Performance Detrerioration." *ASME J. Eng. Gas Turbines Power,,* 116(1), 46-52.

Landersheim, V., Tran, D. D., Pham, T., Manushyna, D., Geury, T., Wilkins, S. and Hegazy, O. . (2021). Emissions and Total Cost of Ownership Assessment of Hybrid Propulsion Concepts for Bus Transport with CNG or Diesel Engine. IEEE, Sixteenth International Conference on Ecological Vehicles and Renewable Energies (EVER).

Ledger, J.D., Benson, R.S., and Furukawa, H. (1973). "Improvements in transient performance of a turbocharged diesel engine by air injection into the compressor." *SAE Paper No. 730665*, SAE, Warrendale, PA.

Ledger, J.D., and Walmsley, N.D. (1971). "Computer simulation of a turbocharged diesel engine operating under transient load conditions." *SAE Paper No. 710117*, SAE, Warrendale, PA.

Li, X., Xi, G., Hua, J. and Gong W. (2012). Investigation of the Wake Effect from the Centrifugal Splitter Impeller Blade to the Vaned Diffuser. Proceeding of ASME Turbo Expo 2012, GT2012-68927, Copenhagen, Denmark, June 11–15.

Liang, L., Naik, C., Puduppakkam, K., Wang, C., Modak, A., Meek, E., Ge, H., Reitz, R., and Rutland, C. (2010). "Efficient Simulation of Diesel Engine Combustion Using Realistic Chemical Kinetics in CFD." *SAE Paper No. 2010-01-0178,* SAE, Warrendale, PA

Lv, G., Yang, J., Shao, W. and Wang, X. (2018). Aerodynamic design optimization of radial-inflow turbine in supercritical CO2 cycles using a one-dimensional model. Elsevier Energy Conversion and Management 165(2018) 827-839.

Mariani, A., Mastellone, M. L., Morrone, B., Prati, M. V. and Unich, A. (2020). An Organic Rankine Cycle Bottoming a Diesel Engine Powered Passenger Car. MDPI Energies, 13(2), 314.

Martínez-Lao, J., Montoya, F. G. Montoya M. G. and Manzano-Agugliaro, F. (2017). Electric vehicles in Spain: An overview of charging systems. Elsevier Renewable and Sustainable Energy Reviews, Volume 77, Pages 970-983.

Meher-Homji, C. B . (1987). Compressor and Hot Section Fouling in Gas Turbines – Causes and Effects. Proceedings of the 9th Industrial Energy Technology Conference. Houston: Texas A&M University.

Murphy A.J., Norman, A.J., Pazouki, K., and Trodden, D.G. (2015). "Thermodynamic simulation for the investigation of marine Diesel engines." *Ocean Engineering*, 102, 117-128.

Nguyen-Schäfer, H.,. (2015). Rotordynamics of Automotive Turbochargers. Spinger International Publishing, Second Edition.

Olmer, N., Comer, B., Roy, B., Mao, X. and Rutherford, D. (2017). Greenhouse gas emissions from global shipping, 2013–2015. The International Council on Clean Transportation (ICCT), Washington.

Pariotis, E., Hountalas, D., and Rakopoulos, C. (2005). "Modeling the Effects of EGR on a Heavy Duty DI Diesel Engine Using a new Quasi-Dimensional Combustion Model." *SAE Paper 2005-01-1125*, SAE, Warrendale, PA, Pages 20.

Pariotis, E. and Hountalas, D. (2004). "Validation of a Newly Developed Quasi-Dimensional Combustion Model - Application on a Heavy Duty DI Diesel Engine." *SAE Paper 2004-01-0923*, SAE, Warrendale, PA, Pages 15.

Pariotis, E. and Hountalas, D. (2003). "A New Quasi-Three Dimensional Combustion Model for Prediction of DI Diesel Engines' Performance and Pollutant Emissions." *SAE Transactions, J. Engines,* 112, 1417-1429 .

Pagán Rubio, J.A., Vera-García, F., Hernandez Grau, J., Muñoz Cámara, J., and Albaladejo Hernandez, D. (2018). "Marine diesel engine failure simulator based on thermodynamic model." *Applied Thermal Engineering.*, 144, 982-995.

Petranović, Z., Sjerić, M., Taritaš, I., Vujanović, M., and Kozarac, D. (2018). "Study of advanced engine operating strategies on a turbocharged diesel engine by using coupled numerical approaches." *Energy Convers. Manage.*, 171, 1-11.

Pesiridis A., Salim, W., and Martinez-Botas, R.F. (2012). *Turbocharger Matching Methodology for Improved Exhaust Energy Recovery*. 10th International Conference on Turbocharging and Turbochargers of the IMechE. Woodhead Publishing.

Pini, M., Persico, G., Casati, E., and Dossena, V.,. (2013). Preliminary Design of a Centrifugal Turbine for Organic Rankine Cycle Applications. Journal of Engineering for Gas Turbines and Power, 135, p. 042312.

Pomfret, M. B., Steinhurst, D. A., and Owrutsky, J. C. (2011). Methanol and Ethanol Fuels in Solid Oxide Fuel Cells: A Thermal Imaging Study of Carbon Deposition. Energy & Fuels, 25(6), 2633–2642.

Popular Science Magazine. (1979). Times-Mirror Magazines, Inc., Vol. 214, No. 1 Paperback.

Qiu, X., Fredriksson, C.F., Baines, N. C. and Backlund, M. (2013). Designing Turbochargers with an integrated design system. Proceeding of ASME TurboExpo, GT2013-94894, San Antonio, Texas, June 3-7.

Rakopoulos, C.D., Rakopoulos, D.C., Kosmadakis, G.M., and Papagiannakis, R.G. (2019). "Experimental comparative assessment of butanol or ethanol diesel-fuel extenders impact on combustion features, cyclic irregularity, and regulated emissions balance in heavy-duty diesel engine." Energy

Rakopoulos, C.D., Rakopoulos, D.C., and Giakoumis, E.G. (2015). "Impact of properties of vegetable oil, bio-diesel, ethanol and n-butanol on the combustion and emissions of turbocharged HDDI diesel engine operating under steady and transient conditions." *Fuel* 156, 1-19.

Rakopoulos, C.D., Rakopoulos, D.C., Mavropoulos, G.C., and Kosmadakis, G.M. (2018). "Investigating the EGR rate and temperature impact on diesel engine combustion and emissions under various injection timings and loads by comprehensive two-zone modeling." *Energy* 157, 990-1014.

Rakopoulos, C.D., Rakopoulos, D.C., and Kyritsis, D.C. (2003). "Development and validation of a comprehensive two-zone model for combustion and emissions formation in a DI diesel engine." *Int. J. Energy Res.* 27(14), 1221-1249.

Reitz, R.D., and Rutland, C.J. (1995). “Development and testing of diesel engine CFD models.” Progress in Energy and Combustion Science, 21, 173-196.

Ricardo M B, Apostolos P and Yang M Y. (2011). Overview of boosting options for future downsized engines. Sci China Tech Sci, 54: 318-331.

Rodgers, C. (1963). “Typical Performance Characteristics of Gas Turbine Radial Compressors.” ASME J. Eng. Power. Apr 1964, 86(2)

Romagnoli, A. and Martinez-Botas, R. (2011). “Performance Prediction of a Nozzled and Nozzleless Mixed-flow.” *Int. J. Mechanical Sciences*, 53(8):557-574.

Rossetti,A., G. Ardizzon,G Pavesi, and G Cavazzini. (2009). An optimum design procedure for an aerodynamic radial diffuser with incompressible flow at different Reynolds numbers.

Sakellaridis, N. and D. Hountalas. (2013). Meanline Modeling of Radial Turbine Performance for Turbocharger Simulation and Diagnostic Applications,. SAE Technical Paper 2013-01-0924, SAE, Warrendale, PA

Sathish, S., Kumar, P., Nambur, A. N., Swam, L., Fuetterer C. and Gopi, P. C. (2019). NOVEL APPROACHES FOR sCO2 AXIAL TURBINE DESIGN. Proceeding of ASME Turbo Expo 2019, GT2019-90606, Phoenix, Arizona, USA, June 17-21.

Schnurr, R. and Walker, T.,. (2019). Marine Transportation and Energy Use. Reference Module in Earth Systems and Environmental Sciences.

Serrano, J. R., Arnau, F.J., De la Morena, J., Gomez-Vilanova, A., Guilain, S. and Batard, S. (2020). A Methodology to calibrate gas-dynamic models of turbocharged petrol engines with variable geometry turbines and with focus on dynamics prediction during tip-in load transient tests. Proceeding of ASME Turbo Expo, GT2020-15169, Virtual online, September 21-25.

Shahed S M. (2003). Gasoline engine downsizing and boosting for CO2 emission reduction. California Air Resource Board, Climate Change-International Vehicle Technology Symposium, Sacramento, CA.

Sher, E. (1998). Handbook of Air Pollution From Internal Combustion Engines, Pollutan Formation and Control. Academic Press.

Stuart S., Spence S., Filsinger D., Starke A., Kim S. K. (2017). "Characterising the influence of impeller exti recirculation on Centrifugal Compressor work input." *Proceeding of ASME Turbo Expo*, GT2017-63047, Charlotte, NC, USA, June 26-30.

Tian, Z., Yue, Y., Gu, B., Gao, W., and Zhang, Y. (2020). Thermo-economic analysis and optimization of a combined Organic Rankine Cycle (ORC) system with LNG cold energy and waste heat recovery of dual-fuel marine engine.

Turcotte, J., Trepanier, J. Y. and Tribes, C. (2004). Integration and Multidisciplinary Design Optimizaion of a Simplified Gas Turbin Model Using Perl and iSIGHT. Proceeding of 10th AIAA/ISSMO Multidisciplinary Analysis and Optimization Conference.

Wang, X., Sun, J., Huo, C., Huo, G., and Song, P. (2019). Design and Flow Analysis of a Radial Outflow Turbo-Expander. Proceedings of ASME Turbo Expo, GT2019-90346, Phoenix, Arizona, USA, June 17-21.

Wasserbauer, C.A. and Glassman, A. J. (1975.). Fortran Program for predicting off-design performance of Radial-Inflow Turbines. TN D-8063. NASA Lewis Resedrcb Center, Cleveland, Ohio.

Watson, N. and M. S. Janota. (1982). Turbocharging the Internal Combustion Engine. MACMILLAN EDUCATION LTD.

Watson, N. and Marzouk, M. (1977). "A non-linear digital simulation for turbocharged diesel engines under transient conditions", *SAE Technical Paper 770123*, SAE, Warrendale, PA.

Xing H, Stuart C, Spence S and Chen H. (2021). Fuel Cell Power Systems for Maritime Applications: Progress and Perspectives. MDPI Sustainability. 13(3):1213.

Yang, J., Gao, Y., Liu, Z., Zhao, C. Kang, T., Gu, L. and Xu, B. (2016). A method for modeling and analyzing the rotor dynamics of a locomotive turbocharger. Nonlinear Dyn (2016) 84:287–293.

Zhai, L., Luo, Y., Wang, Z, and Liu, X. (2014). Failure Analysis and Optimization of the Rotor System in a Diesel Turbocharger for Rotor Speed-Up Test. Hindawi Publishing Corporation, Advances in Mechanical Engineering, Volume 2014, Article ID 476023, 8 pages.

Zhang, H.,Shi, Z. Q., Zhen, D., Gu, F. S. and Ball A. (2012). Stability Analysis of a Turbocharger Rotor System Supported on Floating Ring Bearings. Journal of Physics: Conference Series, 364. 012032. ISSN 1742-6596.

Chapter

2 Introduction to the processes for Turbocharger Design and Retrofitting

Integrated processes for T/C design and retrofitting are developed with three modes of operation, providing a fully automated retrofit-design solution or the option for T/Ced diesel engine simulation. In this Chapter a presentation of each individual process is performed, focusing on their functionality, their development environment, and the coupling between each-other.

2.1 Turbocharged Diesel Engine Simulation mode: Benefits and contribution

The T/Ced diesel engine simulation mode utilizes 1D models for T/C components, a single-zone model for the diesel engine and a T/C-diesel engine matching analysis. As depicted in Figure 2-1, in first step, both T/C components geometry are required as input data for predicting the corresponding performance maps via meanline analysis. Then, having also given the diesel engine input data(geometry, speed, demanded power etc.), required for the single zone model, the entire engine system operation over its whole envelop is predicted, as T/C maps are parsed to the integrated 0-D T/C model for calculating the T/C operation. For ensuring the accurate interpolation and extrapolation for both compressor and turbine performance maps, generated by the corresponding meanline models, the well-established beta lines method, suggested by Kurzke (1996), is applied for. Also, the diesel engine model is adapted to engine-specific data and the overall engine system is validated against available shop trials data. Shop trials data refer to T/Ced ICE bench measurements at specific load points. Note that the simulation mode is also utilized by the design and the retrofit processes.

Concerning T/C meanline models, they consist of the state-of-the-art loss models based on public literature. Also, they are separated into specific sub-domains(e.g. impeller, vaned diffuser, volute, etc.), allowing the simulation of different configurations.

Concerning the "stable operation" margins calculation, the following assumptions are taken into consideration. The impeller and the vaned diffuser stall calculations are based on the approaches, presented by Aungier (2000). Regarding the choke limit prediction, performed for both compressor and turbine, the choking mass flow is calculated in each sub-component inlet and outlet area, for both stationary and relative frames, and then the minimum value is used as the corresponding limit.

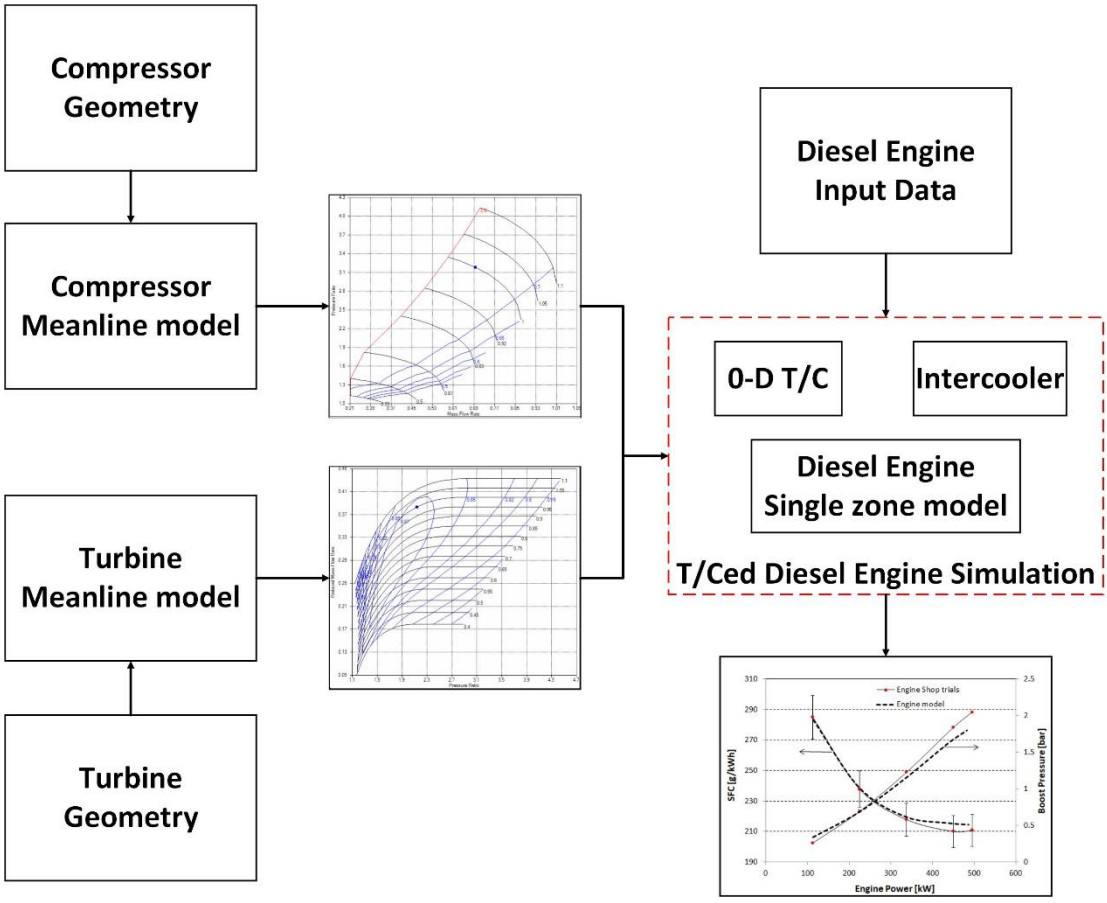

Figure 2-1: T/Ced diesel engine simulation

Taking advantage from the "stable operation" margins calculation, a physically consistent, transparent, and fully automated procedure is integrated in each meanline model, for producing each required turbo-component(CC, RT and AT) performance map.

Additionally, the AT and the RT meanline models are developed with the ability to calculate their performance beyond the choke limit, hence allowing the prediction of T/C operation with choked turbine.

All meanline models are developed within Propulsion Object-Oriented Simulation Software[1](PROOSIS), as it uses a non-standard, high-level, object oriented programming language, named EL, that enables the modelling of engine

[1]EcosimPro |PROOSIS| System Modelling and Simulation Toolkits and Services. http://www.proosis.com/

subsystems and offers all the benefits of an object oriented language [Alexiou 2014].

CC [Aungier 2000] and RT [Aungier 2005] conventional volute models do not consist of secondary losses(losses due to 3D effects). With this 1D model inability to capture volute 3D effects, in case of an optimization process, the solution may be led to geometries with intensive 3D effects, observably only via CFD analysis. Thus, both CC and RT volute sub-components are not included in design process in most cases.

For predicting 3D effects via volute meanline analysis, CFD-based surrogate loss models are developed, aiming to replace the conventional ones. Both the CC and the RT CFD based volute loss models are developed in python environment. Regarding the coupling between the meanline model and the surrogate model, it is accomplished via Fortran wrapper static libraries, allowing the communication between PROOSIS and python.

Considering the diesel engine single zone model, it is utilized for the current study as a black-box software.

Each simulation process, integrating the necessary tools, is developed within Python environment in order to easily manage all the necessary sub-tools. Taking advantage from the multiprocessing python module[1], both turbo-components performance prediction is performed simultaneously, aiming to reduce the computational time.

Having developed a model capable to simulate the system operation over its whole envelope, engine fault analysis is performed in order to determine how fouling in T/C and intercooler affects the whole system operation, using physical consistent parameters as input data such as roughness increase rather than arbitrary mass flow, and efficiency reduction factors [Kurz and Brun 2009]. In this way, the fault effect on the stall margin is obtained, thus, the effect of faults on operability (usually neglected in 1D analysis to the author's knowledge) is assessed as well. Therefore, an alternative, lower fidelity, and time efficient option for studying the faults effect on the stall margin is provided, which otherwise is obtained using higher-fidelity, but time consuming CFD tools [Melino et al. 2011].

2.2 Automatic Turbocharger design mode: benefits and contribution

The design process(Figure 2-2) intends to integrate all the necessary sub-tools, required for designing an operable, efficient, structurally safe and manufacturable T/C in engine system level, while contributing novel elements to the entire engineering community. These elements can be used independent of the turbomachinery design application.

[1] https://docs.python.org/3/library/multiprocessing.html

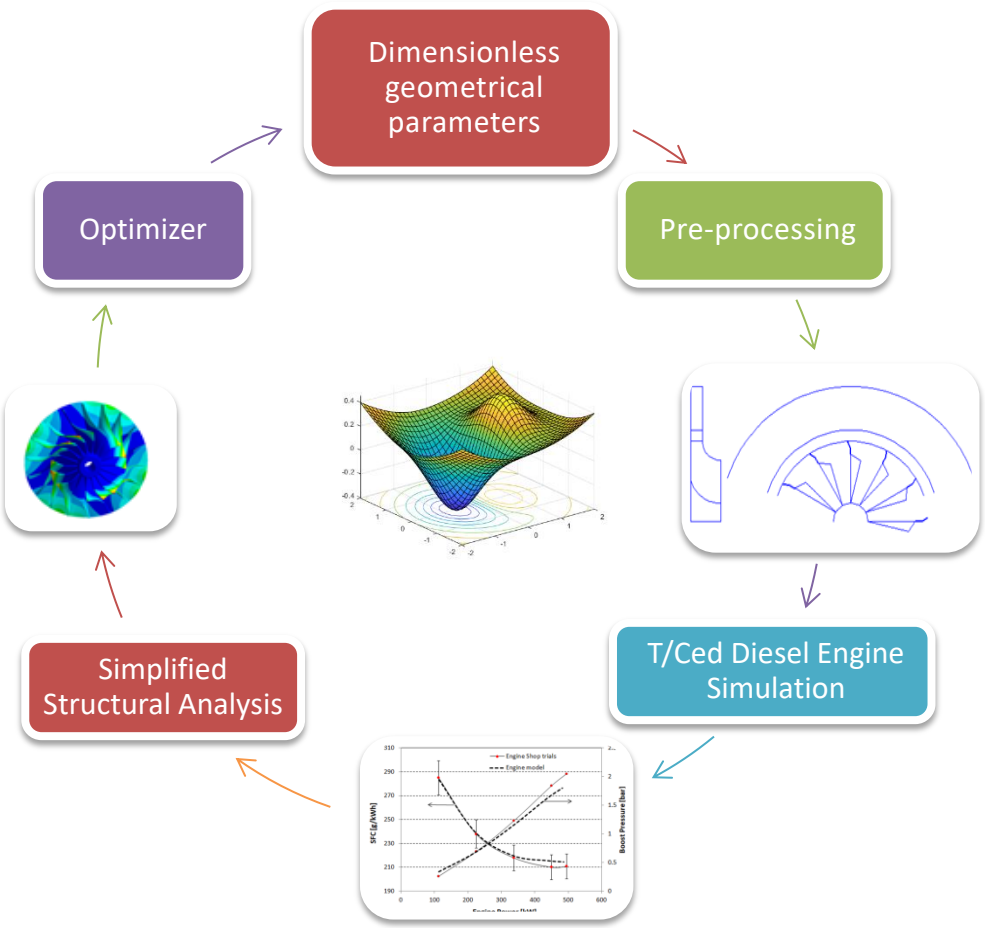

Figure 2-2: Turbocharger design

Both turbo-components design is carried out in engine system level, focusing on T/Ced diesel engine overall operation improvement and fuel consumption reduction, performing a multi-point design calculation. Making use of dimensionless geometrical parameters as optimization variables with defined range instead of dimensional ones, it can provide a more general T/C design procedure. The T/C design available configurations are:

a. Vaneless Diffuser Centrifugal Compressor – Radial Turbine
b. Vaned Diffuser Centrifugal Compressor – Radial Turbine
c. Vaneless Diffuser Centrifugal Compressor – Axial Turbine
d. Vaned Diffuser Centrifugal Compressor – Axial Turbine

Having developed a proper simplified structural tool with the capability of performing both static and modal analysis, the structural integrity of the design solution is ensured. The entire process is conducted within python environment, while all the integrated analysis sub-tools are developed within PROOSIS. The coupling of all these sub-models is extensively described in Chapter 3. Taking advantage from the multiprocessing python library, it parallelizes the T/C components design sub-processes and allows the design of all possible configurations simultaneously, hence reducing the computational time.

Finally, the design process integrates a 3D high fidelity design sub-tool, which is limited to vaneless diffuser centrifugal compressor design. This 3D design tool follows an optimization procedure. In the 3D optimization process, a python in-house utility function is developed, with the aim to run specific sub-processes, such as fluid domain meshing and flow modeling, in order to automate the compressor CFD performance prediction.

The T/C design process is utilized either directly by designing a new T/C for a specific diesel engine, or as an extension of retrofit process in order to examine retrofit options relating to redesigning. Finally, the current process integrates a commercial optimization tool[1]. The coupling between design process and optimization tool can be found in [Γιάχος 2019].

2.3 Automatic Turbocharger Retrofit mode: benefits and contribution

According to Button et al (2015), the main contributors in the life cycle cost of the T/Ced ICE are maintenance and operational costs. Both costs increase as T/C degradation occurs due to the harsh working conditions, leading to frequent turbo-components replacements. In many cases of an aged T/C not available anymore in the market, retrofit is performed, by replacing specific component (compressor or turbine) or entire T/C with a new one available in the market.

The T/C retrofit is a complicated and time consuming process, due to the fact that each turbo-component must be chosen carefully, in order to match the ICE, while retaining or improving the whole system efficiency. The automation of such a process can benefit both T/C manufacturer and marine company, by decreasing the retrofitting process time, hence leading to lower process cost, productivity improvement and anchored ship time reduction. For the majority of retrofitting cases, the most obvious approach is to use market available turbo-components, because of the high cost of new component designing and manufacturing. In case of no available component that suitably matches the ICE, a possible step is the redesigning of a new geometry, able to match the engine. Briefly, the four retrofit options are the following:

- Option 1: Turbo-component (Compressor or Turbine) retrofit, using the corresponding available turbo-components.
- Option 2: Entire T/C retrofit, using available compressor and turbine pairs.
- Option 3: T/C turbo-component re-design (compressor or turbine optimization).
- Option 4: Entire T/C re-design (compressor and turbine combined optimization).

[1] Isight & SIMULIATM Execution Engine - Dassault Systèmes®." [Online]. Available: https://www.3ds.com/products-services/simulia/products/isight-simulia-execution-engine/

Retrofit process relying on engineers personal judgment may not be optimal. Thus a T/Ced diesel engine unnecessary system efficiency reduction occurs, leading to both an engine fuel consumption and emissions (NO_x, HC, etc.) increase.

The automatic T/C retrofitting mode, coupled with the T/Ced diesel engine simulation process, examines all the available turbo-components and selects the one that best matches the entire engine system, aiming to retain or improve the diesel engine efficiency. In case the best selected T/C does not fully satisfy the matching criteria, a developed trimming sub-tool (Swain and Engeda 2014) can be used for adapting the performance map based on the matching requirements.

For completing the option 3 and 4, the current process communicates with the design one, initiating the corresponding sub-tools either for redesigning a turbo-component or the entire T/C.

2.4 Summary and Discussion

Integrated T/C design and retrofitting processes are briefly presented in this Chapter. Focusing on three specific modes of operation, they provide a fully automated retrofit-design solution or the option for T/Ced Diesel Engine Simulation.

The first process simulates the entire T/Ced diesel engine operation and performance over its whole envelope. It also provides the capability of studying how fouling in T/C and intercooler affects the whole system degradation using physically consistent parameters instead of arbitrary mass flow, and efficiency reduction factors.

In the second process(design), an optimization procedure is followed, in order to (re)design specific turbo-component or the whole T/C to match the entire system in an improved way. Utilizing dimensionless parameters as optimization variables with defined range, it can provide a more general T/C design procedure, independent of the T/C scale.

In the third process(retrofit), all available turbo-components (compressors and turbines) are examined in order to select the one that best matches the entire engine system while retaining or improving the diesel engine efficiency. Additionally, taking advantage from the communication with the design process, a retrofit redesign option is provided (option three and four) either for a specific turbo-component or the entire T/C.

2.5 References

Alexiou, A. (2014). Introduction to Gas Turbine Modelling with PROOSIS. Empresarios Agrupados International (E.A.I.) S.A., Madrid, Spain (2014).

Aungier, R. H. (2005). TurbineAerodynamics Axial Flow And Radial Inflow Turbine Design And Analysis. ASME PRESS, New York.

Aungier, R.H. (2000). Centrifugal Compressors, A Strategy for Aerodynamic Design and Analysis. ASME PRESS.

Button, R. W., Martin, B., Sollinger, J. and Tidwell, A. (2015). Assessment of Surface Ship Maintenance Requirements. RAND Corporation, Santa Monica, Calif

Kurz, R. and Brun, K.,. (2009). Degradation of gas turbine performance in natural gas service. Journal of Natural Gas Science and Engineering 1 95–102.

Kurzke, J. (1996). "How to get Component Maps for Aircraft Gas Turbine Performance Calculations." Proceeding of ASME Turbo Expo, Birmingham, UK, 96-GT-164, 2-5 June

Melino, M., Morini, M., Peretto, A., Pinelli M. and Spina,P. R. (2011). Compressor Fouling Modeling: Relationship Between Computational Roughness and Gas Turbine Operation Time. Proceeding of ASME Turbo Expo, GT2011-46089, Vancouver, British Columbia.

Swain, D. and Engeda, A. (2014). Effect of Impeller blade trimming on the performance of a 5,5:1 pressure ratio centrifugal compressor. Imeche Journal of Power and Energy Vol 228: pp. 878–888.

Γιάχος, Γ. (2019). Μελέτες βελτιστοποίησης του συστήματοςσ πρόωσης αεροσκαφών. Διπλωματική Εργασία, Εθνικό Μετσόβιο Πολυτεχνείο, Σχολή Μηχανολόγων Μηχανικών (Greek).

Chapter

3 Turbocharged Diesel Engine Simulation

In the present chapter the T/Ced diesel engine simulation process is presented. All the integrated sub-models, including both the theory and the relevant correlations, are also extensively described. Additionally, both CC and RT surrogate volute loss models are presented, focusing on the learning process and the required training patterns, generated via a CFD parametric analysis. Finally, each sub-model individually and entire T/Ced diesel engine are verified.

3.1 General description

The T/Ced diesel engine simulation process utilizes 1D sub-models for calculating the turbomachinery components maps and then a fully coupled process integrating the turbomachinery components, allowing the calculation of the performance and operating conditions at subsystem and system level. Figure 3-1 depicts the T/Ced diesel engine components and the matching analysis flow chart.

The simulation process consists of four main sub models. The diesel engine, the intercooler, the centrifugal compressor and the turbine (axial or radial) model. The compressor and the turbine geometries are given as input data in the corresponding meanline models for generating the components performance maps. Regarding the diesel model, the required input data are the inlet valve closing angle, the exhaust valve opening angle, the compression ratio, the cylinder bore, the piston stroke, the generator efficiency and the shop trials data. Finally, for setting up the intercooler model, its pressure drop and its effectiveness at 100% of engine load are required.

Having established the integrated models for a specific T/Ced diesel engine, for a single operating point, the ambient conditions, the engine speed and the engine fuel consumption (or demanded output power) should be defined.

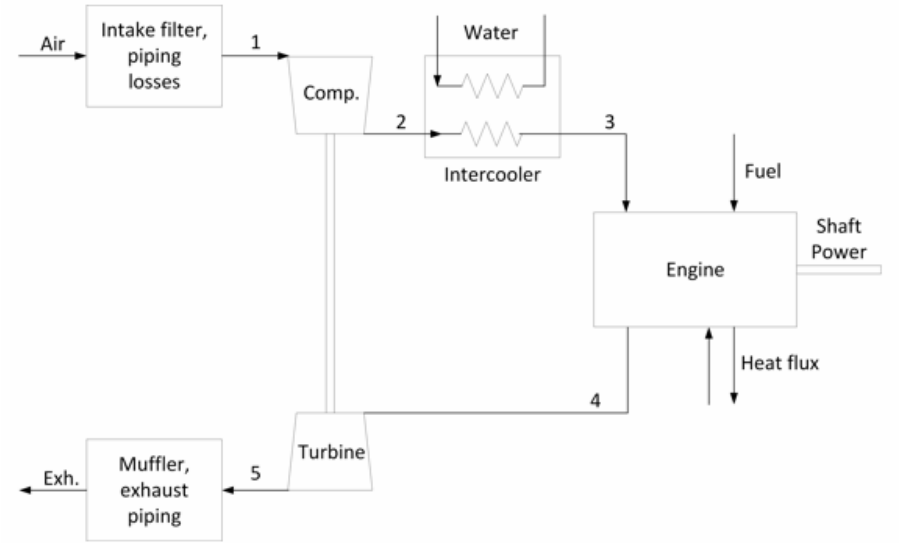

(a)

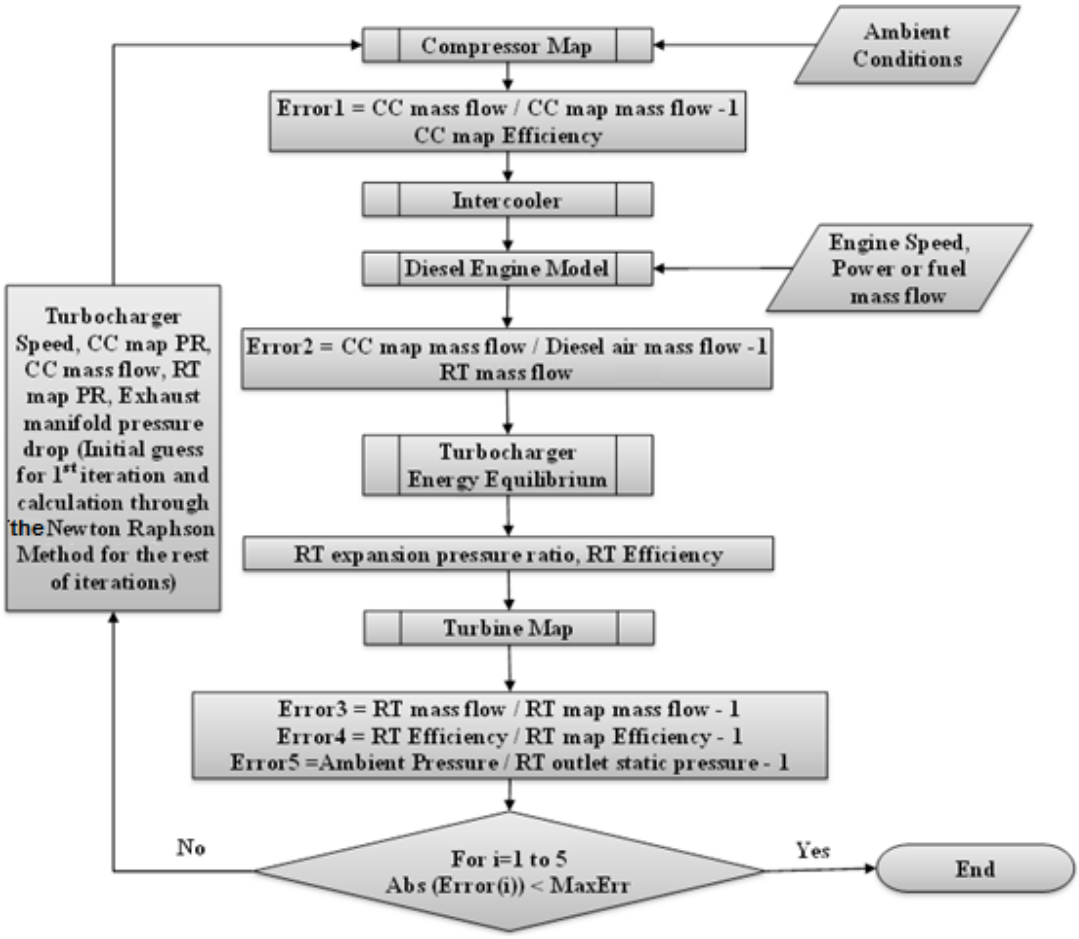

(b)

Figure 3-1: Turbocharged diesel engine: **(a)** layout **(b)** coupling flow chart.

3.2 Diesel Engine model

For the diesel engine, an in-house single zone thermodynamic combustion model has been used for modelling the closed engine cycle. The main purpose of the simulation model is to predict the engine performance, the thermodynamic properties of the working medium and the mass flow rate, in order to be coupled with the compressor and turbine models, using as little as possible experimental data for model calibration. Therefore, a simple approach is followed, based on the application of the first law of thermodynamics, assuming that the combustion chamber burns a single homogeneous mixture. Thus, only the temporal variation of the in-cylinder mixture concentration, temperature and thermodynamic properties is considered, as a function of the instantaneous cylinder volume. In other words, at each crank angle, the model predicts the in-cylinder homogeneous mixture composition (i.e. perfect combustion products concentrations after combustion initiation), the in-cylinder pressure and the uniform in-cylinder bulk gas temperature. For the close part of engine cycle, the energy conservation equation is written as:

$$\frac{dU_{cyl}}{dt} = \frac{dQ_w}{dt} + \frac{dQ_{comb}}{dt} - \frac{dW}{dt} \tag{3.1}$$

The mechanical work performed by the piston during the compression and expansion phases is due to the volume change in the cylinder and is calculated by the following trapezoidal rule:

$$dW = (p_{cyl,i} + p_{cyl,i+1})\ \frac{dV_{cyl}}{2} \tag{3.2}$$

where $p_{cyl,i}$ and $p_{cyl,i+1}$ are two successive values of cylinder pressure and dV_{cyl} is the cylinder volume step.

The heat addition due to the combustion is taken into account assuming complete combustion of the fuel injected having a specified lower heating value. The fuel burning rate at every individual crank angle, is predetermined using a simple empirical model (Wiebe function) according to the following expression [Stiesch 2003]

$$\frac{Q_{comb}(\varphi)}{Q_{comb,tot}} = 1 - \exp\left(-6.908 * \left(\frac{\varphi - \varphi_{SOC}}{\Delta\varphi_c}\right)^{m+1}\right) \tag{3.3}$$

where $Q_{comb,tot} = m_{fuel} * LHV$, m and $\Delta\varphi_c$ are parameters determined by the calibration procedure conducted. The ignition delay is estimated using an Arrhenius type equation [Heywood 1988]:

$$\tau_{id} = A * p_{cyl}^{-n} * exp\left(\frac{E_A}{\tilde{R}} * \frac{1}{T_{cyl}}\right) \tag{3.4}$$

where, P and T are the instantaneous in-cylinder pressure and temperature, E_A is the apparent activation energy of the fuel auto-ignition process, $\tilde{R}$ is the

universal gas constant and A and n are constants dependent on the fuel. In this study the values proposed by Wolfer are used, i.e. n=1.19, A=0.44 and the parameter $E_A/\tilde{R}$=4650 K[Heywood 1988].

The heat transfer between the cylinder gases and the combustion chamber walls can be due to both convection and solid body radiation. The latter originates from hot soot particles. However, due to the assumption of perfect combustion, soot particles are not taken into account. To compensate this, the effect of radiative heat transfer is taken into account by an empirical augmentation of the convective heat transfer coefficient [Stiesch, 2003]. The convective heat transfer rate between the gas and the wall can be described by the Newton's cooling law:

$$\dot{Q_w} = h\ A\ (T_w - T_{cyl}) \tag{3.5}$$

where h is the convective heat transfer coefficient, A is the instantaneous surface area across which the heat transfer takes place and T_w, T_{cyl} are the mean wall and in-cylinder gas temperatures, respectively. The convective heat transfer coefficient is estimated assuming steady turbulent flow over the cylinder wall, using the following expression:

$$Nu = \frac{h\ L}{k} = C\ Re^a\ Pr^b \tag{3.6}$$

where L represents a characteristic length and equals the cylinder bore diameter, C, a and b are empirical constants that are determined by curve fitting experimental data of wall heat transfer rates. In this study a=0.80, b=0.40. To calculate the brake engine power, the correlation proposed by [Chen and Flynn 1965] for T/Ced engines is used, where the friction mean effective pressure FMEP in bar is calculated as:

$$FMEP = 0.137 + 0.005\ P_{max} + 0.162\ c_{piston,mean} \tag{3.7}$$

where P_{max} is the peak combustion in-cylinder pressure in bar and $c_{piston,mean}$ is mean piston speed in m/s. The air mass flow rate is calculated using the following expression:

$$\dot{m}_{AIR} = \frac{P_{im}}{R * T_{im}}\ V_{sw}\ n_{vol}\ \left(\frac{N}{2}\right) \tag{3.8}$$

where P_{im} and T_{im} are the pressure and temperature at the engine inlet manifold (after inter-cooler), n_{vol} is the volumetric efficiency, R is the air gas constant and N is the crankshaft speed. The gas temperature at IVC is calculated using the following equation:

$$T_{IVC} = T_{im} + \Delta T \tag{3.9}$$

where ΔT is an adjustable input parameter to the integrated simulation model. The volumetric efficiency n_{vol} is adjusted in order predicted data for peak

cylinder pressure, brake power output and exhaust gas temperature after turbocharger to match corresponding shop trials data. The exhaust gas flow rate is calculated by:

$$\dot{m}_{EXH} = \dot{m}_{AIR} + \dot{m}_{fuel} \tag{3.10}$$

A polytropic expansion is used to calculate the exhaust gas temperature using the corresponding value of exhaust gas temperature at EVO as follows:

$$T_{exh} = T_{EVO}\left(\frac{P_{exh,manif}}{P_{EVO}}\right)^{\frac{n-1}{n}} \tag{3.11}$$

where P_{EVO} is the cylinder gas pressure at EVO and $P_{exh,manif}$ is the exhaust manifold pressure, which is calculated using the following expression:

$$P_{exh,manif} = \frac{1}{2}P_{im} + \sqrt{(P_{im}100)^2 - 8\dot{m}_{exh}^2 T_{im} + (T_{EVO} - T_{im})} \tag{3.12}$$

At this point it is worth making some observations about the diesel engine closed-cycle simulation model. Specifically, the model predicts the variation of in-cylinder pressure during closed-cycle diesel engine operation and thus, it does not account for the variation of cylinder pressure during intake stroke in order to calculate the pumping work during gas exchange. However, the impact of the negative pumping power on the brake engine power output is rather limited since the highest portion of indicated power results from the closed-cycle engine operation and thus, the error induced in the calculation is not considerably important. Also, it should be underlined that the main scope of the selection of the single-zone approach was based on the fact that it is suitable for cases where there are very limited available data for the geometrical and the operational characteristics of the engine. This is the case that is usually met in practical applications where turbo-matching has to be implemented in existing engines under retrofitting (i.e. replacement of existing T/C with another one) where the only available data are the test records of the diesel engine at shop trials.

The validation analysis of the current diesel engine model is performed as an entire T/Ced diesel engine system and is presented in the section 3.8.

3.3 Intercooler model

An intercooler model has been developed, aiming to predict the charged air pressure and temperature, driven to diesel engine after its cooling. Its performance is estimated by prescribing the intercooler effectiveness and total pressure losses on the hot and cold sides. The temperature effectiveness (ε) and the pressure drop at design point are defined according to the following equations.

$$\varepsilon = \frac{T_{in,hot} - T_{out,hot}}{T_{in,hot} - T_{in,cold}} \tag{3.13}$$

$$P_{out,cold\ or\ hot} = P_{in,cold\ or\ hot}(1 - dP_{cold\ or\ hot}) \tag{3.14}$$

where $dP_{cold\ or\ hot}$ is the pressure drop across the intercooler. In order to estimate the outlet temperatures of both the cold and hot sides of the intercooler, a heat flow balance is performed between the hot and cold sides. For off-design operation, the off-design pressure drop($dP_{cold\ or\ hot,off}$) is defined as [Walsh and Fletcher, 2008]:

$$dP_{cold\ or\ hot,off} = \left(\frac{\dot{m}}{\dot{m}_{des}}\right)^2 dP_{cold\ or\ hot,des} \tag{3.15}$$

while the off-design effectiveness (ε_{off}) as [Walsh and Fletcher, 2008]:

$$\varepsilon_{off} = 1 - \left(\left(\frac{\dot{m}}{\dot{m}_{des}}\right)(1 - \varepsilon_{des})\right) \tag{3.16}$$

3.4 Centrifugal Compressor Meanline model

The centrifugal compressor meanline (CML) model has been developed for simulating any centrifugal compressor "configuration", conducting a mean-line (1D) analysis to establish the off-design performance of a compressor of known geometry. The CC model includes sub-models for modelling the preformance of impellers, vaneless diffusers, vaned diffusers, and volutes. Depending on the desired CC configuration, the vaned diffuser and/or the volute sub-models can be turned on or off.

Exit flow conditions and performance of each individual component, shown in Figure 3-2 (impeller, vaneless diffuser, etc.) are calculated, considering the corresponding loss models and having as input conditions the upstream component outlet conditions. At the end of the CC calculation, the overall performance of the compressor is established and is expressed in the form of isentropic and polytropic efficiencies, flow and work coefficients, etc.

Regarding the CC stations of the mean-line calculation (Figure 3-3), station 1 corresponds to the impeller inlet, 1i to the impeller inlet just downstream of blade leading edge, 3 to the impeller outlet, 4 to the vaneless diffuser outlet, 5 to the vaned diffuser outlet (if exists), and 6 to the scroll volute outlet.

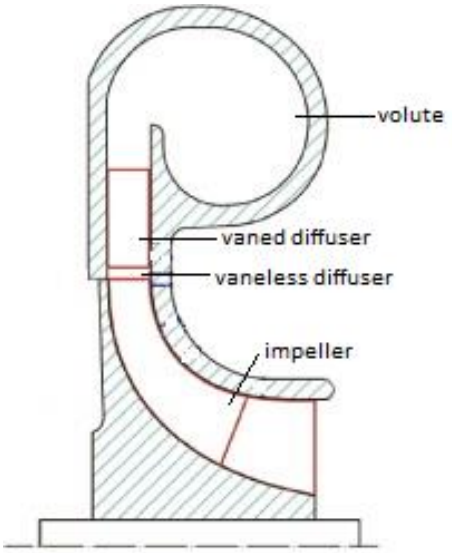

Figure 3-2: Centrifugal Compressor components. [Aungier 2000]

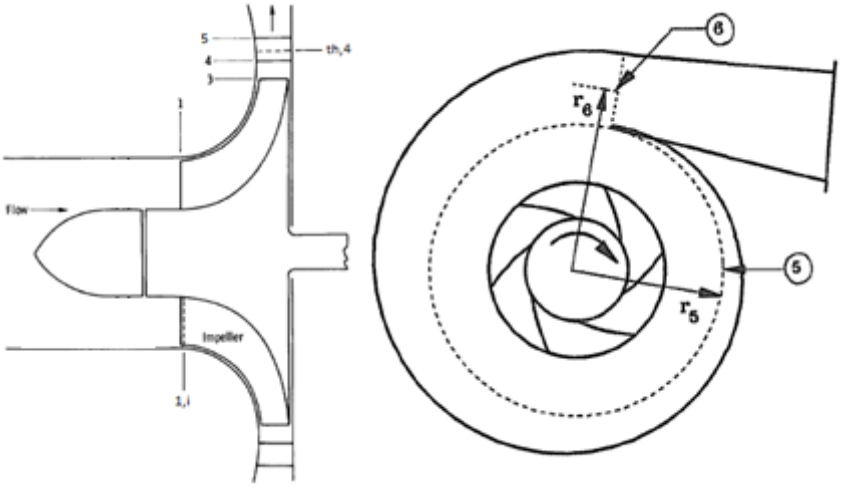

Figure 3-3: Centrifugal Compressor stations. [Galvas, 1973 and Aungier, 2000]]

3.4.1 Meanline analysis input data

The CC meanline analysis is conducted within the PROOSIS environment, depicted in Figure 3-4, with specific input data, presented in Table 3-1. Concerning the geometrical parameters that are included in input data, their graphic representation is shown in Figure 3-5.

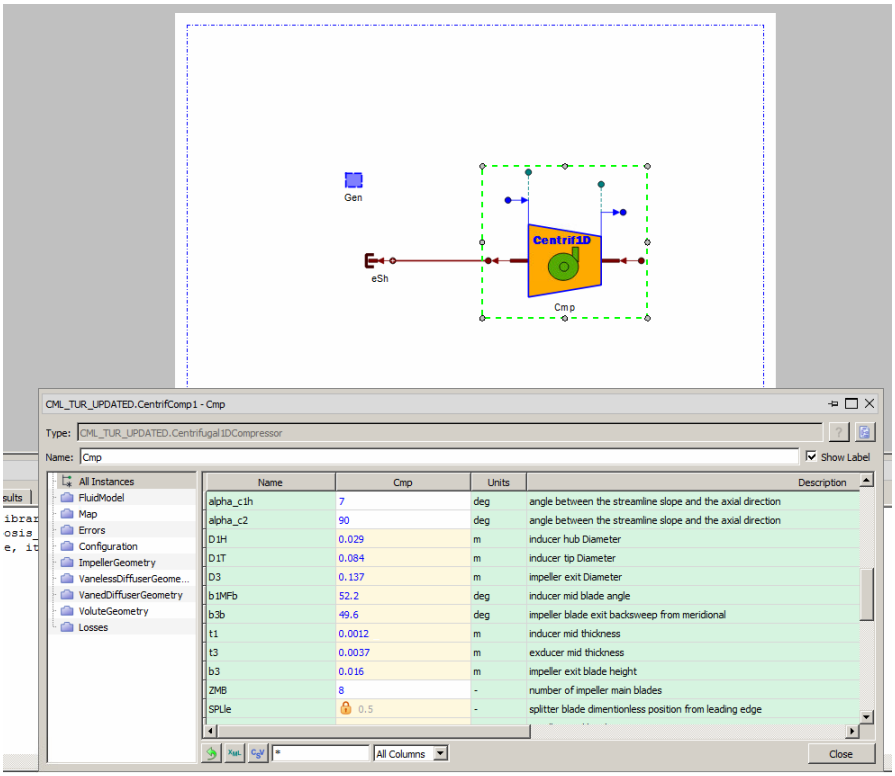

Figure 3-4: CC meanline analysis schematic and input data in PROOSIS environment.

Table 3-1: CC meanline analysis input data.

Centrifugal Compressor Geometry			
Parameter		Parameter	
$D_{1,hub}$	Impeller hub inlet diameter	t_4	Vnd diffuser inlet blade thickness
$D_{1,tip}$	Impeller tip inlet diameter	t_5	Vnd diffuser outlet blade thickness
D_3	Impeller outlet diameter	b_3	Impeller outlet blade height
D_4	Vnless Diffuser inlet diameter	b_4	Vnless diffuser inlet channel width
D_5	Vnd Diffuser inlet diameter	b_5	Vnd diffuser inlet channel width
$\beta_{b,1}$	Impeller inlet blade angle	Z_{MB}	Impeller main blades number
$\beta_{b,3}$	Impeller outlet blade angle	Z_{FB}	Impeller full blades number
$\beta_{v,4}$	Vnd diffuser inlet vane angle	L_A	Impeller axial length
$\beta_{v,5}$	Vnd diffuser outlet vane angle	Z_V	Vnd diffuser vanes number
t_1	Impeller inlet blade thickness	AR_{vol}	Volute aspect ratio
t_3	Impeller outlet blade thickness	N_{mech}	CC speed
le_{spl}	Splitter blades dimensionless position	$P_{t,in}$	Inlet total pressure
Fluid	Working fluid (Air)	$T_{t,in}$	Inlet total temperature
$\dot{m}$	CC mass flow	e	Wall roughness
cl	Impeller clearance		

Typical T/C compressor impeller, vaned diffuser and volute are illustrated in Figure 3-6.

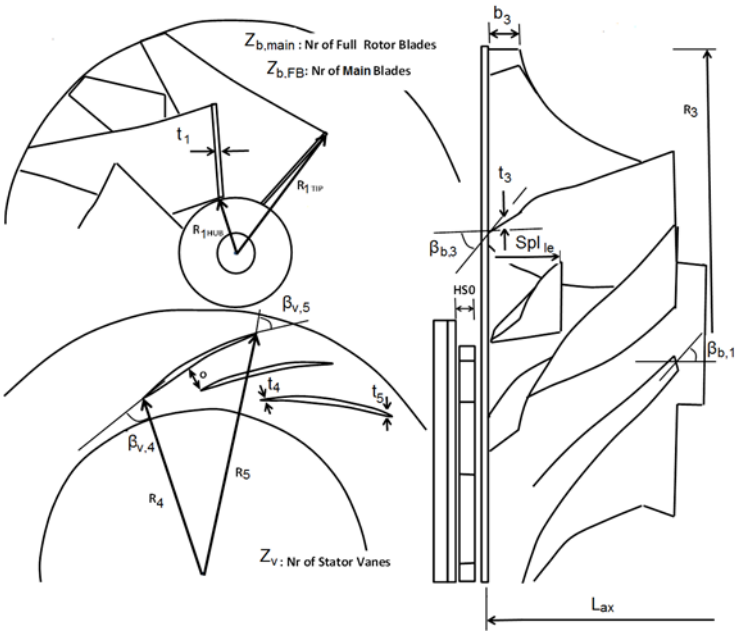

Figure 3-5: CC geometrical parameters.

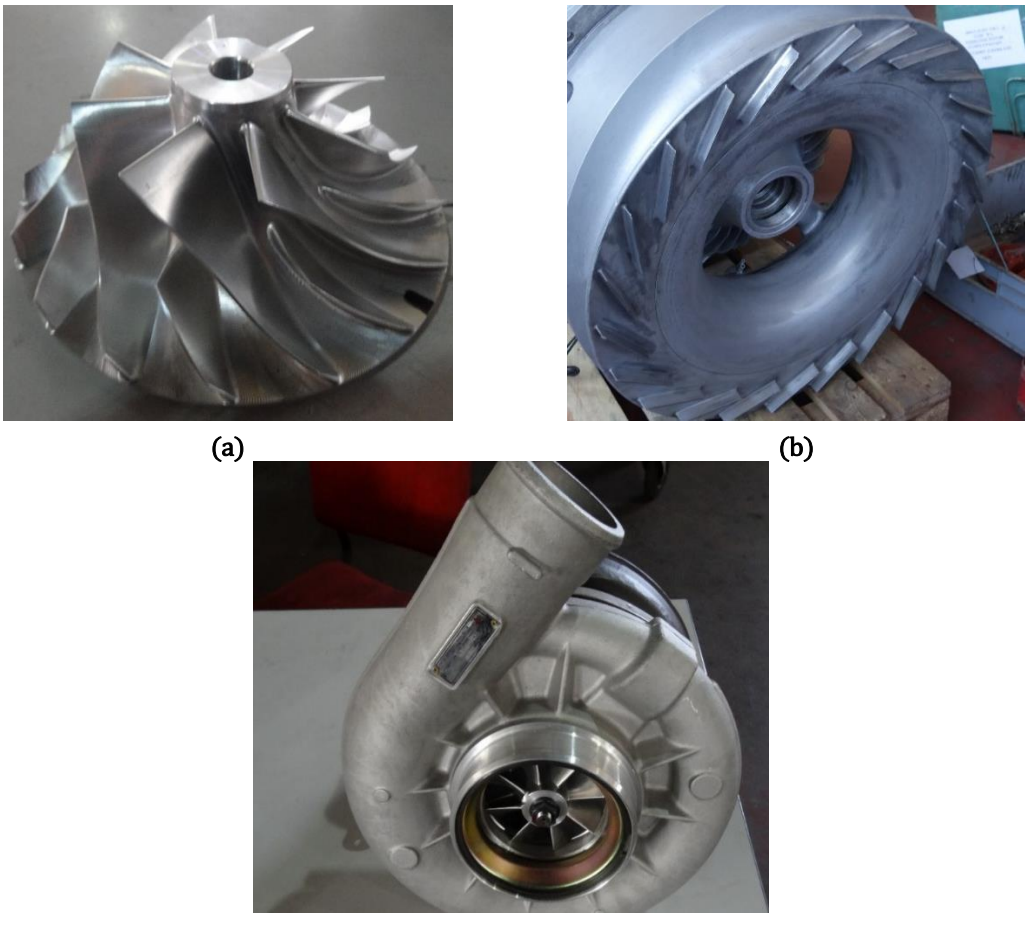

(a) **(b)**

(c)

Figure 3-6: T/C centrifugal compressor[1]: **(a)** impeller **(b)** vaned diffuser **(c)** volute

[1] www.turbomed.gr

3.4.2 Meanline analysis

Considering the meanline analysis, the reference radius is selected to be placed at RMS position,

$$D_{ref,1} = \sqrt{\frac{D_{hub,1}^2 + D_{tip,1}^2}{2}} \tag{3.17}$$

as the compressor inlet area is separated into two equal areas.

Impeller inlet(1)

At the beginning of the analysis, the inlet impeller area(A_1) is:

$$A_1 = \pi \frac{D_{tip,1}^2 - D_{hub,1}^2}{4} \tag{3.18}$$

Note that, as the analysis consists of thermodynamic properties, the definition of specific heat capacity at constant pressure(Cp) is not required and the specific enthalpy is a function of temperature,

$$h = h(T) \; and \; T = T(h) \tag{3.19}$$

Assuming a swirl-free inlet flow, and using an initial value for the meridional velocity in hub position, both rms and tip ones are calculated as,

$$V_{m,ref,1} = V_{m,1}(R_{ref,1}), V_{m,tip,1} = V_{m,1}(R_{tip,1}) \tag{3.20}$$

$$V_{m,1}(\mathrm{R}) = V_{m,hub,1}\, e^{\int_0^{R-R_{hub}} \alpha_{C,R}\, d(R-R_{hub})} \tag{3.21}$$

where $V_{m,1}(\mathrm{R})$ is the meridional velocity as a function of impeller inlet radius and $\alpha_{C,R}$ the streamline curvature in each radial position. Considering the streamline curvature in both hub and tip positions, is defined based on user-given wall curvature[1], while rms one is expressed as:

$$\alpha_{C,ref} = \frac{(\alpha_{C,tip} + \alpha_{C,hub})\,(R_{ref,1} + R_{hub,1})}{R_{tip,1} + R_{hub,1}} + \alpha_{C,hub} \tag{3.22}$$

Then, using the trapezoidal rule at the rms position and by Simpson rule for unequal intervals at the tip position, the previous equation is approximated for the meridional velocity in both rms and tip radius as:

$$V_{m,1} = V_{m,hub,1}\, e^{\mathrm{A}} \tag{3.23}$$

$$V_{m,\mathrm{tip},1} = V_{m,hub,1}\, e^{\mathrm{B}} \tag{3.24}$$

[1] Typical values according to Galvas (1973) : 0° and 7° for hub and tip respectively

where both A and B are defined as:

$$A = \frac{dl_0}{2}\,(\alpha_{C,ref} + \alpha_{C,hub}) \tag{3.25}$$

$$B = \frac{dl_0 + dl_1}{6}\left[\left(2 - \frac{\mathrm{dl}_1}{dl_0}\right)\alpha_{C,hub} + \frac{(dl_0 + dl_1)^2}{dl_1 dl_0}\alpha_{C,ref} + \left(2 - \frac{dl_0}{dl_1}\right)\alpha_{C,tip}\right] \tag{3.26}$$

$$dl_0 = R_{ref,1} + \mathrm{R}_{hub,1} \tag{3.27}$$

$$dl_1 = R_{tip,1} + \mathrm{R}_{hub,1} \tag{3.28}$$

Having calculated inlet velocity in hub, rms and tip positions, the static conditions are also computed at the three radial positions as:

$$h_{s,\mathrm{i},1} = \mathrm{h}_{\mathrm{t},1} - \frac{1}{2}V_{m,i,1}^2\,, \qquad i = hub, ref, tip \tag{3.29}$$

$$T_{s,\mathrm{i},1} = T\big(h_{s,i,1}\big),\; p_{s,i,1} = p_{t,i,1}\, e^{\frac{\varphi(T_{s,i,1}) - \varphi(T_{t,i,1})}{R_{gas}}},\; \rho_{1,\mathrm{i}} = \frac{p_{s,i,1}}{R_{gas}\, T_{s,i,1}} \tag{3.30}$$

where i represents the inlet hub, rms and tip position while the entropy function(φ) expressed as:

$$\varphi(T) = \int \frac{c_p(T)}{T}\,dT \tag{3.31}$$

Thus, the mass flow is calculated as:

$$\dot{m} = 2\pi\left\{\frac{dl_0 + dl_1}{6}\left[\left(2 - \frac{dl_1}{dl_0}\right)A + \frac{(dl_0 + dl_1)^2}{dl_0 dl_1}B + \left(2 - \frac{dl_0}{dl_1}\right)C\right]\right\} \tag{3.32}$$

$$A = \rho_{1,hub} R_{hub,1} V_{m,hub,1} \tag{3.33}$$

$$B = \rho_{1,ref} R_{ref,1} V_{m,ref,1} \tag{3.34}$$

$$C = \rho_{1,tip} R_{tip,1} V_{m,tip,1} \tag{3.35}$$

As the mass flow rate is user-defined, an iterative process is carried out between eq (3.23) and (3.35) for predicting the impeller inlet velocity at hub position until the error between the calculated and the given mass flow reaches a tollerance value.

Considering the initial impeller inlet hub meridional velocity, it can be defined as:

$$V_{m,hub,1,initial} = \frac{\dot{m}}{\rho_{t,1} A_1} \, , \rho_{t,1} = \frac{P_{t,1}}{R_{gas} T_{t,1}} \tag{3.36}$$

As for the blade speed($U_{ref,1}$) and the relative velocity(W_1), they are defined as:

$$U_1 = \omega \, R_{ref,1} = \pi \frac{N}{60} \; D_{ref,1} \, , W_1 = \sqrt{V_{m,1}^2 + U_{ref,1}^2} \tag{3.37}$$

Then, the total relative conditions in rms station are also calculated,

$$h_{t,1,r} = h_{s,1} + \frac{1}{2} W_1^2 , T_{t,1,r} = T\left(h_{t,1,r}\right), \; p_{t,1,r} = p_{s,1} \, e^{\frac{\varphi(T_{t,1,r}) - \varphi(T_{s,1})}{R_{gas}}} \tag{3.38}$$

Impeller inlet just downstream of blade leading edge(1i)

As in both 1 and 1i stations the reference diameter remains constant both total enthalpy and total relative temperature are expressed as:

$$h_{t,1i,r} = \; h_{t,1,r} \rightarrow \; T_{t,1i,r} = \; T_{t,1,r} \tag{3.39}$$

Although, due to blade existence, the overall pressure loss coefficient in the impeller inlet rotating frame is calculated by the following equation:

$$\bar{\omega}_{inlet} = \bar{\omega}_{inc} + \; \bar{\omega}_{contr} \tag{3.40}$$

where $\bar{\omega}_{inc}$ is the impeller inlet incidence and $\bar{\omega}_{contr}$ is the contraction losses. Both loss coefficients are presented in the section 3.4.3.
Having established the overall pressure loss coefficient, the relative pressure after impeller inlet is defined as:

$$p_{t,r,1i} = p_{t,r,1} - \; \bar{\omega}_{inlet} \, (p_{t,r,1} - p_{s,1}) \tag{3.41}$$

Impeller outlet(3)

In impeller outlet station both total relative enthalpy and temperature are expressed as:

$$h_{t,3,r} = h_{t,1i,r} + \frac{U_3^2 - U_1^2}{2} \rightarrow T_{t,3,r} = T(h_{t,3,r}) \tag{3.42}$$

Guessing then an initial impeller outlet meridional velocity ($V_{m,3}$), the circumferential velocity in impeller outlet is calculated:

$$V_{u,3} = \mathrm{V}_{u,3,id} \; \sigma \tag{3.43}$$

where $V_{u,3,id}$ is the ideal circumferential velocity in impeller outlet,

$$V_{u,3,id} = U_3 - V_{m,3} \tan(\beta_{b,3}) \tag{3.44}$$

and σ is the slip factor based on the formula presented by Aungier (2000), which is basicaly a revised Wiesner (1967) slip-factor formula,

$$\sigma = 1 - \sqrt{\sin(\beta_{b,2})}\,\sin(X_3) \;/\; Z_{FB}^{0.7} \tag{3.45}$$

$$\varepsilon_{\mathrm{LIM}} = \frac{\sigma - \sin(19^o + 0.2\,\beta_{b,2})}{1 - \sin(19^o + 0.2\,\beta_{b,2})} \tag{3.46}$$

$$\varepsilon = \frac{D_{ref,1}}{D_3} \tag{3.47}$$

$$\sigma = \begin{cases} \sigma & e \le \mathrm{e_{LIM}} \\ \sigma\left[1 - \left(\dfrac{\mathrm{e} - \mathrm{e_{LIM}}}{1 - \mathrm{e_{LIM}}}\right)^{\sqrt{\frac{\beta_2}{10}}}\right] & e > \mathrm{e_{LIM}} \end{cases} \tag{3.48}$$

With the circumferential velocity in impeller outlet being defined the rest of the velocity components are calculated. Then, the relative total pressure can be computed,

$$p_{t,r,3} = p_{t,r,3,is} - \bar{\omega}_{imp}\left(p_{t,r,1,i} - p_{s,1,i}\right) f_c \tag{3.49}$$

as a function of the correction factor f_c ,

$$f_c = \rho_{t,r,3}\, T_{t,r,3} \;/\; \rho_{t,r,1}\; T_{t,r,1} = \frac{p_{t,3,r}}{p_{t,1,r}} \tag{3.50}$$

and the overall impeller loss coefficient ($\bar{\omega}_{imp}$),

$$\bar{\omega}_{imp} = \bar{\omega}_{BL} + \bar{\omega}_{SF} + \bar{\omega}_{HS} + \bar{\omega}_{mix} + \bar{\omega}_{cl} \tag{3.51}$$

where $\bar{\omega}_{BL}$ is blade loading loss coefficient $\bar{\omega}_{SF}$ is the skin friction loss coefficient $\bar{\omega}_{HS}$ is the hub to shroud loss coefficient $\bar{\omega}_{mix}$ is the mixing loss coefficient and $\bar{\omega}_{cl}$ is the clearance loss coefficient. All the loss coefficients are presented in the section 3.4.4, while the ideal relative total pressure is based on isentropic compression:

$$p_{t,3,r,is} = p_{t,1,r}\, e^{\frac{\varphi(T_{t,3,r}) - \varphi(T_{t,1,r})}{R_{gas}}} \tag{3.52}$$

Then the outlet total pressure is expressed as:

$$p_{t,3} = p_{t,3,r}\, e^{\frac{\varphi(T_{t,3})-\varphi(T_{t,3,r})}{R_{gas}}} \tag{3.53}$$

Then, utilizing the entropy function, the outlet static conditions are computed.

Calculating then the density in outlet position, the mass flow is defined as:

$$\dot{m} = \rho_3 \mathrm{A}_3 \mathrm{V}_{\mathrm{m},3} \tag{3.54}$$

where, outlet are (A_3) is:

$$A_3 = \pi\, D_3\, b_3 - Z_{FB}\, b_3\, t_{b,3}\, Cos\left(\beta_{b,3}\right) \tag{3.55}$$

Given that, the mass flow is user-defined, an iterative process is carried out between eq (3.44) and (3.55) for predicting the impeller outlet meridional velocity until the error between the calculated and the given mass flow reaches a tollerance value.

Considering the initial impeller outlet meridional velocity, it can be defined as:

$$V_{m,3,initial} = \frac{\dot{m}}{\rho_{t,3}\mathrm{A}_3}\,, \rho_{t,3} = \frac{\mathrm{P}_{\mathrm{t},3}}{\mathrm{R}_{\mathrm{gas}}\mathrm{T}_{\mathrm{t},3}} \tag{3.56}$$

where both the total temperature and pressure are approximated with the following equation:

$$\mathrm{T}_{\mathrm{t},3} = \mathrm{T}_{\mathrm{t},1} + \frac{1}{2}\frac{1}{1005}\mathrm{U}_3^2, \qquad \mathrm{P}_{\mathrm{t},3} = \mathrm{P}_{\mathrm{t},1}\left(\frac{0.9\left(\mathrm{T}_{\mathrm{t},3} - \mathrm{T}_{\mathrm{t},1}\right)}{\mathrm{T}_{\mathrm{t},1}} + 1\right)^{\frac{1.4}{0.4}} \tag{3.57}$$

Vaneless diffuser outlet (4)

For calculating the outlet vaneless diffuser conditions, the calculation procedure, presented by Galvas (1973), is followed. Differential equations relating Mach number, flow angle and total temperature to radius ratio through the fundamental relations of continuity, equilibrium, heat transfer and fluid state for adiabatic flow in a geometrically constant depth radial passage are solved,

$$\frac{1}{M^2}\frac{dM^2}{d\overline{R}} = -\frac{2\left(1+\frac{\gamma-1}{2}M^2\right)}{M^2\sec(a)^2}\left[\frac{\zeta}{B\cos(\alpha)} + \frac{1}{B}\frac{dB}{d\overline{R}}\frac{\sec(\alpha)^2}{\overline{R}}\right] \tag{3.58}$$

$$\frac{1}{\tan(\alpha)}\frac{\mathrm{dtan}(\alpha)}{d\overline{R}} = \frac{\sec(\alpha)^2}{M^2 - \sec(\alpha)^2}\left\{[1+(\gamma-1)M^2]\,\frac{\zeta}{B\cos(\alpha)} + \frac{1}{B}\frac{dB}{d\overline{R}} - \frac{M^2}{\overline{R}}\right\} \tag{3.59}$$

where,

$$\zeta = C_{f,vnless}\frac{R_3}{b_3} \tag{3.60}$$

$$\overline{R} = \frac{R}{R_3} \tag{3.61}$$

$$B = \frac{b}{b_3} \tag{3.62}$$

where the required Reynolds number and hydraulic diameter are computed as follow:

$$Re_{vnless} = \frac{4\,\dot{m}}{\pi\, D_{hyd,vnless}\,\mu_{s,3}} \tag{3.63}$$

$$D_{hyd,vnless} = \sqrt{\frac{4}{\pi}\left(\frac{A_4}{2}+\frac{A_3}{2}\right)} \tag{3.64}$$

while vaneless diffuser friction coefficient is calculated based on eq. (3.92)-(3.99).

Having computed both outlet absolute Mach number and flow angle and knowing that inlet total temperature is equal to outlet one, both meridional and circumferential velocities are calculated. Concerning the total pressure loss in the vaneless space, it is computed from the following equation:

$$\frac{1}{\frac{P_{t,4}}{P_{t,3}}} = 1 + \frac{\gamma C_{f,vnless}}{\cos(\mathrm{a_3})}\frac{\mathrm{R_3}}{\mathrm{b_3}}\frac{\int_1^R M^3\,\frac{\mathrm{a}}{\mathrm{a_t}}\frac{\rho}{\rho_t}\,\mathrm{RdR}}{M_3\left(\frac{\mathrm{a}}{\mathrm{a_t}}\right)_3\left(\frac{\rho}{\rho_t}\right)_3} \tag{3.65}$$

where a is the local acoustic velocity in the corresponding radial position.

Vaned diffuser outlet (5)

As vaned diffuser is a stationary component then:

$$h_{t,5} = h_{t,4} \rightarrow \mathrm{T_{t,5}} = \mathrm{T_{t,4}} \tag{3.66}$$

Guessing then an absolute velocity (V_5):

$$h_{s,5} = h_{t,5} - \frac{1}{2}V_5^2 \rightarrow T_{s,5} = T\left(h_{s,5}\right) \tag{3.67}$$

Also, both meridional and circumferential velocity components are calculated, assuming that the deviation angle is zero:

$$V_{m,5} = V_5 \cos\left(\beta_{v,5}\right) , V_{u,5} = V_5 \sin\left(\beta_{v,5}\right) \tag{3.68}$$

Concerning outlet total pressure, it is defined as:

$$p_{t,5} = p_{t,4} - \left(\bar{\omega}_{inc,vnd} + \bar{\omega}_{SF,vnd}\right)\left(p_{t,4} - p_{s,4}\right) \tag{3.69}$$

where both incidence($\bar{\omega}_{inc,vnd}$) and skin friction($\bar{\omega}_{SF,vnd}$) loss coefficients are presented in the section 3.4.5.

Having computed the total pressure in vaned diffuser outlet station, then both outlet static conditions and density are also calculated, using the entropy function φ. Finally, the mass flow calculation is following:

$$\dot{m} = \rho_5 A_5 V_{m,5} \tag{3.70}$$

where outlet area (A_5) is expressed as:

$$A_5 = \pi D_5 b_5 - z_v b_5 t_{b,5} Cos\left(\beta_{v,5}\right) \tag{3.71}$$

Then, an iterative process is carried out between eq (3.67) and (3.71) for predicting the outlet absolute velocity until the error between the calculated and the given mass flow reaches a tollerance value.

Considering the initial outlet velocity, it can be defined as:

$$V_{5,initial} = \frac{\dot{m}}{\rho_4 A_5} \tag{3.72}$$

Volute outlet (6)

As volute is a stationary component then:

$$h_{t,6} = h_{t,5} \rightarrow T_{t,6} = T_{t,5} \tag{3.73}$$

Guessing then an absolute velocity (V_6):

$$h_{s,6} = h_{t,6} - \frac{1}{2}V_6^2 \rightarrow T_{s,6} = T\left(h_{s,6}\right) \tag{3.74}$$

Also, both meridional and circumferential velocity components are calculated, assuming that the outlet flow angle is zero. Concerning outlet total pressure, it is calculated as follows:

$$p_{t,6} = p_{t,5} - \left(\bar{\omega}_{m,vol} + \bar{\omega}_{SF,vol}\right)\left(p_{t,5} - p_{s,5}\right) \quad (3.75)$$

where both meridional velocity ($\bar{\omega}_{m,vol}$) and skin friction($\bar{\omega}_{SF,vol}$) loss coefficients are presented in the subsection 3.4.6.

Having computed the total pressure in outlet station, then both outlet static conditions and density are also calculated, using the entropy function φ. Finally, the mass flow calculation is following:

$$\alpha_6 = 0 \rightarrow V_6 = V_{m,6} \rightarrow \dot{m} = \rho_6 \mathrm{A}_6 \mathrm{V}_{\mathrm{m},6} \quad (3.76)$$

where the outlet area (A_6) is defined as [Ceyrowsky et al 2018]:

$$\mathrm{A}_6 = \mathrm{AR}\ \mathrm{D}_6\ \mathrm{D}_5 = \pi\ R_{vol}^2 \quad (3.77)$$

Then, an iterative process is carried out between eq (3.67) - (3.76) for predicting the impeller outlet velocity until the error between the calculated and the given mass flow reaches a tollerance value.

Considering the initial outlet velocity, it can be defined as:

$$V_{6,initial} = \frac{\dot{m}}{\rho_5 \mathrm{A}_6} \quad (3.78)$$

3.4.3 Impeller inlet loss coefficients

The total impeller inlet loss model, described in this section consists of both impeller inlet incidence and contraction losses. Concerning the impeller incidence losses calculation, two approaches are followed, the one described by Aungier (2000), and the one given by Galvas (1973). The Aungier approach is the following:

$$\bar{\omega}_{inc} = 0.8\left[1 - V_{m1} \,/\, \left(W_1\, Cos\left(\beta_{b,1}\right)\right)\right]^2 + [1 - B_1]^2 \quad (3.79)$$

$$W_1\, Cos\left(\beta_{b,1}\right) = \frac{W_{U1}}{Tan\left(\beta_{b,1}\right)} \quad (3.80)$$

The Galvas (1973) approach is the following:

$$\bar{\omega}_{inc} = 0.8\left[1 - V_{m1} \,/\, \left(W_1\, Cos\left(\beta_{opt}\right)\right)\right]^2 \quad (3.81)$$

$$\beta_{opt} = \beta_{b,1} + e \quad (3.82)$$

$$e = \mathrm{atan}\left[\frac{(1 - B_1)\, tan\left(\beta_{blade,1}\right)}{1 + B_1\, tan\left(\beta_{blade,1}\right)^2}\right] \quad (3.83)$$

where B_1 is the impeller inlet blockage factor.

The contraction losses are considered to be the results of the flow passage area reduction due to the inducer blade thickness and they are estimated by the following equation as presented in [Goudas 2019],

$$\bar{\omega}_{contr} = \left(1 - \frac{A_{th,axial}}{A_1}\right)^2 \tag{3.84}$$

$$A_{th,axial} = A_1 - t_{b,1}\, Cos(\beta_{b,1})\ \left(\frac{D_{\text{tip},1}}{2} - \frac{D_{\text{hub},1}}{2}\right)\ Z_{MB} \tag{3.85}$$

where $A_{th,axial}$ is the impeller axial throat area.

3.4.4 Impeller loss coefficients

The loss coefficients correspond to impeller blade loading, skin friction, hub to shroud (tip) loading and wake mixing ones.

For calculating the impeller blade loading losses the following correlation, quoted by Aungier (2000), is used:

$$\bar{\omega}_{BL} = \left(\frac{\Delta W}{W_1}\right)^2 \ / \ 24 \tag{3.86}$$

where blade velocity difference ΔW is computed by Aungier (2000) from irrotational flow relations, assuming the ideal or optimum blade loading style,

$$\Delta W = 2\,\pi \frac{D_3 U_3 I_b}{Z_{eff}\ L_{B,imp}} = 2\,\pi \frac{D_3\ pwr_{imp}}{Z_{eff}\ L_{B,imp}\ \dot{m}\ U_3} \tag{3.87}$$

where Z_{eff} is the effective impeller blade number:

$$Z_{eff} = Z_{MB} + Z_{MB}\left(1 - le_{spl}\right) \tag{3.88}$$

while the impeller blade mid-stream length($L_{B,imp}$) is defined as[Galvas 1973]:

$$L_{B,imp} = \frac{D_3}{2}\ \frac{1 - \frac{D_{ref,1}}{0.3048}}{Cos\left(\beta_{b,3}\right)} \tag{3.89}$$

For impeller skin friction losses calculation, the following correlation is used:

$$\bar{\omega}_{SF} = 2\ K_{sf}\ \mathrm{C_{f,imp}} \left(\frac{\bar{W}}{W_3}\right)^2 \frac{L_{B,imp}}{D_{hyd,imp}} \tag{3.90}$$

$$\bar{W}^2 = \left(\ W_1^2 + W_2^2\ \right) / 2 \tag{3.91}$$

where Aungier (2000) proposes a value of skin friction parameter K_{sf} equal to 2 while Galvas (1973) proposes a value of 5.6 for compact impellers and 7.0 for impellers with tandem blades.

Considering the impeller friction coefficient $C_{f,imp}$, Aungier (2000) pointed out that it depends on component Reynolds number and wall roughness. For a Reynolds number below 2000, the flow is laminar, hence the friction coefficient is expressed as:

$$C_f = C_{f,l} \tag{3.92}$$

In case of Reynolds number between 2000 and 4000, the friction coefficient is expressed as:

$$C_f = C_{f,l} + \left(C_{f,t} - C_{f,l}\right)\left(\frac{Re_d}{2000} - 1\right) \tag{3.93}$$

For a Reynolds number higher than 4000 (turbulent flow) the friction coefficient is equal to turbulent friction coefficient:

$$C_f = C_{f,t} \tag{3.94}$$

For calculating the laminar and turbulent friction coefficients based on wall roughness, the following correlations are utilized:

$$C_{f,l} = \frac{16}{Re_d} \tag{3.95}$$

$$C_{f,t} = \begin{cases} C_{f,t,s} & Re_e < 60 \\ C_{f,t,s} + \dfrac{C_{f,t,r} - C_{f,t,s}}{1 - \dfrac{60}{Re_e}} & Re_e \geq 60 \end{cases} \tag{3.96}$$

where,

$$Re_e = (Re - 2000)\frac{e}{D_{hyd}} \tag{3.97}$$

$$\frac{1}{\sqrt{4\,C_{f,t,s}}} = -2\log_{10}\left(\frac{2.51}{Re_d\sqrt{4\,C_{f,t,s}}}\right) \tag{3.98}$$

$$\frac{1}{\sqrt{4\,C_{f,t,s}}} = -2\log_{10}\left(\frac{e}{3.71\,D_{hyd}}\right) \tag{3.99}$$

For impeller hydraulic diameter calculation (D_{hyd}), Boyce (2003) correlation is used and is expressed as:

$$D_{hyd,imp} = \frac{\frac{\pi}{2}\,Cos(\beta_{b,1})\,(\,D_{tip,1}^2 - D_{hub,1}^2\,)}{\pi\,Cos(\,\beta_{b,1}\,)\,(D_{tip,1} + D_{hub,1}) + 2\,z_{eff}\,(D_{tip,1} - D_{hub,1})} + \frac{\pi\,D_3\,b_3\,Cos(\beta_{b,3})}{\pi\,D_3\,Cos(\beta_{b,3}) + Z_{eff}\,b_3} \tag{3.100}$$

Concerning the impeller hub to shroud loading loss coefficient, it is calculated through the following correlations, described by Aungier (2000):

$$\overline{W} = (W_1 + W_2) / 2 \tag{3.101}$$

$$X_1 = \left(X_{tip,1} - X_{hub,1} \right) \frac{D_{\text{ref},1} - D_{\text{hub},1}}{D_{\text{tip},1} - D_{\text{hub},1}} + X_{hub,1} \tag{3.102}$$

$$\bar{\kappa}_m = (X_2 + X_1) / L_B \tag{3.103}$$

$$b_1 = \frac{\left(D_{\text{tip},1} - D_{\text{hub},1}\right)}{2} \tag{3.104}$$

$$\bar{b} = (b_1 + b_2) / 2 \tag{3.105}$$

$$\bar{\omega}_{HS} = (\bar{\kappa}_m \, \bar{b} \, \overline{W} / \ W_1)^2 / 6 \tag{3.106}$$

where X_i represents the streamline slope in each station.

For the wake mixing loss coefficient calculation, the formula presented by Aungier (2000) is used:

$$\bar{\omega}_{mix} = \left[\left(V_{m,wake} - V_{m,mix} \right) / \ W_1 \right]^2 \tag{3.107}$$

The velocity, at which separation takes place, is estimated by the following equation:

$$W_{SEP} = \begin{cases} W_3 & , \quad D_{eq} \leq 2 \\ W_3 \, D_{eq} / \ 2 & , \quad D_{eq} > 2 \end{cases} \tag{3.108}$$

where,

$$D_{eq} = \frac{(W_1 + \ W_3 + \Delta W)}{2 \, W_3} \tag{3.109}$$

The meridional velocities before and after mixing are estimated by the following correlations:

$$V_{m,wake} = \sqrt{W_{SEP}^2 - W_{U3}^2} \tag{3.110}$$

$$V_{m,mix} = V_{m3} \frac{A_3}{\pi \, D_3 b_3} \tag{3.111}$$

For the impeller clearance losses calculation due to blade to blade pressure difference and clearance leakage, the following equation, described by Aungier (2000) is used.

$$\bar{\omega}_{cl} = 2 \, \dot{m}_{\text{cl}} \frac{\Delta p_{cl}}{\dot{m} \, \rho_1 \, W_1^2} \tag{3.112}$$

where the parameters used for calculating clearance losses, are computed as follows:

$$\dot{m}_{cl} = \rho_3 \, Z_{eff} \, s \, L \, U_{cl} \tag{3.113}$$

$$U_{cl} = 0.816 \sqrt{2 \frac{\Delta p_{cl}}{\rho_3}} \tag{3.114}$$

$$\Delta p_{cl} = \dot{m} \frac{0.5 \, D_3 \, V_{u3} - 0.5 \, D_{ref,1} \, V_{u1}}{z \; 0.25 \left(D_3 + \; D_{ref,1}\right) L_{mer,imp}} \tag{3.115}$$

For calculating the impeller mean stream meridional length($L_{mer,imp}$) calculation, it is assumed that the impeller meridional curvature corresponds to an arc with radius R_{arc}:

$$X_1 = \frac{X_{\text{tip},1} - \; X_{\text{hub},1}}{D_{\text{tip},1} - D_{\text{hub},1}} \left(D_{\text{ref},1} - D_{\text{hub},1}\right) + \; X_{\text{hub},1} \tag{3.116}$$

$$R_{arc} = \frac{L_{axial,imp} - \frac{b_3}{2}}{2} + \frac{\frac{D_3}{2} - \frac{D_{\text{ref},1}}{2}}{2} \tag{3.117}$$

$$L_{mer,imp} = \left[\frac{\pi}{2} - \; [X_1 + (90^o - X_3)]\right] R_{arc} \tag{3.118}$$

3.4.5 Vaned diffuser loss coefficients

Concerning the vaned diffuser overall loss coefficient, it consists of both vaned diffuser incidence and skin friction loss coefficients. For the vaned diffuser incidence loss coefficient calculation, the Aungier (2000) impeller incidence loss coefficient formula is utilized. Although, a proper modification is performed, in order the incidence loss correlation to be properly integrated to vaned diffuser component,

$$\bar{\omega}_{inc,vnd} = \; 0.8 \left[1 - \frac{Cos(\alpha_4)}{Cos(\beta_{b,4})}\right]^2 + [1 - B_4]^2 \tag{3.119}$$

For the vaned diffuser skin friction loss coefficient, it can be defined as [Aungier 2000]:

$$\bar{\omega}_{SF,vnd} = \; 4 \, C_{f,vnd} \left(\frac{\overline{V}}{V_5}\right)^2 \frac{L_{B,vnd}}{D_{hyd,vnd}} \left(\frac{D_{hyd,vnd}}{2\delta}\right)^{0.25} \tag{3.120}$$

where,

$$\frac{2\delta}{D_{hyd,vnd}} = 5.142 \, C_{f,vnd} \frac{L_{B,vnd}}{D_{hyd,vnd}} \tag{3.121}$$

Note that, the friction coefficient($C_{f,vnd}$) is calculated based on eq. (3.92)-(3.99), while the vane rms stream length($L_{B,vnd}$) and the vane diffuser hydraulic diameter are expressed as:

$$L_{B,vnd} = \frac{D_5 - D_4}{2} \; \frac{2}{Cos(\beta_{v,4}) + \; Cos(\beta_{v,5})} \tag{3.122}$$

$$D_{hyd,vnd} = \sqrt{\frac{2\,(\pi\, D_4\, b_4 + \pi\, D_5\, b_5 - Z_v\, t_{v,5}\, \mathrm{Cos}(\beta_{v,5})}{\pi}} \tag{3.123}$$

3.4.6 Volute loss coefficients

The volute loss is based on the calculation of its both meridional velocity and skin friction loss coefficients.

For the meridional velocity loss coefficient calculation in a volute component, Aungier (2000) proposed the following equation,

$$\bar{\omega}_{m,vol} = \left(\frac{V_{m5}}{V_5}\right)^2 \tag{3.124}$$

The skin friction loss coefficient, presented by Aungier (2000), is expressed as:

$$\bar{\omega}_{SF,vol} = 4\, C_{f,vol} \left(\frac{V_6}{V_5}\right)^2 \frac{L_{vol}}{D_{hyd,vol}} \tag{3.125}$$

where both volute hydraulic diameter and average path length are defined as:

$$D_{vol,hyd} = \sqrt{4\, A_6 \,/\, \pi} \tag{3.126}$$

$$L_{vol} = \pi \frac{(\, D_6 + D_5\,)}{4} \tag{3.127}$$

3.4.7 Choke and Stall Indices calculation

The choke-stall indices, described in this section are expressions for calculating how far away an operating point is from choke and stall. When choke and stall index are positive and negative respectively, then the compressor operates stably. The choke indices are calculated at four/six stations along the compressor, namely impeller inlet, impeller outlet, volute inlet, volute outlet and, in case of vaned diffuser centrifugal compressor, vaned diffuser inlet and outlet.

$$index_{ch,i} = \frac{\dot{m}_{ch,i} - \; \dot{m}}{\dot{m}_{ch,i}} \tag{3.128}$$

For the stall index, the calculation takes place at the impeller inlet (1) and vaned diffuser inlet (5),

$$index_{stall,1} = I_R \tag{3.129}$$

$$index_{stall,5} = \frac{0.39 - (K + K_0)}{0.39} \tag{3.130}$$

where,

$$I_R = \begin{cases} \left(\frac{D_{eq}}{2} - 1\right)\left(\frac{W_{u,3}}{V_{m,3}} - 2\,Cot(90^o - \beta_{b3})\right) & , \quad D_{eq} > 2 \\ < 0 & , \quad D_{eq} \leq 2 \end{cases} \tag{3.131}$$

$$K = \frac{D_4}{2\,h_{th}}\left[\frac{Cos(\alpha_4)}{Cos(\alpha_{th,4})} - 1\right] \tag{3.132}$$

$$K_0 = \frac{M_4^2\,Sin(\beta_{v,4})^2\,Cos(\beta_{v,4})}{1 - M_4^2\,Sin(\beta_{v,4})^2} \tag{3.133}$$

3.4.8 Centrifugal compressor performance map generation

For generating the performance map of a CC component , the user has to define both the desired design and off-design speeds (e.g 50%, 60%, 110%, etc.). In map generation mode, the mass flow is not required as input, as the meanline model automatically predicts and defines the mass flow range(stall, choke) for each speed and then calculates the CC pressure ratio and efficiency for all points along the characteristic speed-line between stall and choke. Concerning the stall and choke point estimation, the process, followed in the current analysis, is based on the one presented by Kolias et al. (2021). Specifically, a secant method is used to establish numerically the compressor stall and choking mass flow rates for each compressor speed. In each speed, the secant method updates the compressor inflow, until both stall and choke minimum indices are zeroed.

3.4.9 Centrifugal compressor meanline analysis verification

The comparison between the predictions of the vaneless and the vaned diffuser CML and the corresponding measured data are depicted in Figure 3-7 and Figure 3-8, for specific commercial centrifugal compressors, for which geometry and measured data are provided by a T/C manufacturer[1]. Also, both 1D compressor geometries are given in Table 3-2 and Table 3-3.

[1] www.turbomed.gr

Table 3-2: Vaneless Diffuser Centrifugal Compressor geometry.

Vaneless Diffuser Centrifugal Compressor Geometry			
Parameter	Value	Parameter	Value
$D_{1,hub}$	0.029 [m]	b_3	0.016 [m]
$D_{1,tip}$	0.085 [m]	b_4	0.016 [m]
D_3	0.137 [m]	Z_{MB}	8 [-]
D_4	0.16 [m]	Z_{FB}	16 [-]
$\beta_{b,1}$	52.25^o	L_A	0.036 [m]
$\beta_{b,3}$	36.5^o	AR_{vol}	0.23 [-]
t_1	0.0021 [m]	N_{des}	60000 [Rpm]
t_3	0.0017 [m]	cl	0.00035
le_{spl}	0.3 [-]		

Table 3-3: Vaned Diffuser Centrifugal Compressor geometry.

Vaned Diffuser Centrifugal Compressor Geometry			
Parameter	Value	Parameter	Value
$D_{1,hub}$	0.040 [m]	t_4	0.0007 [m]
$D_{1,tip}$	0.118 [m]	t_5	0.011 [m]
D_3	0.176 [m]	b_3	0.0084 [m]
D_4	0.202 [m]	b_4	0.0082 [m]
D_5	0.545 [m]	b_5	0.0082 [m]
$\beta_{b,1}$	50^o	Z_{MB}	8 [-]
$\beta_{b,3}$	25^o	Z_{FB}	16 [-]
$\beta_{v,4}$	68^o	L_A	0.051 [m]
$\beta_{v,5}$	60^o	Z_V	18 [-]
t_1	0.0016 [m]	AR_{vol}	0.26 [-]
t_3	0.0009 [m]	N_{des}	55000 [Rpm]
le_{spl}	0.3 [-]	cl	0.00035

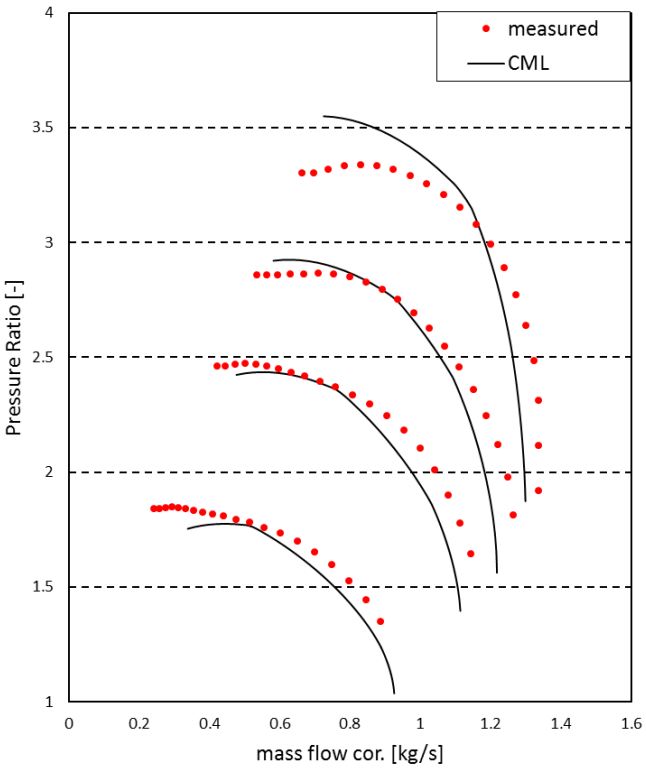

(a)

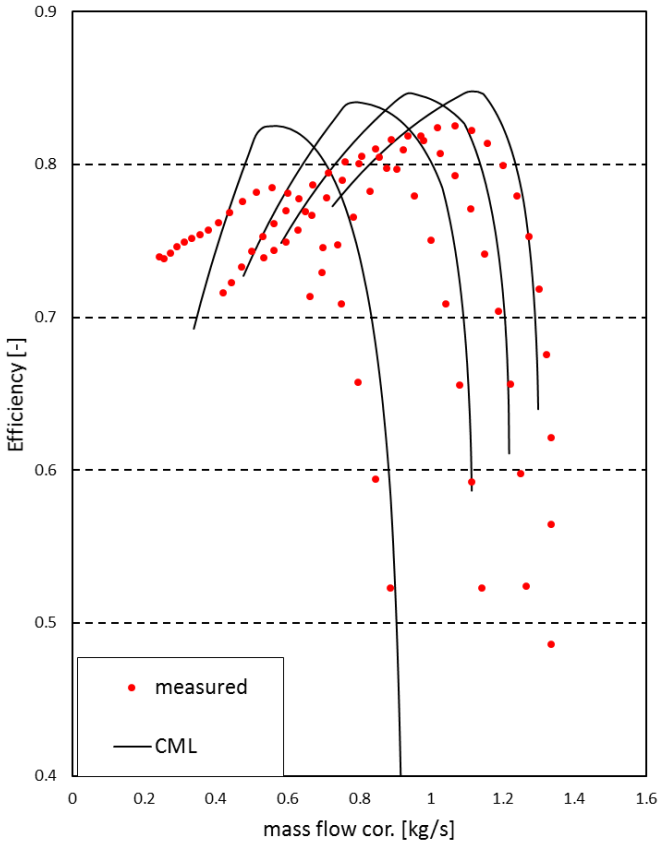

(b)

Figure 3-7: Vaneless CML validation against measured data: **(a):** Pressure ratio **(b)** Efficiency

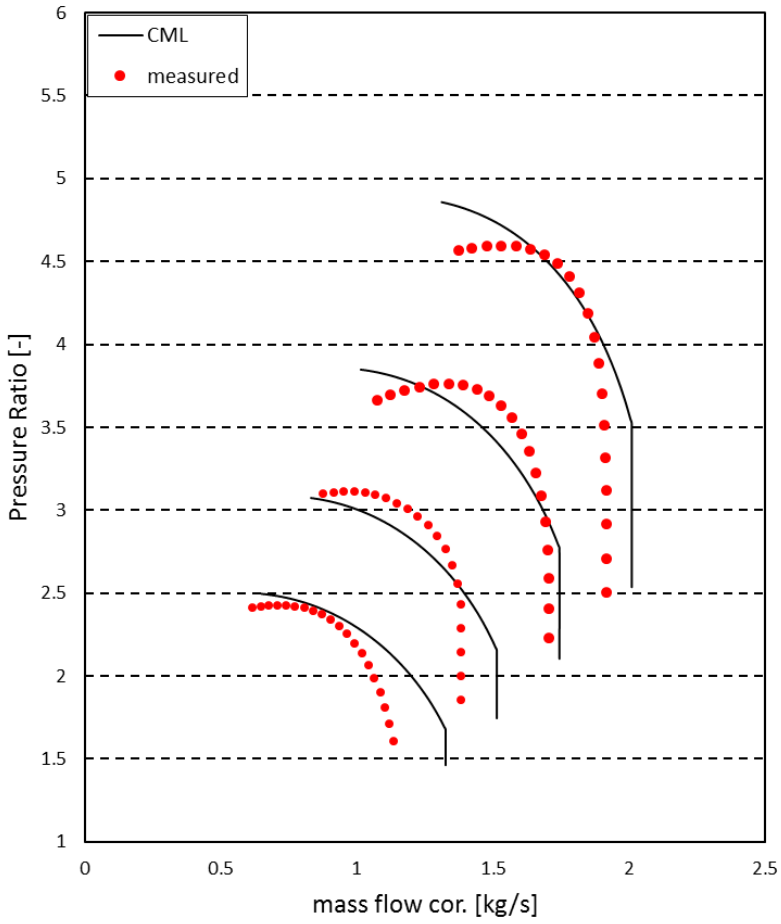

(a)

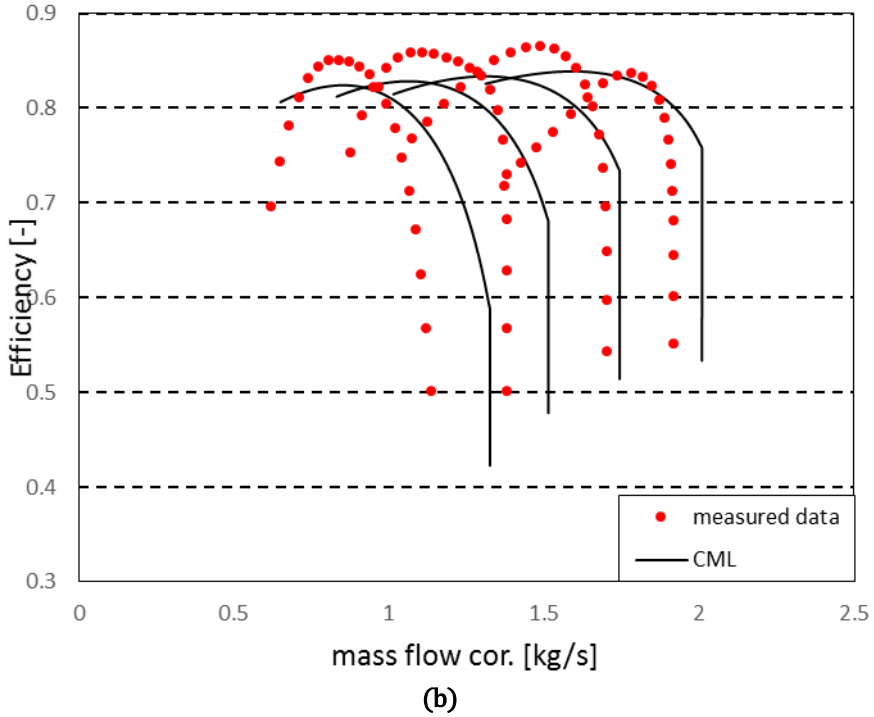

(b)

Figure 3-8: Vaned CML validation against measured data: **(a):** Pressure ratio **(b)** Efficiency

The centrifugal compressor meanline model, developed in this thesis, shows acceptable agreement with the measured data, with similar or better behavior compared to other published works [Stuart et al. 2017,2018].

3.5 Radial Turbine Meanline model

The RT meanline (Radial-TML) model conducts a mean-line (1D) analysis to establish the off-design performance of a radial turbine of known geometry. The RT model comprises models for estimating the performance of volutes, vaned nozzles, vaneless nozzles, and impellers. Depending on the user-defined RT configuration, the vaned nozzle and/or volute sub-models can be turned on or off.

Exit flow and performance conditions in each individual component sub-model, shown in Figure 3-9 (impeller, vaneless nozzle, etc.) are calculated, considering the corresponding loss models, and then are used as inputs in the next downstream component. At the end of the radial turbine calculation, overall performance of the turbine is established and is expressed in the form of isentropic and polytropic efficiencies, flow coefficient, work coefficient, etc.

Regarding the RT stations for the mean-line calculation (Figure 3-10), station 1 corresponds to the volute inlet, 2 to the vaned nozzle inlet, 3 to the vaneless nozzle inlet, 4 to the impeller inlet, 5 to the impeller outlet just upstream of blade trailing edge, and 6 to the impeller outlet.

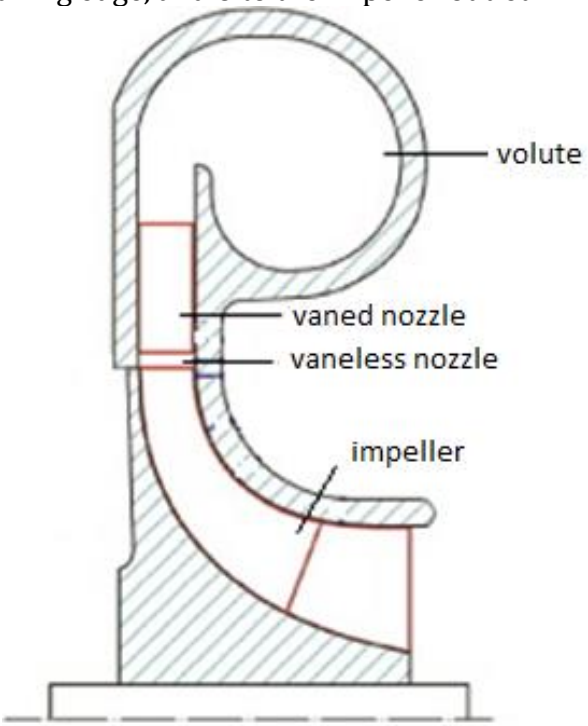

Figure 3-9: Radial Turbine components.[Aungier 2005]

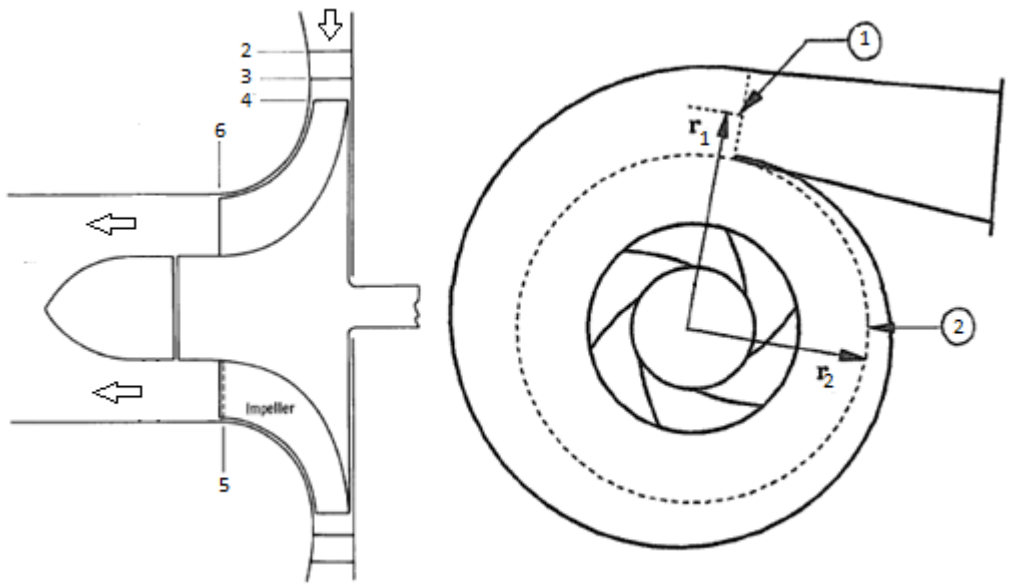

Figure 3-10: Radial turbine stations. [Wasserbauer and Glassman 1975, Aungier 2005]

3.5.1 Meanline analysis input data

The RT meanline analysis is conducted within the PROOSIS environment, depicted in Figure 3-11, with input data as presented in Table 3-4. Concerning the geometrical parameters that are included in input data, their graphic representation is shown in Figure 3-12. Typical T/C radial turbine impeller, vaned nozzle and volute are illustrated in Figure 3-13.

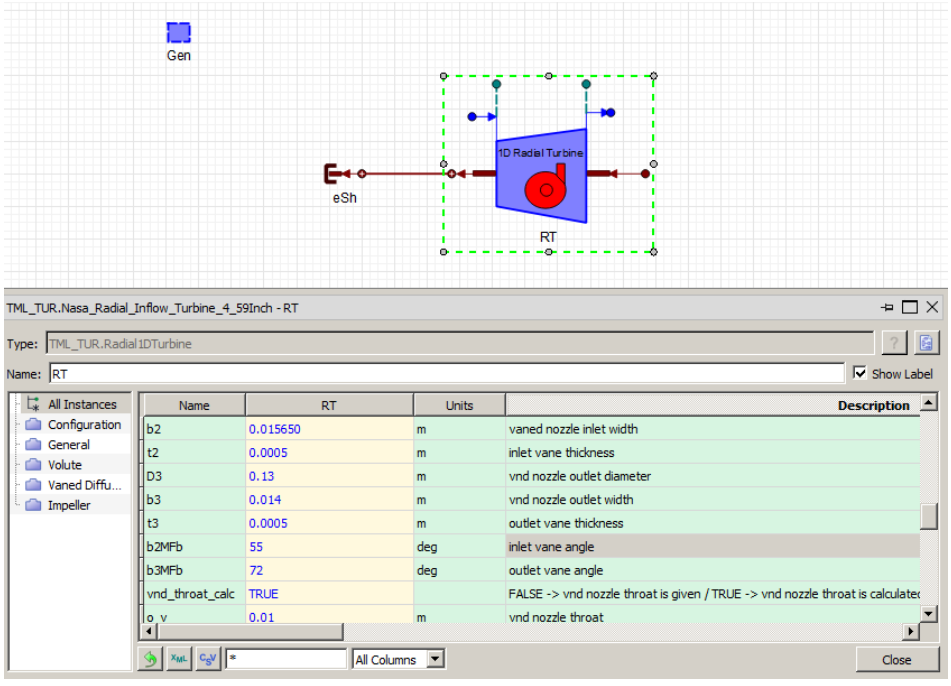

Figure 3-11: RT meanline analysis schematic and input data in PROOSIS environment.

Table 3-4: RT meanline analysis input data..

Radial turbine geometry			
Parameter		Parameter	
$D_{hub,5}$	Impeller hub outlet diameter	t_3	Vnd nozzle outlet blade thickness
$D_{tip,5}$	Impeller tip outlet diameter	t_2	Vnd nozzle inlet blade thickness
D_4	Impeller inlet diameter	b_4	Impeller inlet blade height
D_3	Vnless Nozzle inlet diameter	b_3	Vnless nozzle inlet channel width
D_2	Vnd Nozzle inlet diameter	b_2	Vnd nozzle inlet channel width
$\beta_{b,5}$	Impeller outlet blade angle	Z_{MB}	Impeller main blades number
$\beta_{b,4}$	Impeller inlet blade angle	Z_{FB}	Impeller full blades number
$\beta_{v,3}$	Vnd nozzle outlet vane angle	L_A	Impeller axial length
$\beta_{v,2}$	Vnd nozzle inlet vane angle	Z_V	Vnd nozzle vanes number
t_5	Impeller outlet blade thickness	AR_{vol}	Volute aspect ratio
t_4	Impeller inlet blade thickness	N_{mech}	RT speed
le_{spl}	Splitter blades dimensionless position	$P_{t,in}$	Inlet total pressure
Fluid	Working fluid (Air)	$T_{t,in}$	Inlet total temperature
$\dot{m}$	CC mass flow	e	Wall roughness
cl	Impeller clearance		

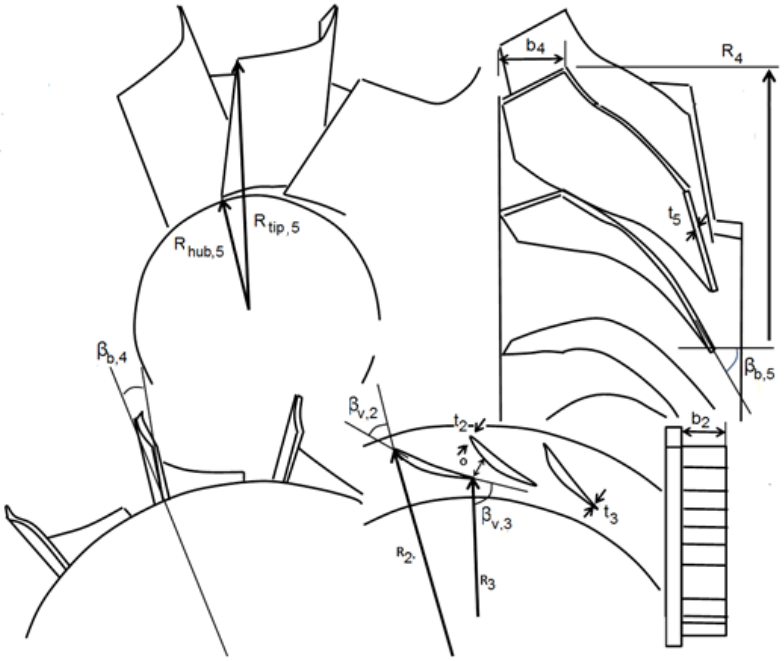

Figure 3-12: RT geometrical parameters.

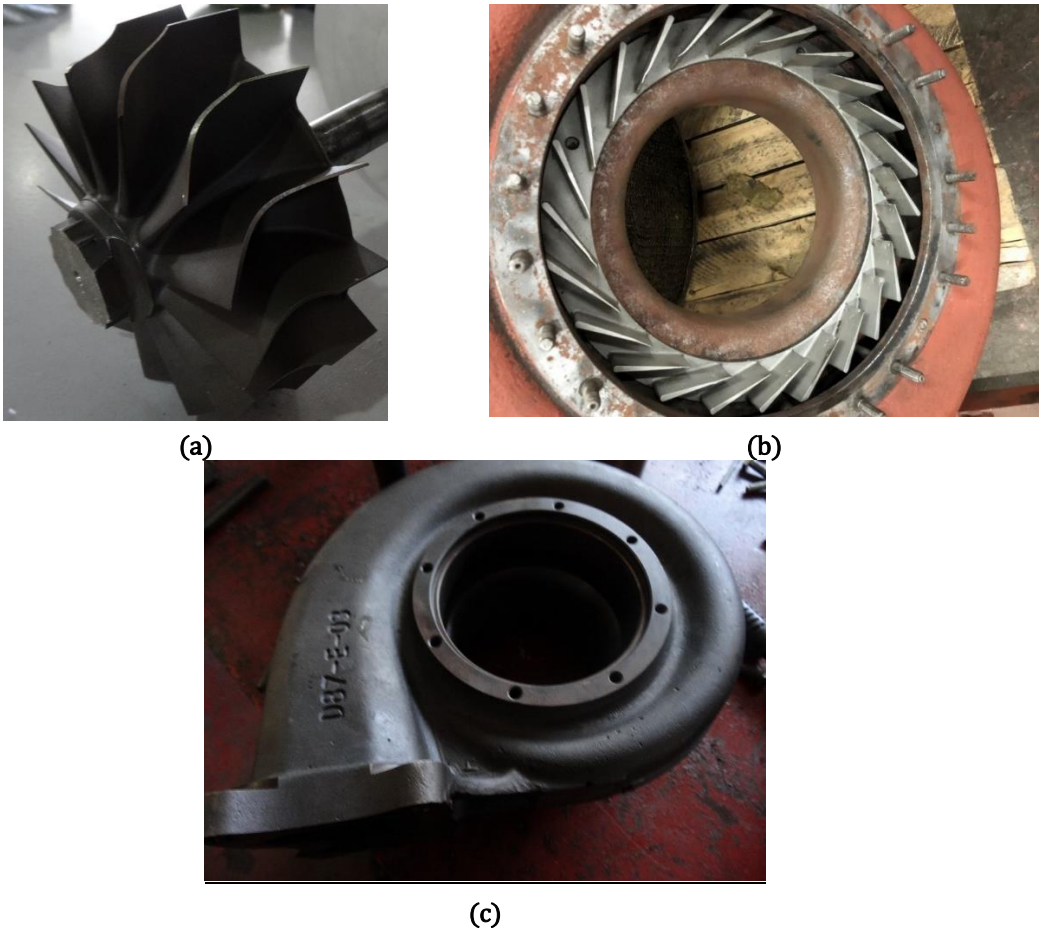

Figure 3-13: T/C radial turbine[1]: **(a)** impeller **(b)** vaned nozzle **(c)** volute

3.5.2 Meanline analysis

To conduct the meanline analysis, the reference radius is placed at the RMS position, where the turbine inlet area is divided into two equal areas.

Volute inlet(1)

According to the Aungier (2005) volute model, the passage area and the mean radius are specified at station 1, where the flow is inside the volute, but has not yet started to exit the volute. These parameters are also specified at station 2i, where half of the flow has exited from the volute passage. Hence the analysis is not restricted to a classical volute configuration. For example, a constant area plenum where the passage mean radius and area at stations 1 and 2i are identical can be accommodated. Station 2 is the annular passage at the volute exit, where the radius and the hub-to-shroud passage width, are specified.

First the inlet volute area is calculated based on the user-defined aspect ratio. Then, as inlet flow is axial, the meridional velocity and the static conditions are computed using the continuity equation, as both the mass flow and the inlet total conditions have been defined:

[1] www.turbomed.gr

$$[V_1, V_{m,1}, P_{s,1}, T_{t,1}] = f[a_1 = 0, A_1, \dot{m}, T_{t,1}, P_{t,1}] \quad (3.134)$$

where the outlet area (A_1) is defined as [Ceyrowsky et al 2018]:

$$A_1 = AR\ D_1\ D_2 = \pi\ R_{vol}^2 \quad (3.135)$$

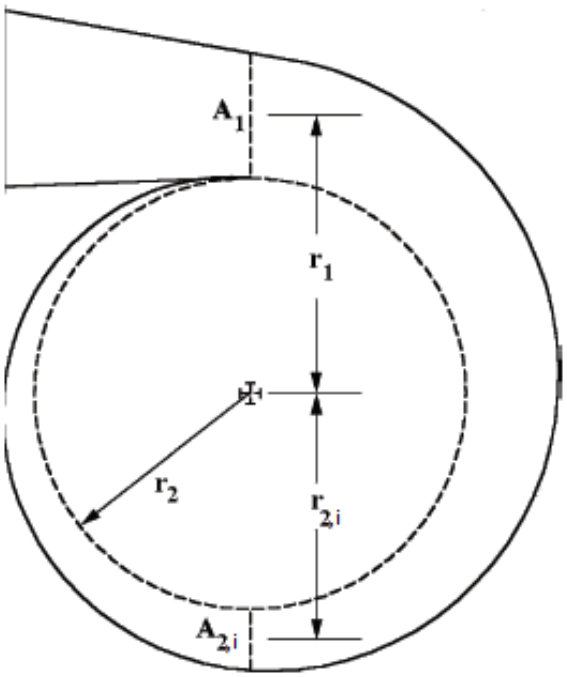

Figure 3-14: Radial turbine volute.

Volute mid station(2i)

Assuming no losses($Y_{vol} = 0$) and that half of the inlet mass flows across station 2i [Aungier (2005)], the flow conditions at station 2i are calculated as follows:

$$h_{t,2i} = h_{t,1}\ , T_{t,2i} = T_{t,1} \xrightarrow{Y_{vol}=0} P_{t,2i} = P_{t,1} \quad (3.136)$$

Then, the meridional velocity and the static conditions are computed using continuity equation as:

$$[V_{2i}, V_{m,2i}, P_{s,2i}, T_{s,2i}] = f[a_{2i}, A_{2i}, \dot{m}_{2i}, T_{t,2i}, P_{t,2i}] \quad (3.137)$$

where the flow angle at station 2i is, in turn, calculated as:

$$V_{u,2i} = V_{m,2i}\frac{A_1}{A_2}, \tan a_{2i} = \frac{A_1}{A_2} \quad (3.138)$$

Volute outlet(2)

The angular momentum at the volute exit is estimated from conservation of angular momentum based on the flow data at station 2i. A mass balance using the inlet mass flow and this assigned tangential velocity component supplies the other flow conditions at station 2. However, the losses and the corresponding total thermodynamic conditions at station 2 must also be determined, so an iterative process is required[Aungier 2005]. Thus,

$$h_{t,2} = h_{t,1} \rightarrow T_{t,2} = T_{t,1} \tag{3.139}$$

and

$$V_{u,2} = V_{u,2i}\frac{D_{2i}}{D_2} \tag{3.140}$$

Then, guessing an initial meridional velocity ($V_{m,2}$) in volute outlet the volute mass flow is predicted as follows:

$$V_2 = \sqrt{V_{u,2}^2 + V_{m,2}^2} \tag{3.141}$$

$$h_{s,2} = h_{t,2} - \frac{1}{2}V_2^2 \rightarrow T_{s,2} = T(h_{s,2}) \tag{3.142}$$

About the outlet total and static pressures, they are both calculated based on the following equation.

$$p_{t,2} = p_{t,1} - \mathrm{Y}_{vol}\left(p_{t,2} - p_{s,2}\right), p_{s,2} = p_{t,2}e^{\frac{\varphi(T_{s,2}) - \varphi(T_{t,2})}{R_{gas}}} \tag{3.143}$$

where $\mathrm{Y}_{vol}$is the overall volute loss coefficient, presented in section 3.5.3.

Having established all the required static conditions, the outlet density (ρ_2) is predicted, allowing the outlet mass flow calculation,

$$\dot{m} = \rho_2 \mathrm{A}_2 \mathrm{V}_{\mathrm{m},2} \tag{3.144}$$

Given that the outlet mass flow is user-defined, an iterative process is carried out between eq. (3.141) and (3.144), for predicting the outlet meridional velocity until the error between the calculated and the given mass flow reaches a tollerance value.

Considering the initial outlet meridional velocity, it is calculated as:

$$V_{m,2,initial} = \frac{\dot{m}}{\rho_{2i}\mathrm{A}_2} \tag{3.145}$$

Vaned nozzle outlet(3)

Having computed both the total and static conditions in vaned nozzle inlet via volute outlet analysis, both total enthalpy and temperature are defined as:

$$h_{t,3} = h_{t,2} \rightarrow T_{t,3} = T_{t,2} \tag{3.146}$$

Similar to the axial turbine nozzle (stator) blades, the outlet flow angle depends on both blade angle and throat. Wasserbauer and Glassman (1975) proposes that the impeller deviation angle during the un-choked operation is equal to zero, while Aungier (2005) suggests that it depends on the impeller geometrical parameters. Specifically, according to Wasserbauer and Glassman (1975), the outlet flow angle (a_3) is expressed as:

$$a_3 = \beta_{v,3} \tag{3.147}$$

while, according to Aungier (2005) and based on Figure 3-15 as:

$$\tan(\alpha_3) = \frac{r_3}{r_{th}} \tan(\alpha_{os}) \tag{3.148}$$

where,

$$\sin(\alpha_{os}) = \frac{b_{th}\, o}{s_3 b_3} \tag{3.149}$$

$$\left[\frac{dr}{dm}\right]_3 = \frac{m_3\,(r_3 - r_2)}{m_2\,(m_3 - m_2)} - \frac{(m_3 - m_2)\,(r_3 - r_2)}{m_2\, m_3} \tag{3.150}$$

$$\mathrm{o} = \cos(\beta_{b,3}) \left(\frac{\pi\, D_3}{Z_{vanes}} - t_3\, \cos(\beta_{b,3})\right) \tag{3.151}$$

$$r_{th} = r_3 - \left[\frac{dr}{dm}\right]_3 \frac{o^2}{2\, s_3} \tag{3.152}$$

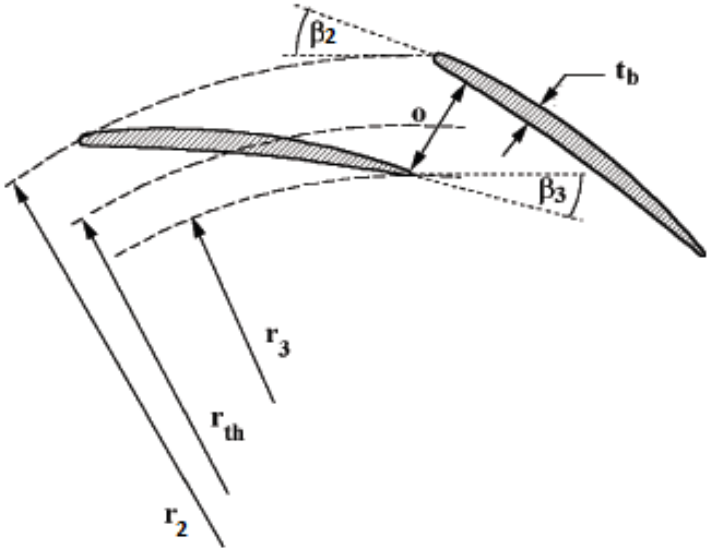

Figure 3-15: Vaned nozzle Row Geometry (Aungier 2005).

Then, guessing an initial outlet meridional velocity ($V_{m,3}$), both the vaned nozzle outlet velocity(V_3) and static enthalpy($h_{s,3}$) are predicted as follows:

$$V_3 = V_{m,3} \cos \alpha_3 \tag{3.153}$$

$$h_{s,3} = h_{t,3} - \frac{1}{2} V_3^2, T_{s,3} = T(h_{s,3}) \tag{3.154}$$

Concerning the outlet total and static pressures, they calculated based on the following equation:

$$p_{t,3} = PR_{vnd}\, p_{t,2}\,, p_{s,3} = p_{t,3} e^{\frac{\varphi(T_{s,3}) - \varphi(T_{t,3})}{R_{gas}}} \tag{3.155}$$

where $PR_{vnd}$is the vaned nozzle pressure ratio, presented in section 3.5.4.

Having established all the required static conditions, the outlet density (ρ_3) is computed, allowing the outlet mass flow calculation to be performed as follows,

$$\dot{m} = \rho_3 A_3 V_{m,3} \tag{3.156}$$

where the outlet area(A_3) is expressed as:

$$A_3 = \pi D_3 b_3 - z_v b_3 t_{b,3} cos(\beta_{v,3}) \tag{3.157}$$

Then, an iterative process is carried out between eq. (3.153) and (3.156), for predicting the outlet meridional velocity until the error between the calculated and the given mass flow reaches a tollerance value.

Considering the initial outlet meridional velocity, it can be defined as:

$$V_{m,3,initial} = \frac{\dot{m}}{\rho_2 \mathrm{A}_3} \tag{3.158}$$

Vaneless nozzle outlet (4)

For calculating the outlet flow conditions, it is assumed that there are no losses in this component(the losses in reality tend to be close to zero [Aungier 2005]). Thus, the outlet flow conditions are calculated using continuity equation as follows:

$$[V_4, V_{m,4}, a_4, T_{s,4}, P_{s,4}] = f[V_{u,4}, A_4, \dot{m}, T_{t,4}, P_{t,4}] \tag{3.159}$$

where vaneless nozzle outlet area(A_4) and the circumferential velocity ($V_{u,4}$) are defined as:

$$A_4 = \pi D_4 b_4 \tag{3.160}$$

$$V_{u,4} = \frac{V_{u,3} D_3}{D_4} \tag{3.161}$$

Impeller inlet(4)

Having computed the impeller inlet static conditions via vaneless nozzle outlet analysis, the relative ones are calculated as,

$$h_{t,4,r} = \mathrm{h}_{\mathrm{s},4} + \frac{1}{2}\mathrm{W}_4^2 \rightarrow \mathrm{T}_{\mathrm{t,4,r}} = T(h_{t,4,r}) \tag{3.162}$$

and

$$p_{t,4,r} = p_{s,4} e^{\frac{\varphi(T_{t,4,r}) - \varphi(T_{s,4})}{R_{gas}}} \tag{3.163}$$

where the relative velocity (W_4) is expressed as:

$$W_4 = \sqrt{V_{m,4}^2 + \left(V_{u,4} - U_4\right)^2} \tag{3.164}$$

Impeller outlet just upstream of blade trailing edge (5)

In impeller outlet station both total relative enthalpy and temperature are expressed as:

$$h_{t,5,r} = h_{t,4,r} + \frac{U_5^2 - U_4^2}{2} \rightarrow T_{t,5,r} = T(h_{t,5,r}) \tag{3.165}$$

Similarly to the vaned nozzle, the outlet relative flow angle depends on both blade angle and throat. Thus, according to Wasserbauer and Glassman (1975), the outlet flow angle (β_5) is expressed as:

$$\beta_5 = \beta_{b,5} \tag{3.166}$$

while, according to Aungier (2005) as:

$$\tan \beta_5 = \frac{R_{tip,5} + R_{hub,5}}{2\, R_{th}} \tan a'_{os} \tag{3.167}$$

Both the discharge flow (a'_{os}) and the throat radius (R_{th}) are expressed as:

$$\sin a'_{os} = \frac{b_{th} o_{imp}}{s_5 (R_{tip,5} - R_{hub,5})} \tag{3.168}$$

$$R_{th} = \frac{R_{tip,5} + R_{hub,5}}{2} - \frac{o_{imp}^2 \sin \overline{\varphi_5}}{2\, s_5} \tag{3.169}$$

where (s_5) and ($\overline{\varphi_5}$) are the pitch angle and the streamline slope in station 5, respectively, while both throat width (o_{imp}) and blade height at throat position(b_{th}) are expressed as:

$$o_{imp} = \left(\pi \frac{D_{ref,5}}{Z_{eff}} - t_5 \cos \beta_{b,5} \right) cos(\beta_{b,5}) \tag{3.170}$$

$$b_{th} = \frac{\left[b_4 - \left(R_{tip,5} + R_{hub,5} \right) \right]}{R_4 - R_{ref,5}} \left(R_{th} - R_{ref,5} \right) + \left(R_{tip,5} + R_{hub,5} \right) \tag{3.171}$$

Guessing then an initial impeller outlet meridional velocity ($V_{m,5}$) and considering that the outlet blade velocity is calculated as:

$$U_5 = \pi \frac{N_{mech}}{60} D_{ref,5} \tag{3.172}$$

both the relative and absolute velocity components are calculated as:

$$W_5 = V_{m,5} \cos \beta_5 \, , W_{u,5} = V_{m,5} \tan \beta_5 \tag{3.173}$$

$$V_5 = \sqrt{V_{m,5}^2 + \left(U_5 + W_{u,5} \right)^2} \tag{3.174}$$

Next, the static enthalpy and temperature are predicted as:

$$h_{s,5} = h_{t,5,r} - \frac{1}{2}\mathrm{W}_5^2 \rightarrow \mathrm{T}_{s,5} = \mathrm{T}(\mathrm{h}_{s,5}) \tag{3.175}$$

$$h_{t,5} = h_{s,5} - \frac{1}{2}\mathrm{V}_5^2 \rightarrow \mathrm{T}_{t,5} = \mathrm{T}(\mathrm{h}_{t,5}) \tag{3.176}$$

Then, the relative total pressure can be computed as follows:

$$p_{t,r,5} = p_{\mathrm{t,5,r,is}} \left(1 - \frac{\gamma - 1}{\gamma + 1} \frac{\frac{2\, L_{imp}}{W_{cr,4}^2}}{1 - \frac{\gamma - 1}{\gamma + 1}\frac{W_4^2}{W_{cr,4}^2}} \right)^{\frac{\gamma}{\gamma - 1}} \tag{3.177}$$

where L_{imp} is the overall kinetic energy loss coefficient. All the kinetic energy loss coefficients are presented in the section 3.5.5, while the ideal relative total pressure($p_{\mathrm{t,5,r,is}}$) is based on isentropic expansion:

$$p_{\mathrm{t,5,r,is}} = p_{t,4,r} e^{\frac{\varphi(T_{t,5,r}) - \varphi(T_{t,4,r})}{R_{gas}}} \tag{3.178}$$

Having calculated the relative total pressure, then both the static and total pressure at station 5 are also predicted as,

$$p_{t,5} = p_{t,5,r} e^{\frac{\varphi(T_{t,5}) - \varphi(T_{t,5,r})}{R_{gas}}}, p_{s,5} = p_{t,5,r} e^{\frac{\varphi(T_{s,5}) - \varphi(T_{t,5,r})}{R_{gas}}} \tag{3.179}$$

allowing the calculation of the mass flow.

Then, an iterative process is carried out between eq. (3.172) and (3.179), for predicting the outlet meridional velocity until the error between the calculated and the given mass flow reaches a tollerance value.

Regarding the initial impeller outlet meridional velocity, it is set as:

$$V_{m,5,initial} = \frac{\dot{m}}{\rho_{t,5}\mathrm{A}_5}, \rho_{t,5} = \frac{P_{t,5}}{R_{gas} T_{t,5}} \tag{3.180}$$

where the total enthalpy, temperature and pressure are approximated with the following equation:

$$\mathrm{h}_{\mathrm{t,5}} = h_{t,4} - U_4^2 + \frac{U_5^2}{2}, \mathrm{T}_{\mathrm{t,5}} = \mathrm{T}(\mathrm{h}_{\mathrm{t,5}}), \qquad \mathrm{P}_{\mathrm{t,5}} = \mathrm{P}_{\mathrm{t,4}} \left(\frac{(1 - 0.9)\,\mathrm{T}_{\mathrm{t,4}} - \mathrm{T}_{\mathrm{t,5}}}{0.9\,\mathrm{T}_{\mathrm{t,4}}} + 1 \right)^{\frac{1.36}{0.36}} \tag{3.181}$$

and the outlet area is expressed as:

$$A_5 = A_6 - t_{b,5}Cos(\beta_{b,5})\left(\frac{D_{\text{tip},5}}{2} - \frac{D_{\text{hub},5}}{2}\right)Z_{MB}, A_6 = \pi\frac{D_{\text{tip},5}^2 - D_{\text{hub},5}^2}{4} \quad (3.182)$$

Impeller outlet (6)

Station 6 compared to 5, has the same total pressure and temperature contrary to the static conditions. Thus, the outlet flow angle, the outlet velocity and the static conditions using the continuity equation are calculated as:

$$[V_6, P_{s,6}, T_{t,6}] = f[a_6, A_6, \dot{m}, T_{t,5}, P_{t,5}] \quad (3.183)$$

3.5.3 Volute loss coefficients

The volute total loss is calculated based on both the circumferential distortion($Y_{\theta,vol}$) and the skin friction($Y_{p,vol}$) loss coefficients. Thus, the volute total pressure loss coefficient is expressed as:

$$Y_{vol} = Y_{p,vol} + Y_{\theta,vol} \quad (3.184)$$

For the circumferential distortion loss coefficient calculation in volute component, Aungier (2005) proposes the following equation,

$$Y_{\theta,vol} = \left(\frac{\left(\frac{R_1}{R_2}V_1 - V_{u2}\right)}{V_2}\right)^2 \quad (3.185)$$

For the skin friction losses calculation inside volute, the following equation, described by Aungier (2000)

$$Y_{p,vol} = \frac{2\Theta + \Delta^2}{(1-\Delta)^2} \quad (3.186)$$

is used, where volute normalized momentum defect thickness(Θ) and the normalized mass defect thickness(Δ) are defined as follows,

$$\Theta = 1 - \left[1 - \sum\frac{\theta_W}{b_w}\right] \quad (3.187)$$

$$\Delta = 1 - \left[1 - \sum\frac{\delta_W^*}{b_w}\right] \quad (3.188)$$

where θ_W is the volute end wall boundary layer momentum thickness, δ_W^* is the end wall boundary layer displacement thickness and b_w the volute passage width,

$$\theta_w = c_{f,vol}\,\bar{\rho}\left[\left(\frac{V_1}{V_2}\right)^5 + 2\left(\frac{V_1}{V_2}\right)^5 + 1\right]\frac{L_{vol}}{8\,\rho_2} \tag{3.189}$$

$$\delta_W^* = 1.2857\,\theta_w \tag{3.190}$$

The volute friction coefficient is calculated according to eq. (3.92)-(3.99).

3.5.4 Vaned nozzle pressure loss

For the vaned nozzle total losses calculation, Meitner and Glassman (1980) correlations are used,

$$\mathrm{PR_{vnd}} = \left(\frac{1 - \bar{e}_{3D} - Q_3}{(1 - \bar{e}_{3D})(1 - Q_3)}\right)^{\frac{\gamma}{\gamma-1}} \tag{3.191}$$

where, vaned nozzle kinetic energy loss coefficient $\bar{e}_{3D}$ and its parameters E, H, Q are defined as follows:

$$\bar{e}_{3D} = \frac{E\left(\frac{\theta_t}{l}\right)_{ref}\left(\frac{Re}{Re_{ref}}\right)^{-0.2}\left(\frac{l}{s}\right)\left(\frac{A_{3D}}{A_{2D}}\right)}{\cos(\alpha_3) - \frac{t_{te}}{s} - H\left(\frac{\theta_t}{l}\right)_{ref}\left(\frac{Re}{Re_{ref}}\right)^{-0.2}\left(\frac{l}{s}\right)} \tag{3.192}$$

$$\mathrm{E} = \frac{2\left[\frac{1}{1.92} + \frac{Q_3}{3.2} + \frac{Q_3^2}{4.8} + \frac{Q_3^3}{6.72}\right]}{\frac{1}{1.68} + \frac{Q_3}{2.88} + \frac{Q_3^2}{4.4} + \frac{Q_3^3}{6.24}} \tag{3.193}$$

$$\mathrm{H} = \frac{\frac{1}{1.12} + \frac{3\,Q_3}{1.6} + \frac{5\,Q_3^2}{2.0} + \frac{9\,Q_3^3}{2.8}}{\frac{1}{1.68} + \frac{Q_3}{2.88} + \frac{Q_3^2}{4.4} + \frac{Q_3^3}{6.24}} \tag{3.194}$$

$$\mathrm{Q} = \frac{\gamma - 1}{\gamma + 1}\left(\frac{V}{V_{cr}}\right)^2 \tag{3.195}$$

$$\left(\frac{\theta_t}{l\,Re^{-0.2}}\right)_{ref} = 0.03734 \tag{3.196}$$

Concerning, isentropic coefficient(γ) is calculated as a function of vaned nozzle outlet static temperature.

3.5.5 Impeller kinetic energy total loss

The kinetic energy total loss L_{imp} consists of the impeller incidence(L_{inc}), the impeller rotor losses(L_R), the clearance losses(L_{cl}) and the impeller

trailing(L_{te}) losses [Wasserbauer and Glassman 1975]. Thus, the total pressure loss in the impeller rotating frame is expressed as:

$$L_{imp} = \mathrm{L}_{inc} + L_R + L_{cl} + L_{te} \tag{3.197}$$

Concerning the impeller blade incidence kinetic energy losses prediction, Wasserbauer and Glassman (1975) proposes the following correlation:

$$\mathrm{L}_{inc} = \frac{1}{2}\ \mathrm{W}_4^2\ \left(1 - \cos\left(\beta_{b,4} - \ \beta_{b,4,opt}\right)\right)^{\mathrm{n}} \tag{3.198}$$

The exponential parameter n is equal to:

$$n = \begin{cases} 2 \quad , & \beta_{b,4} - \beta_{b,4,opt} \geq 0 \\ 3 \quad , & \beta_{b,4} - \ \beta_{b,4,opt} < 0 \end{cases} \tag{3.199}$$

where optimum blade angle($\beta_{b,4,opt}$) is expressed as:

$$\beta_{b,4,opt} = \tan^{-1}\frac{W_{u,4,id}}{V_{m,4}} \tag{3.200}$$

Concerning the relative ideal circumferential velocity($W_{u,4,id}$) calculation, first the computation of the impeller slip factor has to be carried out.

The impeller slip factor prediction is based on eq. (3.45)-(3.48).

Then, the relative ideal circumferential velocity is defined as:

$$W_{u,4,id} = \mathrm{V}_{\mathrm{u,4,id}} - \mathrm{U}_4 \tag{3.201}$$

where the absolute ideal circumferential velocity is calculated as:

$$\mathrm{V}_{\mathrm{u,4,id}} = \ \mathrm{U}_4\ \sigma \tag{3.202}$$

For impeller rotor kinetic energy losses calculation, the following correlation is used based on Moustapha et al. (2003) loss model,

$$L_R = L_p + L_f \tag{3.203}$$

where rotor kinetic losses consist of profile(L_p) and friction kinetic losses(L_f),

$$L_p = \ \frac{1}{2}\ \mathrm{K}\ (\mathrm{W}_4^2 - \mathrm{W}_5^2) \tag{3.204}$$

$$L_f = \frac{\mathrm{C_f}}{2}\ \frac{\mathrm{L_{hyd}}}{D_{hyd}}\ \left(\frac{\mathrm{W}_4 + W_5}{2}\right)^2 \tag{3.205}$$

where parameter K is equal to 0.24 according to Moustapha et al. (2003), friction coefficient is calculated based on eq. (3.92)-(3.99) and hydraulic diameter is expressed as:

$$D_{hyd,imp} = \frac{\frac{\pi}{2}\, Cos(\beta_{b,5})\, (\, D_{tip,5}^2 - D_{hub,5}^2\,)}{\pi\, Cos(\,\beta_{b,5}\,)\,(D_{tip,5} + D_{hub,5}) + 2\, z_{eff}\,(D_{tip,5} - D_{hub,5})} + \frac{\pi\, D_4\, b_4\, Cos(\beta_{b,4})}{\pi\, D_4\, Cos(\beta_{b,4}) + Z\, b_4} \quad (3.206)$$

The impeller tip clearance kinetic energy losses are calculated by the following correlations, described by Dambach et al. (1998) and Moustapha et al. (2003),

$$C_a = \frac{1 - \frac{R_{tip,5}}{R_4}}{V_{m,4}\, b_4} \quad (3.207)$$

$$\mathrm{C_r} = \frac{R_{tip,5}}{R_4} \frac{L_{axial} - b_4}{V_{m5}\, R_4\, (R_{tip,5} - R_{hub,5})} \quad (3.208)$$

$$L_{cl} = \frac{Z_{eff}\, U_4^3}{8\,\pi}\, \left(\mathrm{K}_a\, cl_x\, C_a + K_r\, cl_r\, C_r + K_{ar} \sqrt{cl_r\, cl_a\, C_a\, C_r}\right) \quad (3.209)$$

According to Moustapha et al. (2003), K_a is equal to 0.4, K_r is equal to 0.75 and K_{ar} is equal to -0.3. For the Impeller blade trailing edge Kinetic energy losses calculation in impeller component, the next correlation, presented by Ghosh et al. (2011)

$$L_{te} = \frac{2}{\gamma\, M_{r,4}^2} \frac{dP_{0r}}{P_5 \left(1 + \frac{W_5^2}{2\, h_{s,5}}\right)^{\frac{\gamma}{\gamma-1}}} \quad (3.210)$$

is followed, where the parameter dP_{0r} is defined as follows:

$$dP_{0r} = \rho_5 \frac{W_5^2}{13.34} \left(\frac{Z_{MB}\, t_5 \cos\, \beta_{b,5}}{\pi\, (R_{tip,5} + R_{hub,5})}\right)^2 \quad (3.211)$$

3.5.6 Choke Indices calculation

The choke indices, described in this section, are expressions for calculating how far away operating point is from choke point. When one choke index takes values positive, then the turbine operates unchoked. The choke indices are calculated in five stations along turbine, namely impeller inlet, impeller outlet, vaned nozzle inlet, outlet and volute inlet. All choke indices are integrated as correlations in impeller and vaned nozzle sub-models.

$$index_{ch,i} = \frac{\dot{m}_{ch,i} - \dot{m}}{\dot{m}_{ch,i}} \quad (3.212)$$

3.5.7 Radial turbine performance map generation

For generating the performance map of an RT component, the process followed is similar to the one followed for CC components. Regarding the minimum mass flow point, where either the RT efficiency or the pressure ratio tend to zero or unity, respectively, the secant method establishes it numerically.

For calculating the turbine choked operation, the procedure based on Wasserbauer and Glassman (1975) work is followed. Specifically, after calculating the first sub-component(impeller, nozzle, etc.) where the flow is choked, a new sub-component exit-flow angle is computed from the area required to pass the choking mass flow rate for higher axial Mach-number values until the axial Mach-number reaches a unity value or the next to it sub-component be choked. In case the next to it sub-component is choked this procedure is repeated.

3.5.8 Radial turbine meanline analysis verification

The comparison between the predictions of the radial TML and the corresponding measured data is depicted in Figure 3-16. The selected Turbine geometry and its measured data are provided by Wasserbauer et al. (1966). The results show that the predicted performance data are in good agreement with the measured data. The 1D radial turbine geometry is given in Table 3-5. The results indicate that the chocking line is predicted with good accuracy. Note that in the validation test case, radial turbine does not include a volute.

Table 3-5: Radial turbine geometry.

Radial turbine Geometry			
Parameter	Value	Parameter	Value
$D_{6,hub}$	0.029 [m]	t_3	0.0006 [m]
$D_{6,tip}$	0.084[m]	t_2	0.0006 [m]
D_4	0.126 [m]	b_4	0.0146 [m]
D_3	0.130 [m]	b_3	0.0146 [m]
D_2	0.545 [m]	b_2	0.0146 [m]
$\beta_{b,5}$	46.8^o	Z_{MB}	6 [-]
$\beta_{b,4}$	0^o	Z_{FB}	12 [-]
$\beta_{v,3}$	72^o	L_A	0.046 [m]
$\beta_{v,2}$	55^o	Z_V	14 [-]
t_5	0.00145 [m]	AR_{vol}	-
t_4	0.00146[m]	N_{des}	29550 [Rpm]
le_{spl}	0.6 [-]		

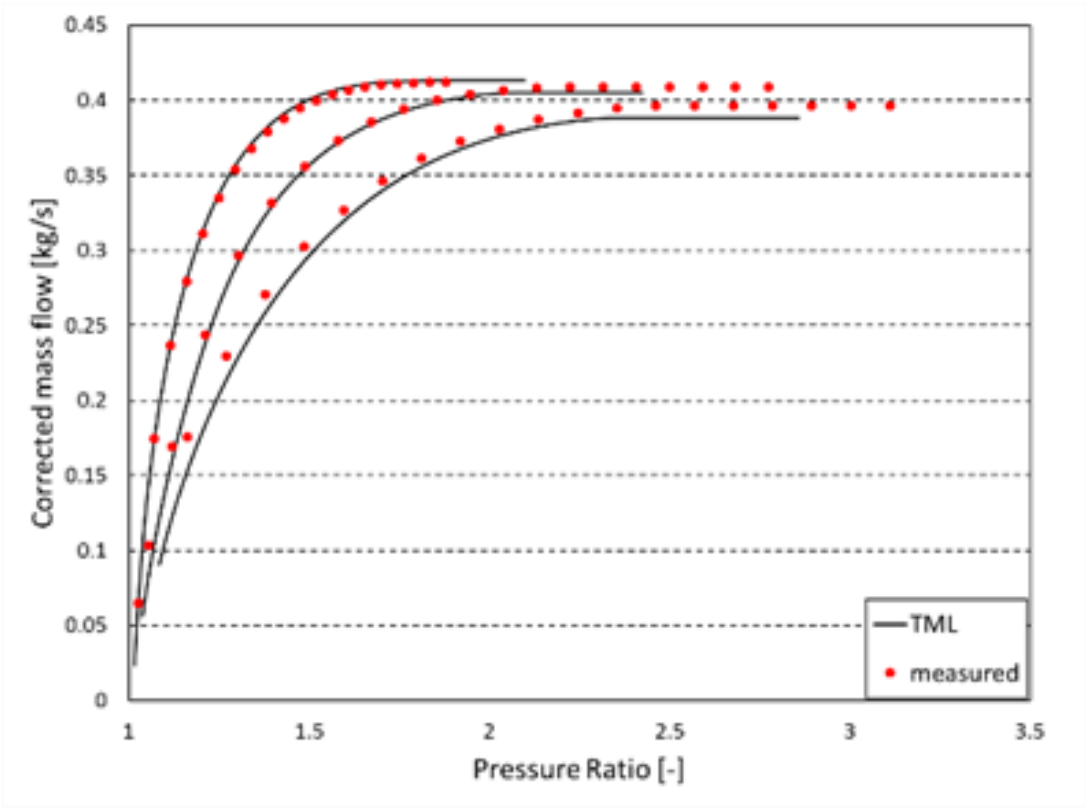

(a)

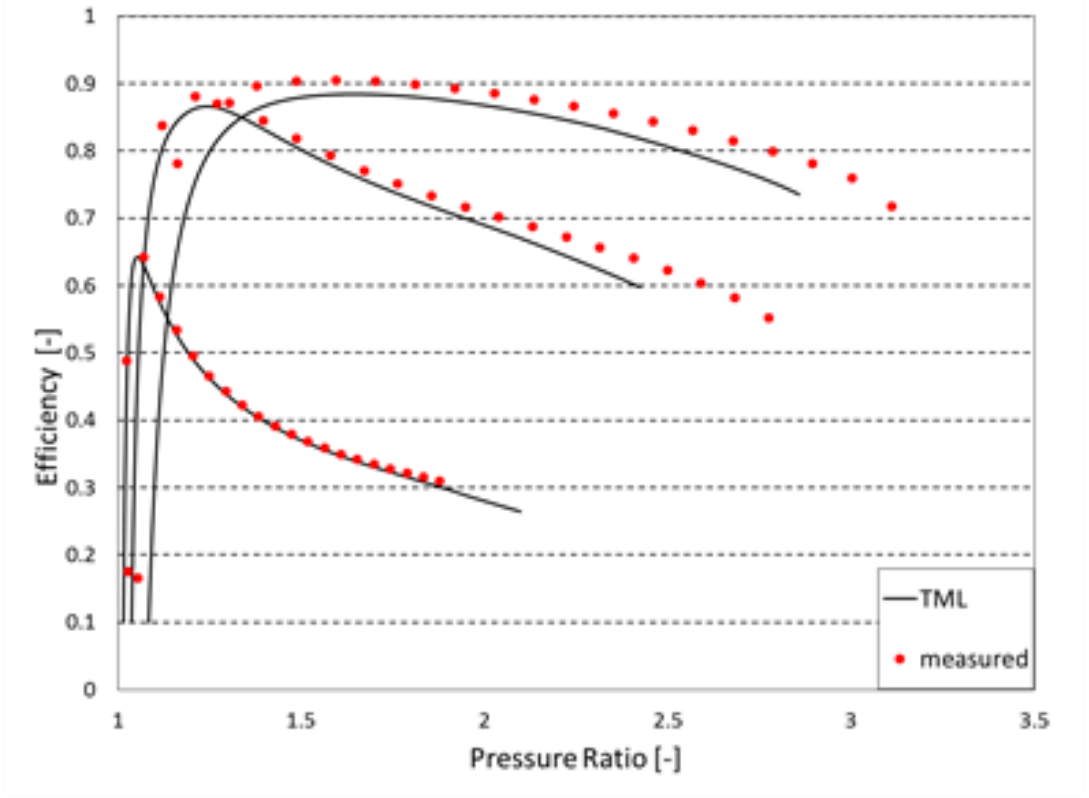

(b)

Figure 3-16: Radial TML validation against measured data: **(a):** Pressure ratio **(b)** Efficiency

3.6 Axial Turbine Meanline model

As part of the present work, a mean line model for Axial-Flow turbines has also been developed, aiming to establish the off-design performance of an N-stage axial turbine of known geometry. The AT mean-line model comprises sub-models for estimating the performance of both stationary and rotating frame components, that is, stators (S) and rotors (R).

Exit flow and performance conditions in each individual sub-component model, shown in Figure 3-17, are predicted considering the corresponding loss models and then are used as inputs in the next downstream component. At the end of the AT mean-line calculation, overall performance of the axial turbine is established and expressed in the form of isentropic and polytropic efficiencies, flow and work coefficients, etc.

The AT model, comprising stator and rotor performance sub-models, calculates the outlet flow and performance conditions for a turbine of any number of use-defined stages. A typical layout of the AT mean-line model is depicted in Figure 3-17. Regarding the mean-line stations for calculating the performance of the Nth-stage stator and rotor, station 1S represents the stator inlet, station 2S the stator outlet, station 1R the rotor inlet, and 2R the rotor outlet.

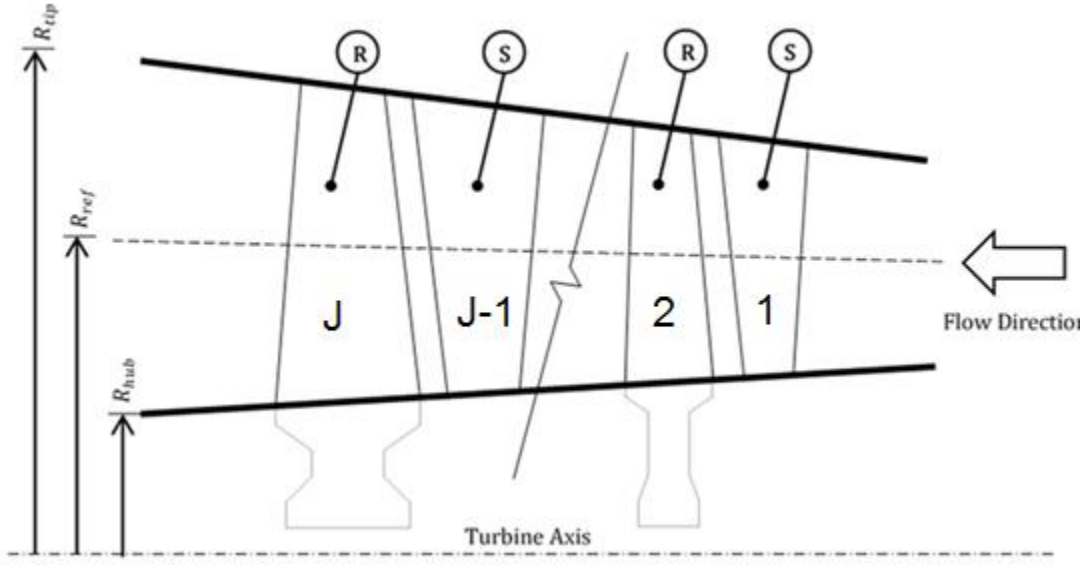

Figure 3-17: Axial Turbine sub-components.

3.6.1 Meanline analysis input data

The AT meanline analysis is conducted within the PROOSIS environment, depicted in Figure 3-18 and Table 3-6. Concerning the geometrical parameters that are included in input data, their graphic representation is shown in both Figure 3-17 and Figure 3-19.

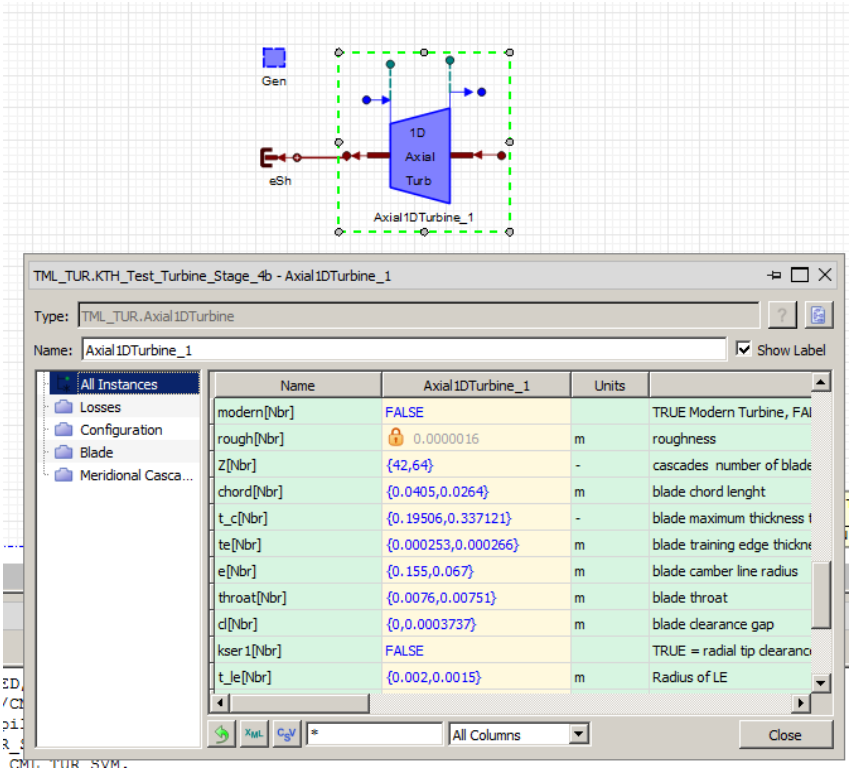

Figure 3-18: AT meanline analysis schematic and input data in PROOSIS environment.

Table 3-6: AT meanline analysis input data.

Axial Turbine			
Parameter		Parameter	
$R_{1,hub}$[J]	Inlet hub radius	$R_{2,hub}$[J]	Outlet hub radius
$R_{1,tip}$[J]	Inlet tip radius	$R_{2,tip}$[J]	Outlet tip radius
$\beta_{b,1}$[J]	Inlet blade angle	$\beta_{b,2}$[J]	Outlet blade angle
t_{le}[J]	Leading edge thickness	t_e[J]	Trailing edge thickness
cl[J]	Clearance	Z[J]	Number of blades
o[J]	Throat width	t_{max}/c[J]	Maximum thickness to chord length
c[J]	Chord lenght	e[J]	Blade camber line radius
Type[J]	Rotating or stationary	N_{mech}	AT speed
Fluid	Working fluid (Air)	$P_{t,in}$	Inlet total pressure
$\dot{m}$	CC mass flow	$T_{t,in}$	Inlet total temperature
cl	Impeller clearance	e	Wall roughness
kser	Radial tip clearance or shroud seal	J	Cascade number

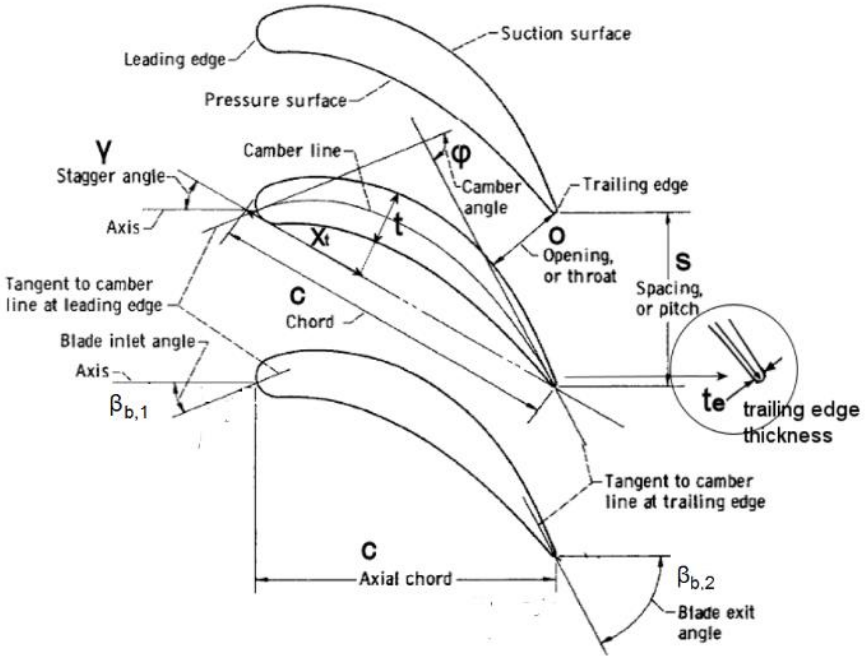

Figure 3-19: AT blade parameters.

Typical T/C radial turbine impeller, vaned nozzle and volute are illustrated in Figure 3-20.

(a)

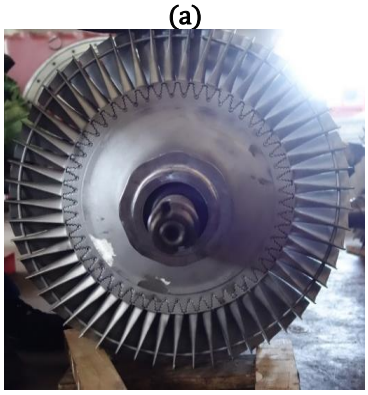

(b)

Figure 3-20: T/C axial turbine[1]: **(a)** Stator **(b)** Rotor

[1] www.turbomed.gr

3.6.2 Meanline analysis

Regarding the meanline analysis, the reference radius is placed at mid position, as depicted in Figure 3-17.

Stator Inlet(1S)

First the inlet stator area is calculated as:

$$A_1 = \pi \left(R_{tip,1}^2 - R_{hub,1}^2\right) \tag{3.213}$$

Then, the meridional velocity and the static conditions using continuity equation are computed:

$$\left[V_1, V_{m,1}, P_{s,1}, T_{t,1}\right] = f[a_1, A_1, \dot{m}, T_{t,1}, P_{t,1}] \tag{3.214}$$

Stator Outlet(2S)

In the outlet station, both the total enthalpy and temperature are expressed as:

$$h_{t,2} = h_{t,1} \rightarrow T_{t,2} = T(h_{t,2}) \tag{3.215}$$

Guessing then, an initial impeller outlet meridional velocity ($V_{m,2}$), first the absolute velocity in stator outlet is calculated as:

$$V_2 = V_{m,2} \cos a_2 \tag{3.216}$$

where the outlet flow angle calculation(a_2) is described in section 3.6.3. As it depends on both the blade geometry and the absolute velocity, an internal iterative process is performed between eq. (3.216) and the ones presented in section 3.6.3 until the calculated outlet flow reach the one given in eq. (3.216) with certain tolerance. Regarding the initial outlet flow angle, it is set equal to outlet blade angle.

Having established the outlet flow angle, the static temperature is calculated as:

$$h_{s,2} = h_{t,2} - \frac{1}{2}V_2^2, T_{s,2} = T(h_{s,2}) \tag{3.217}$$

while both the total and the static pressure are expressed as:

$$p_{t,2} = p_{t,1} - \left(p_{t,2} - p_{s,2}\right) Y_{csd}\ , p_{s,2} = p_{t,2} e^{\frac{\varphi(T_{s,2}) - \varphi(T_{t,2,r})}{R_{gas}}} \tag{3.218}$$

where Y_{csd} is the overall cascade loss coefficient, presented in section 3.6.4. As the cascade loss coefficient depends on both total and static pressure, an internal iterative process is carried out between eq. (3.218) and the ones presented in section 3.6.4. until the calculated outlet total pressure reaches the one given in

eq. (3.218) with certain tolerance. Regarding the initial total pressure, it is defined as,

$$P_{t,2,init} = P_{t,1} \tag{3.219}$$

Calculating then the density in outlet position, the mass flow is defined as:

$$\dot{m} = \rho_2 \mathrm{A}_2 \mathrm{V}_{\mathrm{m},2} \tag{3.220}$$

where outlet area (A_2) is expressed as:

$$A_2 = \pi \left(R_{tip,2}^2 - R_{hub,2}^2\right) - t_e Cos\left(\beta_{b,2}\right)\left(R_{tip,2}^2 - R_{hub,2}^2\right)Z \tag{3.221}$$

Given that, the outlet mass flow is user-defined, an iterative process is carried out between eq. (3.216) and (3.220), for predicting the outlet meridional velocity until the error between the calculated and the given mass flow reaches a tollerance value.

Considering the outlet meridional velocity, it can be defined as:

$$V_{m,2,initial} = V_{m,1} \tag{3.222}$$

Rotor Inlet(1R)

For calculating both the meridional velocity and the static conditions in rotor inlet, the procedure, presented in stator inlet, is followed. Then, by calculating the blade speed,

$$U_1 = \frac{2\pi N_{mech}}{60} R_{ref,1} \tag{3.223}$$

the relative total conditions are defined as:

$$h_{t,1,r} = h_{s,1} + \frac{1}{2}W_1^2, T_{t,1,r} = T\left(h_{t,1,r}\right), p_{t,1,r} = p_{s,1} e^{\frac{\varphi(T_{t,1,r}) - \varphi(T_{s,1})}{R_{gas}}} \tag{3.224}$$

Where the relative velocity is calculated as follows:

$$V_{u,1} = V_1 \, sin(a_1), W_{u,1} = V_{u,1} - U_1, W_1 = \sqrt{W_{u,1}^2 + V_{m,1}^2} \tag{3.225}$$

Rotor Outlet(2R)

In the outlet station, both the relative total enthalpy and temperature are expressed as:

$$h_{t,2,r} = h_{t,1,r} + \frac{1}{2}(\mathrm{U}_2^2 - \mathrm{U}_1^2), \mathrm{T}_{\mathrm{t,2,r}} = \mathrm{T}(\mathrm{h}_{\mathrm{t,2,r}}) \quad (3.226)$$

where,

$$U_2 = \frac{2\pi N_{mech}}{60} R_{ref,2} \quad (3.227)$$

Guessing then an initial impeller outlet meridional velocity ($V_{m,2}$), first the relative velocity in rotor outlet is calculated as:

$$W_2 = V_{m,2} \cos\beta_2 \quad (3.228)$$

where the outlet flow angle calculation process is the same with the one presented in stator outlet. Regarding the initial outlet flow angle, it is set equal to outlet blade angle.

Having established the outlet flow angle, the static temperature is calculated as:

$$h_{s,2} = h_{t,2,r} - \frac{1}{2}W_2^2 \rightarrow T_{s,2} = T(h_{s,2}) \quad (3.229)$$

while both the total and static pressure are expressed as:

$$p_{t,2,\mathrm{r}} = p_{t,1,\mathrm{r}} - (p_{t,2,\mathrm{r}} - p_{s,2})Y_{csd}\ , p_{s,2} = p_{t,2,r}e^{\frac{\varphi(T_{s,2}) - \varphi(T_{t,2,r})}{R_{gas}}} \quad (3.230)$$

Where the overall cascade loss coefficient calculation process is the same with the one presented in stator outlet. Regarding the initial relative total pressure, it is defined assuming a cascade loss coefficient of about 7%.

Having established both the outlet static and total relative pressure, then, the total conditions are also computed,

$$h_{t,2} = h_{s,2} + \frac{1}{2}V_2^2, T_{t,2} = T(h_{t,2}), p_{t,2} = p_{t,2,r}e^{\frac{\varphi(T_{t,2}) - \varphi(T_{t,2,r})}{R_{gas}}} \quad (3.231)$$

where absolute velocity (V_2) is defined as:

$$V_2 = \sqrt{V_{m,2}^2 + (W_{u,2} + U_2)^2} \quad (3.232)$$

Utilizing both the static temperature and pressure, the outlet density(ρ_2) is also computed, allowing the mass flow calculation:

$$\dot{m} = \rho_2 A_2 V_{m,2} \tag{3.233}$$

Then, an iterative process is carried out between eq. (3.228)and (3.234), for predicting the outlet meridional velocity until the error between the calculated and the given mass flow reaches a tolerance value.

Considering the initial outlet meridional velocity, it can be defined as:

$$V_{m,2,initial} = V_{m,1} \tag{3.234}$$

3.6.3 Cascade outlet flow angle

For calculating the outlet flow angle, Ainley and Mathieson (1951) propose a method which differs for zero and non-zero blade clearance. Regarding the relative frame parameters such as relative Mach number($M_{r,2}$) and outlet flow angle(β_2), in case of analyzing a stationary component(Stator), they corresponds to the absolute ones. For the case of blades with zero tip clearance, the deviation angle is expressed as follows:

$$\beta_2 = \begin{cases} (\beta_2)_{0.5} = \beta_2^* - 4\dfrac{s}{e} & , \quad M_{r,2} \leq 0.5 \\ 2[(\beta_2)_1 - (\beta_2)_{0.5}]M_{r,2} + 2(\beta_2)_{0.5} - (\beta_2)_1 & , \quad 0.5 > M_{r,2} < 1 \\ (\beta_2)_1 = -\cos^{-1}\dfrac{A_{th}}{A_{out}} & , \quad M_{r,2} = 1 \end{cases} \tag{3.235}$$

where $(\beta_2)_{0.5}$ and $(\beta_2)_1$ are outlet flow for Mach number under 0.5 and equal to one, respectively.

The outlet flow angle for relative Mach numbers between 0.5 and 1 can be computed by assuming linear behavior in terms of Mach number, between the outlet flow angles corresponding to 0.5 and 1 Mach number, respectively. Parameter β_2^* is calculated using Figure 3-21 and the parameters A_{th} and A_{out} are defined as follows:

$$A_{th} = \frac{o}{s}\left(\frac{5\,A_{out} + A_{in}}{6}\right) \tag{3.236}$$

$$A_{in} = A_1 \cos\beta_1 \tag{3.237}$$

$$A_{out} = A_2 \cos\beta_2 \tag{3.238}$$

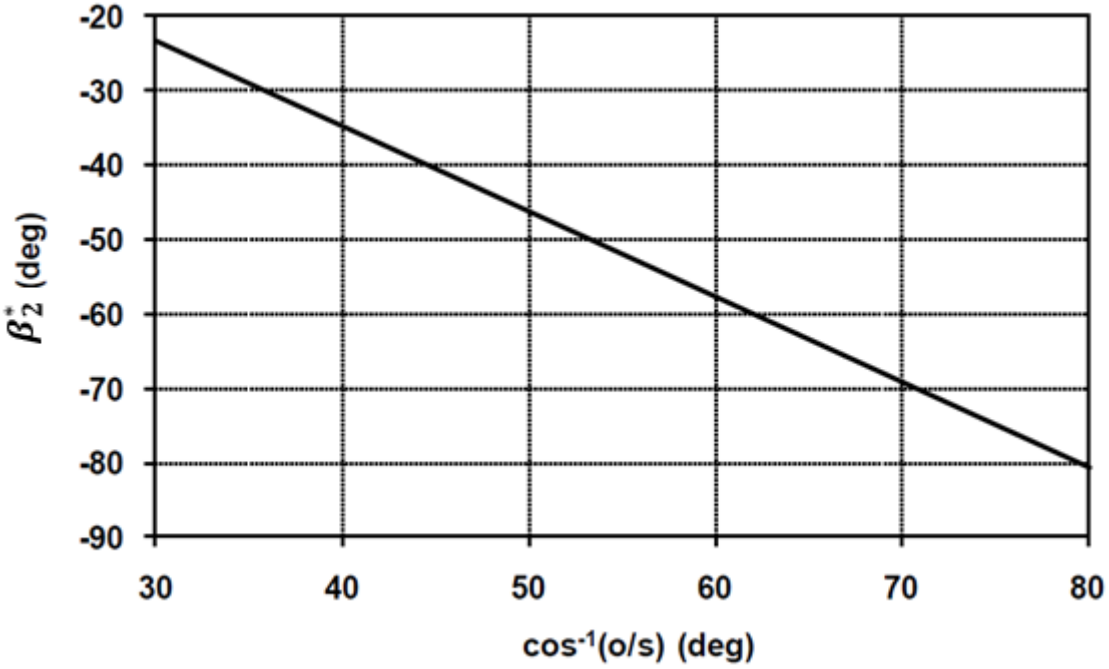

Figure 3-21: $\boldsymbol{\beta_2^*}$ parameter [Ainley and Mathieson 1951].

For blades with non-zero tip clearance:

$$\beta_2 = \begin{cases} \tan^{-1}\left[\tan\beta_{2(cl=0)} + X\frac{cl}{h}\frac{\cos\beta_{b,1}}{\cos(\beta_{2(cl=0)})}\left(\tan\beta_{b,1} - \tan\beta_{2(cl=0)}\right)\right] & , \quad M_{r,2} \le 0.5 \\ -\cos^{-1}\frac{A_{th}}{A_{out}} & , \quad M_{r,2} = 1 \end{cases} \tag{3.239}$$

where $\beta_{2(\mathrm{cl=0})}$ refers to the outlet flow angle with zero blade clearance. Similar to the zero clearance calculations, the outlet flow angle for relative Mach numbers between 0.5 and 1 can be computed by assuming linear behavior in terms of Mach number, between the outlet flow angles corresponding to 0.5 and 1 Mach number, respectively. Parameter X is 1.35 for radial tip clearance and 0.7 for shroud band clearance. The parameters h and A_{th} are calculated as follows:

$$h = \bar{R}_{tip} - \bar{R}_{hub} \tag{3.240}$$

$$A_{th} = \begin{cases} A_{th,(cl=0)}\left(1 - \frac{\mathrm{cl}}{\mathrm{h}}\right) + 2\pi\, cl\, \bar{R}_{tip} & , \quad Radial\ tip \\ A_{th,(cl=0)} + 2\pi\, cl\, \bar{R}_{tip} & , \quad Shroud\ band \end{cases} \tag{3.241}$$

Zhu and Sjolander (2005) propose an alternative outlet flow angle calculation model, independent of the blade clearance which is defined as:

$$\beta_2 = \beta_{b,2} + \frac{17.3\left(\frac{\beta_{stag}}{c}\right)^{0.05}\left(\frac{\beta_1}{\beta_{b,2}}\right)^{0.63}\cos^2(\beta_{stag})\left(\frac{t_{max}}{c}\right)^{0.29}}{\left(30 + 0.01\,\beta_{b,1}^{2.07}\right)\tanh^{0.2}\left(\frac{Re_r}{2\cdot 10^5}\right)} \tag{3.242}$$

while Aungier (2005) proposes the following outlet flow angle correlation:

$$\beta_2 = 90 - \delta - \sin^{-1}\left(\frac{o}{s}\right) \tag{3.243}$$

$$\delta = \begin{cases} \dfrac{o}{s}\left(1 + \left(1 - \dfrac{o}{s}\right)\left(\dfrac{\beta_g}{90}\right)^2\right) & , \quad M_{r,2} \leq 0.5 \\ \delta_{(M_{r,2}=0.5)}\,(1 - 10x^3 + 15x^4 - 6x^5) & , \quad 0.5 < M_{r,2} > 1 \\ 1 & , \quad M_{r,2} \geq 1 \end{cases} \tag{3.244}$$

where,

$$x = 2\,M_{r,2} - 1 \tag{3.245}$$

$$\beta_g = \sin^{-1}\left(\frac{o}{s}\right) \tag{3.246}$$

3.6.4 Cascade loss coefficient

The overall cascade loss coefficient consists of the profile losses(Y_p), the secondary losses(Y_s), the trailing edge(Y_{te}), and the clearance (Y_{cl}).

Concerning the profile losses calculation, first the design profile losses are calculated. These losses correspond to zero incidence angle. Then, the off-design profile losses are computed in terms of the incidence angle. In contrast to this procedure, Aungier (2005) proposes a direct profile loss correlation, hence skipping the design profile loss part. According to Ainley and Mathieson (1951), the design profile losses are defined:

$$Y_{p,\mathrm{d},AM} = Y_1\,Y_2 \tag{3.247}$$

where the loss parameters Y_1 and Y_2 are defined as follows:

$$Y_1 = \mathrm{Y}_{\mathrm{p,d,AM}\,(\beta_{b,1}=0)} + \left(\frac{\beta_{b,1}}{\alpha_2}\right)^2 \left(Y_{p,AM\,(\beta_{b,1}=\alpha_{b,1})} - Y_{p,AM\,(\beta_{b,1}=0)}\right) \tag{3.248}$$

$$Y_2 = \left(\frac{t_{max}}{0.2\,c}\right)^{-\left(\frac{\beta_{b,1}}{\alpha_2}\right)} \tag{3.249}$$

where both design profile loss parameters $Y_{p,\mathrm{d},AM\,(\beta_{b,1}=\beta_{b,1})}$ and $Y_{p,\mathrm{d},AM\,(\beta_{b,1}=0)}$ can be computed from Figure 3-22.

Additionally, Dunham and Came (1970) adds two extra profile loss parameters, the supersonic Mach number correction C_{fm} and the trailing edge loss coefficient k_m. Thus, the Dunham and Came (1970) design profile losses can be expressed as follows:

$$Y_{p,\mathrm{d},DC} = C_{fm}\,\mathrm{Y}_1\,\mathrm{Y}_3 \tag{3.250}$$

where Y_3 is defined as:

$$Y_3 = \left(\frac{t_{max}}{0.2\ c}\right)^{-\left(\frac{\beta_{b,1}}{\beta_2}\right) k_m} \tag{3.251}$$

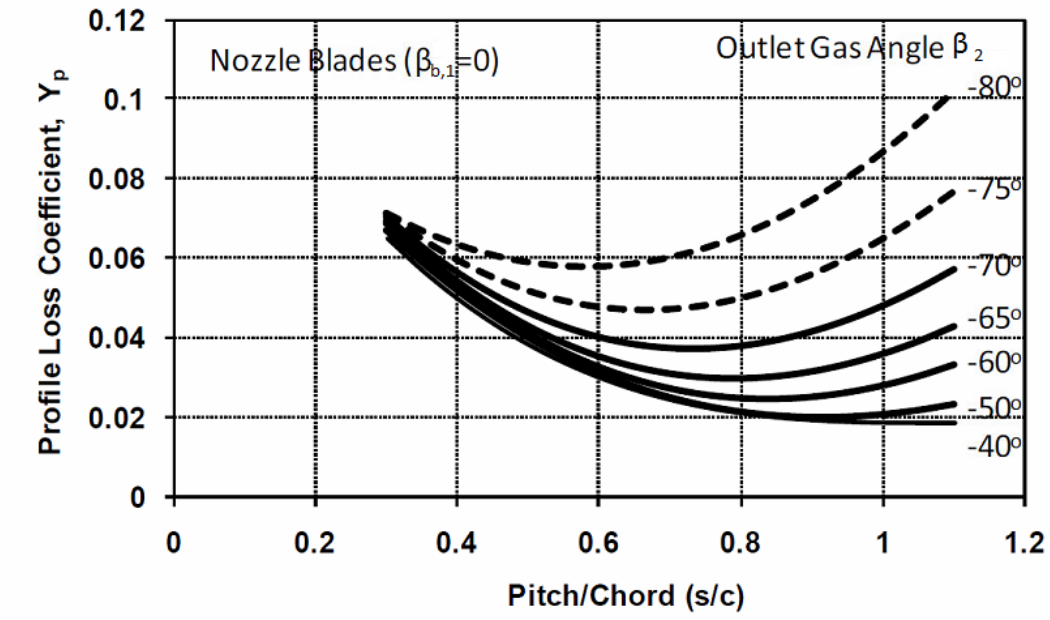

(a)

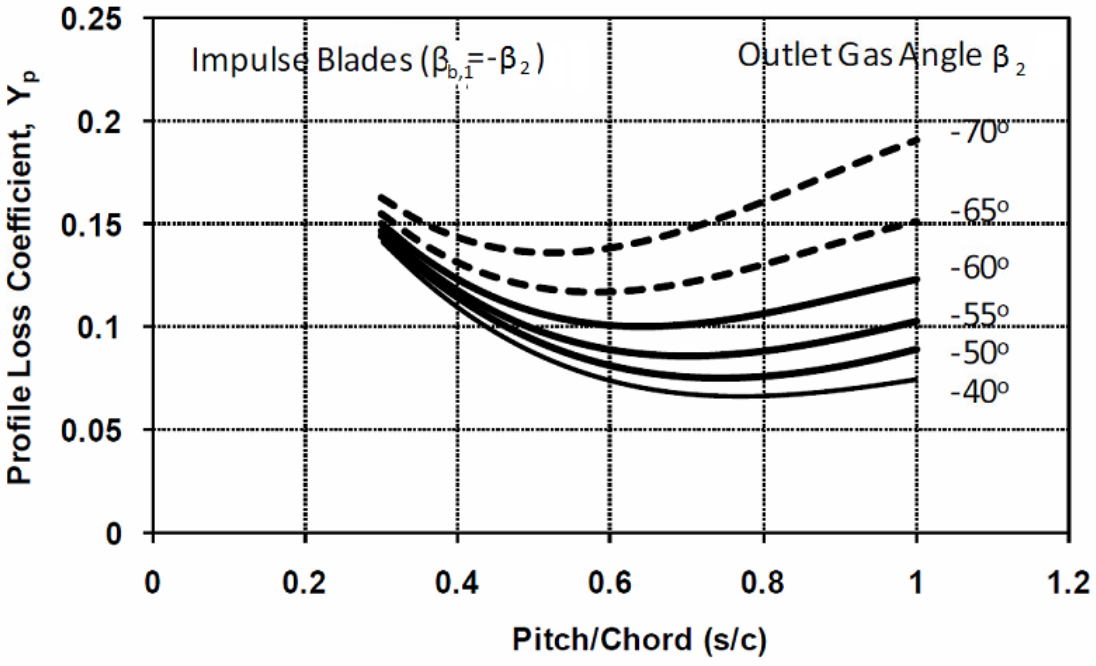

(b)

Figure 3-22: Design profile losses calculation: **(a):** nozzle blades **(b)** impulse blades. [Ainley and Mathieson, 1951]

Additionally, both Kacker and Okapuu (1982) and Zhu and Sjolander (2005) modify the Dunham and Came (1970) as follows:

$$Y_{p,d,KO,ZS} = \begin{cases} 0.91\left(k_{in}\, Y_{p,\mathrm{d},AM-DC}\, k_p + Y_{sh}\right) f_{Re}^{-0.575} + c_{te} & , \quad Re_r > 2 * 10^5 \\ 0.91\left(k_{in}\, Y_{p,\mathrm{d},AM-DC}\, k_p + Y_{sh}\right) f_{Re} + c_{te} & , \quad Re_r \geq 2 * 10^5 \end{cases} \tag{3.252}$$

where (k_{in}) is the blade row correction, (k_p) is the subsonic Mach number and flow acceleration, (c_{te}) is the trailing edge coefficient and (f_{Re}) is the Reynolds number correction(see section 3.6.5). As for the shock losses (Y_{sh}), in contrast to the Aungier (2005) methodology, Kacker and Okapuu (1982) and Zhu and Sjolander (2005) integrate them in the design profile losses. Note that Ainley and Mathieson (1951) Dunham and Came (1970) do not include shock losses in their loss models.

Concerning the off-design profile losses($Y_{p,off}$), they consist of both incidence angle and design profile losses, according to Ainley and Mathieson (1951). Thus, knowing both parameters, it is computed using the following equation,

$$Y_{p,off} = C_{off}\, Y_{p,d}\, m_{te} \tag{3.253}$$

where profile losses off-design coefficient and trailing edge multiplier are calculated according to Figure 3-23 and Figure 3-24, respectively.

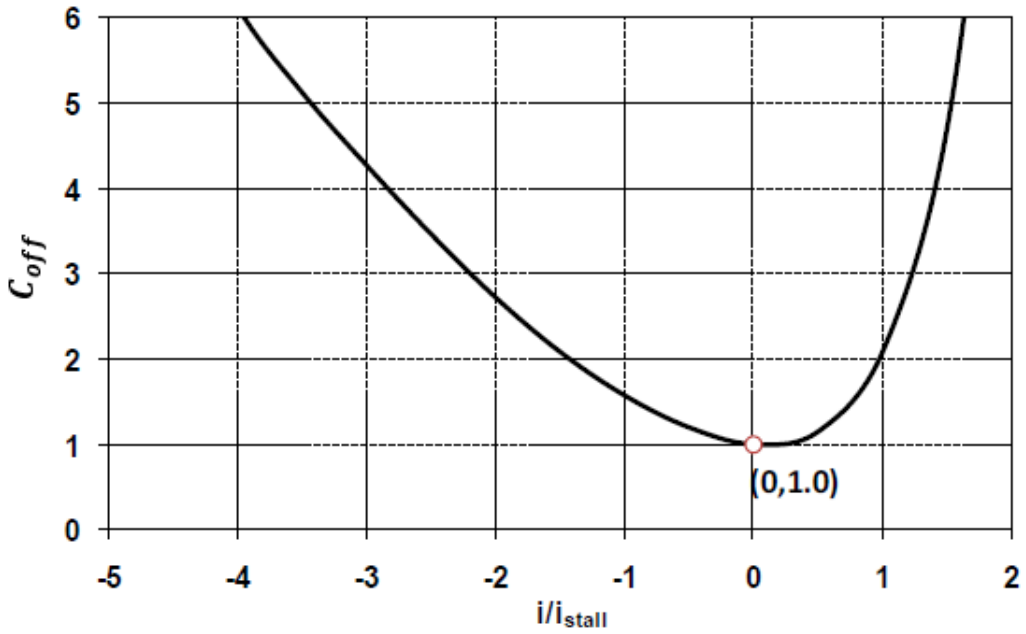

Figure 3-23: Profile losses off-design coefficient calculation.[Ainley and Mathieson, 1951]

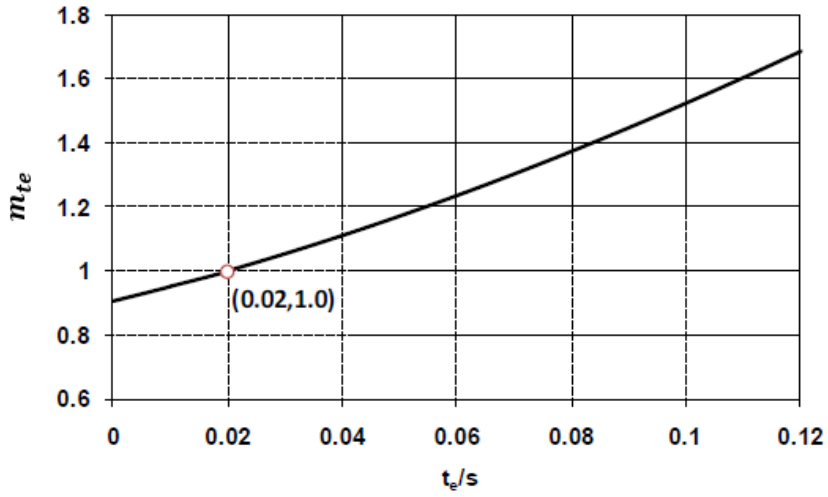

Figure 3-24: Trailing edgemultiplier. [Ainley and Mathieson, 1951]

In Figure 3-23, i refers to incidence angle and i_{stall} reference to stall incidence angle. The stall incidence is defined as:

$$i_{stall} = i_{stall}(s/c \ = \ 0.75) + \Delta i_{stall} \tag{3.254}$$

where the above parameters can be computed using the Figure 3-25.

In contrast to the previous off-design profile losses, Moustapha et al. (1990) do not calculate them directly from design profile losses but connect design and off-design profile kinetic energy loss coefficients with incidence angle and then calculate the corresponding pressure loss coefficient. Specifically, they propose the following steps:

In the first step, the profile kinetic energy loss coefficient are calculated as follows:

$$\Delta\varphi_p^2 = \begin{cases} C_1\, x + C_2\, x^2 + C_3\, x^3 + C_4\, x^6 & , \quad 0 < x < 800 \\ C_5\, x + C_6\, x^2 & , \quad -800 < x \leq 0 \end{cases} \tag{3.255}$$

where loss coefficient parameters C_1, C_2, C_3, C_4, C_5, C_6 values are shown in Table 3-7, while parameter x is defined as:

$$\mathrm{x} = \left(\frac{\mathrm{t_{le}}}{s}\right)^{-1.6} \left(\frac{\cos\beta_{b,1}}{\cos\beta_{b,2}}\right)^{-2} i \tag{3.256}$$

Next the parameter $(\Delta\varphi_{p,des}^2)$ is calculated based on the following equation,

$$Y_{p,des} = \frac{\left[1 - \frac{\gamma-1}{2} M_{r,2}^2 \left(\frac{1}{\Delta\varphi_{p,\mathrm{des}}^2} - 1\right)\right]^{\frac{-\gamma}{\gamma-1}} - 1}{1 - \left(1 + \frac{\gamma-1}{2} M_{r,2}^2\right)^{\frac{-\gamma}{\gamma-1}}} \tag{3.257}$$

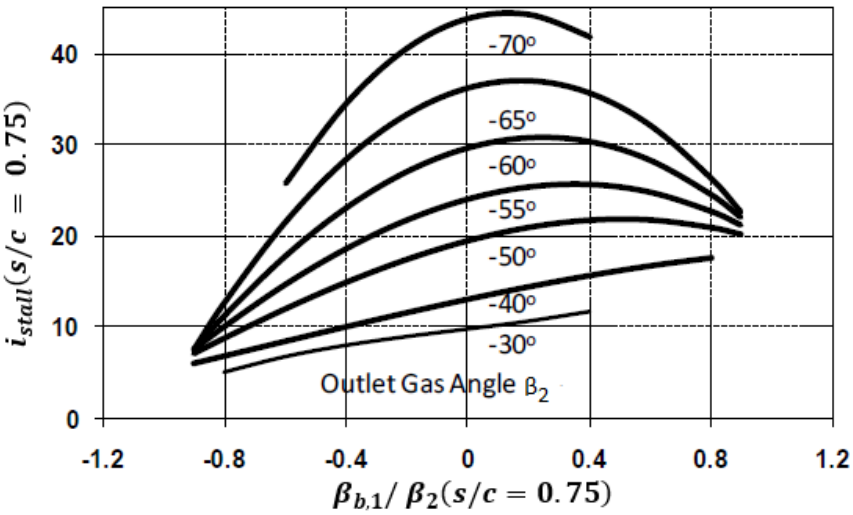

(a)

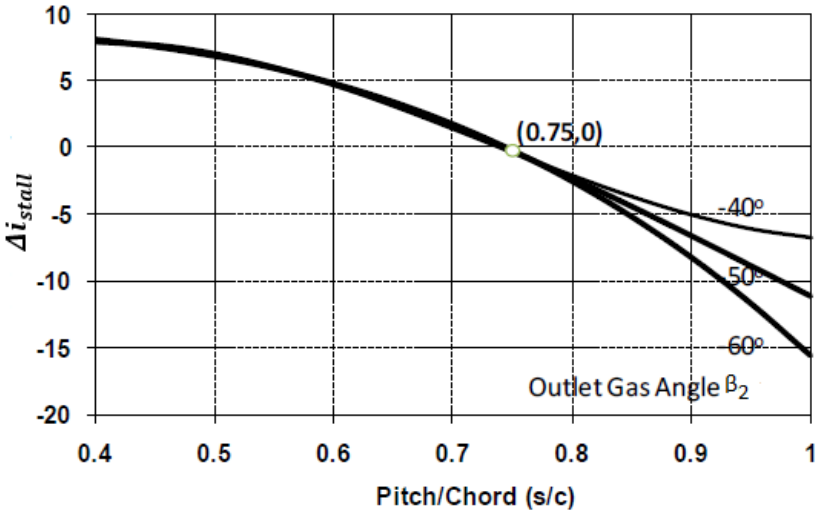

(b)

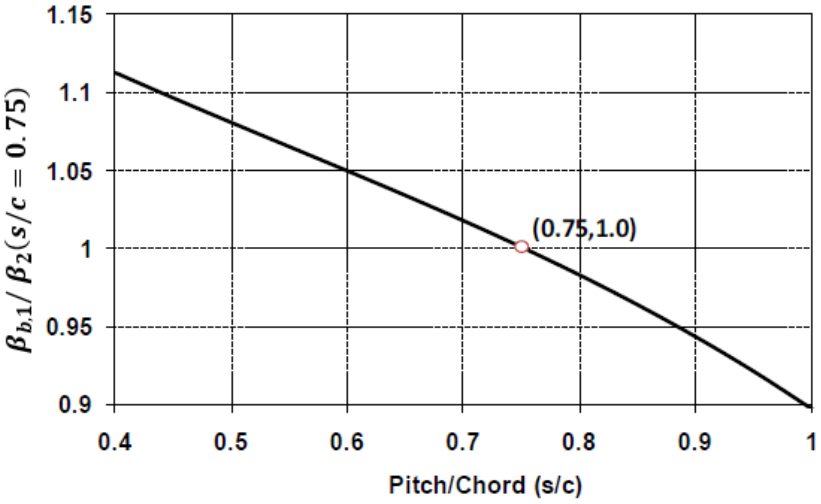

(c)

Figure 3-25: Stall incidence **(a)** angle for 0.75 pitch to chord ratio **(b)** deviation, **(c)** Relative outlet flow deviation [Ainley and Mathieson, 1951]

Table 3-7: Profile kinetic energy loss parameters. [Moustapha et al. 1990]

Parameter	Value	Parameter	Value
C_1	$0.778 \cdot 10^{-5}$	C_4	$2.054 \cdot 10^{-19}$
C_2	$0.56 \cdot 10^{-7}$	C_5	$-5.1734 \cdot 10^{-6}$
C_3	$0.4 \cdot 10^{-10}$	C_6	$7.6902 \cdot 10^{-9}$

Then, the parameter $(\Delta\varphi^2_{p,off})$ is expressed as:

$$\Delta\varphi^2_{p,off} = \Delta\varphi^2_{p,des} - \Delta\varphi^2_p \tag{3.258}$$

Having established the parameter $\Delta\varphi^2_{p,off}$ and using the eq. (3.257) the off-design profile losses $Y_{p,off}$ are calculated.

Benner et al. (1997) follow the same process with Moustapha et al. (1990), changing only the $(\Delta\varphi^2_p)$ parameter, which is expressed as:

$$\Delta\varphi^2_p = \begin{cases} K_1 x^2 + K_2 x & x < 0 \\ L_1 x^8 + L_2 x^7 + L_3 x^6 + L_4 x^5 + L_5 x^4 + L_6 x^3 + L_7 x^2 + L_8 x & x \geq 0 \end{cases} \tag{3.259}$$

where K and L constants are shown in where We is the wedge angle at leading edge.

Table 3-8 and parameter x is defined as,

$$\mathrm{x} = \left(\frac{\mathrm{t_{le}}}{s}\right)^{-0.05} W_e^{-0.2} \left(\frac{\cos\beta_{b,1}}{\cos\beta_{b,2}}\right)^{-1.4} i \tag{3.260}$$

where W_e is the wedge angle at leading edge.

Table 3-8: Profile kinetic energy loss parameters [Benner et al. 1997].

Parameter	Value	Parameter	Value
K_1	$1.358 \cdot 10^{-4}$	K_2	$-8.72 \cdot 10^{-4}$
L_1	$3.711 \cdot 10^{-7}$	L_2	$-5.318 \cdot 10^{-6}$
L_3	$1.106 \cdot 10^{-5}$	L_4	$9.017 \cdot 10^{-5}$
L_5	$-1.542 \cdot 10^{-4}$	L_6	$-2.506 \cdot 10^{-4}$
L_7	$1.327 \cdot 10^{-3}$	L_8	$-6.149 \cdot 10^{-5}$

Aungier (2005) provides a modified Ainley and Mathieson (1951) profile loss model, consisting both the design and the off-design parts, as follows:

$$Y_{p,AU} = K_{mod}\, C_{off,AM}\, k_M k_p f_{Re} \left(Y_{p,\mathrm{d},AM} - \Delta Y_{te}\right) \tag{3.261}$$

where $Y_{p,\mathrm{d},AM}$ is the Ainley and Mathieson (1951) design profile losses. The parameter K_{mod} adjusts the loss model to account for the higher performance of modern designs. It is suggested a value of 1.0 and 0.67 for modern and older designs, respectively. The profile loss off-design coefficient $C_{off,AM}$ is the one presented by Ainley and Mathieson (1951) and can be calculated based on

Figure 3-23. ΔY_{te} represents the trailing edge loss coefficient computed by the present trailing edge loss model for ($t_e/s = 0.02$). The reason is that the Ainley and Mathieson (1951) design profile loss model includes the trailing edge loss specifically assuming that ($t_e/s = 0.02$).

Concerning the trailing edge losses(Y_{te}), Ainley and Mathieson (1951) impose a multiplier in the off-design profile loss coefficient. This multiplier is also used by Dunham and Came (1970) model. Kacker and Okapuu (1982) impose a trailing edge loss coefficient in the overall design profile losses as a correction parameter. This approach is also followed by Zhu and Sjolander (2005). Finally, Aungier (2005) proposes an independent and stand-alone trailing edge loss coefficient,

$$Y_{te,AU} = \left(\frac{t_e}{s \sin \beta_g - t_e} \right)^2 \tag{3.262}$$

For calculating the cascade shock losses(Y_{sh}), both Kacker and Okapuu (1982) and Zhu and Sjolander (2005) impose shock losses into the profile loss calculation as a correction parameter, while Aungier (2005) as individual stand-alone cascade loss. As for both the Ainley and Mathieson (1951) and the Dunham and Came (1970) models, shock losses are not included in the analysis. For Kacker and Okapuu (1982) and Zhu and Sjolander (2005) models, the shock losses can be defined as,

$$Y_{sh,KO} = \frac{R_{hub,1} + R_{hub,2}}{R_{tip,1} + R_{tip,2}} \left(\frac{\Delta p}{q_1} \right)_{hub} \frac{p_{s1}}{p_{s2}} \frac{1 - \left(1 + \frac{\gamma - 1}{2} M_{r,1}^2 \right)^{\frac{\gamma}{\gamma - 1}}}{1 - \left(1 + \frac{\gamma - 1}{2} M_{r,2}^2 \right)^{\frac{\gamma}{\gamma - 1}}} \tag{3.263}$$

The shock losses developed near the blade hub $\left(\frac{\Delta p}{q_1}\right)_{hub}$ can then be expressed as,

$$\left(\frac{\Delta p}{q_1} \right)_{hub} = 0.75 \left(M_{r,hub,1}^2 - 0.4 \right)^{1.75} \tag{3.264}$$

where the relative Mach number at Hub position ($M_{r,hub,1}^2$) can be computed using the Figure 3-26. Aungier (2005) on the other hand, insists that the Kacker and Okapuu (1982) shock model requires some modifications. Thus, the modified shock losses are expressed as:

$$Y_{sh,AU} = \sqrt{\frac{\tilde{Y}_{sh}^2}{1 + \tilde{Y}_{sh}^2}} \tag{3.265}$$

The preliminary estimation of the shock loss coefficient ($\tilde{Y}_{sh}$) is computed by

$$\tilde{Y}_{sh} = 0.8\, X_1^2 + X_2^2 \tag{3.266}$$

where parameters X_1 and X_2 can be computed as:

$$X_1 = \begin{cases} 0 & , \quad M_{r,1} \leq 0.4 \\ M_{r,1} - 0.4 & , \quad M_{r,1} > 0.4 \end{cases} \tag{3.267}$$

$$X_2 = \begin{cases} 0 & , \quad M_{r,1} \leq M_{r,2} \\ \dfrac{M_{r,1}}{M_{r,2}} - 1 & , \quad M_{r,1} > M_{r,2} \end{cases} \tag{3.268}$$

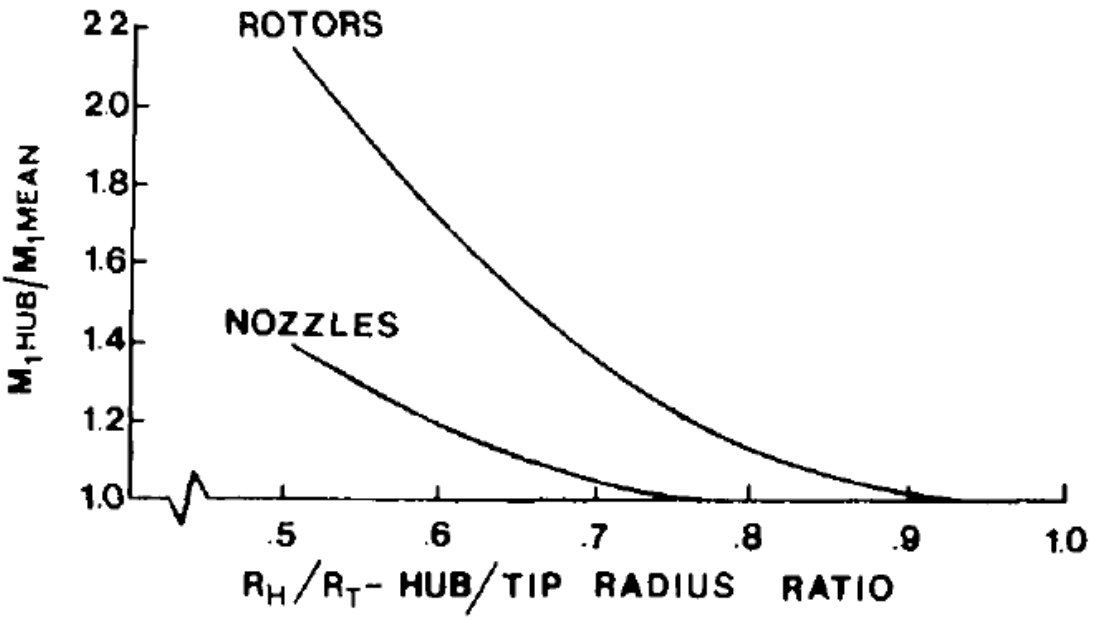

Figure 3-26: Inlet Mach number ratio for non-free-vortex turbine blades. (Kacker and Okapuu 1982)

When the flow at the discharge of a blade row is over-expanded to supersonic Mach numbers, shock waves form to produce additional losses, commonly referred to as supersonic expansion losses(Y_{ex}) or supersonic drag losses. Dunham and Came (1970) suggest a model for this loss contribution, imposed as a multiplier on the Ainley and Mathieson (1951) design profile loss coefficient, described in section 3.6.1. They note that their model is a rather arbitrary correction factor based on very limited information. Aungier (2005) proposes a loss system where the supersonic expansion loss is independent and stand-alone loss coefficient.

$$Y_{ex,AU} = \begin{cases} 0 & , \quad M_{r,2} \leq 1 \\ \left[\dfrac{(M_{r,2} - 1)}{M_{r,2}}\right]^2 & , \quad M_{r,2} > 1 \end{cases} \tag{3.269}$$

Regarding the calculation of the cascade secondary losses (Y_s), Ainley and Mathieson (1951) propose the following correlation:

$$Y_{s,AM} = \lambda \, Z_{load} \, m_{te} \tag{3.270}$$

It is important to note that the secondary losses include the blade trailing edge losses. The parameter λ can be calculated from the Figure 3-27, and the blade load coefficient can be expressed as:

$$Z_{load} = \left(\frac{\mathrm{C_L}}{s/c}\right)^2 \left(\frac{\cos^2\beta_2}{\cos^2\bar{\beta}}\right) \tag{3.271}$$

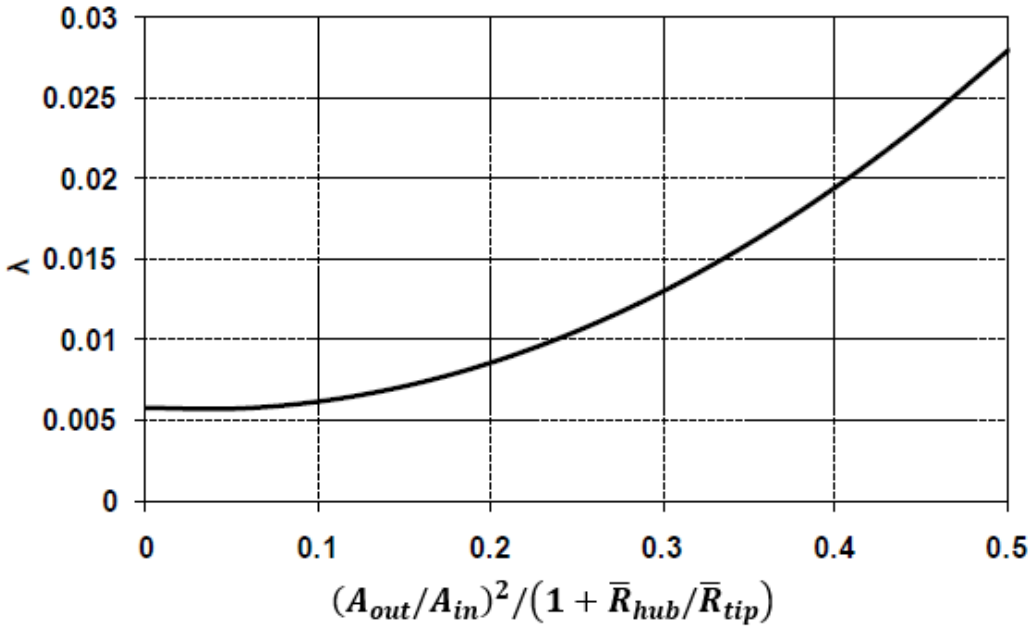

Figure 3-27: Parameter λ calculation.
(Ainley and Mathieson 1951)

where,

$$A_{in} = A_1 \cos\beta_1 \tag{3.272}$$

$$A_{out} = A_2 \cos\beta_2 \tag{3.273}$$

$$C_L = 2\left(\frac{S}{c}\right)(\tan\beta_1 - \tan\beta_2)\cos\bar{\beta} \tag{3.274}$$

Additionally, Dunham and Came (1970) provide a revised secondary loss correlation based on the above approach, which can be defined as:

$$Y_{s,DC} = \frac{0.0334}{\mathrm{AR}} \, Z_{load} \frac{\cos\beta_2}{\cos\beta_1} \, f_{Re} \, m_{te} \tag{3.275}$$

where AR is the aspect ratio and f_{Re} is the Reynolds number correction.

The secondary loss calculation method, presented by Kacker and Okapuu (1982) is similar with the above ones. Specifically, in this method an aspect ratio parameter is added for capturing the secondary loss dependency on Aspect ratio,

$$Y_{s,KO} = 1.2\ \mathrm{k_s}\ 0.0334\ \mathrm{f_{AR}}\ Z_{load}\frac{\cos\beta_2}{\cos\beta_1}\ f_{Re} \tag{3.276}$$

where,

$$k_\mathrm{s} = 1 - k_3\left(1 - k_p\right) \tag{3.277}$$

$$k_3 = \left(\frac{\cos\left(\beta_{stag}\right)}{AR}\right)^2 \tag{3.278}$$

$$f_{AR} = \begin{cases} \dfrac{1 - 0.25\sqrt{2 - AR}}{AR} & , \quad AR \leq 2 \\ \dfrac{1}{AR} & , \quad AR > 2 \end{cases} \tag{3.279}$$

The parameter m_{te} is not included in the secondary loss correlation, because Kacker and Okapuu (1982) treat trailing edge losses in the form of a coefficient which is then added to the profile loss instead of multiplying it.

Moustapha et al. (1990) propose a method for secondary loss calculation, especially in off-design conditions. This method requires the calculation of secondary design loss coefficient, which can be performed by replacing relative inlet flow angle with the inlet blade angle and can be expressed as:

$$Y_{s,d} = Y_{s,AM,DC,KO}\left(\beta_1 = \beta_{b,1}\right) \tag{3.280}$$

Then, the off-design secondary losses can be defined as:

$$\frac{Y_s}{Y_{s,d}} = \begin{cases} e^{0.9x} + 13x^2 + 400x^4 & , \quad 0 < x \leq 0.3 \\ e^{0.9x} & , \quad -0.4 \leq x \leq 0 \end{cases} \tag{3.281}$$

where x is given in eq. (3.256).

Aungier (2005) revises the Kacker and Okapuu (1982) loss model, by imposing an asymptotic upper limit on the f_{AR} parameter calculation formula to permit an analysis under extreme off-design conditions near the end-wall contours.

$$Y_{s,AU} = k_s\ f_{Re}\frac{\tilde{Y}_\mathrm{s}^2}{1 + 7.5\tilde{Y}_s^2} \tag{3.282}$$

where,

$$\tilde{Y}_\mathrm{S} = 0.0334\ f_{AR}\ Z_{load}\frac{\cos\beta_2}{\cos\beta_1} \tag{3.283}$$

$$f_{AR} = \begin{cases} 0.5\left(\dfrac{2}{AR}\right)^{0.7} & AR \leq 2 \\ \dfrac{1}{AR} & AR > 2 \end{cases} \tag{3.284}$$

$$k_s = 1 - \frac{\left(1 - \mathrm{k_p}\right)\frac{1}{AR_{ax}^2}}{1 + \frac{1}{AR^2}} \tag{3.285}$$

For calculating the tip clearance loss coefficient (Y_{cl}), Ainley and Mathieson (1951) propose the following correlation:

$$Y_{cl,AM} = \mathrm{B}\frac{\mathrm{cl}}{\bar{R}_{tip} - \bar{R}_{hub}} Z_{load}\, m_{te} \tag{3.286}$$

where B is 0.5 for blades with radial tip clearance and 0.25 for blades with shroud seal. Additionally, Dunham and Came (1970) revise the above formula, while keeping the same parameters calculation, i.e,

$$Y_{cl,DC} = \mathrm{B}\frac{c}{\bar{R}_{tip} - \bar{R}_{hub}}\left(\frac{\mathrm{cl}}{\mathrm{c}}\right)^{0.78} Z_{load}\, m_{te} \tag{3.287}$$

where parameter B is 0.47 for blades with radial tip clearance and 0.37 for blades with shroud seal.

3.6.5 Cascade loss model parameters

The following correlations are used by the above loss models in order to calculate required correction parameters. The parameters are the Reynolds number correction, blade row correction, subsonic Mach number and flow acceleration correction, blade maximum thickness correction, supersonic Mach number correction, trailing edge coefficient and trailing edge multiplier.

According to Dunham and Came (1970) the Reynolds number correction is calculated as:

$$f_{Re} = \begin{cases} \left(\frac{Re_r}{2\ 10^5}\right)^{-0.2} & , \quad Re_r < 2\ 10^5 \\ 1 & , \quad Re_r \geq 2\ 10^5 \end{cases} \tag{3.288}$$

while according to Kacker and Okapuu (1982) as:

$$f_{Re} = \begin{cases} \left(\frac{Re_r}{2\ 10^5}\right)^{-0.4} & , \quad Re_r < 2 * 10^5 \\ 1 & , \quad 2 * 10^5 < Re_r \leq 10^6 \\ \left(\frac{Re_r}{10^6}\right)^{-0.2} & , \quad Re_r > 10^6 \end{cases} \tag{3.289}$$

Zhu and Sjolander (2005) keep the Kacker and Okapuu (1982) model with a minor revision in the correlation for $Re < 2\ 10^5$:

$$f_{Re} = \begin{cases} \left(\frac{Re_r}{2\ 10^5}\right)^{-0.575} & , \quad Re_r < 2\ 10^5 \\ 1 & , \quad 2\ 10^5 < Re_r \geq 10^6 \\ \left(\frac{Re_r}{10^6}\right)^{-0.2} & , \quad Re_r > 10^6 \end{cases} \tag{3.290}$$

Finally, Aungier (2005) proposes a Reynolds number correction, including the blade roughness parameter similar to the one presented by Kacker and Okapuu (1982). Parameter Re_r refers to roughness Reynolds which is expressed as:

$$\mathrm{Re_e} = \frac{\rho We}{\mu} \tag{3.291}$$

Specifically, the Reynolds number correction for laminar and transition flow is defined as:

$$f_{Re} = \begin{cases} \sqrt{\frac{10^5}{Re_r}} & , \quad Re_r \leq 10^5 \\ 1 & , \quad 10^5 < Re_r \leq 5 * 10^5 \end{cases} \tag{3.292}$$

For turbulent flow the Reynolds number correction depends on both the relative Reynolds Re_r and roughness Reynolds Re_e numbers. Thus, the correction parameter can be expressed as:

$$f_{Re} = \begin{cases} \left[\frac{\log_{10}(5 \cdot 10^5)}{\log_{10}(Re_r)}\right]^{2.58} & , \quad Re_e \leq 100 \\ 1 + \left\{\left[\frac{\log_{10}(5 \cdot 10^5)}{\log_{10}(Re_{cr})}\right]^{2.58} - 1\right\}\left[1 - \frac{5 \cdot 10^5}{Re_r}\right] & , \quad Re_e > 100 \end{cases} \tag{3.293}$$

where Re_{cr} represent the critical blade chord Reynolds number above which roughness effects become significant, i.e.,

$$Re_{cr} = \frac{100\ c}{e} \tag{3.294}$$

The blade row correction parameter according to both Kacker and Okapuu (1982) is defined as:

$$K_{in} = \frac{2}{3} \tag{3.295}$$

while, Zhu and Sjolander (2005) propose different blade row correction parameters for both Rotor and Stator:

$$K_{in} = \begin{cases} \frac{2}{3} & Rotor \\ 0.825 & Stator \end{cases} \tag{3.296}$$

The subsonic Mach number & flow acceleration correction parameter, according to both Kacker and Okapuu (1982) and Zhu and Sjolander (2005), is expressed as:

$$k_p = 1 - k_1\,(1 - k_2) \tag{3.297}$$

where k_1 refers to the subsonic Mach number correction and k_2 to the flow acceleration correction and are defined as:

$$k_1 = \begin{cases} 1 & , \quad M_{r,2} < 0.2 \\ 1 - 1.25\left(M_{r,2} - 1\right)^2 & , \quad M_{r,2} \geq 0.2 \end{cases} \tag{3.298}$$

$$k_2 = \frac{M_{r,1}}{M_{r,2}} \tag{3.299}$$

The subsonic Mach number correction parameter, presented by Aungier (2005), is defined as:

$$k_M = \begin{cases} 1 & M_{r,2} < 0.6 \\ 1 + \left[1.65\left(M_{r,2} - 0.6\right)^2 + 240\left(M_{r,2} - 0.06\right)^2\right]\left(\frac{s}{R_c}\right)^{3M_{r,2}-0.6} & M_{r,2} \geq 0.6 \end{cases} \tag{3.300}$$

where R_c is the blade suction surface radius of curvature. Also, the loss associated with $M_{r,2} > 1$ is handled separately as individual loss coefficient, entitled as supersonic expansion loss.

The blade maximum thickness correction parameter, presented by Zhu and Sjolander (2005), is defined as:

$$k_m = \begin{cases} 1 & \frac{t_{max}}{c} \leq 0.2 \\ -1 & \frac{t_{max}}{c} > 0.2 \end{cases} \tag{3.301}$$

The supersonic Mach number correction parameter is defined as:

$$C_{fm} = \begin{cases} 1 & M_{r,2} < 1 \\ 1 + 60\left(M_{r,2} - 1\right)^2 & M_{r,2} \geq 1 \end{cases} \tag{3.302}$$

The trailing edge coefficient (c_{te}) is defined as:

$$c_{te} = \frac{\left[1 - \frac{\gamma - 1}{2}\,M_{r,2}^2\left(\frac{1}{1 - \Delta\varphi_{te}^2} - 1\right)\right]^{-\frac{\gamma}{\gamma - 1}} - 1}{1 - \left(1 + \frac{\gamma - 1}{2}\,M_{r,2}^2\right)^{-\frac{\gamma}{\gamma - 1}}} \tag{3.303}$$

where, the trailing edge energy loss coefficient ($\Delta\varphi_{te}^2$) is calculated from the following equation:

$$\Delta\varphi_{te}^2 = \Delta\varphi_{te(\beta_{b,1}=a_2)}^2 + \left|\frac{\beta_{b,1}}{\beta_2}\right| \left(\frac{\beta_{b,1}}{\beta_2}\right)\left[\Delta\varphi_{te(\beta_{b,1}=\beta_2)}^2 - \Delta\varphi_{te(\beta_{b,1}=0)}^2\right] \quad (3.304)$$

where the trailing edge energy loss coefficients for Impulse ($\Delta\varphi_{te(\beta_{b,1}=\beta_2)}^2$) and Nozzle blades ($\Delta\varphi_{te(\beta_{b,1}=0)}^2$) are computed based on **Error! Reference source not found.**.

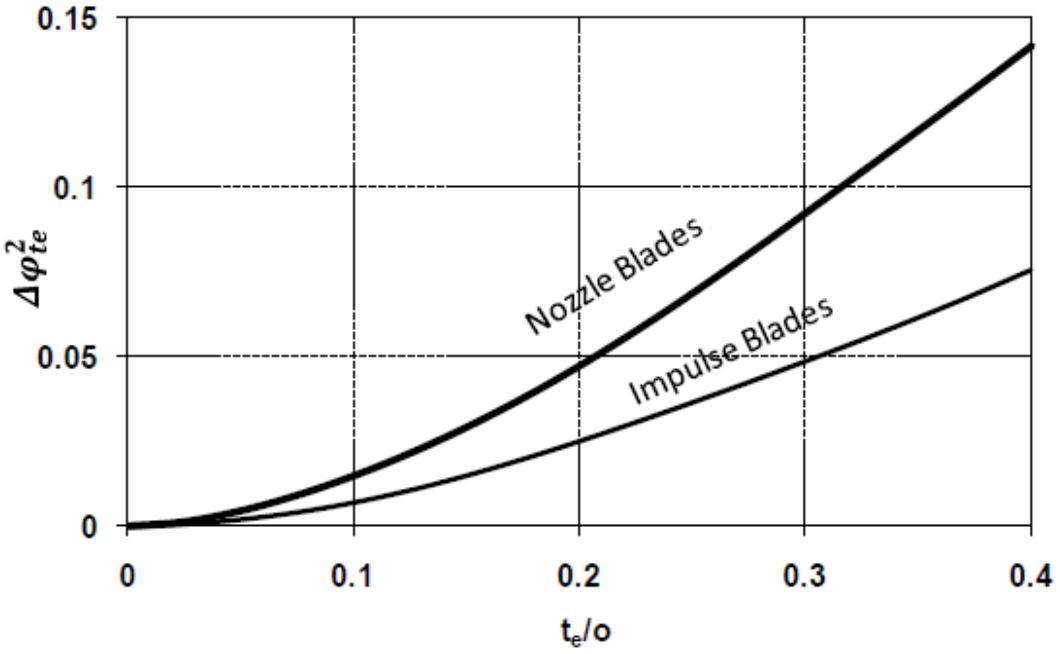

Figure 3-28: Trailing edge: energy coefficient. [Ainley and Mathieson, 1951]

3.6.6 Choke Indices calculation

The choke indices are calculated in the same way with the radial turbine(3.5.6).

3.6.7 Axial turbine performance map generation

The AT performance map is generated in the same way with the radial turbine one (3.5.7).

3.6.8 Axial turbine meanline analysis verification

The comparison between the predictions of the axial turbine meanline model(using all possible loss and deviation models combinations) and the corresponding measured data are depicted in Figure 3-29 for specific AT, presented by Person (2015). The axial turbine geometry is given in Table 3-9.

Table 3-9: Axial turbine geometry.

Axial Turbine			
Stator			
Parameter	Value	Parameter	Value
$R_{1,hub}$	0.178 [m]	$R_{2,hub}$	0.178 [m]
$R_{1,tip}$	0.202 [m]	$R_{2,tip}$	0.202 [m]
$\beta_{b,1}$	0^o	$\beta_{b,2}$	74.5^o
t_{le}	0.002 [m]	t_e	0.000253 [m]
cl	0 [m]	Z	42 [-]
o	0.0076 [m]	t_{max}/c	0.195
c	0.0405 [m]	e	0.155 [m]
clearance type: Shroud seal			
Rotor			
Parameter	Value	Parameter	Value
$R_{1,hub}$	0.1775 [m]	$R_{2,hub}$	0.1775 [m]
$R_{1,tip}$	0.2025 [m]	$R_{2,tip}$	0.2025 [m]
$\beta_{b,1}$	43^o	$\beta_{b,2}$	-63.5^o
t_{le}	0.0015 [m]	t_e	0.000266 [m]
cl	0.0003737 [m]	Z	64 [-]
o	0.00751[m]	t_{max}/c	0.337
c	0.0264[m]	e	0.067 [m]
clearance type: Shroud seal			

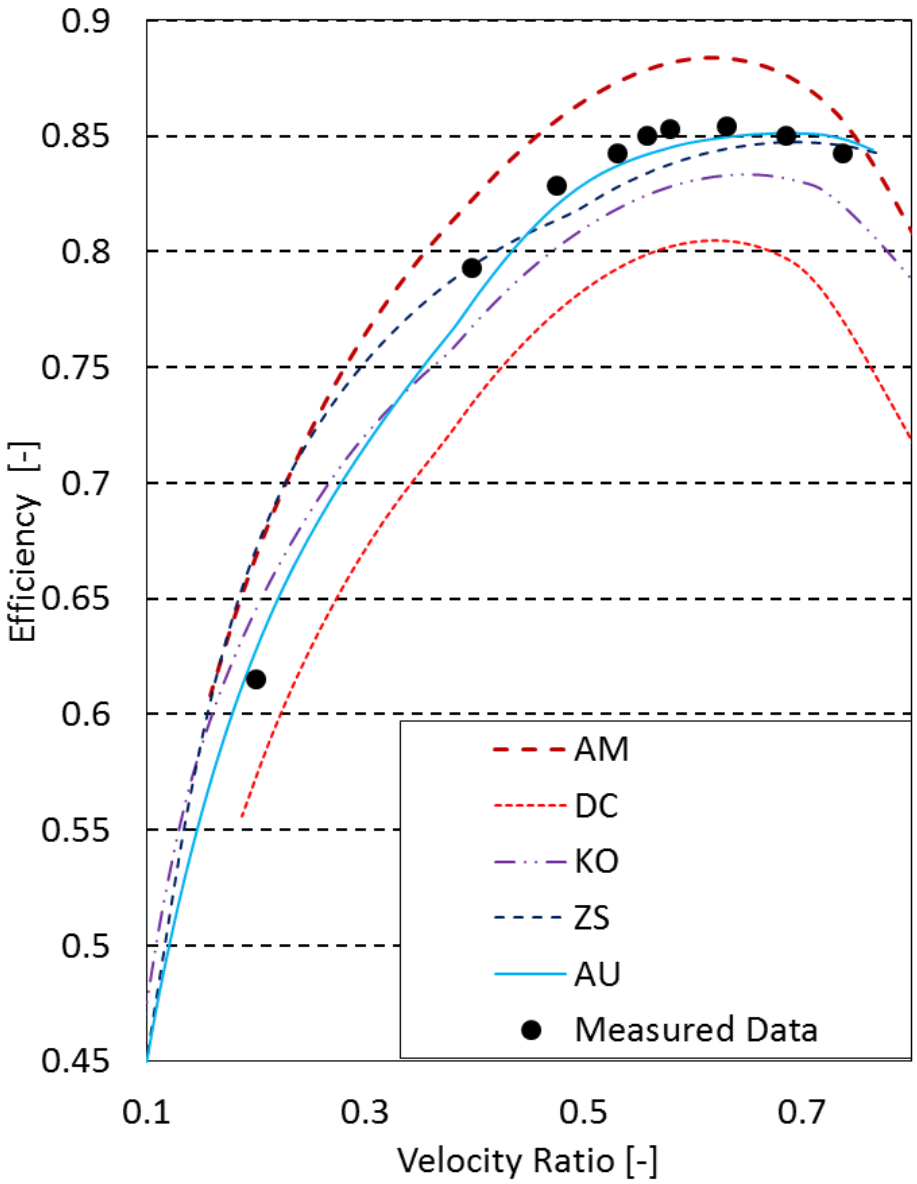

Figure 3-29: Axial TML validation against measured data

where velocity ratio(VR) is defined as:

$$VR = \frac{U}{\sqrt{2\,\Delta h_{t-s,is}}} \tag{3.305}$$

According to the results, it is observed that the most recent loss models such as the ones presented by Zhu and Sjolander (2005) and Aungier (2005) have better agreement with the measured data in comparison with the older ones which underestimate the turbine performance. For the current PhD study, the Aungier (2005) model is chosen as it is the one with the best agreement among all and also is considered more appropriate for new turbine designs.

3.7 Surrogate Volute loss models

A big disadvantage of the CC and RT meanline models is the volute inability to calculate the pressure losses due to 3D effects. For this reason, CC and RT volute data-driven [Wang 2005] loss models based on CFD results are developed. For RT and CC volute CFD-based models, an in-house utility function is developed, with the aim to run specific CFD sub-processes in the background, such as fluid domain meshing and flow modeling, in order to automate the RT and CC volute CFD-based loss prediction training data, generation for creating the corresponding surrogate models.

The entire surrogate loss model training process, shown in Figure 3-30, is developed with the aim to allow further re-training procedures without negatively affecting the T/C design and retrofit processes, such as pausing the processes during the training period. The training process is developed within Python environment, while the CFD simulation part is conducted within commercial CFD software[1]. The whole process is properly developed in order to launch simultaneous CFD runs for generating the required training patterns through enabling multiple simulators.

According to Figure 3-30, for training a volute surrogate model, first a number of randomly selected parameters generations(randomly selected sets of input parameters) are created with respect to the parameters defined ranges(Table 3-10).

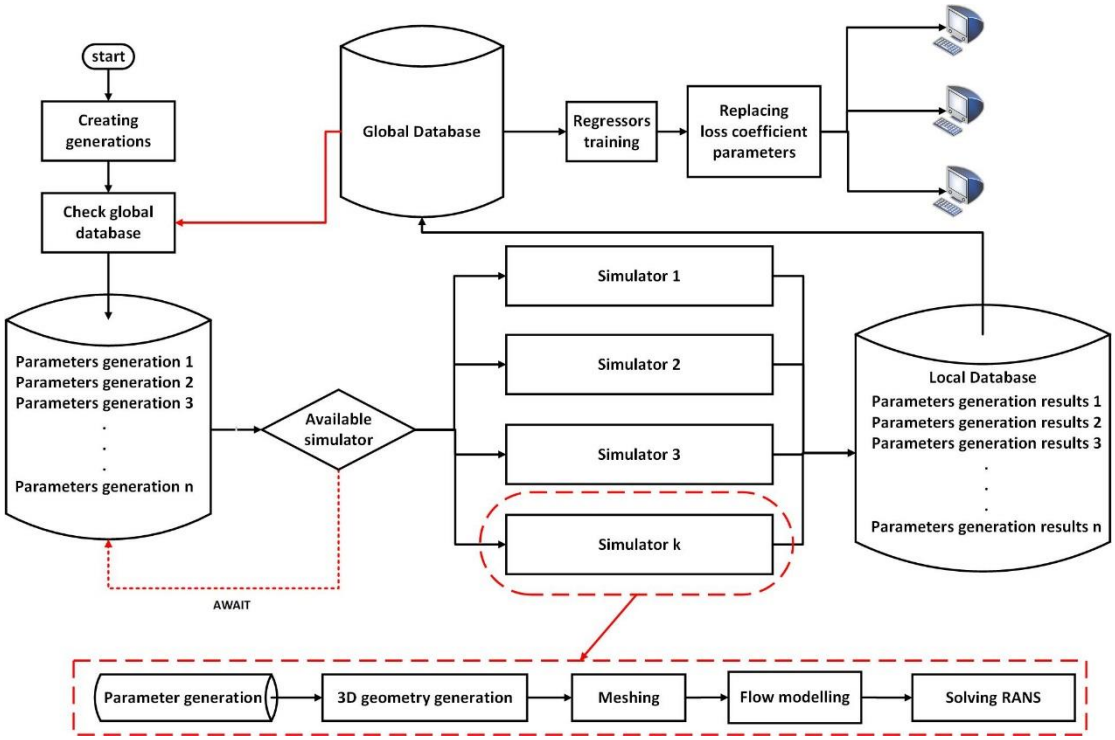

Figure 3-30: Entire surrogate loss models training process.

[1] https://www.ansys.com/products/fluids/ansys-cfx

During the re-training(not initial training) procedure, each generation is checked in case that has been previously utilized in a training process, hence avoiding unnecessary CFD simulations.

Having set a number of parameters generation, each one of them is waiting for an available simulator(not performing CFD simulation) to be parsed. Regarding the simulators, they are basically python modules which utilize the necessary CFD commercial sub-tools such as 3D geometry drawing[1], meshing[2], flow modeling[3] and RANS solver[3]. The number of in operation simulators are user defined and they can be dynamically change during the process without negatively affecting the rest of the sub-processes. Note that each simulator approximately time for completing one CFD simulation is about 15 minutes.

Having completed the training patterns generation and parsed them in a local database, the next step is to append them to a global one, which includes training patterns from previous training procedures, triggering the surrogate models training process. With the training process been completed, a new file, which includes the updated loss coefficient parameters, is created for each component(CC and RT volute), aiming to replace the corresponding out-of-date one in each workstation(used for T/C design and retrofit) through the local network.

3.7.1 Centrifugal Compressor and Radial Turbine Volute geometrical parameters

For the volute geometries parameterization, the use of dimensionless geometrical parameters (Table 3-10) is selected along with imposing specific boundary conditions for developing more general CC and RT volute models.

Table 3-10: CC and RT Volute geometrical dimensionless and flow parameters.

CC Volute		RT Volute	
Parameter	Range	Parameter	Range
b_{in}/R_{in}	(0.05,0.24)	b_{in}/R_{out}	(0.05,0.35)
R_{out}/R_{in}	(1.1,1.4)	$R_{Vol,0^o}/R_{out}$	0.06
$R_{vol,\,360^o}/R_{in}$	(0.2,0.73)	$R_{Vol,180^o}/R_{out}$	(R_{0^o}/R_{out}, R_{360^o}/R_{out})
M_{inlet}	(0.05,0.8)	$R_{Vol,360^o}/R_{out}$	(0.1,0.5)
α_{inlet}	(20,80)	M_{inlet}	(0.05,0.8)

CC and RT volute parameters can be shown in Figure 3-31. Concerning CC volute, it is assumed that the R_{vol,θ^o} is proportional to circumferential angle. Also, ratio $Y_{vol,\theta^o}/R_{vol,\theta^o}$, which is a function of the circumferential direction as well, is based on the 3D designed volute geometry, presented in application case A. For

[1] ANSYS Design modeler
[2] ANSYS Meshing
[3] ANSYS CFX

RT parameters, it is also assumed that the volute cross section curvature(r) is constant across circumferential direction.

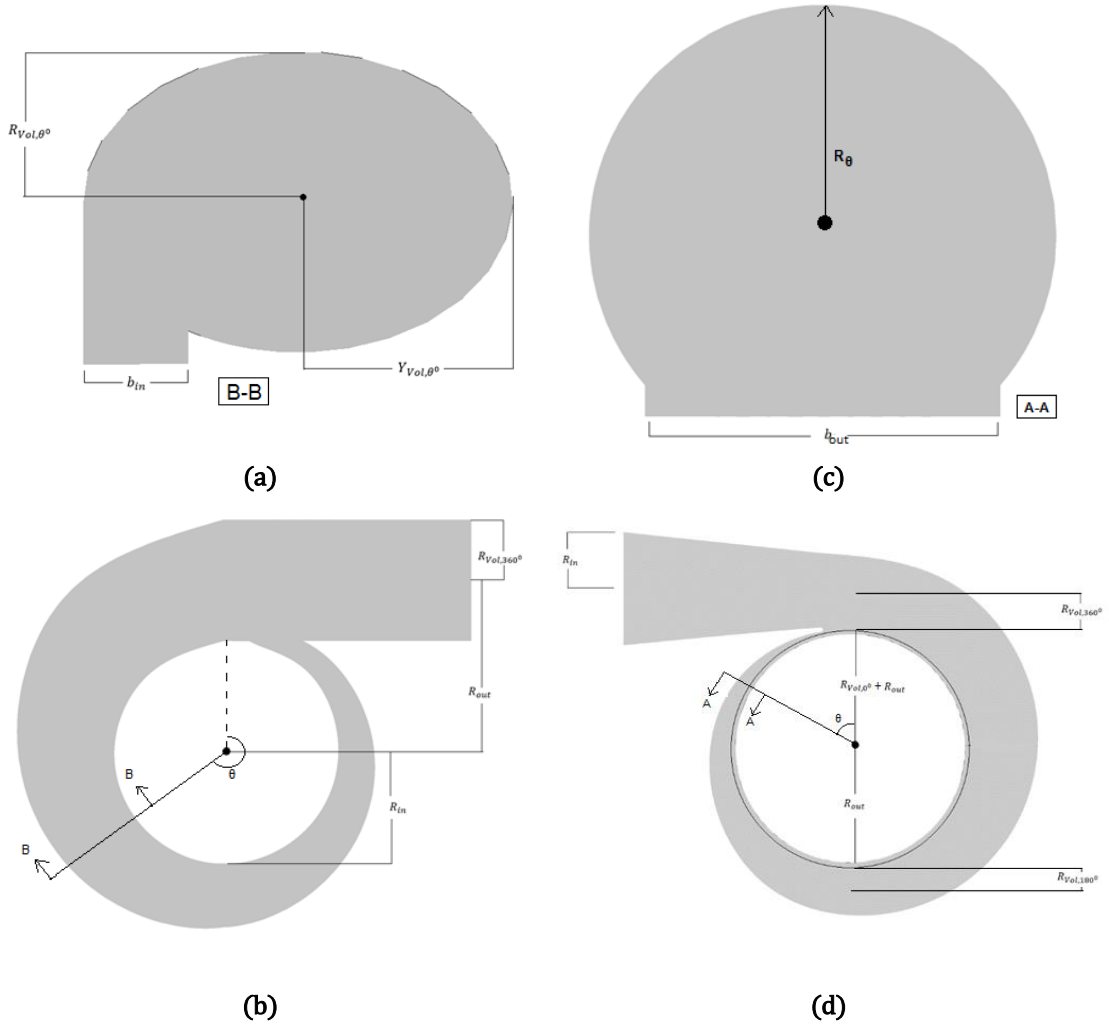

Figure 3-31: Volute: **(a):** CC cross section [B-B] **(b)** CC meridional view **(c)** RT cross section [A-A] **(d)** RT meridional view.

3.7.2 Volutes CFD flow model

The simulation, conducted for the purpose of the volute simulation, is steady. The fluid is considered to be continuous, air ideal gas and the gauge pressure is set to 0 atm. The set of governing equations, solved by the CFD software, are the Navier-Stokes equations which consist of the continuity, momentum and energy equations.

A heat transfer model is used to predict the flow temperature along the volute. The most suitable for the volute case is the total energy model. This model is used to consider the transport of enthalpy while taking into account the kinetic energy effects.

Concerning the turbulence model, the k-ω based SST model [Menter 1992] accounts for the transport of the turbulent shear stress is selected. This model is

extensively used for CFD analysis in turbomachinery components such as the presented one, as it is expected to provide accurate calculations for the boundary layer, simulating both the viscous sub-layer and the log-law layer, as well as valid predictions of the amount of flow separation under adverse pressure gradients. It is suggested a grid with $y^+ < 5$ for capturing the laminar and transitional boundary layers correctly [ANSYS Inc. 2011].

Considering advection scheme, a second order upwind scheme is selected "High Resolution" [ANSYS Inc. 2011] for the mean flow, turbulence and transition equations. The CFD software is using pseudo-transient solution approach for steady-state computations by creating an equivalent transient problem and simulating until steady-state is reached [Fletcher, 1998]. For the volute case, the timescale of the pseudo-transient solution method is set to automatic timescale. [ANSYS Inc. 2011]

3.7.3 Volutes CFD boundary conditions

Concerning the boundary conditions, all CC and RT volutes walls are modeled as no-slip wall boundaries. Thus, as both volutes are stationary components, the wall boundaries absolute velocity is set equal to the wall velocity(zero). Considering the thermal conditions for the wall boundaries, these are adiabatic.

The volute inlet in both CC and RT cases are set as subsonic inlet boundaries. For the inlet boundary, the total temperature, absolute velocity magnitude and direction are specified. The total temperature in both cases is set equal to 288.15 [K]. The inlet velocity direction is given in terms of two angles, namely peripheral (θ_r) and axial (θ_a). For the case of the CC volute, the axial angle(θ_a) is set to 90^o (axial velocity component is 0 m/s), while the peripheral angle (θ_r) varies and is equal to the input parameter α_{inlet} (if peripheral angle is 0 the circumferential velocity is 0 [m/s]). For RT volute, the flow is always axial and thus both the axial and radial angles are set equal to 0^o. Concerning the absolute velocity magnitude, as the entire process has the Mach number as input data for both CC and RT cases, the inlet absolute velocity magnitude is calculated in terms of the given inlet Mach number and total temperature.

Concerning the inlet turbulence intensity(I), it is set equal to 5%. The intensity is defined as:

$$I = \frac{u'}{U} = \frac{\sqrt{\frac{1}{3}\left(u_x'^2 + u_y'^2 + u_z'^2\right)}}{\sqrt{U_x^2 + U_y^2 + U_z^2}} \tag{3.306}$$

where u' is the fluctuating velocity component due to turbulence and U is the velocity magnitude [ANSYS Inc. 2011]. Considering the outlet boundary conditions, an outlet mean static pressure equal to 1 [atm] is imposed for both cases.

3.7.4 Volutes mesh generation

Concerning volute mesh[1] generation(Figure 3-32), the multi-zone method is used. This meshing technique provides automatic decomposition of the body geometry into mapped and free regions. In the first one, a hexahedral mesh is utilized, while in the latter, unstructured regions, where the creation of hexahedral elements is not possible, a free mesh is generated. Considering the boundary layer, the first layer thickness inflation method is also utilized, in order to determine the first element height.

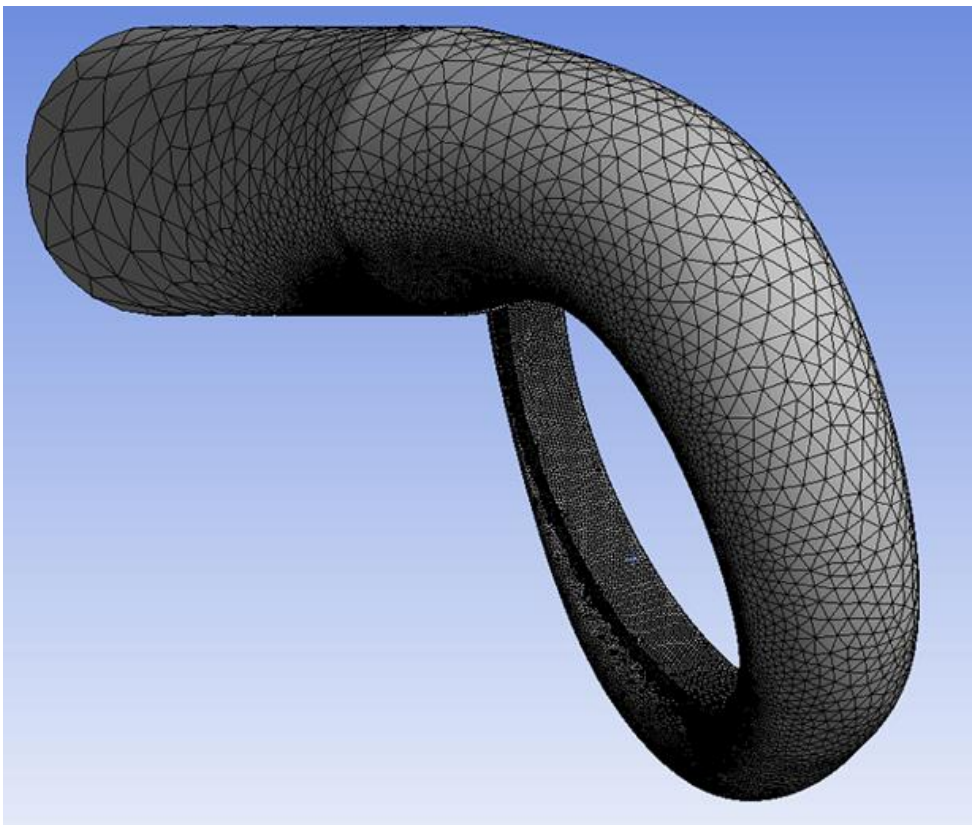

Figure 3-32: Volute 3D mesh.

According to mesh independency study for both volute fluid domains, depicted in Figure 3-33, a 1.6 million nodes for CC Volute and 1.4 million nodes for RT Volute are chosen, achieving a maximum y^+ value of the first nodes off the wall about 2.1 and 3.2 respectively. Both components y^+ values are lower than five, which ensures according to the software manual that the CFD model captures the laminar and transitional boundary layers correctly. [ANSYS Inc. 2011]

[1] ANSYS Meshing

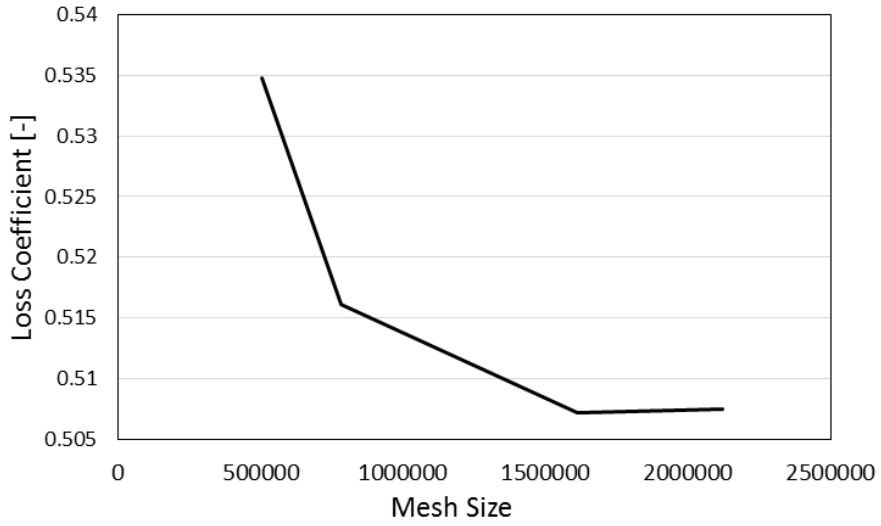

(a)

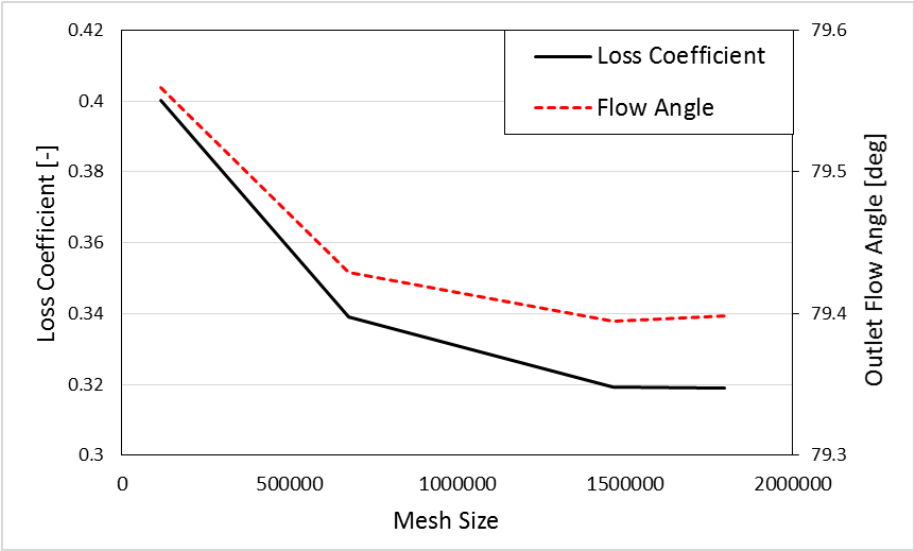

(b)

Figure 3-33: Volute mesh independent study: **(a)** CC **(b)** RT.

The loss coefficients for both CC and RT volutes are computed by mass averaging the CFD results and are defined as:

$$\omega_{Vol,CC} = \frac{P_{t,in} - P_{t,out}}{P_{t,in} - P_{in}} \tag{3.307}$$

$$Y_{Vol,RT} = \frac{P_{t,in} - P_{t,out}}{P_{t,out} - P_{out}} \tag{3.308}$$

The RT Volute CFD model, apart from the value of the loss coefficient, provides the mass averaged outlet flow angle. Figure 3-34 depicts both volutes 3D geometry, including the flow pattern, developed within, in the form of streamlines.

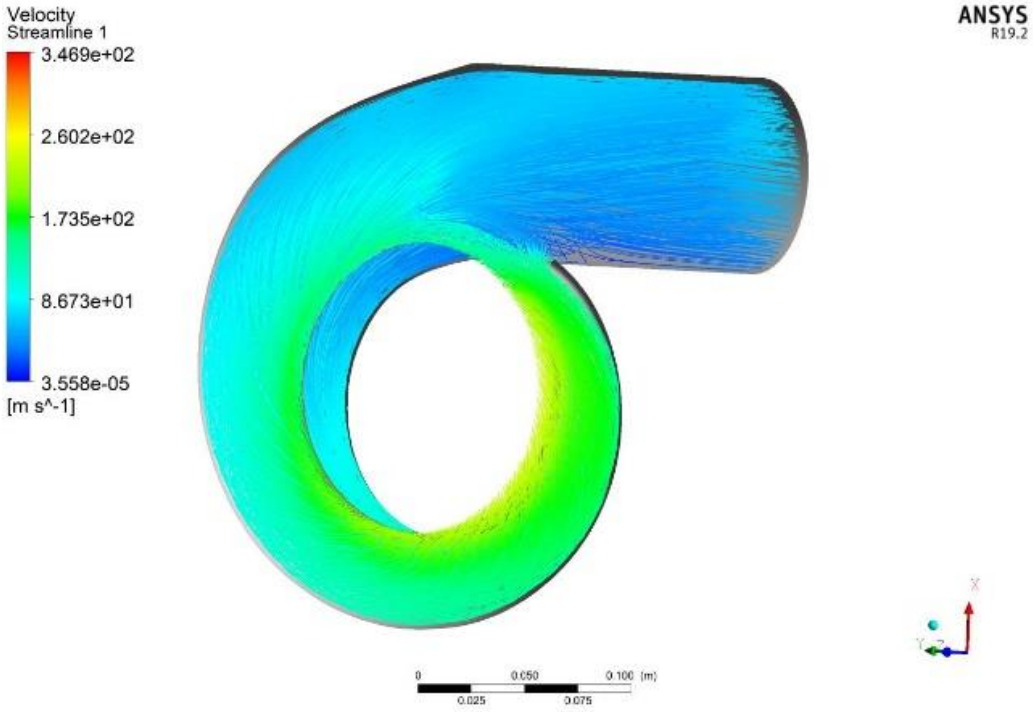

(a)

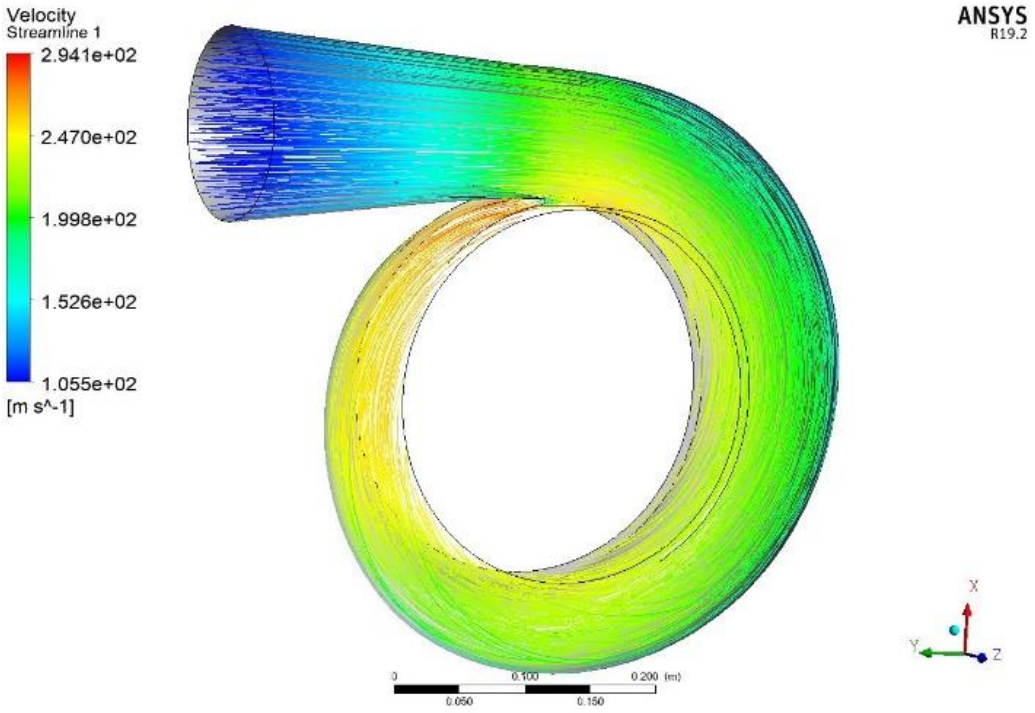

(b)

Figure 3-34: Volute Flow Simulation: **(a)** CC **(b)** RT.

3.7.5 Volute surrogate loss model training and results

Having generated the necessary training patterns to train the surrogates models, they are yielded into 2 datasets of about 1000 points each, from which the 90% is used in the training and the 10% in the testing process.

The preprocessing step entails filtering both datasets in order to keep the ones that corresponds to stable operation. Thus, for both CC and RT volute data the filtering criteria are defined as:

- Loss coefficient value <= 1
- 0 <= Outlet flow angle <= 90(For RT volute)
- Velocity and Energy RMS residuals $<=10^{-5}$
- Velocity and Energy imbalance <0.1%

Additionally, data points are normalized using a min-max scaler in order to improve the convergence of the training and to scale the features to an appropriate range for fitting the model. The min-max scaling formula is as follows:

$$X_{SC} = \frac{X - X_{min}}{X_{max} - X_{min}} \tag{3.309}$$

Several methods are trialed in order to find the best fit for each problem. The support vector machine (SVM) was deemed best for the compressor model, whereas a K-nearest neighbor (KNN) regressor is chosen for the turbine volute problem due to SVM inability to consists of more than one outputs. For CC volute SVM and RT Volute KNN models, both "*sklearn.svm.svr*" [1] and "*sklearn.neighbors.KNeighborsRegressor*"[2] python modules are utilized.

In order to obtain the best SVM parameters on the training set a random search method is used. The search is configured to use a cross-validation of 5 folds in order to obtain more accurate R^2 scores for each set of parameters. A similar approach but using a grid search is followed in order to find out the best number of neighbors for the turbine volute model. The tunable parameters and the search spaces are shown in Table 3-11 and Table 3-12 for the compressor and the turbine, respectively.

Table 3-11: CC SVM model parameters and search spaces.

Centrifugal Compressor Volute SVM model		
	Optimal Value	Search space
C	12	(0 , 1000)
ε	0.01	(10^{-4} , 10^{-3})

Table 3-12: RT KNN model parameters and search spaces.

Radial Turbine Volute KNN model		
	Optimal Value	Search space
n neighbors	2	(1,30)

[1] https://scikit-learn.org/stable/modules/generated/sklearn.svm.SVR.html
[2] https://scikit-learn.org/stable/modules/generated/sklearn.neighbors.KNeighborsClassifier.html

Regarding the surrogate models error analysis, the Figure 3-35 shows the histograms of the errors in the testing set for each volute surrogate model. It can be observed that almost all errors are below 10% for both models. For the compressor volute model, 90% of the errors are below 5% and for the turbine volute 74% of the loss errors and 100% of the angle errors are below 5%.

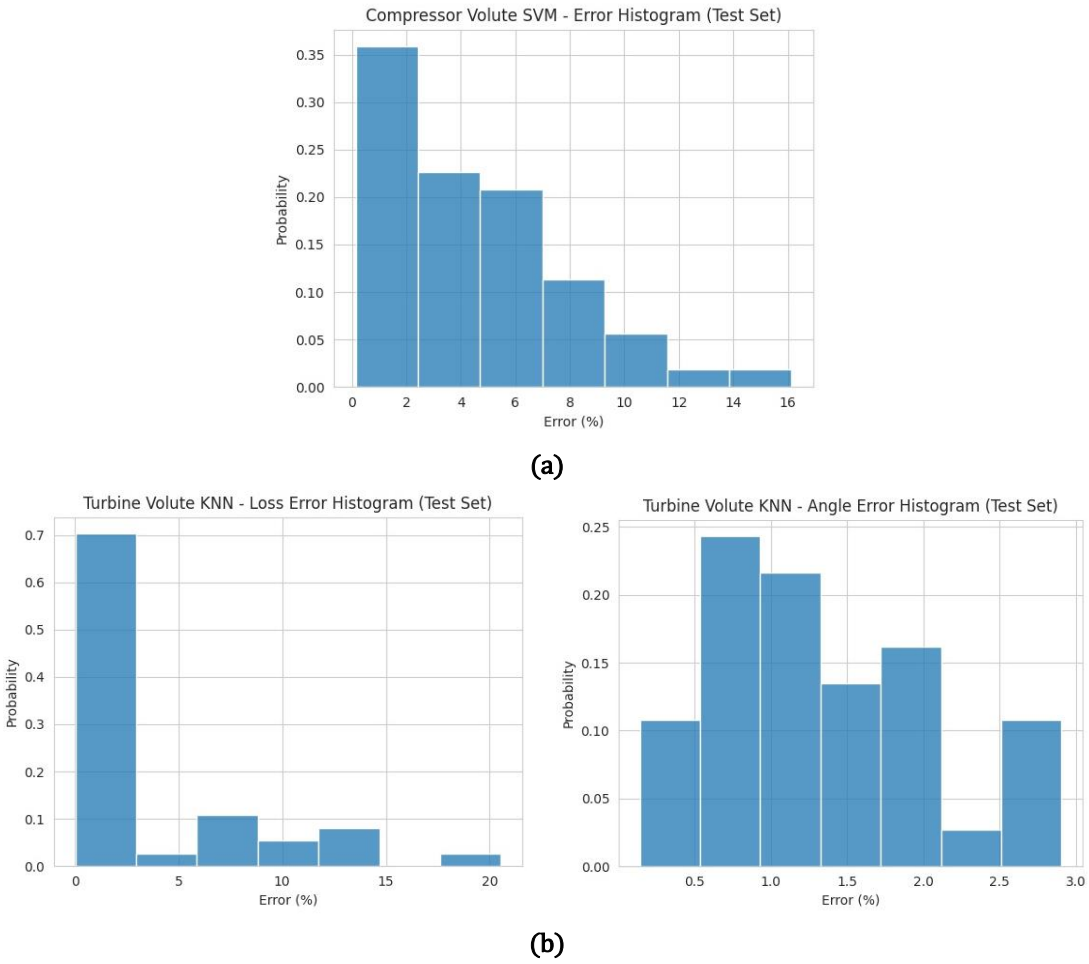

Figure 3-35: Volute Error Histogram: **(a)** CC **(b)** RT.

Concerning R-square analysis, the R^2 score(eq. (3.310)) on the training set for the compressor volute model is 0.98 and (0.99,0.96) for the turbine volute, while the R^2 score on the test set is 0.95 and (0.99,0.92) respectively.

$$R^2 = \frac{\sum(y_i - \hat{y}_i)^2}{\sum(y_i - \bar{y}_i)^2} \tag{3.310}$$

where $y_i$is the actual value, $\hat{y}_i$ is the predicted y value by the regressor and $\bar{y}_i$ is the mean value.

For evaluating the above CC model, a comparison between the corresponding CFD based and the Aungier (2000) model results is performed and depicted in Figure 3-36.

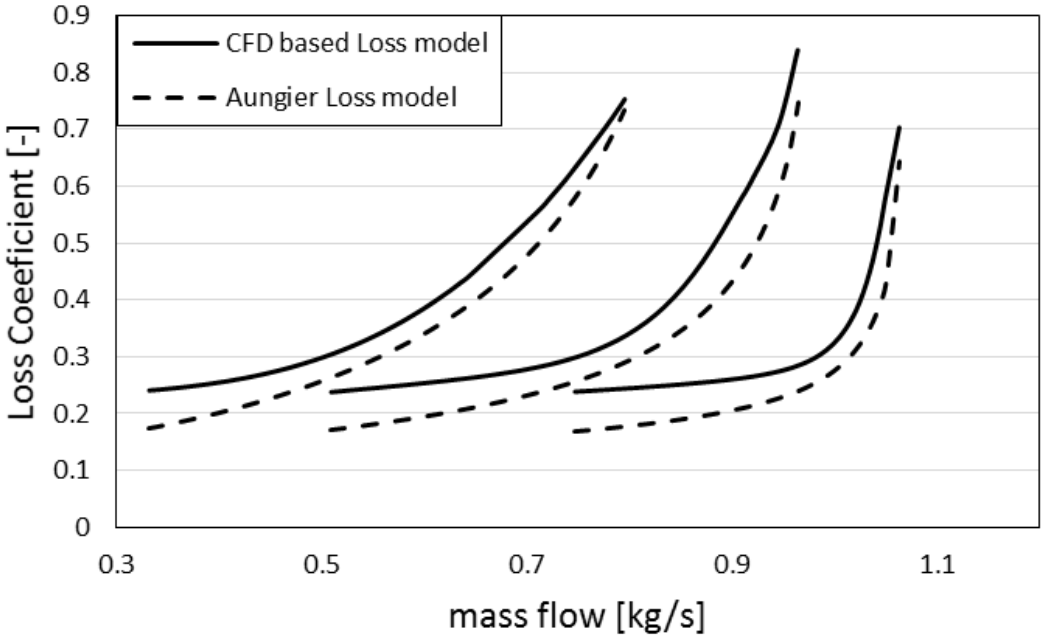

Figure 3-36: CC Volute model comparison.

According to the results, both models have similar trend. As inlet volute Mach number goes to lower values, it is observed that the deviation between both models increases due to the secondary effects. Specifically, the Aungier (2000) loss model integrates both meridional velocity and skin friction loss coefficients (equations (3.124) and (3.125)). Even if both loss coefficients are primary ones, they are unable to capture the secondary effects, which are highly increased in low Mach numbers, hence leading to model loss deviation increase as Mach number decreases.

For further evaluation of the CFD based CC volute loss model, a parametric study is carried out. In Figure 3-37(a) the volute loss coefficient is depicted and calculated based on outlet to inlet radius and inlet width to inlet radius ratio. In Figure 3-37(b) the volute loss coefficient is shown and is calculated based on outlet tube to inlet radius and inlet width to inlet radius ratios.

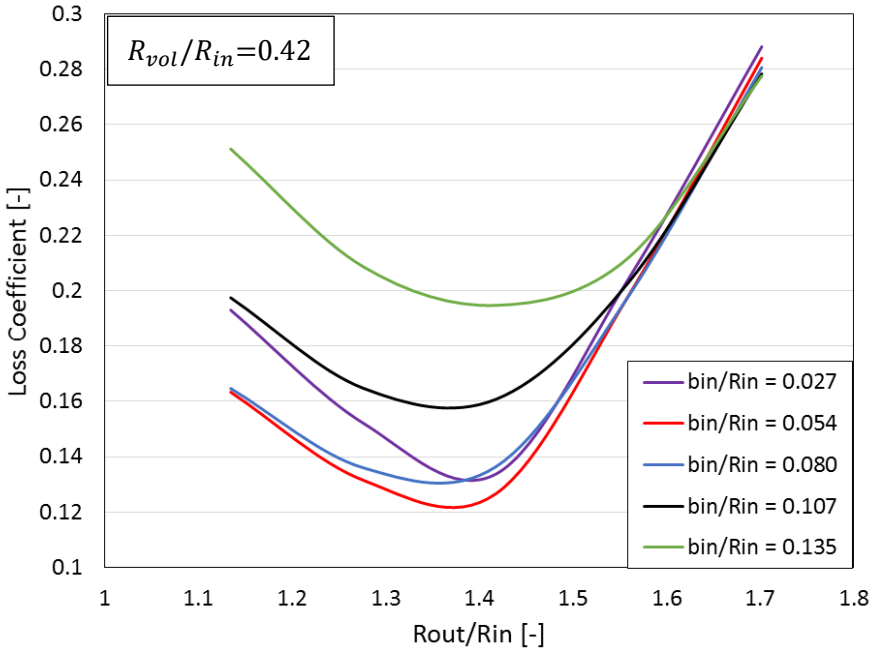

(a)

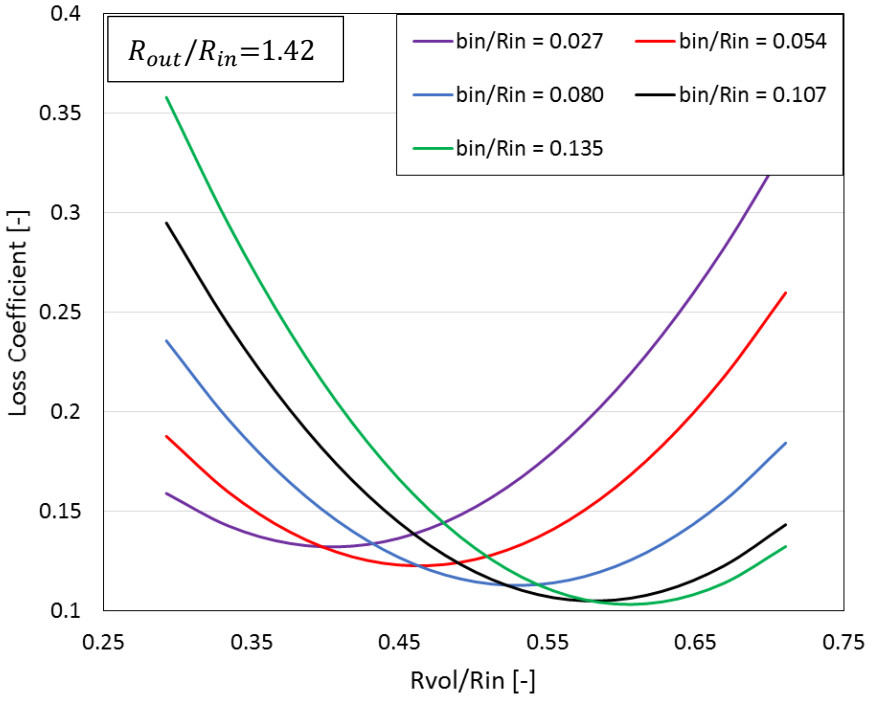

(b)

Figure 3-37: CC Volute model parametric study.

According to Figure 3-37, both (R_{out}/R_{in}) and (R_{vol}/R_{in}) highly affect the volute loss coefficient.

Concerning the (R_{out}/R_{in}) parameter, it seems to be independent of the other geometrical ones, as seen in Figure 3-37a, for specific flow angle and Mach number, as the optimum point is not affected by the (b_{in}/R_{in}) variation and corresponds to a value of about 1.35. On the other hand, the (R_{vol}/R_{in})

parameter is strongly influenced by (b_{in}/R_{in}), as the optimum point varies from 0.42 to 0.58 as (b_{in}/R_{in}) is changed(Figure 3-37b). In the current case, the minimum loss coefficient is achieved by designing a volute with a (R_{out}/R_{in}) equal to 1.35, a (b_{in}/R_{in}) equal to 0.135 and a (R_{vol}/R_{in}) equal to 0.59.

For evaluating the above RT Volute model, a comparison between the corresponding CFD-based and the Aungier (2005) model results is performed and depicted in Figure 3-36.

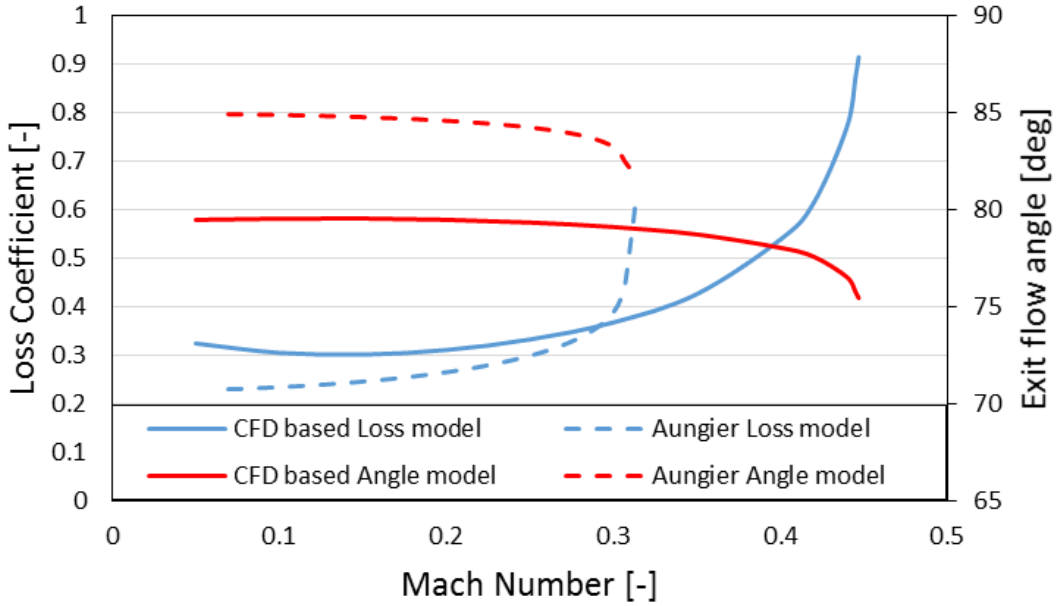

Figure 3-38: RT Volute model comparison.

According to the results, both models have similar trend for Mach numbers lower to 0.25 (turbine volute operates in most cases with volute inlet Mach numbers lower than 0.25). Also, it can be seen that both models achieve different maximum Mach number. In contrast to the CC volute model, the RT volute model affects choke point as it is the first upstream RT component, hence affecting all the downstream turbine components performances.

The Aungier (2005) loss model consists of circumferential distortion and boundary layer losses (equations (3.185)and (3.186)). Similar to CC volute loss model, the RT one consists of primary losses, hence it is unable to capture the secondary effects, which are increased in low Mach numbers, hence leading to model loss deviation increase as Mach number decreases.

Concerning volute outlet flow angle prediction, Aungier (2005) assumes that no losses occur from inlet to the station in volute half, where the mass flow that supplies its flow conditions is the half of the inlet one. Thus, for calculating the flow conditions in volute outlet, angular momentum at the volute exit is estimated from conservation of angular momentum between mid and outlet volute station, while assuming pressure losses existence only between mid and outlet station. These assumptions lead to both loss coefficient and flow angle deviation increase between the 1D and the CFD based model predicted data.

For further evaluating RT volute model, a geometrical parametric study is performed. In Figure 3-39(a) the volute loss coefficient(continues line) and exit flow angle(dash line) is depicted and calculated based on Rvol(360°) to outlet radius and outlet width to outlet radius ratio. In Figure 3-39(b) the volute loss coefficient(solid line) and exit flow angle(dashed line) is shown and are calculated based on Rvol(360°) to outlet radius and volute inlet diffuser ratio.

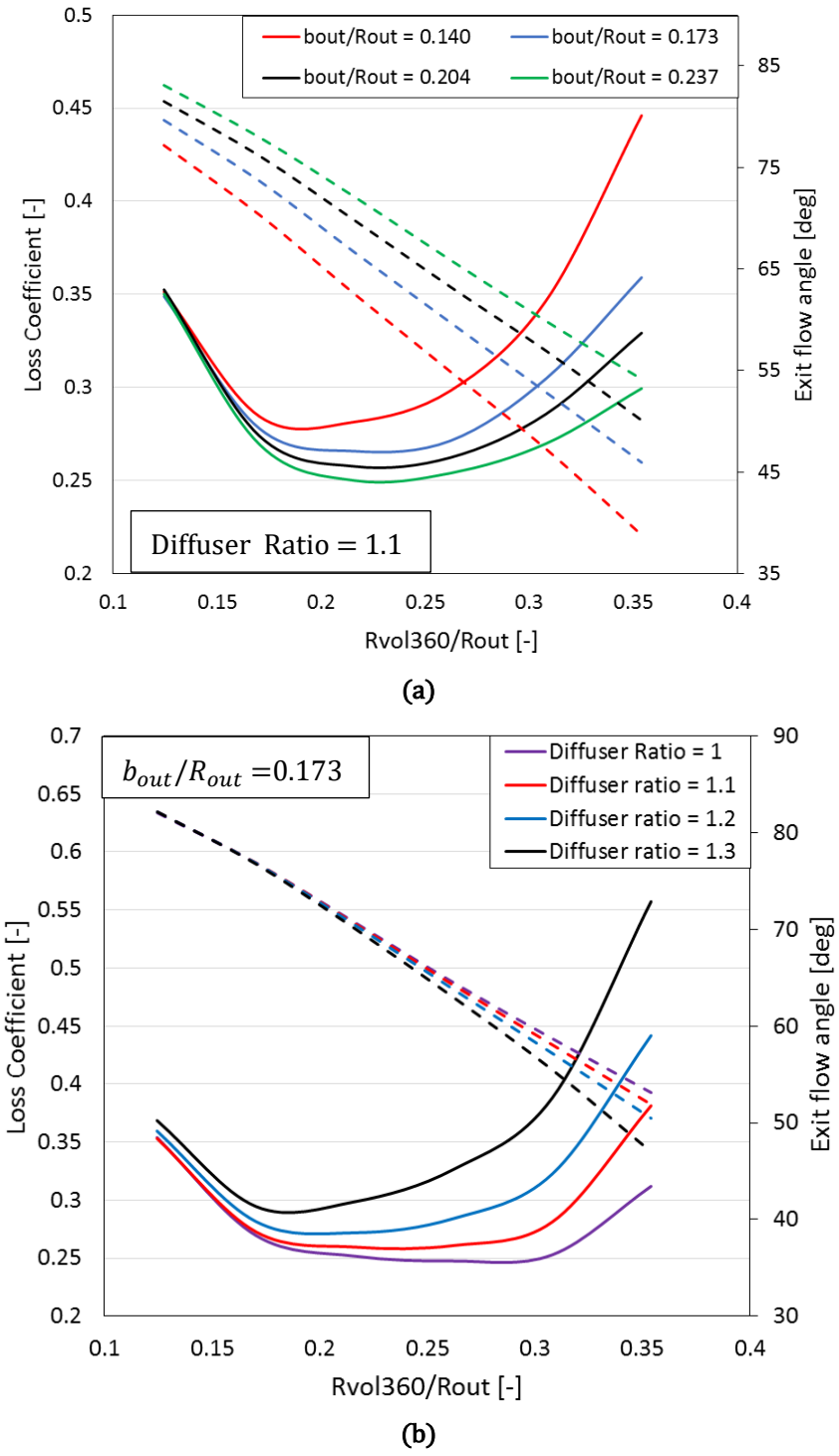

Figure 3-39: RT Volute model parametric study.

According to Figure 3-39, all three parameters depend on each other, as seen by the variation of the optimum point for different parameter combinations. Specifically, the volute loss coefficient is strongly affected by (R_{vol360}/R_{out}) parameter, rather than the (b_{out}/R_{out}) and the diffuser ratio, as it varies from 0.25 to 0.55. Regarding the outlet flow angle, it depends mostly on (R_{vol360}/R_{out}) and (b_{out}/R_{out}) as diffuser ratio slightly affects it. Additionally, the diffuser ratio level of influence in outlet flow angle depends on (R_{vol360}/R_{out}) parameter. Concluding, in contrast to CC volute design, in the RT one, seeking a volute geometry with minimum loss coefficient may lead to an overall turbine efficiency decrease, since the outlet flow angle may negatively affect both the nozzle and impeller operation. Thus, the volute component should not be design separately.

3.8 Matching criteria

For matching criteria, turbocharger must provide the necessary boost pressure, in order for the diesel engine to generate the demanded nominal power [Emara et al. 2016]. For ensuring that the entire engine system energy equilibrium is achieved, the following criterion is applied:

$$\frac{p_{im} - p_{exh,manif}}{p_{im}} \leq 15\% \tag{3.311}$$

where p_{im} and $p_{exh,manif}$ are the inlet and exhaust manifold pressure, respectively.

Ideally, the turbo-components operating nominal points should be in high efficiency area while compressor operating line distance from stall line must be as large as possible [Emara et al. 2016]. For ensuring the T/C stable operation, the following criterion is applied:

$$\frac{\dot{m} - \dot{m}_{stall}}{\dot{m}_{stall}} \leq 15\% \tag{3.312}$$

3.9 Turbocharged Diesel Engine Experimental Verification

As it discussed above, the approach followed for the simulation of T/Ced diesel engine operation is based on empirical and semi-empirical expressions to determine the fuel burning rate, heat transfer and friction power losses. Therefore, it is necessary to calibrate the model constants by comparing the output of the simulation model with corresponding available shop trial data(Table 3-13).

Table 3-13: Diesel engine shop trials data.

Load [%]	Output [kW]	Fuel [kg/h]	C.P [barg]	C.T [C]	P_{amb} [mbar]	T_{amb} [C]	RH [%]	P_{max} [bar]	T_{exh} [C]
25	113	32.2	0.36	35	1001.5	31	62	62	283
50	225	53.5	0.69	37	1003.7	30.5	66	83	339
75	338	73.6	1.23	42	1003.5	31	65	108	365
100	450	94.5	1.84	45	1003	31.5	59	131	399
110	495	104.3	2.05	47	1002.7	32.5	54		

Concerning the T/Ced diesel engine verification test case, its technical specifications are depicted in Table 3-14, while the Table 3-15 and Table 3-16 show the baseline T/C components geometry. The baseline turbo-components geometry is used as input data to the corresponding mean line models. Calibration constants are determined, following an optimization procedure to minimize the error when comparing calculated and measured values at each operating point (25%, 50%, 75%, and 100% of full engine load) and at rated engine speed.

Table 3-14: Diesel engine technical specifications.

Parameter	Value	Parameter	Value
Cycle	4	Fuel LHV [kJ/kg]	42700
Cylinders	5	Number of turbochargers	1
Bore[mm]	200	Injection timing[CA]	10^o BTDC
Stroke[mm]	300	Injection pressure[bar]	294
Fuel Type	Diesel	Number of injector nozzle holes	8

Table 3-15: Baseline centrifugal compressor geometry.

Vaneless Diffuser Centrifugal Compressor Geometry			
Parameter	Value	Parameter	Value
$D_{1,hub}$	0.029 [m]	b_3	0.0082 [m]
$D_{1,tip}$	0.085 [m]	b_4	0.0082 [m]
D_3	0.137 [m]	Z_{MB}	7 [-]
D_4	0.17 [m]	le_{spl}	0.3 [-]
$\beta_{b,1}$	52.25^o	Z_{FB}	7 [-]
$\beta_{b,3}$	36.5^o	L_A	0.04 [m]
t_1	0.0021 [m]	AR_{vol}	0.23 [-]
t_3	0.0017 [m]	N_{des}	60000 [Rpm]
cl	0.006 [m]		

Table 3-16: Baseline radial turbine geometry.

Vaneless Nozzle Radial Turbine Geometry			
Parameter	Value	Parameter	Value
$D_{6,hub}$	0.038 [m]	t_3	-
$D_{6,tip}$	0.109[m]	t_2	-
D_4	0.120 [m]	b_4	0.0209 [m]
D_3	0.160 [m]	b_3	0.0209 [m]
D_2	0.160 [m]	b_2	0.0209 [m]
$\beta_{b,5}$	46.8^o	Z_{MB}	11 [-]
$\beta_{b,4}$	22.49^o	Z_{FB}	11 [-]
$\beta_{v,3}$	-	L_A	0.046 [m]
$\beta_{v,2}$	-	Z_V	-
t_5	-	AR_{vol}	0.21
t_4	-	N_{des}	60000 [Rpm]
le_{spl}	-	cl	0.0006[m]

In Figure 3-40, the comparison between the measured and the calculated values for brake engine power, peak combustion pressure and exhaust gas temperature, at the engine operating conditions used for calibration is depicted.

As observed, there is a good matching between measured and calculated values, which indicates that the model reliably reproduces the specific engine operation for the entire range of the conditions examined. It should be noted that one set of calibration parameters is used for the whole operating envelope.

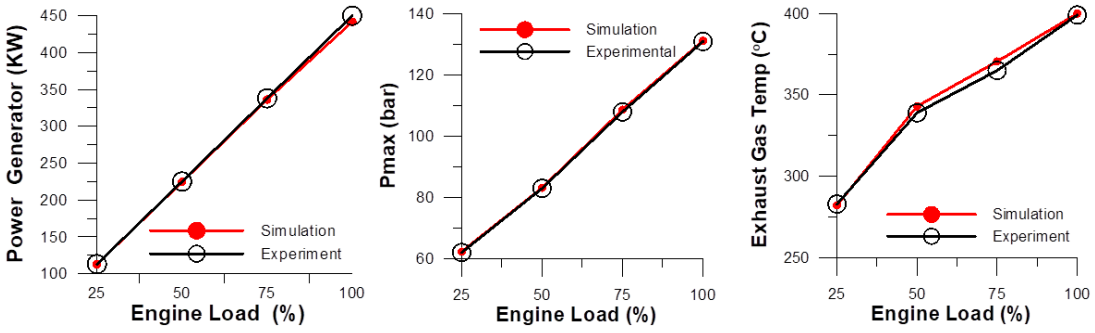

Figure 3-40: Comparison between calculated and measured values used for model calibration.

The specific fuel consumption and boost pressure against engine power is presented in Figure 3-41 for five different operating points (Load: 25, 50, 75, 100 and 110%) as reported in the engine shop trials, shown in Table 3-13.

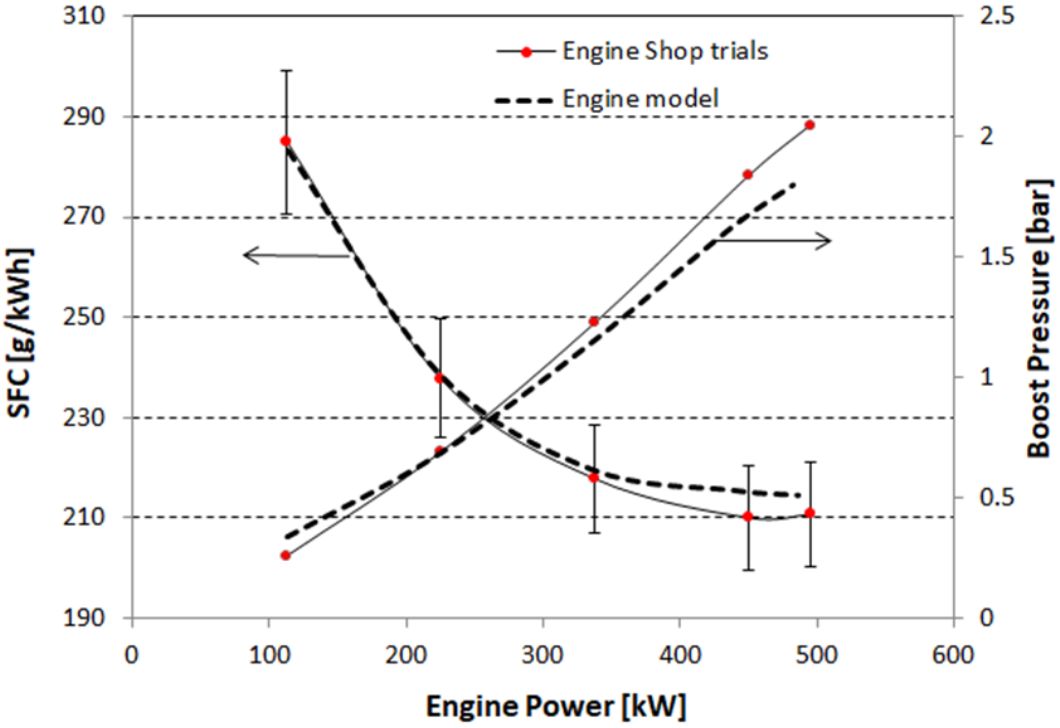

Figure 3-41: Comparison between calculated and measured SFC and boost pressure.

As seen in Figure 3-41, the integrated T/Ced engine model simulates the overall engine operation in very good agreement to the engine shop trials data. The maximum deviation from the reported mean SFC is 2.6%. During design and retrofitting processes, the overall fuel consumption is utilized. Utilizing the overall specific consumption function in the following applications, the errors corresponding to the 100% and 110% loads do not significantly contribute to the overall processes errors.

The matching of T/C components with the engine is presented in Figure 3-42 and Figure 3-43, where both compressor and turbine maps with corresponding operating lines are shown.

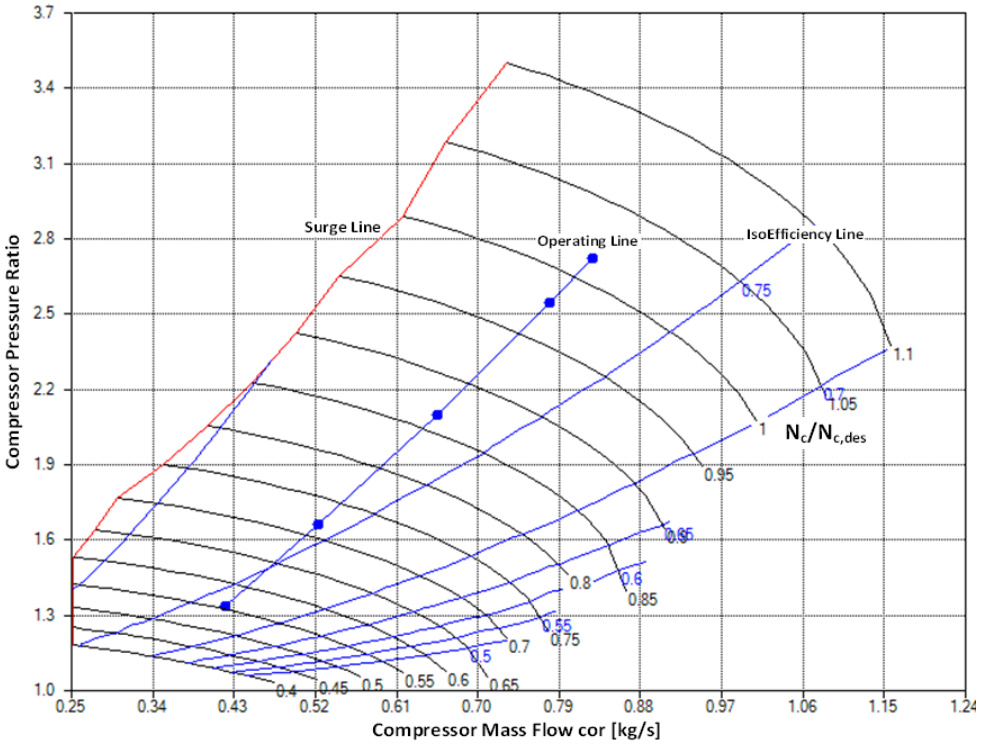

Figure 3-42: Compressor map and operating line.

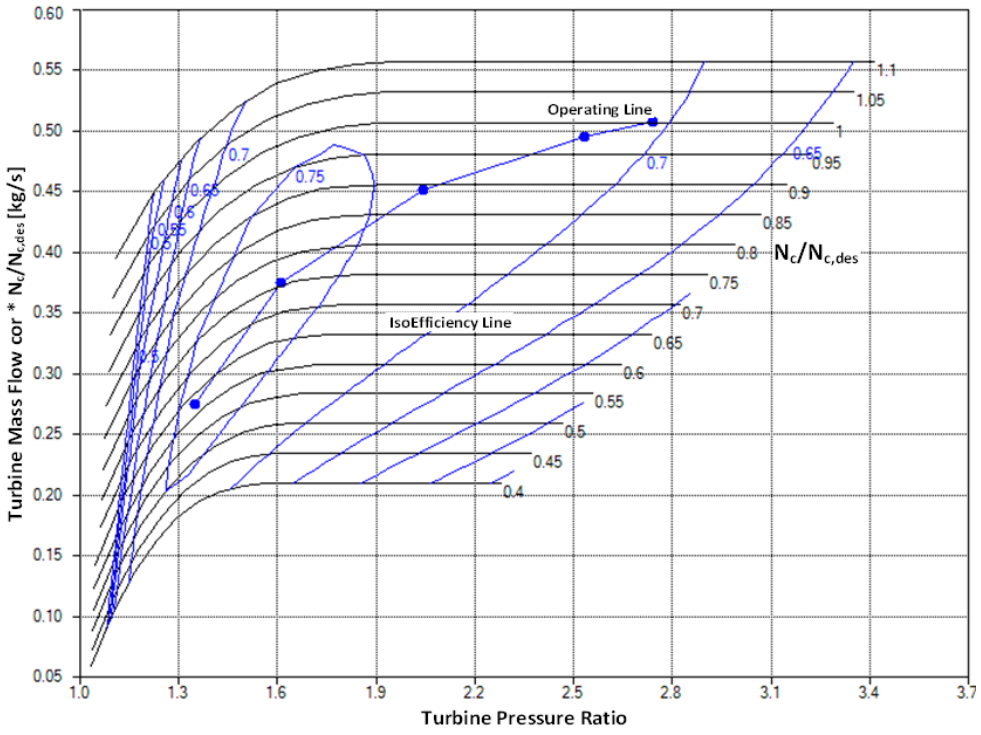

Figure 3-43: Turbine map and operating line.

3.10 Summary and Discussion

In this chapter, the T/Ced diesel engine simulation process was analyzed. Basically, it utilizes 1D sub-models for calculating the turbomachinery components maps and then a fully coupled process integrating the turbomachinery components. An extensive presentation of each sub-model was carried out, including the corresponding theory and correlation.

Additionally, new CC and RT CFD-based surrogate volutes loss models are developed. Comparing CFD-based loss models with the corresponding conventional meanline ones, it is obvious that even they have similar trends, the surrogate ones provide higher accuracy, especially in off design conditions where secondary losses, which are not included in the conventional loss models, increase.

In order to ensure the applicability of the simulation process in capturing the T/Ced diesel engine operation, a verification process was carried out. The verification of the model of each individual component, namely CML, TML and diesel single zone model as well as the entire T/Ced diesel engine was performed and presented. The individual components and the entire engine system verification analysis showed that the current process can simulate the diesel engine throughout its operating envelope.

3.11 References

Ainley, D. G. and Mathieson, G. C. R.,. (1951). A Method Of Performance Estimation For Axial Flow Turbines.

Alexiou, A. and A. Tsalavoutas . (2013). Turbo 3.2 Library Reference Manual. Madrid: Empresarios Agrupados Internacional S.A.

Ansys, Inc. (2011) ANSYS CFX-Solver Theory Guide. Canonsburg, PA 15317.

Aungier, R. H. (2005). TurbineAerodynamics Axial Flow And Radial Inflow Turbine Design And Analysis. ASME PRESS, New York.

Aungier, R.H. (2000). Centrifugal Compressors, A Strategy for Aerodynamic Design and Analysis. ASME PRESS.

Benner, M.W., Sjolander, S.A. and Moustapha, S.H. (1997). Influence of Leading-Edge Geometry Losses in Turbines at Off-Design Incidence: Experimental Results and an Improved Correlation. ASME J. Turbomach. Apr 1997, 119(2): 193-200 (8 pages).

Boyce, M. P. (2003). Centrifugal Compressors, a basic guide. Pennwell Pub.

Chen, S. and Flynn, P. (1965). Development of a Single Cylinder Compression Ignition Research Engine. SAE Technical Paper 650733.

Dambach, R., Hodson, H. P. and Huntsman, I. (1998). An Experimental Study of Tip Clearance Flow in Radial Inflow Turbine. Proceedings of the ASME 1998 International Gas Turbine and Aeroengine Congress and Exhibition. Volume 1: Turbomachinery. Stockholm, Sweden. June 2–5, 1998.

Dunham, J. and Came, P.,M.,. (1970). Improvements to the Ainley-Mathieson Method of Turbine Performance Prediction. Trans. ASME,Journal of Engineering for Power, July, pp. 252–256.

Emara, K., Emara, A. and Razek, E. S. A., "Turbocharger selection and matching criteria in a heavy duty diesel engine." Journal of Scientific & Engineering Research, Vol. 7 No 12 (2016): pp. 609-615.

Fletcher. (1998). Computational Techniques for Fluid Dynamics 1. Springer-Verlag Berlin Heidelberg

Galvas, M.R. (1973.). Fortran program For predicting off design performance of Centrifugal Compressor. TN D-7487. NASA Lewis Research Center, Cleveland, Ohio.

Ghosh, S. K., Sahoo, R. K. and Sarangi, S, K. (2011). Mathematical Analysis for Off-Design Performance of Cryogenic Turboexpander Trans. ASME Journal of Fluids Eng 133(3), p, 031001.

Goudas, A. (2019). Design and Modeling of Printed-Circuit Heat Exhangers and Centrifugal Compressors for Supercritical Carbon Dioxide Power Cycles. PhD Thesis, AUTH.

Heywood, J. B. (1988). Internal combustion engine fundamentals. McGraw-Hill.

Kacker, S. C. and Okapuu, U.,. (1982). A Mean Line Prediction Method for Axial Flow Turbine Efficiency. ASME Journal of Engineering for Power, 104(1): 111-119.

Kolias I, Alexiou A, Aretakis N, Mathioudakis K. (2021) Axial Compressor Mean-Line Analysis: Choking Modelling and Fully-Coupled Integration in Engine Performance Simulations. International Journal of Turbomachinery, Propulsion and Power. 6(1):4.

Meitner, P. L., and Glassman A. J. (1980). Off-Design Performance Loss Model for Radial Turbines With Pivoting, Variable-Area Stators. TP 1708. NASA Lewis Research Center, Cleveland, Ohio.

Menter, F. R. (1992). Improved two-equation k-omega turbulence models for aerodynamic flows, STI/TR, NASA Lewis Research Center, Cleveland, Ohio.

Moustapha, H., Zelesky, M.F., Baines, N.C. and Japikse, D. (2003). Axial and Radial Turbines. Chapters 7-9, Concepts NREC, White River Junction.

Moustapha, S. H., Kacker, S. C., Tremblay, B.,. (1990). An Improved Incidence Losses Prediction Method for Turbine Airfoils. ASME Journal of Turbomachinery, 112(2): 267-276.

Person, J.,. (2015). 1D Turbine Design Tool Validation and Loss Model Comparison: Performance Prediction of a 1-stage Turbine at Different Pressure Ratios, Master of Science Thesis, KTH, School of Industrial Engineering and Management Energy Technology.

Serrano, J. R., Arnau, F.J., De la Morena, J., Gomez-Vilanova, A., Guilain, S. and Batard, S. (2020). A Methodology to calibrate gas-dynamic models of turbocharged petrol engines with variable geometry turbines and with focus on dynamics prediction during tip-in load transient tests. Proceeding of ASME Turbo Expo, GT2020-15169, Virtual online, September 21-25.

Stiesch, G. (2003). Modeling Engine Spray and Combustion Processes. Heat and Mass Transfer. . Springer Berlin Heidelberg, Berlin, Heidelberg.

Stuart, C.,Spence, S.,Filsinger, D., Starke A. and Kim, S. I. (2017). Characterising the influence of impeller exti recirculation on Centrifugal Compressor work input. Proceeding of ASME. GT2017-63047. Charlotte, NC, USA, June 26 - 30.

Stuart, C., Spence, S., Filsinger, D., Starke, A. and Kim S. (2018) A three-zone modelling approach for centrifugal compressor slip factor prediction." Proceeding of ASME Turbo Expo. GT2018-75324. Oslo, Norway, June 11-15.

Walsh, P. P. and P. Fletcher. (2008). Gas Turbine Performance (second edition). Blackwell Science Ltd.

Wang, L. (2005). Support Vector Machines: Theory and Applications. Springer-Verlag Berlin Heidelberg.

Wasserbauer, C. A., Kofskey, M. G. and Nusbaum, W. J. (1966). Cold performance evaluation of a 4.59-inch Radial-Inflow Turbine designed for a Brayton-cycle space power system. NASA TN D-3260, Lewis Research Center, Cleveland Ohio.

Wasserbauer, C.A. and Glassman, A. J. (1975.). Fortran Program for predicting off-design performance of Radial-Inflow Turbines. TN D-8063. NASA Lewis Resedrcb Center, Cleveland, Ohio.

Wiesner, F.J. (1967). A Review of Slip Factors for Centrifugal Impellers. ASME Journal of Eng. Power Vol 89: pp. 558–572.

Zhu, J. and Sjolander, S. A.,. (2005). Improved Profile Loss And Deviation Correlations For Axial Turbine Blade rows. Proceeding of ASME Turbo Expo 2005, GT2005-69077, June 6-9, 2005, Reno-Tahoe, Nevada, USA.

Chapter

4 Automatic Turbocharger design process

In this chapter, the automatic T/C design process is described. It is basically a 1D multi-point design (optimization) process, aiming to provide a fast and reliable solution based on the T/Ced diesel engine operating range. The design process can be performed for each turbo-component individually or for the entire T/C. Additionally, both the static and the modal structural integrity is ensured by utilizing an integrated, simplified structural analysis tool. Dimensionless geometrical parameters are also utilized as optimization variables, for given nominal mass flow, speed and power.

Finally, a CFD CC multi-point design (optimization) option is also provided, producing an improved 3D compressor geometry. It complies with the T/Ced diesel engine range of operation, while its structural integrity is ensured by using a 3D static analysis using Finite Elements.

4.1 General description

The design process focuses on a multi-point T\C operation, with the capability of being adjusted to design or retrofitting requirements for all possible T/C configurations, providing either a T/C component or an entire T/C (re)design solution.

Concerning the T/C component preliminary design, the process follows the next steps:

- Designs a turbo-component, focusing on the entire system improvement.
- Ensures matching quality with the ICE.
- Ensures that the designed turbo-component operates stably (in case of compressor design).
- Ensures the designed turbo-component static structural integrity.
- Ensures the designed turbo-component dynamic structural integrity.

Similar to the partial component design, for the T/C design, the process:

- Designs a T/C , focusing on the entire system improvement.
- Ensures the matching quality with the ICE.
- Ensures that the designed compressor operates stably.
- Ensures static/dynamic structural integrity for both designed components.
- Chooses the best fitted T/C configuration

Regarding the T/C possible configurations, these are the following:

a) Vaneless Diffuser Centrifugal Compressor – Radial Turbine
b) Vaned Diffuser Centrifugal Compressor – Radial Turbine
c) Vaneless Diffuser Centrifugal Compressor – Axial Turbine
d) Vaned Diffuser Centrifugal Compressor – Axial Turbine

4.2 Automatic Turbocharger Multi-point preliminary Design process

A general flow chart of the multi-point design process is illustrated in Figure 4-1. According to this, when an engine model is available, an iterative process is performed between T/C and the diesel engine, in order to correct the design mass flow, speed and power. The current process is utilized for designing either specific T/C configuration or all four possible ones, in order the user to be able to choose the most suitable one among them.

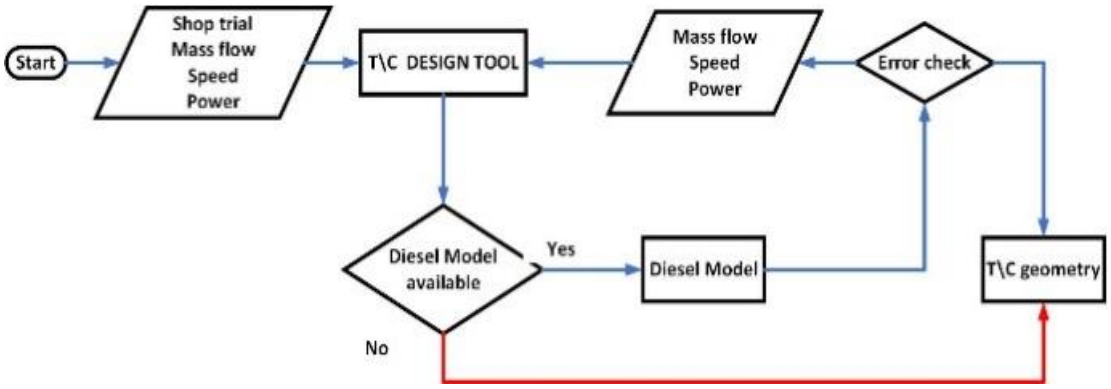

Figure 4-1: Automatic Turbocharger preliminary design tool.

The process consists of two component sub-tools(Figure 4-2), one for each turbo-component (compressor or turbine). Each design sub tool, combining a preprocessor (reverse problem model) and a meanline model, allows the use of dimensionless parameters(e.g. Table 4-1) instead of dimensional ones(e.g. Table 3-2) as optimization variables. This technique provides a more general and

automated design process, since there is no need of redefining both the range of the design variables and the initial geometry for different T/C scale.

The process also, integrating a simplified structural analysis(static, modal) tool, ensures that the designed T/C will operate structurally safe. Additionally, utilizing an embedded 1D to 3D transformation sub-tool, the preliminary 1D geometry can be transformed into a 3D one, hence providing a fast retrofit-design solution. Finally, a high fidelity design option is also provided, applying a CFD-FEA optimization process, using the preliminary design geometry as the initial one.

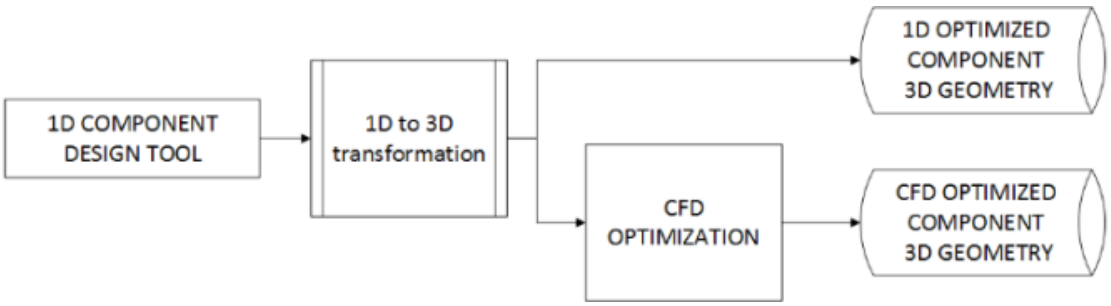

Figure 4-2: Component design process sub-tools.

In this PhD thesis, the 3D design process is limited only on centrifugal compressor 3D design (original turbine is retained), presented in the section 4.6.

4.2.1 Turbo-component preliminary Multi-point Design process

The T/C component design process, follows a weighted single objective optimization procedure to (re)design the turbo-component in order to match the entire system in an optimal way.

For automating the optimization process, constant variable ranges are imposed to satisfy every component performance requirement, while the initialization is performed using random values from the defined ranges. The usage of dimensionless parameters is achieved by coupling a typical component 1D mean line model, presented in Chapter 3, with a pre-processor, capable of transforming dimensionless parameters into geometry as explained in the section 4.3. This transformation is accomplished by using component mass flow, speed and power as input data. Note that the process also checks that there is no overlapping between the volute and the impeller volumes, by automatically setting an upper limit in volute volume in every optimization cycle.

In case of no available engine model, the design process focuses on maximizing turbo-component efficiency,

$$max: z = \frac{\sum hr_i \, \eta_i}{\sum hr_i} \tag{4.1}$$

where hr_i is the engine operating hours and η_i the turbo-component efficiency that corresponds to each operating point i. All the weight factors ($hr_i / \sum hr_i$) are user defined. Regarding the optimization constraints, they are appropriately selected in order to make the new component, manufacturable and functional.

For ensuring component static structural integrity, its maximum tensile stress (σ_{max}) at the highest compressor speed operating point must not exceed the yield stress by a given safety factor (see section 4.4.2). Concerning the dynamic structural integrity, the turbo spool vibration should be stable with the eigenfrequency as function of the rotating speed for the first two modes, not crossing the synchronous frequency curve, hence avoiding resonance operation(see section 4.4.4). Finally, for providing a manufacturable, by a CNC machine, design solution, the blade thickness must be greater than a given minimum value.

In case of a compressor design, it must operate in the stable region with an acceptable stall margin(eq. (3.312)) while its volute pressure recovery must be greater than 0.21 according to Ceyrowsky et al. (2018). For the present work, the CC and RT volutes are set as semi-external and external, respectively. About the stall margin constraint, as the performance map generation is not required, the stall index, presented in section 3.4.7, is utilized.

Regarding the selected design points, one operating point is chosen as a nominal point and the rest of them as base points. During the turbine design, the operating points which correspond to lower T/C speed than the nominal one (including the nominal) are checked as unchoked (mandatory operation in unchoked region), while the ones with higher rotational speed are checked as free (can operate either in choked or unchoked region).

The Figure 4-3 shows the structure of the turbo-component 1D design procedure. In each optimization cycle, a component is generated to satisfy the performance conditions ($\dot{m}$, N, Pwr_{cmp}), required by the diesel engine at nominal operating point. Component efficiency is also evaluated.

Then, having a component geometry, the off design analysis is performed for each rotational speed, according to the shop trial data for all the selected base points, in order to calculate both the efficiency and the performance conditions. Having the performance data from the shop trials, the error between the calculated and the given ones must not exceed a certain tolerance.

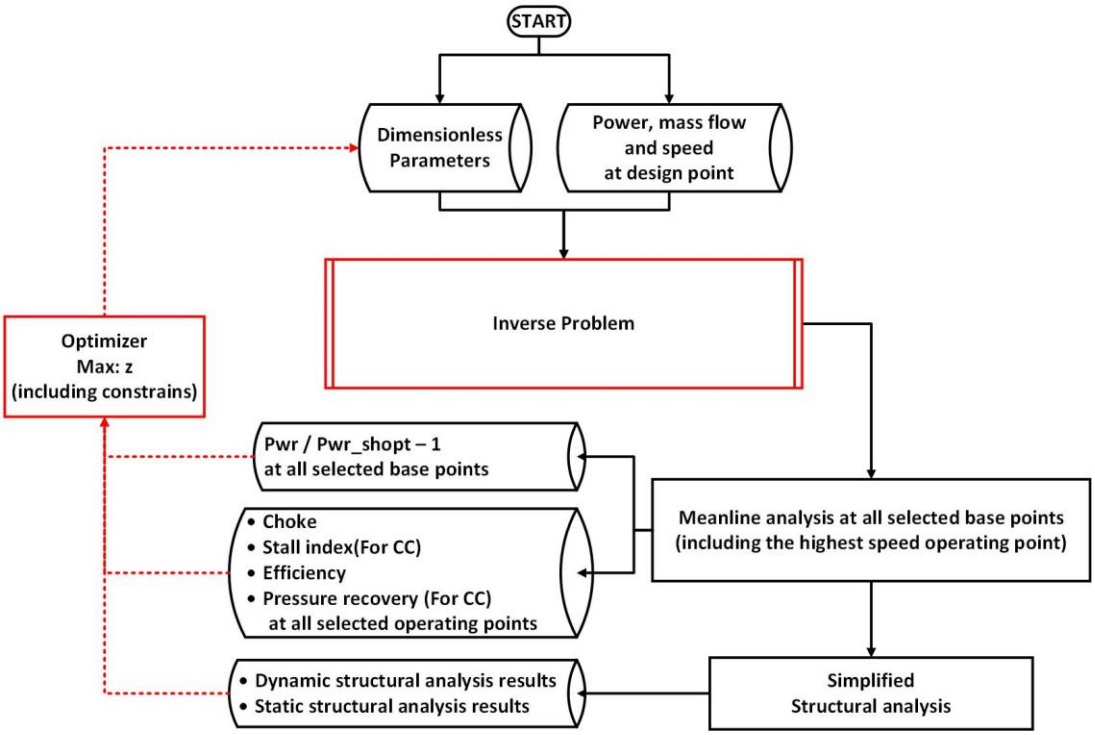

Figure 4-3: Turbo-component 1D design flow chart (no available Diesel Engine model)

In case of an available engine model, the process focuses on minimizing the annual average fuel consumption of the diesel engine, thus the objective function is expressed as:

$$min: z = \frac{\sum hr_i \, \dot{m}_{fuel,i}}{\sum hr_i} \tag{4.2}$$

where hr_i is the engine operating hours and $\dot{m}_{fuel,i}$ the fuel consumption that corresponds to each operating point i. All the weight factors ($hr_i / \sum hr_i$) are user defined. Regarding the optimization constraints, they are the same with the "no available diesel engine model" case. Additionally, as the engine model is available, the constraints, presented in 3.8, are also taken into consideration, for ensuring the matching quality between the turbocharging system and the engine.

Considering the T/C component design process with an available diesel engine model, the Figure 4-4 depicts a compressor design process flow chart. Regarding the turbine design, the procedure is similar, with the compressor inverse problem tool been replaced with the compressor performance map and the turbine map been replaced with the turbine inverse problem.

In each optimization cycle, it designs a component to satisfy the given performance conditions ($\dot{m}$, N, Pwr_{cmp}) required by the diesel engine. Having generated the component geometry, an off design analysis is performed, generating the corresponding performance map. Combining then, both the generated and the pre-existing(from the baseline component that is not designed) maps with diesel model, the new T/C performance conditions are re-

computed. This internal iterative process stops when a tolerance value is achieved.

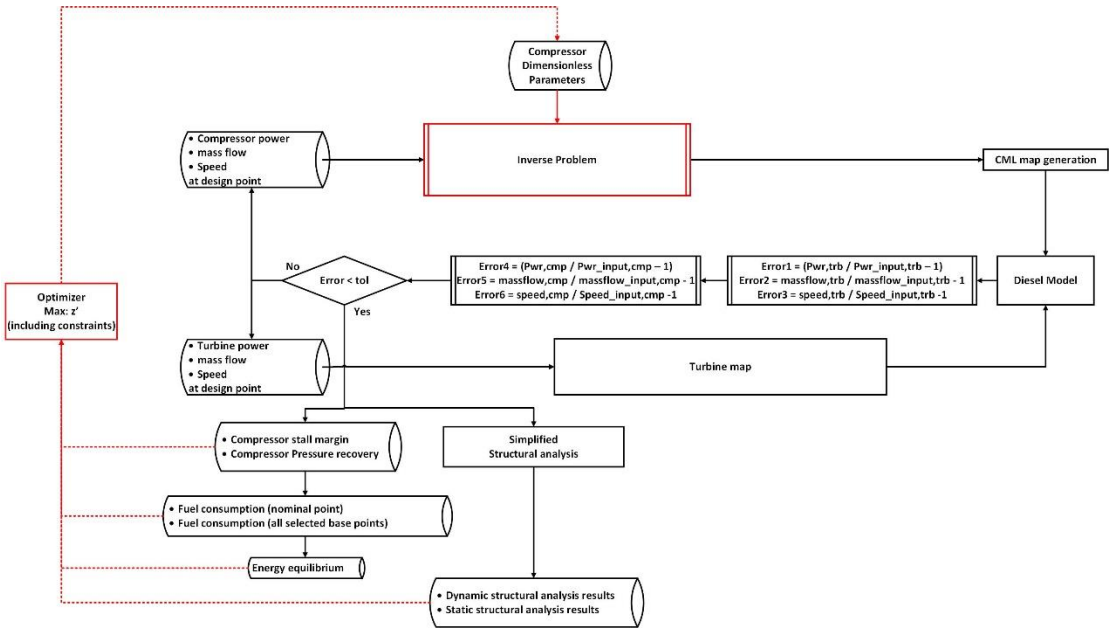

Figure 4-4: Compressor design process flow chart (available Diesel Engine model).

4.2.2 Entire Turbocharger Multi-point Design process

About the T/C design process, it follows an optimization procedure, designing both turbo-components in order to match the entire system in an improved way.

Similarly to the turbo-component design process, constant variable ranges are imposed to satisfy every component performance requirement, while the initialization is performed using random values from the ranges chosen.

In case of no available diesel engine model, the design process focuses on maximizing T/C efficiency,

$$min: z = \frac{\sum hr_i \, \eta_{tc,i}}{\sum hr_i} \tag{4.3}$$

Regarding the optimization constraints, are the same with the no available diesel engine T/C component geometry optimization process.

In case of an available diesel engine model, the process is similar to the available diesel engine T/C component design process. The main difference is that there is no pre-existing map, hence the process consists of two preprocessors (inverse problem models), one for each turbo-component.

Concerning the T/C design process, the Figure 4-5 shows a T/C design process flow chart. In each optimization cycle, it designs a T/C(compressor and turbine pair) to satisfy the given performance conditions ($\dot{m}$, N, $\mathrm{Pwr_{cmp}}$) required by diesel engine.

Having generated both geometries(compressor and turbine), an off design analysis is carried out, generating both performance maps. Then, combining both maps with the diesel model, the new T/C performance conditions are re-computed. This internal iterative process stops when a tolerance value is achieved.

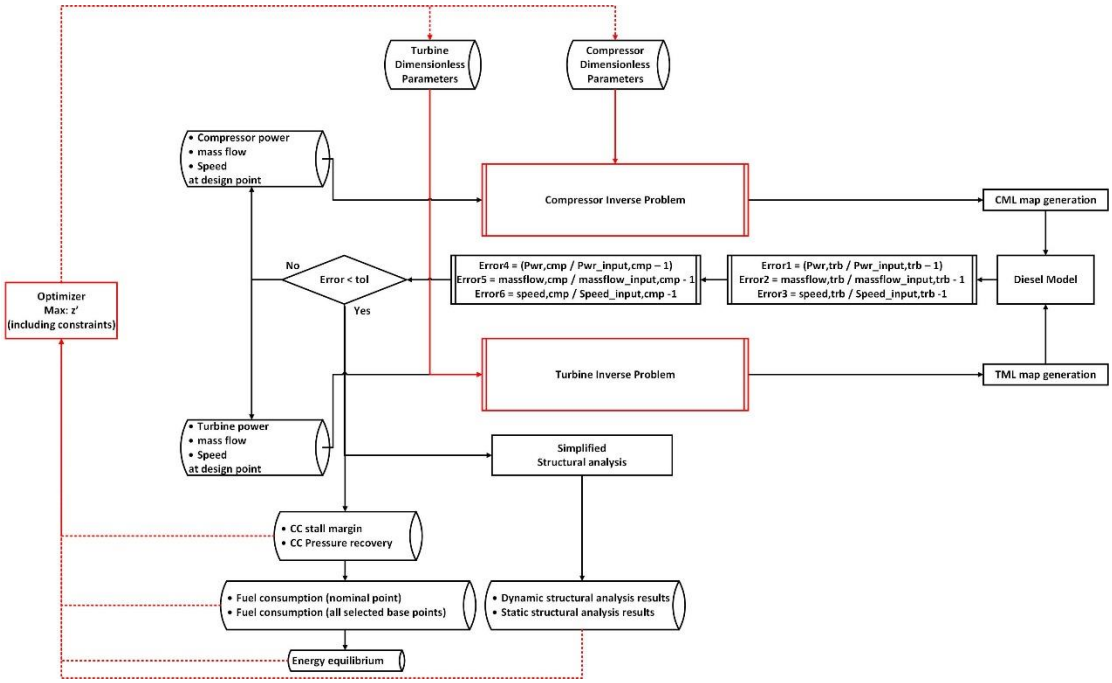

Figure 4-5: T/C design process overall flow chart (available Diesel Engine model).

4.2.3 Optimization method

For the optimization process, a commercial optimization tool[1] is utilized. Even if the optimization method is user defined, for the current study, the adaptive simulated annealing (ASA) method is selected.

Both Li et al. (2015) and Tang et al. (2019), aiming to design a centrifugal compressor via 1D geometrical parameters optimization, similarly to the one conducted in the present thesis [1], chose ASA method, as a suitable method for turbo-components geometry optimization.

4.3 Turbo-components Dimensionless Variables

As described in section 4.2, aiming to develop a more general optimization process (independent of the T/C scale), constant variables ranges are imposed in order to satisfy every component performance requirement, while the

[1] Isight & SIMULIATM Execution Engine - Dassault Systèmes®." [Online]. Available: https://www.3ds.com/products-services/simulia/products/isight-simulia-execution-engine/

initialization can be performed using random values with respect to the defined rages.

The ranges have been defined by both examining a number of available T/C geometries, provided by T/C manufacturing company[1], and collecting-analyzing geometrical data from public literature (e.g. Japikse (1996), Japikse and Baines (1997)).

4.3.1 Centrifugal Compressor dimensionless variables and inverse problem

A typical layout of a CC inverse problem is shown in Figure 4-6, showing the coupling of both compressor 1D mean line model and pre-processor, in order to transform dimensionless parameters into geometry.

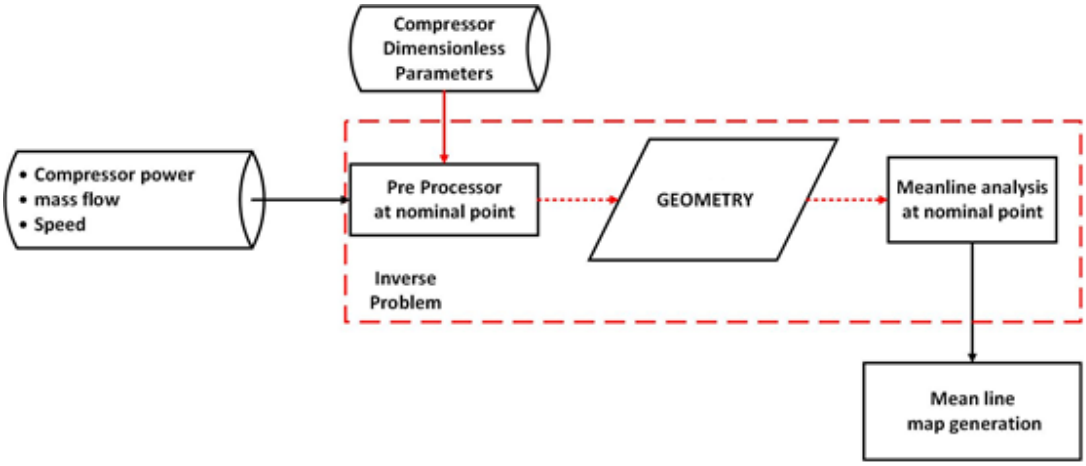

Figure 4-6: Centrifugal Compressor inverse problem model.

This transformation is accomplished by using compressor mass flow, speed and power as input data. Thus, the compressor dimensionless geometrical parameters, including their defined ranges, are presented in Table 4-1 and Table 4-2, while the output data, required by the meanline model, are depicted in both Table 3-2 and Table 3-3. Note that the clearance ratio is set equal to 0.8% as typical value and the dimensionless splitter position equal to 0.5 as the compressor used in CC meanline model validation case, presented in Chapter 3.

Table 4-1: Vaneless CC Dimensionless geometrical input parameters.

Parameter	Range	Parameter	Range
inc	(-10,10°)	B_3	(0,0.3)
$\beta_{b,3}$	(0,70)	AR_{vnl}	>1.15
M_1	(0.1,0.9)	AR_{vol}	>0
φ_3	(0.1,0.5)	$Z_{b,main}$	(6,40)
B_1	(0,0.3)	$R_{hub,1}/R_{tip,1}$	(0.25,0.70)

[1] www.turbomed.gr

Table 4-2: Vaned CC Dimensionless geometrical input parameters.

Parameter	Range	Parameter	Range
inc	(-10,10°)	B_3	(0,0.3)
$\beta_{b,3}$	(0,70)	AR_{vnl}	>1.15
M_1	(0.1,0.9)	AR_{vol}	>0
φ_3	(0.1,0.5)	$Z_{b,main}$	(6,40)
B_1	(0,0.3)	$R_{hub,1}/R_{tip,1}$	(0.25,0.70)
$\beta_{v,4}$	(0,90°)	B_4	(0,0.3)
$\beta_{v,5}$	(0,70)	B_5	(0,0.3)
Z_v	(6,40)	AR_{vnd}	>1.15

For transforming the compressor dimensionless geometrical parameters into geometry, the mass flow ($\dot{m}$), the external power (Pwr_{turb}) and the speed (N) are required.

First, having established the external power, the compressor one is defined as:

$$Pwr_{cmp} = Pwr_{trb}\, n_m \tag{4.4}$$

where the turbo cartridge mechanical efficiency (n_m) is set equal to 95%.

The inlet area is calculated via the continuity equation in terms of the inlet Mach number, the given mass flow and the inlet total conditions.

Then, the inlet geometrical parameters are computed for a given hub to tip ratio:

$$D_{hub,1} = 2\sqrt{\frac{A_1}{\pi\left(\frac{1}{\mathrm{R_{hub,1}/R_{tip,1}}}\right)^2 - \pi}} \tag{4.5}$$

$$D_{tip,1} = \frac{D_{hub,1}}{\mathrm{R_{hub,1}/R_{tip,1}}} \tag{4.6}$$

Regarding the blade angle, it is calculated in terms of both the given incidence angle(inc) and the relative flow angle(β_1)

$$\beta_{b,1} = \beta_1 - inc \tag{4.7}$$

where the relative flow angle is estimated from the corresponding velocity triangle.

In next step, the impeller outlet total temperature is calculated in terms of both the inlet total enthalpy and the compressor power:

$$h_{t,1} = h\left(T_{t,1}\right), h_{t,3} = \frac{Pwr_{cmp}}{\dot{m}_{cmp}} + h_{t,1}\,, T_{t,3} = \mathrm{T}(h_{t,3}) \tag{4.8}$$

Guessing then, an impeller outlet blade velocity (U_3), the outlet total temperature is re-calculated as:

$$h_{t,1,\mathrm{r}} = h\left(T_{t,1,r}\right), h_{t,3,\mathrm{r}} = h_{t,1,\mathrm{r}} + \frac{U_3^2 - U_1^2}{2}\,, T_{t,3,\mathrm{r}} = T(h_{t,3,\mathrm{r}}) \tag{4.9}$$

$$V_{m,3} = \varphi_3\, U_3 \tag{4.10}$$

$$V_{u,3,id} = U_3 - V_{m,3} \tan \beta_{b,3} \tag{4.11}$$

$$V_{u,3} = V_{u,3,id}\, \sigma \tag{4.12}$$

$$h_{t,3} = V_{u,3}\, U_3 \tag{4.13}$$

where the outlet flow coefficient (φ_3) belongs to the given input data and the slip factor (σ) is calculated regarding the eq. (3.45)-(3.48).

Given that, the total enthalpy at exit ($h_{t,3}$) is established by eq. (4.8), an iterative process is carried out between eq (4.9) and (4.13) for predicting the (U_3), until the error between both calculated total enthalpies, reaches a tollerance value.

Considering the initial impeller outlet meridional velocity, it can be defined as:

$$U_{3,init} = \sqrt{\frac{\mathrm{h_{t,3}}}{1 - \varphi_3 \tan \beta_{b,3}}} \tag{4.14}$$

Also, the impeller axial length can be calculated according to Goudas (2019).

$$L_{axial} = D_3 \left(0.014 + 0.023 \frac{D_3}{D_{tip,3}} + 1.58\, \varphi_3\right) \tag{4.15}$$

Regarding the blade height (b_3), it is calculated as:

$$b_3 = \frac{A_3}{\pi\, D_3\, B_3} \tag{4.16}$$

where the outlet area(A_3) is computed based on the procedure presented in section 3.4.2 for a given mass flow.

About the impeller blades thickness at leading and trailing edge, they can be expressed as:

$$t_1 = B_1 \frac{\left(D_{tip,1} + \mathrm{D_{hub,1}}\right) \pi}{2\, Z_{MB} \cos \beta_{b,1}} \tag{4.17}$$

$$t_3 = B_3 \frac{D_3\, \pi}{2\, Z_{FB} \cos \beta_{b,3}} \tag{4.18}$$

Then assuming that the diffuser channel width is constant across the vaneless/vaned diffuser, the corresponding diffuser outlet diameters are expressed as:

$$D_4 = AR_{vnl}\, D_3 \tag{4.19}$$

$$D_5 = \begin{cases} D_4 & , \quad Vnlss\ Diffuser\ CC \\ AR_{vnd}\, D_4 & , \quad Vnd\ Diffuser\ CC \end{cases} \tag{4.20}$$

4.3.2 Radial Turbine dimensionless variables

Similarly to the CC inverse problem, for the RT one, the usage of dimensionless parameters is achieved by coupling a typical 1D mean line model with a pre-processor, capable of transforming dimensionless parameters into geometry.

Concerning the RT dimensionless geometrical parameters and their defined ranges, they are presented in Table 4-3, while the output data, required by the meanline model, are depicted in Table 3-4.

Table 4-3: RT Dimensionless geometrical input parameters.

Parameter	Range	Parameter	Range
M_1	(0.1,0.9)	AR_{vol}	>0
AR_{vnd}	1.58	b_2/D_2	(0.01,0.5)
$\beta_{v,2}$	(0,90°)	B_2	(0,0.3)
$\beta_{v,3}$	(0,90°)	B_3	(0,0.3)
$\beta_{b,4}$	=0°	B_4	(0,0.3)
$\beta_{b,5}$	(0,90°)	B_5	(0,0.3)
L_{axial}/D_4	(0.05,0.7)	AR_{vnl}	=1.15
Z_b	(6,40)	Z_v	(6,40)
$R_{hub,5}/R_{tip,5}$	(0.25,0.70)		

Considering the inverse problem procedure, the following equations describe how the RT geometry is generated based on a given dimensionless parameters.

At first, having known the volute inlet Mach number, the inlet absolute velocity and the inlet area are computed according to the continuity equation.

Then, both the inlet volute diameter(D_{vol}) and the inlet/outlet volute diameters from the rotating axis (D_1,D_2) are computed in terms of a given volute aspect ratio and the predicted inlet area(A_1).

Then, using the dimentionless parameter (b_2/D_2), the inlet vaned nozzle width is also calculated. Also, it is selected a constant width across nozzle and equal to the impeller inlet blade height:

$$b_2 = b_3 = b_4 \tag{4.21}$$

As for both the vaned and the vaneless nozzles, their geometrical dimensional parameters can be defined as:

$$A_2 = \pi b_2 D_2 \tag{4.22}$$

$$t_2 = \frac{A_2\ B_2}{b_2 \cos\beta_{b,2}\ Z_v} \tag{4.23}$$

$$D_3 = \frac{b_2 D_2}{b_3}\frac{1}{AR_{vnd}} \tag{4.24}$$

$$A_3 = \pi b_3 D_3\ (1 - B_3) \tag{4.25}$$

$$t_3 = \frac{\pi b_3 D_3 B_3}{b_3 \cos\beta_{b,3}\ Z_v} \tag{4.26}$$

$$D_4 = \frac{b_3 D_3}{b_4}\frac{1}{AR_{vnl}} \tag{4.27}$$

Both the vaneless and vaned nozzle flow and performance conditions, required for the next computations, are calculated, according to the process, presented in section 3.5.2, imposing the above predicted geometrical parameters.

In next step, the impeller inlet geometrical dimensional parameters are calculated as:

$$A_4 = \pi b_4 D_4 \tag{4.28}$$

$$t_4 = \frac{A_4\ B_4}{b_4 Z_b \cos\beta_{b,4}} \tag{4.29}$$

$$L_{axial} = D_4(\mathrm{L_{axial}}/D_4) \tag{4.30}$$

The relative conditions and the velocity components in impeller inlet, required for the next calculations, are predicted based on the methodology presented in section 3.5.2, as the impeller inlet geometry was established.

Then, having known the turbine output power, the impeller outlet enthalpy is established as:

$$h_{t,5} = h_{t,4} - \frac{Pwr_{trb}}{\dot{m}_{trb}} \, , T_{t,5} = T\left(h_{t,5}\right) \tag{4.31}$$

Guessing then an initial impeller outlet meridional velocity ($V_{m,5}$), the impeller outlet conditions are calculated, following an iterative process. First the velocity components in relative frame are calculated from the corresponding velocity triangle, in terms of both the meridional velocity and the relative outflow angle.

Concerning the outflow relative angle(β_3), if the selected outlet flow model is the one presented by Wasserbauer and Glassman (1975) (eq. (3.166)) then the outflow relative angle is equal to the outlet blade angle. If the Aungier (2005) model (eq. (3.167)) is used, then, because it depends on both the hub and the tip radius, the outflow relative angle is set equal to the blade angle at the beginning of the iterative process and is updated after the hub and tip radii are established.

Then guessing an initial outlet blade speed, both the outflow angle and the outlet velocity are computed from the corresponding velocity triangle, in terms of the blade speed, the meridional velocity and the relative circumferential velocity.

Next the outlet total enthalpy is re-calculated as:

$$h_{t,5} = h_{s,5} + \frac{1}{2} V_5^2 \tag{4.32}$$

where,

$$h_{s,5} = \left[h_{t,1,r} + (U_5^2 - U_4^2)\right] - \frac{1}{2} W_5^2 \tag{4.33}$$

Given that, the total enthalpy at exit ($h_{t,5}$) is established by eq. (4.31) and re-calculated by eq.(4.33), an iterative process is carried out for predicting the outlet blade speed(U_5), until the error between both calculated total enthalpies, reaches a tollerance value. Regarding the initial outlet blade speed, it is set equal to the square of the turbine specific power.

Having enstablished the blade speed, the rest of the required impeller outlet geometrical dimensional parameters are calculated for a given hub to tip ratio:

$$D_{tip,5} = \frac{60\, U_5}{\pi N} \sqrt{\frac{2}{1 + \left(R_{hub,6}/R_{tip,6}\right)^2}} \tag{4.34}$$

$$D_{hub,5} = D_{tip,5} \left(R_{hub,5}/R_{tip,5}\right) \tag{4.35}$$

$$A_5 = (1 - B_5)\, \pi \, \frac{D_{tip,5}^2 - D_{hub,5}^2}{2} \tag{4.36}$$

$$t_5 = \frac{\pi \frac{D_{tip,5}^2 - D_{hub,5}^2}{2} B_5}{\frac{\left(R_{tip,5} - R_{hub,5}\right)}{2} \cos \beta_{b,5}} \tag{4.37}$$

Having determined the impeller outlet geometry, the eq. (3.154) - (3.156) are applied, for calculating the outlet mass flow. Given that, the mass flow is user-defined, an iterative process is carried out between eq. (4.32) and (4.37), until the error between the calculated and the given mass flow reaches a tollerance value.

Considering the initial impeller outlet meridional velocity, it can be defined as:

$$V_{m,5,initial} = \frac{\sqrt{\frac{Pwr_{trb}}{\dot{m}_{trb}}}}{tan\, \beta_{b,5}} \tag{4.38}$$

4.3.3 Axial Turbine dimensionless variables

Similar to the CC inverse problem, for the AT one, the usage of dimensionless parameters is achieved by coupling a typical 1D mean line model with a pre-processor, capable of transforming dimensionless parameters into geometry.

Concerning the AT dimensionless geometrical parameters and their defined ranges, they are presented in Table 4-4, while the output data, required by the meanline model, are depicted in Table 3-9. In contrast to both CC and RT preprocessors, apart from the turbine speed, the mass flow and the output power, the output power distribution across turbine stages and the number of stages should be also provided. Note that the stator inlet Mach number ($M_{1,S}$) and flow angle ($a_{1,S}$) input data are used only for the first stage.

Table 4-4: AT Dimensionless geometrical input parameters.

Parameter	Range	Parameter	Range
e_R/c_R	(1.5,6)	$R_{hub,1,S}/R_{tip,1,S}$	(0.25,0.70)
e_S/c_S	(1.5,6)	$R_{hub,2,S}/R_{tip,2,S}$	(0.25,0.70)
t_S/c_S	(0.05,0.98)	$R_{hub,1,R}/R_{tip,1,R}$	(0.25,0.70)
t_R/c_R	(0.05,0.98)	$R_{hub,2,R}/R_{tip,2,R}$	(0.25,0.70)
x_S/c_S	(0.05,0.98)	Z_R	(10,50)
x_R/c_R	(0.05,0.98)	Z_S	(10,50)
$\beta_{b,1,S}$	(0,90°)	$B_{1,S}$	(0,0.3)
$\beta_{b,2,S}$	(0,90°)	$B_{2,S}$	(0,0.3)
$\beta_{b,1,R}$	(0,90°)	$B_{1,R}$	(0,0.3)
$\beta_{b,2,R}$	(0,90°)	$B_{2,R}$	(0,0.3)
$M_{1,S}$[1]	(0.1,0.9)	$\alpha_{1,S}$[1]	= 0

[1] Used in the first stage only

Setting the turbine output power distribution across turbine stages and the number of stages, the corresponding stage output power can be defined as:

$$Pwr_{trb,J} = X_{pwr,J}\, Pwr_{trb}\ ,\ \ X_{pwr,J} \geq 0\ and\ \sum X_{pwr,J} = 1 \tag{4.39}$$

where the parameter $X_{pwr,J}$ refers to the percentage of output power that the stage contributes to the total one. It is important to note that the preprocessor procedure, presented below is repeated for each stage. Additionally, the inlet Mach number and the inlet flow angle are given as input data ($M_{1,S}[1]$, $\alpha_{1,S}[1]$).

Regarding the stator geometry calculations, in the first step, knowing the cascade inlet Mach number and flow angle, the inlet area is predicted via the continuity equation.

Next, the inlet geometrical dimensional parameters can be computed for a given hub to tip ratio:

$$D_{hub,1} = 2\ \sqrt{\frac{A_1}{\pi \dfrac{1}{\left(R_{hub,1}/R_{tip,1}\right)^2} - \pi}} \tag{4.40}$$

$$D_{tip,1} = \frac{D_{hub,1}}{\left(R_{hub,1}/R_{tip,1}\right)} \tag{4.41}$$

$$t_{le} = \frac{\pi \dfrac{D_{tip,1}^2 - D_{hub,1}^2}{4} B_1}{Z \cos \beta_{b,1}} \tag{4.42}$$

$$D_{ref,1} = \frac{D_{tip,1} + D_{hub,1}}{2} \tag{4.43}$$

For establishing the stator outlet station geometry, the user should select between constant hub, mid or tip radius across stator. In the current analysis, the constant mid diameter is selected as it is more common in T/C axial turbines (Figure 3-20). Thus,

$$D_{ref,2} = D_{ref,1} \tag{4.44}$$

$$D_{hub,2} = \frac{2\ D_{ref,2}\left(R_{hub,2}/R_{tip,2}\right)}{1 + \left(R_{hub,2}/R_{tip,2}\right)} \tag{4.45}$$

$$D_{tip,2} = 2\, D_{ref,2} - D_{hub,2} \tag{4.46}$$

$$A_2 = \pi \frac{D_{tip,2}^2 - D_{hub,2}^2}{4}(1 - B_2) \tag{4.47}$$

$$t_e = \frac{\pi \frac{D_{tip,2}^2 - D_{hub,2}^2}{4} B_2}{Z \cos \beta_{b,2}} \tag{4.48}$$

For calculating the rotor geometry, the stator outlet flow conditions should be predicted(section 3.6.2). Having established both the inlet flow conditions and the stator geometry, the calculation process that are followed, is described in section 3.6.2.

Regarding the rotor geometry calculations, the rotor inlet geometrical parameters are calculated in the same way with the stator ones, using as input both the stator outlet Mach number and the flow angle. Having established the rotor geometry in the inlet station, the flow and the performance conditions in both the stationary and the relative frame, required for the following calculations, are predicted based on the procedure, presented in section 3.6.2.

Having determined the stage output power, the outlet enthalpy can be expressed as:

$$h_{t,2} = h_{t,1} - \frac{Pwr_{trb,J}}{\dot{m}_{trb}} \tag{4.49}$$

Concerning the reference diameter calculation, an iterative process is performed by providing an initial rotor blade speed(U_2) value,

$$h_{t,r,2} = h_{t,r,1} + \frac{U_2^2 - U_1^2}{2}, T_{t,r,2} = T(h_{t,r,2}) \tag{4.50}$$

$$D_{ref,2} = \frac{60\ U_2}{\pi\ N} \tag{4.51}$$

Having computed the outlet mid diameter, the remaining of the outlet blade geometrical parameters are calculated based on equations (4.45)-(4.48). Then, having established the entire rotor geometry, the rotor outlet mass flow is predicted based on the procedure presented in section 3.6.2.

Given that, the outlet mass flow is user-defined, the calculations, started from eq. (4.50), are repeated until the error between the calculated and the given mass flow reaches a tolerance value. Regarding the outlet initial blade speed, it is set equal to the inlet one.

4.4 Simplified Structural Analysis

For ensuring static and dynamic structural integrity, a simplified structural tool is developed in the frame of this PhD thesis, consisting of two modes of operation, aiming to perform both static and modal analysis.

4.4.1 Turbocharger turbo-components material

Generally, the most common material for T/C compressor impeller has been aluminum alloys. The nickel alloy and titanium material also studied by many researchers towards its implementation in impeller of the turbochargers. Additionally, various composite materials also developed and analyzed for matching the specific properties, required by the impeller, aiming to provide a more lightweight option.

Considering, the T/C axial turbine, the nozzle ring is where the energy in the exhaust gas is converted into kinetic energy. It is fabricated from a creep resistant chromium nickel alloy, heat resisting moly-chrome nickel steel or a nimonic alloy which will withstand the high temperatures and be resistant to corrosion. Similarly, turbine blades are usually made of nickel chrome alloy or nimonic material[1] (a nickel alloy containing chrome, titanium, aluminium, molybdenum and tungsten) due to their good resistance to creep, fatigue and corrosion.

Concerning T/C radial turbine material, according to Shettigar and Pesiridis (2014), high grade stainless steels are used for both impeller and vaned nozzle. Additionally, super alloys and high temperature alloys are suitable candidates as exhibit excellent mechanical strength, creep resistance, corrosion and oxidation resistance and surface stability at high temperature where the base alloy element is nickel, Cobalt or Nickel Iron. As for compressor impeller material choice, aluminum alloy or the more expensive titanium are used.

For the current analysis, typical aluminum alloy is chosen for the centrifugal compressor, while for both the axial and radial turbines the user can select between the following materials:

- Stainless steel 304, 309, 316, 430
- Nimonic Alloy 75, 81.

It is assumed that the T/C shaft has the same material with the Turbine.

4.4.2 Static Structural Analysis

The static structural analysis is based on the evaluation of two kinds of stresses, centrifugal forces and blade bending. The Centrifugal load introduces normal stresses due to tensile and blade bending as it is depicted in Figure 4-7. The pressure distribution is also taken into account in bending moment calculation(Figure 4-8), even if its effect on bending normal stress is lower than that of centrifugal loading.

[1] http://www.marinediesels.info/Turbocharging/turbocharger_principles.htm

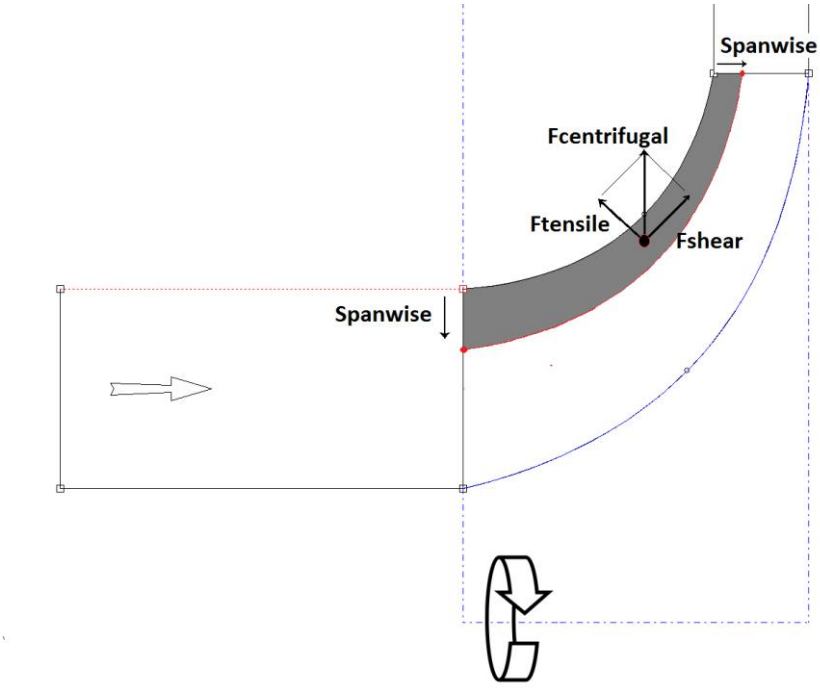

Figure 4-7: Impeller Centrifugal force.

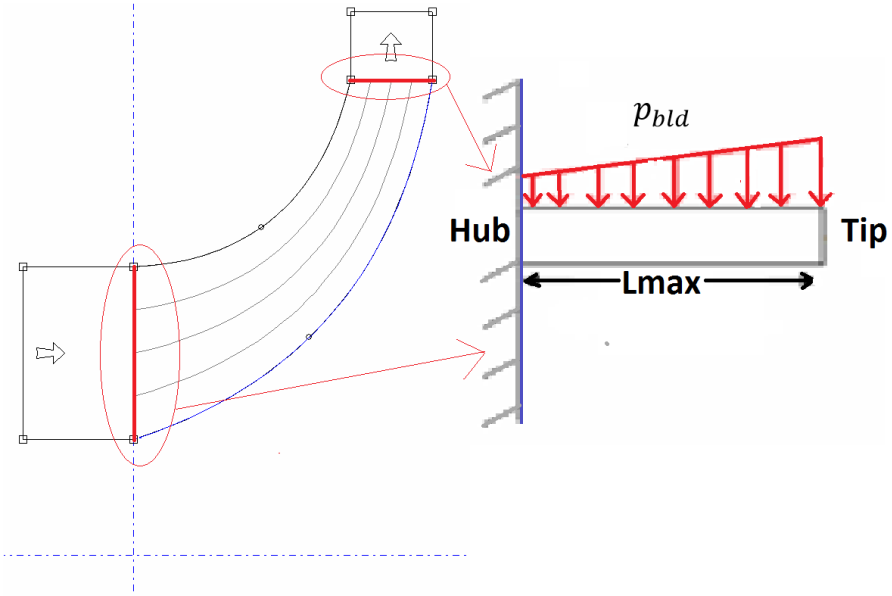

Figure 4-8: Impeller Pressure distribution load.

For centrifugal compressor and radial turbine wheels the introduced stresses are the following:

- Tensile stresses:
  - ✓ Centrifugal Force.
- Blade bending stresses:
  - ✓ Centrifugal Force.
  - ✓ Pressure Distribution.

while for the axial turbine wheel, the introduced stresses are the following:

- Tensile stresses:
  - ✓ Centrifugal Force.
- Blade bending stresses:
  - ✓ Pressure Distribution.

In axial impellers (in contrast to radial ones), the centrifugal load introduces normal stresses only due to tensile, as hub surface is almost parallel to rotational axis. The stationary components such as the vaned diffuser and axial stator are subjected only to blade bending due to pressure distribution, as centrifugal load is zero.

For generating a turbomachinery sub-component 3D geometry(impeller, axial stator, etc.) using the 1D analysis geometrical dimensional parameters, a 1D to 3D geometry tool is developed in the context of the present work.

The transformation process follows a turbomachinery sub-component blade angle/thickness adaptation approach, based on known 3D geometries. The correlations of the adaptation technique are presented below.

$$k_1(S) = \frac{f(S)}{f(0)}\, g_{le} \tag{4.52}$$

$$k_2(S) = \frac{f(S)}{f(1)}\, g_{te} \tag{4.53}$$

$$g(\mathrm{M}) = \begin{cases} \mathrm{k_1(S)} & , \quad \mathrm{S} = 0 \\ \mathrm{S\, k_1(S) + (1-S)\, k_2(S)} & , \quad \mathrm{S} = (0,1) \\ \mathrm{k_2(S)} & , \quad \mathrm{S} = 1 \end{cases} \tag{4.54}$$

The parameter S is the dimensionless distance between blade leading and trailing edge, thus, for leading edge is equal to zero and for trailing edge is equal to one. The f function is the corresponding known blade data, thus, it represents both the angle $\left(\beta_b(S)\right)$ and thickness $\left(t_b(S)\right)$ in function of dimensionless streamwise position, shown in Table 4-5, for each blade position while the g function corresponds to the adopted blade data according to given leading and trailing edge blade data (g_{le} and g_{te}).

Regarding the assumption made, first the blade thickness is constant across spanwise while the blade angle in hub and tip is calculated following the free vortex theory. About both axial turbine rotor and stator 3D geometry generation, the equations (4.52)-(4.54) are used for blade angle function calculation, while the thickness function across streamwise calculation is performed by creating a second-order polynomial based on given leading, trailing and maximum thickness values. Note that the maximum thickness dimensionless(0-1) position is either being given as input or is the same with the one presented by Person

(2015) for each component. Figure 4-9 illustrates an 1D to 3D transformation example.

Table 4-5: Turbo-components Corresponding blade data.

T/C component	Name	Reference
CC-Impeller	NASA B30-D2	(Medic et al. 2014)
RT-Impeller	4.59-inch Radial-Inflow Turbine	(Wasserbauer et al. 1966)
AT-Rotor	KTH Legacy one stage axial turbine	(Person 2015)
AT-Stator	KTH Legacy one stage axial turbine	(Person 2015)

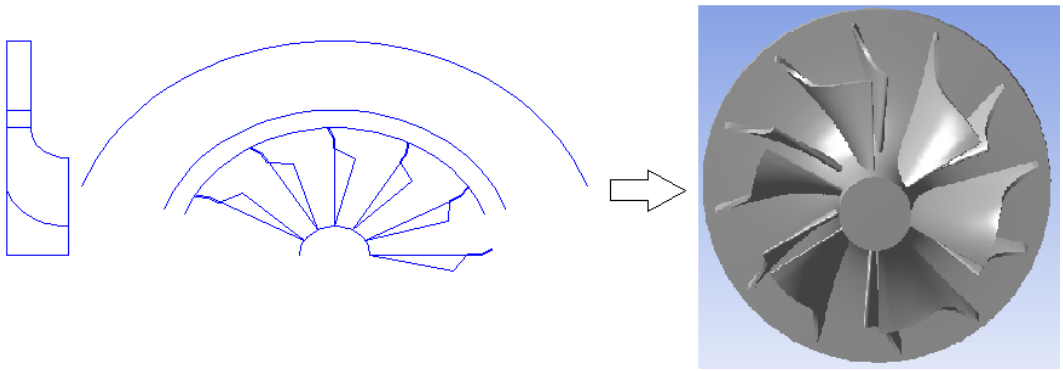

Figure 4-9: 1D to 3D transformation.

For Vaned diffuser-nozzle, the tool follows a more simplified approach. Specifically, it is assumed that the vane angle and thickness are a linear function of the streamwise position and constant in the spanwise direction. Also, both blade thickness and blade angle are assumed constant across the span. Regarding the blade data of Table 4-5, their graphic representation is shown in Figure 4-10.

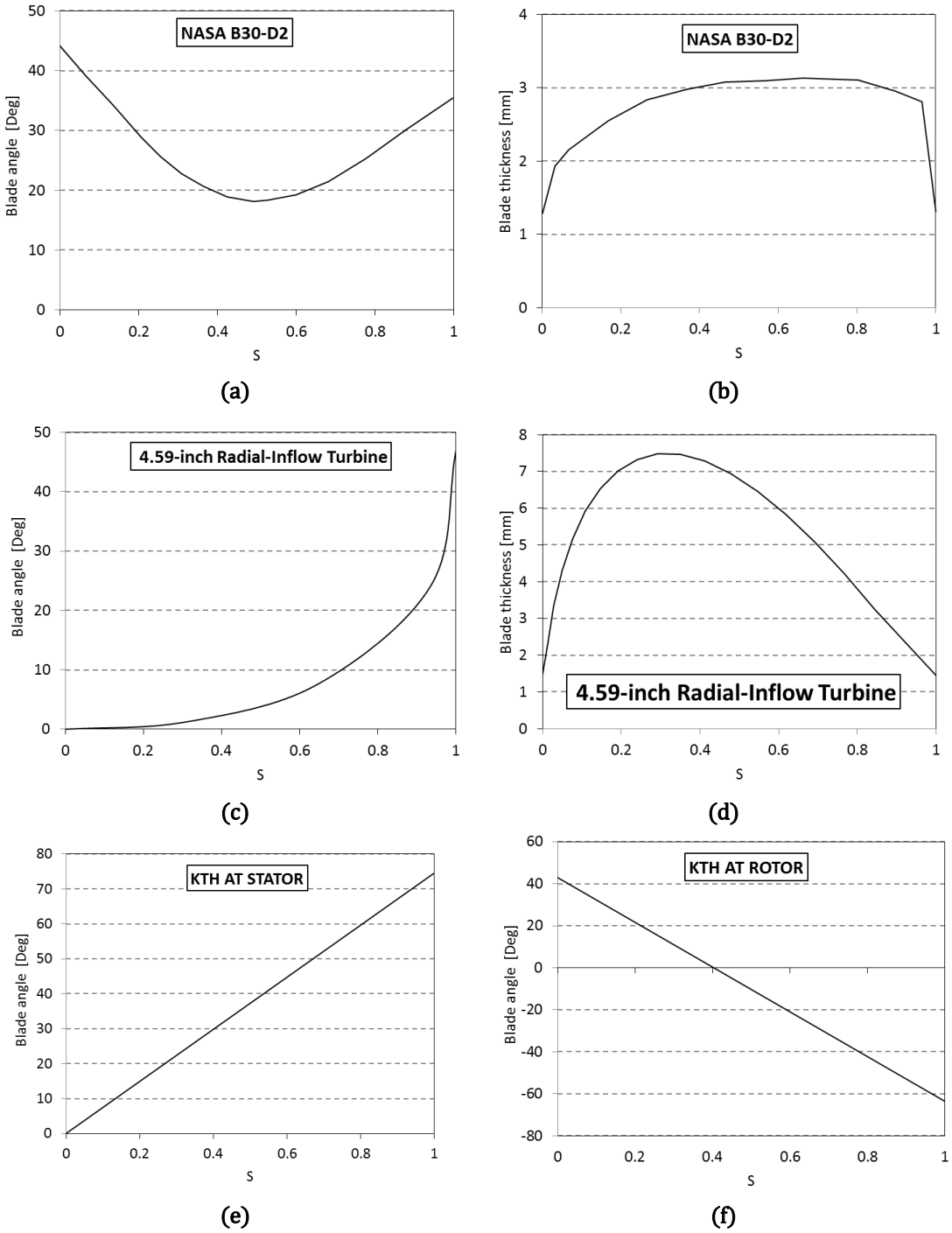

Figure 4-10: Blade data: **(a):** CC blade angle **(b)** CC blade thickness **(c)** RT blade angle **(d)** RT blade thickness **(e)** AT stator blade angle **(f)** AT rotor blade angle.

Having generated the 3D sub-component geometry, both mass and spanwise center of mass are computed, by discretizing the volume into small sub volumes as shown in Figure 4-11.

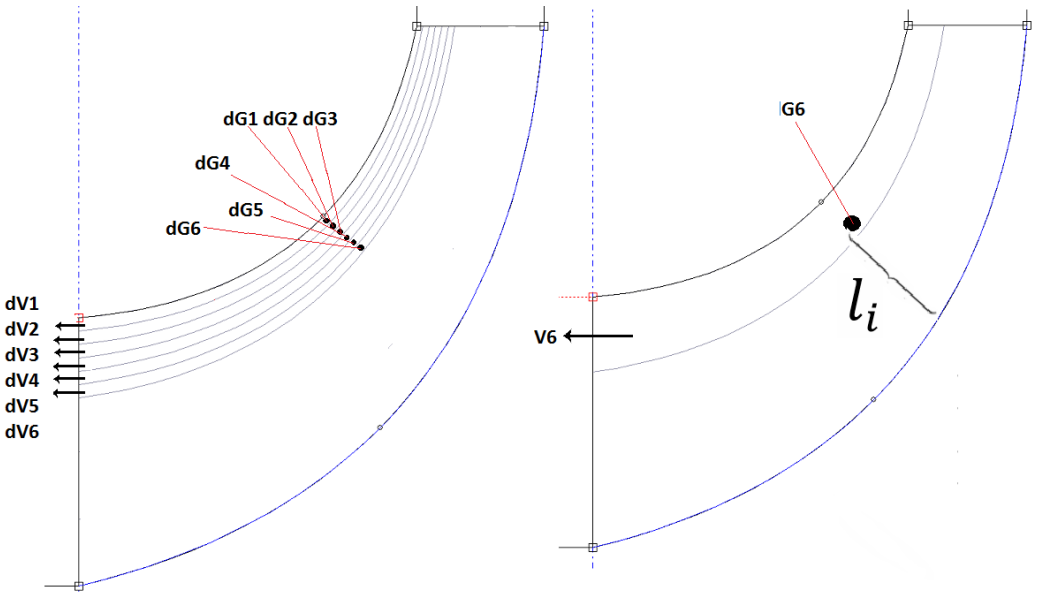

Figure 4-11: Impeller blade and spanwise center of mass calculation along spanwise.

In each volume, both the lower and the upper areas are calculated by considering that the blade area is divided into a sufficient number of elementary parallelogram elements, which in turn are splitted into two triangular elements (A and C) and one rectangular (B).

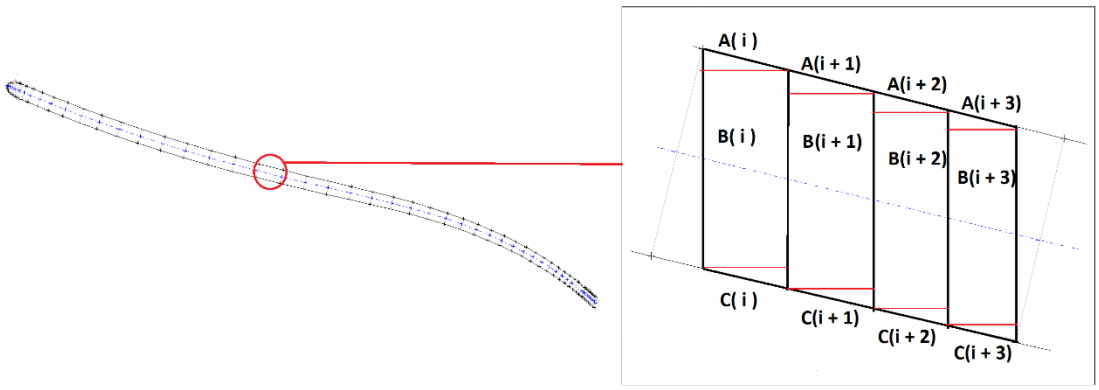

Figure 4-12: Impeller blade in meridional plane.

Figure 4-13 shows the impeller blade parallelogram elements in meridional plane.

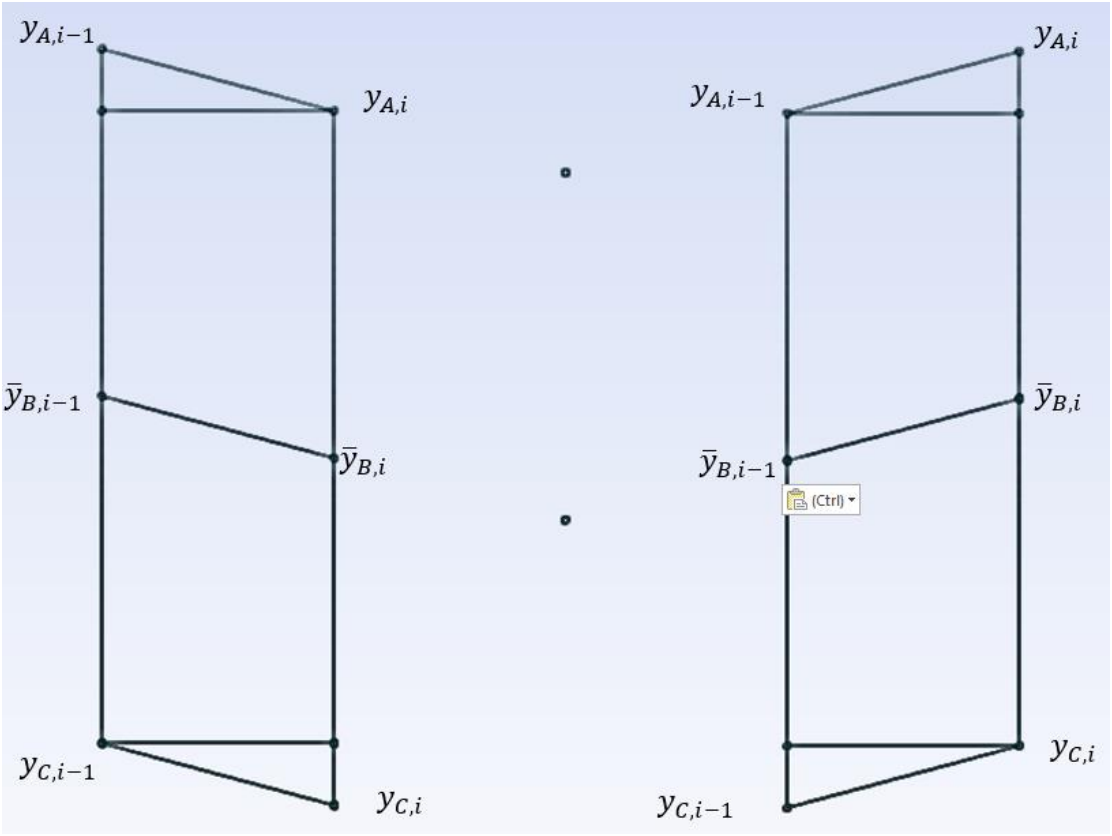

Figure 4-13: Impeller blade parallelogram elements in meridional plane.

Considering both the area(A) and the center of mass(y_G) for all the three elements(A, B and C), they are defined as follows:

$$A_{A,i} = \frac{\left|y_{A,i} - y_{A,i-1}\right| \ (x_i - x_{i-1})}{2} \quad i \in 2,3,..N \tag{4.55}$$

$$y_{G,A,i} = \frac{\left|y_{A,i} - y_{A,i-1}\right|}{3} + min\left(y_{A,i}, y_{A,i-1}\right) \quad i \in 2,3,..N \tag{4.56}$$

$$A_{B,i} = \left(min\left(y_{A,i}, y_{A,i-1}\right) - max\left(y_{C,i}, y_{C,i-1}\right)\right)(x_i - x_{i-1}) \ i \in 2,3,..N \tag{4.57}$$

$$y_{G,B,i} = \frac{min\left(y_{A,i}, y_{A,i-1}\right) - max\left(y_{C,i}, y_{C,i-1}\right)}{2} \quad i \in 2,3,..N \tag{4.58}$$

$$A_{C,i} = \frac{\left|y_{C,i} - y_{C,i-1}\right| \ (x_i - x_{i-1})}{2} \quad i \in 2,3,..N \tag{4.59}$$

$$y_{G,C,i} = -\frac{\left|y_{C,i} - y_{C,i-1}\right|}{3} + min\left(y_{C,i}, y_{C,i-1}\right) \quad i \in 2,3,..N \tag{4.60}$$

$$A_i = A_{A,i} + A_{B,i} + A_{C,i} \quad i \in 2,3,..N \tag{4.61}$$

$$y_{G,i} = \frac{y_{G,A,i}\, A_{A,i} + y_{G,B,i} A_{B,i} + y_{G,C,i} A_{C,i}}{A_i} \quad i \in 2,3,..N \tag{4.62}$$

where according to the Figure 4-14, the calculation of the x and y parameters is carried out as follows:

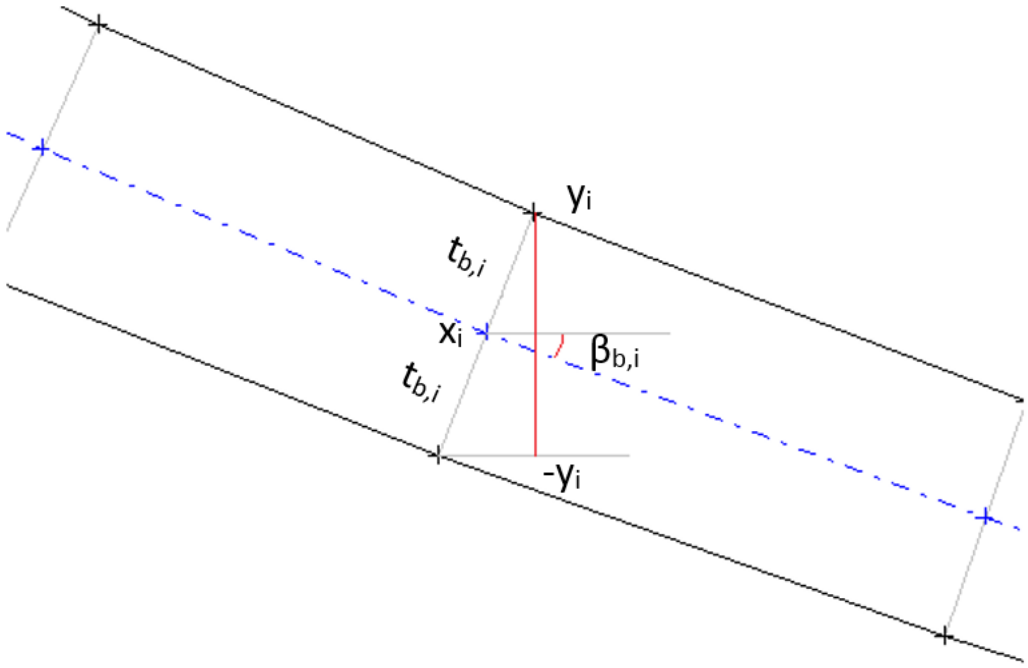

Figure 4-14: Impeller blade x and y parameters definition.

$$x_i = (s_i - s_{i-1}) + x_{i-1} \quad i \in 2,3,..N \tag{4.63}$$

$$y_{C,i} = -\frac{t_{b,i}}{2} Cos(\beta_{b,i}) + \bar{y}_{i-1} \quad i \in 2,3,..N \tag{4.64}$$

$$y_{up,i} = +\frac{t_{b,i}}{2} \mathrm{Cos}(\beta_{b,i}) + \bar{y}_{i-1} \quad i \in 2,3,..N \tag{4.65}$$

$$\bar{y}_i = \frac{y_{C,i} + y_{A,i}}{2} \quad i \in 2,3,..N \tag{4.66}$$

Having established the parallelogram areas and their centers of mass, the blade/vane area(A_{bld}) and its center of mass($y_{bld,G}$) in the corresponding spanwise position can be expressed as:

$$A_{bld} = \sum_{i=2}^{N} A_i \tag{4.67}$$

$$y_{bld,G} = \left(\sum_{i=2}^{N} y_{G,i}\, A_i \right) / A_{bld} \tag{4.68}$$

Using then, both the blade/vane area and the center of mass, the corresponding area moment of inertial(I_{bld}) is defined as:

$$I_i = I_{A,i} + I_{B,i} + I_{C,i} + A_{A,i} \left(y_{G,A,i} - y_{bld,G}\right)^2 + A_{B,i} \left(y_{g,B,i} - y_{bld,G}\right)^2 + A_{C,i} \left(y_{G,C,i} - y_{bld,G}\right)^2 \quad i \in 2,3,..N \tag{4.69}$$

$$I_{bld} = \sum_{i=2}^{N} I_i \tag{4.70}$$

Then, by multiplying the average value of both areas with the equivalent sub volume length ($\bar{l}_V$), the sub volume (dV) and the sub mass (dm) are computed:

$$dV_{i+1} = \frac{A_{bld,i+1} + A_{bld,i}}{2}\, \bar{l}_V \tag{4.71}$$

$$dm_{i+1} = dV_{i+1}\, \rho_{material} \tag{4.72}$$

where sub volume the equivalent sub volume length ($\bar{l}_V$) is calculated as follows:

$$\bar{l}_V = \frac{l_{inlet} + l_{outlet}}{2} \tag{4.73}$$

$$l_{inlet} = (span_{i+1} - span_i)(R_{tip} - R_{hub}) \tag{4.74}$$

$$l_{outlet} = (span_{i+1} - span_i) b_3 \tag{4.75}$$

The maximum stress is based on the evaluation of two kind of stresses, centrifugal forces and blade bending. According to Schaber et al. (2019), the centrifugal forces can be computed as follows:

$$F_{centrifugal_i} = \rho_{material}\, \omega_{bld} \sum_{i=span}^{1} dV_i\, \frac{(R'_{max} - R'_i)}{2} \tag{4.76}$$

which is separated into shear and normal force:

$$F_{tensile_i} = F_{centrifugal_i}(span)\,\mathrm{Cos}(45^o) \tag{4.77}$$

$$F_{shear_i} = F_{centrifugal_i}\,\mathrm{Sin}(45^o) \tag{4.78}$$

In case of an axial impeller, the tensile and shear loads are expressed as follows:

$$F_{tensile_{i,AT}} = F_{centrifugal_i}(span) \tag{4.79}$$

$$F_{shear_{i,AT}} = 0 \tag{4.80}$$

Then, the normal stress in each spanwise position is defined as:

$$\sigma_{centrifugal,tensile,i} = \frac{F_{tensile_i}}{A_i} \tag{4.81}$$

For calculating the bending stress, the impeller geometry is transformed into an equivalent beam. In more details, the bending analysis is performed at both the inducer (inlet) and the exducer (outlet) station, for calculating the corresponding torque as a function of the streamwise length,

$$M_{blade}(L_{eq}) = \int_0^{s_{max}(L_{eq})} M'(s)ds = \frac{s_{max}(L_{eq})\,(\,M'_{exducer}(L_{eq}) + M'_{inducer}(L_{eq})\,)}{2} \tag{4.82}$$

where (s) is the integration variable and (L_{eq}) is the equivalent spanwise length (blade is analysed as a beam with equal length in each side), calculated by averaging the inlet and outlet L_{max}. Also, S_{max} is the streamwise position as a function of spanwise (L_{eq}) position. By discretizing the continuous expression (4.82) , it is transformed as follows:

$$M_{blade,i} = \frac{s_{max,i}\,(\,M'_{exducer,i} + M'_{inducer,i}\,)}{2}\ [Nm] \tag{4.83}$$

where i represents the impeller blade sections from tip to hub. In the $M_{blade,i}$ the centrifugal force shear part contributes as well,

$$M'_{blade,i} = M'_{blade,i} + F_{shear,i}\ l_i\,cos(\beta_{stag})\ \ [Nm] \tag{4.84}$$

where l_i is the distance of the middle point in i spanwise position from hub(Figure 4-11). In next step the bending stress($\sigma_{bending,i}$) is calculated in each spanwise position (i):

$$\sigma_{bending,i} = M'_{blade,i} \frac{y_{max,i}}{I_{blade,i}} \quad (4.85)$$

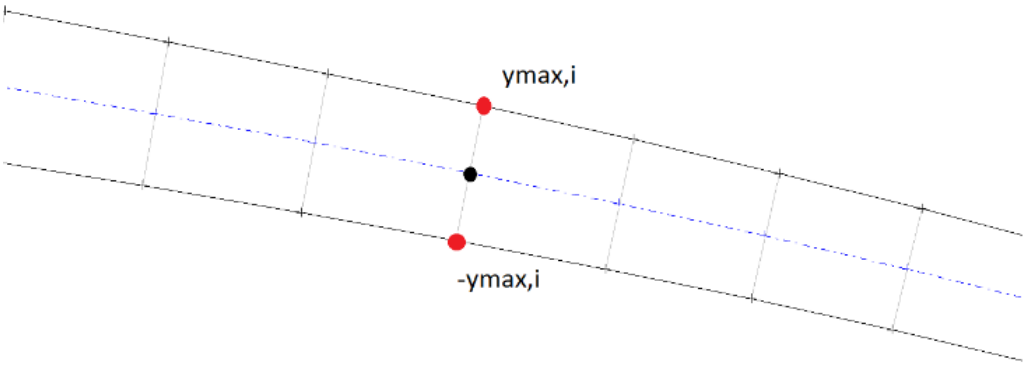

Figure 4-15: $y_{max,i}$ definition.

In case of Stationary components (Vaned Nozzle, Vaned Diffuser, Axial Turbine Stator), as blade both sides are fixed, the hyperstatic blade bending methodology is followed.

Having calculated the stress for each stress type (bending – centrifugal force), the total stress in each spanwise position (i) is calculated as follows:

$$\sigma_{blade,i} = \sigma_{bending,i} + \sigma_{centrifugal,tensile,i} \quad (4.86)$$

Then, the maximum stress($\sigma_{blade,max}$) and the corresponding safety factor(sf) are calculated as follows:

$$\sigma_{blade,max} = max(\sigma_{blade,i}) \quad (4.87)$$

$$sf = \frac{\sigma_y}{\sigma_{blade,max}} \quad (4.88)$$

4.4.3 Static Structural model Verification

For verifying static analysis, a fluid to structure interaction simulation(one way) is performed, utilizing CFD and FEA software, respectively. In this analysis, due to the fact that the results are used for verifying the simplified static analysis tool, it is chosen to use default fine mesh size for both CFD and FEA simulations, which offers reasonable accuracy at economic computer runtime.

According to Table 4-6, the SSA and FEA static analysis shows that the results are close, leading to a safe estimate using the simplified model. As for the

geometry selection, the radial and axial turbine components are the ones presented in the corresponding validation cases(Table 3-5 and Table 3-9), while the centrifugal compressor impeller is the one designed(Figure 6-12) in the section 6.3.

Table 4-6: Simplified structural analysis validation with FEA.

T/C component	Sub-Component	FEA maximum stress	SSA maximum stress
CC	Impeller	347 MPa	369 MPa
RT	Impeller	375 MPa	349 MPa
RT	Vnd nozzle	3.90 MPa	3.70 MPa
AT	Rotor	13.0 MPa	13.7 MPa
AT	Stator	0.70 MPa	0.84 MPa

The difference between the SSA and FEA results is higher for the rotating frame components, especially for the radial impellers where, as discussed above, the centrifugal load affects both tensile and blade bending stresses making the analysis more complex. For ensuring the simplified structural analysis (SSA) ability to capture the rotating frame components maximum stress behavior in function of rotational speed, a comparison between SSA and FEA is performed for both axial and radial impellers for a rotational speed range, as depicted in Figure 4-16 and Figure 4-17. The SSA model can capture the components maximum stress behavior according to rotational speed, providing a reliable tool during preliminary design for ensuring structural integrity.

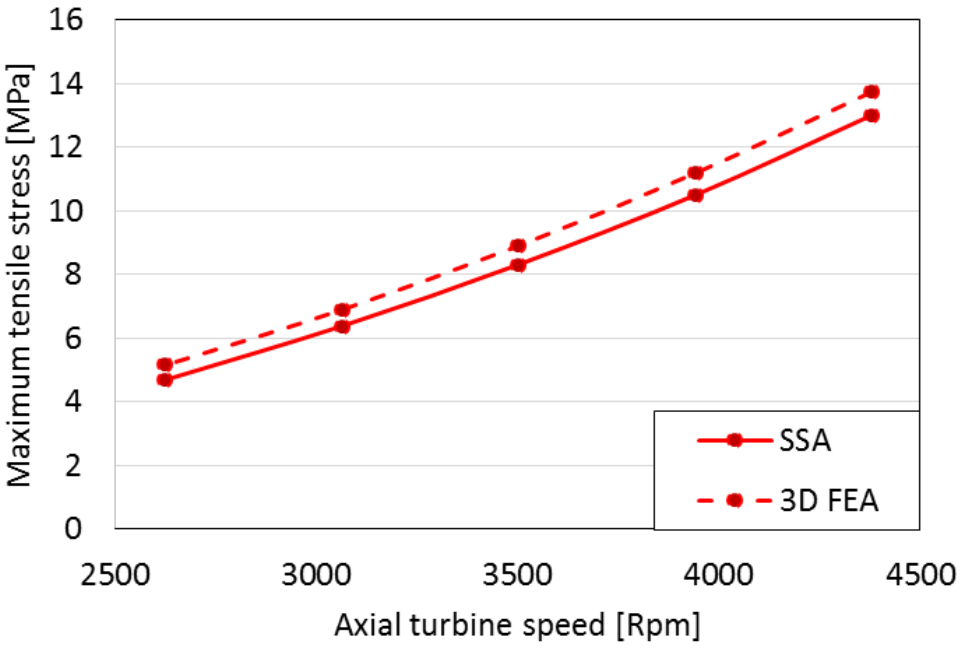

Figure 4-16: Axial Turbine [Person 2015] SSA calculated maximum stress against FEA calculated maximum stress.

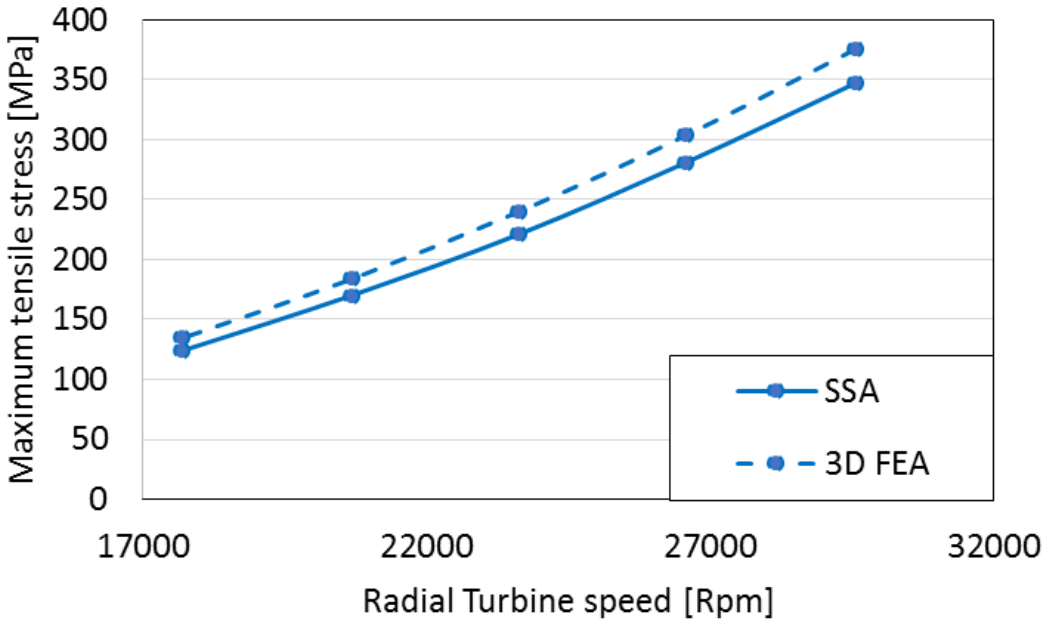

Figure 4-17: Radial Turbine [Wasserbauer et al. 1966] SSA calculated maximum stress against FEA calculated maximum stress.

4.4.4 Modal Structural Analysis

For ensuring that the T/C dynamic operation is stable and the T/C speed points is not close to the critical ones, hence avoiding resonance phenomena or significant additional vibrating loads, a T/C turbo spool modal analysis is performed. For this reason, a simplified modal analysis is developed for this work in order to be integrated to the simplified structural analysis.

The current analysis is limited to T/C with journal bearings, placed between compressor and turbine. Thus, the developed model, depicted in Figure 4-18, approximates the turbo spool by considering the shaft and the two impellers/rotors as the main elementary bodies.

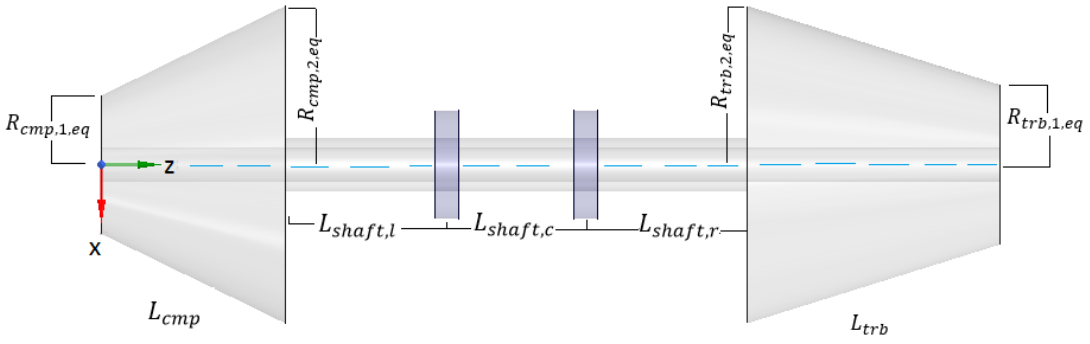

Figure 4-18: Simplified structural modal analysis turbo spool.

Particularly, the shaft is divided into three segments, called elastic sub-shafts; the one between the two journals (shaft center), the one supporting the compressor impeller (shaft left) and the one supports the turbine impeller (shaft right). Each shaft segment and compressor/turbine wheels are approached as discrete discs (five in total), described by mass and inertia. Each mechanical connection between two neighboring discs is considered as a linear spring in order to take the shaft elasticity effect on provided vibrations into account.

Additionally, the journal bearings are represented by a pair of linear spring and absorber for estimating both bearing elasticity and friction. In this analysis both lateral displacements (x,y) and rotations (θ_x, θ_y) due to bending moments are treated as degrees of freedom for each body separately, analyzing in that way the vibrations caused by gyroscopic phenomena [Nguyen-Schäfer 2015].

Concerning axial displacement (z) and rotational turn (θ_z), they are excluded from the analysis, as imbalance operating conditions are not the aim of current study. For this reason the thrust bearing is not included in the simplified modal model. Specifically, for the current analysis, it is assumed that the shaft consists of two journal bearings and is separated into three elastic sub-shafts (left, center and right shaft). Both compressor and turbine components are assumed to be conical frustum rigid bodies, with inlet and outlet equivalent radius (Eq. (4.89)).

$$R_{i,eq} = R_{hub,i} + B_i \, h_{bld,i} \tag{4.89}$$

The journal bearing damping and stiffness coefficients, used by Nguyen-Schäfer (2015) in his test cases, are used. Each sub-shaft lateral and circulant stiffness coefficients are calculated as follows:

$$K_{x,y} = \frac{E \, A}{L} \tag{4.90}$$

$$K_{\theta_{x,y}} = \frac{G \, I}{L} \tag{4.91}$$

For creating the rotordynamic differential equations system, the turbo spool model is transformed into an equivalent one (Figure 4-19) with 20 degrees of freedom in total, consisted of two lateral displacements and rotations for each one of the five discrete discs.

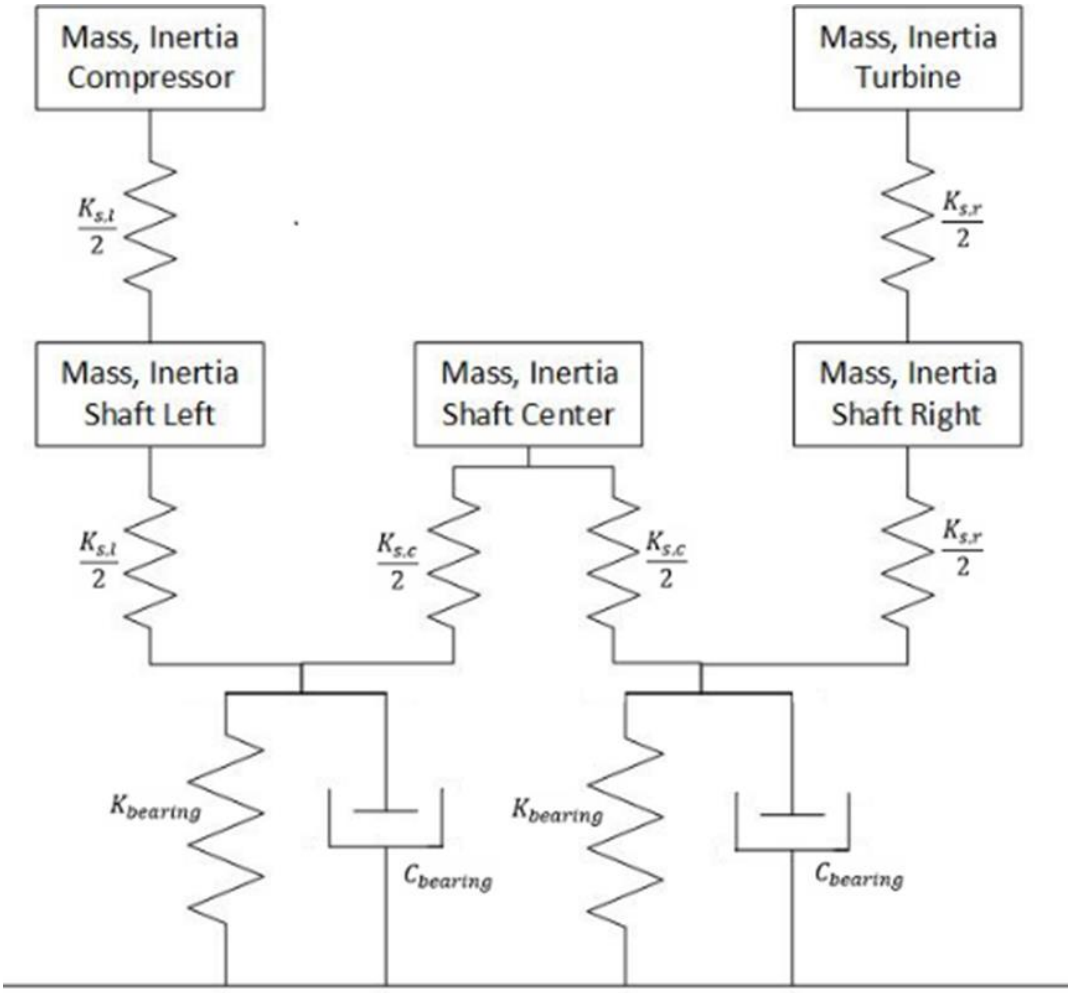

Figure 4-19: Turbo spool equivalent model.

To elaborate further, the modal analysis model is defined as follows. Regarding the lateral displacement, the gyroscopic effect variables and the transverse mass moments of inertia, they are expressed as a vector:

$$\mathbf{X} = \begin{bmatrix} x \\ y \end{bmatrix}, \boldsymbol{\Theta}_i = \begin{bmatrix} \theta_x \\ \theta_y \end{bmatrix}, \boldsymbol{\Theta}_j = \begin{bmatrix} \theta_y \\ \theta_x \end{bmatrix}, \boldsymbol{J} = \begin{bmatrix} J_x \\ J_y \end{bmatrix} \tag{4.92}$$

Starting with the shaft center body, its lateral motion is expressed as:

$$m_{s,c}\,\ddot{\boldsymbol{X}}_{s,c} + 2\,c_{br}\,\dot{\boldsymbol{X}}_{s,c} + \left[\frac{k_{s,c}\,k_{br}}{\frac{k_{s,c}}{2} + k_{br}}\,\boldsymbol{X}_{s,c}\right] + \left[\frac{k_{tr,s,c}\,k_{tr,br}}{\frac{k_{tr,s,c}}{2} + k_{tr,br}}\,\boldsymbol{\Theta}_{s,c,x}\right] = 0 \tag{4.93}$$

where ($m_{s,c}$) is the shaft center body mass, (c_{br}) and (k_{br}) are the bearing lateral damping and stiffness coefficients, ($k_{s,c}$) is the body lateral stiffness coefficient, ($k_{tr,br}$) and ($k_{tr,s,c}$) are the shaft center and bearing interaction stiffness coefficient, respectively.

The shaft center body rotation is defined as:

$$\boldsymbol{J}_{s,c}\,\ddot{\boldsymbol{\Theta}}_{s,c,i} + I_{s,c,zz}\,\Omega\,\dot{\boldsymbol{\Theta}}_{s,c,j} + 2\,c_{r,br}\,\dot{\boldsymbol{\Theta}}_{\boldsymbol{s,c,i}} + \left[\frac{k_{r,s,c}\,k_{r,br}}{\frac{k_{r,s,c}}{2}+k_{r,br}}\,\boldsymbol{\Theta}_{s,c,i}\right] + \left[\frac{k_{tr,s,c}\,k_{tr,br}}{\frac{k_{tr,s,c}}{2}+k_{tr,br}}\,\boldsymbol{X}_{s,c}\right] = 0 \tag{4.94}$$

where $(c_{r,br})$ and $(k_{r,s,c})$ are the bearing circulant damping and stiffness coefficient, $(k_{r,s,c})$ is the body circulant stiffness coefficient, $(I_{s,c,zz})$ is the body polar mass inertia and Ω the angular velocity.

Both the right and left body lateral motions are described as follows:

$$m_{s,r}\,\ddot{\boldsymbol{X}}_{s,r} + 2\,c_{br}\,\dot{\boldsymbol{X}}_{s,r} + \left[\left(\frac{k_{s,r}}{2}+\frac{k_{s,r}\,k_{br}}{\frac{k_{s,r}}{2}+k_{br}}\right)\boldsymbol{X}_{s,r} - \frac{k_{s,r}}{2}\,\boldsymbol{X}_{T}\right] + \left[\left(\frac{k_{tr,s,r}}{2}+\frac{k_{tr,s,r}\,k_{tr,br}}{\frac{k_{tr,s,r}}{2}+k_{tr,br}}\right)\boldsymbol{\Theta}_{s,r,i} - \frac{k_{tr,s,r}}{2}\,\boldsymbol{\Theta}_{T,i}\right] = 0 \tag{4.95}$$

$$m_{s,l}\,\ddot{\boldsymbol{X}}_{s,l} + 2\,c_{br}\,\dot{\boldsymbol{X}}_{s,l} + \left[\left(\frac{k_{s,l}}{2}+\frac{k_{s,l}\,k_{s}}{\frac{k_{s,l}}{2}+k_{s}}\right)\boldsymbol{X}_{s,l} - \frac{k_{s,l}}{2}\,\boldsymbol{X}_{C}\right] + \left[\left(\frac{k_{tr,s,l}}{2}+\frac{k_{tr,s,l}\,k_{tr,br}}{\frac{k_{tr,s,l}}{2}+k_{tr,br}}\right)\boldsymbol{\Theta}_{s,l,x} - \frac{k_{tr,s,l}}{2}\,\boldsymbol{\Theta}_{C,x}\right] = 0 \tag{4.96}$$

while their rotation as:

$$J_{s,r}\,\ddot{\boldsymbol{\Theta}}_{s,r,i} + I_{s,r,zz}\,\Omega\,\dot{\boldsymbol{\Theta}}_{rr,j} + 2\,c_{r,br}\,\dot{\boldsymbol{\Theta}}_{s,r,i} + \left[\left(\frac{k_{r,s,r}}{2}+\frac{k_{r,s,r}\,k_{r,br}}{\frac{k_{r,s,r}}{2}+k_{r,br}}\right)\boldsymbol{\Theta}_{s,r,i} - \frac{k_{r,s,r}}{2}\,\boldsymbol{\Theta}_{T,i}\right] + \left[\left(k_{tr,s,r}+\frac{k_{tr,s,r}\;k_{tr,br}}{k_{tr,s,r}+\;k_{tr,br}}\right)\boldsymbol{X}_{s,r} - \frac{k_{tr,s,r}}{2}\,\boldsymbol{X}_{T}\right] = 0 \tag{4.97}$$

$$\boldsymbol{J}_{s,l}\,\ddot{\boldsymbol{\Theta}}_{s,l,i} + +I_{s,l,zz}\,\Omega\,\dot{\boldsymbol{\Theta}}_{s,l,j} + 2\,c_{r,br}\,\dot{\boldsymbol{\Theta}}_{s,l,i} + \left[\left(\frac{k_{r,s,l}}{2} + \frac{k_{r,s,l}\,k_{r,br}}{\frac{k_{r,s,l}}{2} + k_{r,br}}\right)\boldsymbol{\Theta}_{s,l,i} - \frac{k_{r,s,l}}{2}\,\boldsymbol{\Theta}_{T,i}\right] + \left[\left(k_{tr,s,l} + \frac{k_{tr,s,l}\;k_{tr,br}}{\frac{k_{tr,s,l}}{2} + \;k_{tr,br}}\right)\boldsymbol{X}_{s,l} - k_{tr,s,l}\,\boldsymbol{X}_{C}\right] = 0 \tag{4.98}$$

where $(m_{s,r})$ and $(m_{s,l})$ are both the right and left shaft body masses, $(k_{s,r})$ and $(k_{s,l})$ are the corresponding lateral stiffness coefficients, $(k_{r,s,r})$ and $(k_{r,s,l})$ are the corresponding circulant stiffness coefficients, $(I_{s,r,zz})$ and $(I_{s,l,zz})$ are the bodies polar mass inertias.

Regarding the compressor and turbine wheels, their lateral motions are expressed as:

$$m_T\,\ddot{\boldsymbol{X}}_T + \left[\frac{k_{s,r}}{2}\,\boldsymbol{X}_T - \frac{k_{s,r}}{2}\,\boldsymbol{X}_{s,r}\right] + \left[\frac{k_{tr,s,r}}{2}\,\boldsymbol{\Theta}_{T,i} - \frac{k_{tr,s,r}}{2}\,\boldsymbol{\Theta}_{s,r,i}\right] = 0 \tag{4.99}$$

$$m_C\,\ddot{\boldsymbol{X}}_C + \left[\frac{k_{s,l}}{2}\,\boldsymbol{X}_C - \frac{k_{s,l}}{2}\,\boldsymbol{X}_{s,l}\right] + \left[\frac{k_{tr,s,l}}{2}\,\boldsymbol{\Theta}_{C,i} - \frac{k_{tr,s,l}}{2}\,\boldsymbol{\Theta}_{s,l,i}\right] = 0 \tag{4.100}$$

while their rotation as:

$$\boldsymbol{J}_T\,\ddot{\boldsymbol{\Theta}}_{T,i} + I_{T,zz}\,\Omega\,\dot{\boldsymbol{\Theta}}_{T,j} + \left[\frac{k_{r,s,r}}{2}\,\boldsymbol{\Theta}_{T,i} - \frac{k_{r,s,r}}{2}\,\boldsymbol{\Theta}_{s,r,i}\right] + \left[\frac{k_{tr,s,r}}{2}\,\boldsymbol{X}_T - \frac{k_{tr,s,r}}{2}\,\boldsymbol{X}_{s,r}\right] = 0 \tag{4.101}$$

$$J_C\,\ddot{\boldsymbol{\Theta}}_{C,x} + I_{C,zz}\,\Omega\,\dot{\boldsymbol{\Theta}}_{C,j} + \left[\frac{k_{r,s,l}}{2}\,\boldsymbol{\Theta}_{C,x} - \frac{k_{r,s,l}}{2}\,\boldsymbol{\Theta}_{s,r,x}\right] + \left[\frac{k_{tr,s,l}}{2}\,\boldsymbol{X}_C - \frac{k_{tr,s,l}}{2}\,\boldsymbol{X}_{s,l}\right] = 0 \tag{4.102}$$

where (m_T) and (m_C) corresponds to both the compressor and turbine wheel mass, $(I_{T,r,zz})$ and $(I_{T,l,zz})$ are the wheels polar mass inertias.

Having established the differential equation system, for calculating the desired eigenfrequencies as function of the angular velocity for each mode and the decay rate, the 20x20 second order equation system is transformed into an equivalent 40x40 first order one as:

$$\begin{bmatrix}\dot{z}\\ \ddot{z}\end{bmatrix} = \begin{bmatrix}0 & I\\ -M^{-1}K & -M^{-1}C\end{bmatrix}\begin{bmatrix}z\\ \dot{z}\end{bmatrix} = A\begin{bmatrix}z\\ \dot{z}\end{bmatrix} \tag{4.103}$$

where M is the diagonal matrix containing mass and mass inertia moments, K is the stiffness coefficient matrix, C is the damping coefficient and the array z is defined as:

$$z = \begin{bmatrix} \boldsymbol{x} \\ \boldsymbol{\theta}_x \\ \boldsymbol{y} \\ \boldsymbol{\theta}_y \end{bmatrix}, \boldsymbol{x} = \begin{bmatrix} x_{s,c} \\ x_{s,r} \\ x_{s,l} \\ x_T \\ x_C \end{bmatrix}, \boldsymbol{\theta}_x = \begin{bmatrix} \theta_{s,c,x} \\ \theta_{s,r,x} \\ \theta_{s,l,x} \\ \theta_{T,x} \\ \theta_{C,x} \end{bmatrix}, \boldsymbol{y} = \begin{bmatrix} y_{s,c} \\ y_{s,r} \\ y_{s,l} \\ y_T \\ y_C \end{bmatrix}, \boldsymbol{\theta}_y = \begin{bmatrix} \theta_{s,c,y} \\ \theta_{s,r,y} \\ \theta_{s,l,y} \\ \theta_{T,y} \\ \theta_{C,y} \end{bmatrix} \quad (4.104)$$

Finally, both the eigenvalues and eigenfrequencies of A matrix are calculated via a python module[1], for defining the decay rate and generating the Campbell diagram. Note that the conjugate values of eigenfrequency matrix are removed.

For this work, in order to reduce the optimization time, the variables $L_{s,l}/ L_s$ and $L_{r,l}/ L_s$ are set equal to $1/3$. Also, for simplicity, the shaft material is chosen to be the same with turbine. As for the shaft size, it is assumed that the shaft internal radius to compressor hub radius ratio is equal to 0.5 and the shaft external radius to compressor hub radius ratio is equal to 0.8. The turbo spool dynamic structural integrity criteria are the followings:

$$max(\alpha) \leq 0 \quad (4.105)$$

$$\omega_{m1}(N) \neq \Omega(N) \quad (4.106)$$

$$\omega_{m2}(N) \neq \Omega(N) \quad (4.107)$$

4.4.5 Modal Structural Analysis evaluation

For evaluating the present model, a modal analysis is performed, conducted within commercial 3D modal analysis software[2], which input data are presented in Table 4-7. For simplicity, during the validation test case both compressor and turbine impellers are chosen to be typical aluminum alloy as 3D commercial modal analysis requires more complex setup in case of multi-material analysis.

Table 4-7: Validation Turbo-spool velocity.

Parameter	Range	Parameter	Range
N_{min}	32117	N_{max}	65946
$R_{1,cmp,eq}$	0.014602	$R_{6,trb,eq}$	0.014602
$R_{3,cmp,eq}$	0.069	$R_{4,cmp,eq}$	0.069
L_{cmp}	0.11	L_{trb}	0.08
L_s	0.1	$R_{s,int}/ R_{hub,1,CC}$	0.5
$R_{s,ext}/R_{hub,1,CC}$	0.8		

[1] https://numpy.org/
[2] ANSYS Modal: https://courses.ansys.com/index.php/courses/modal-analysis/

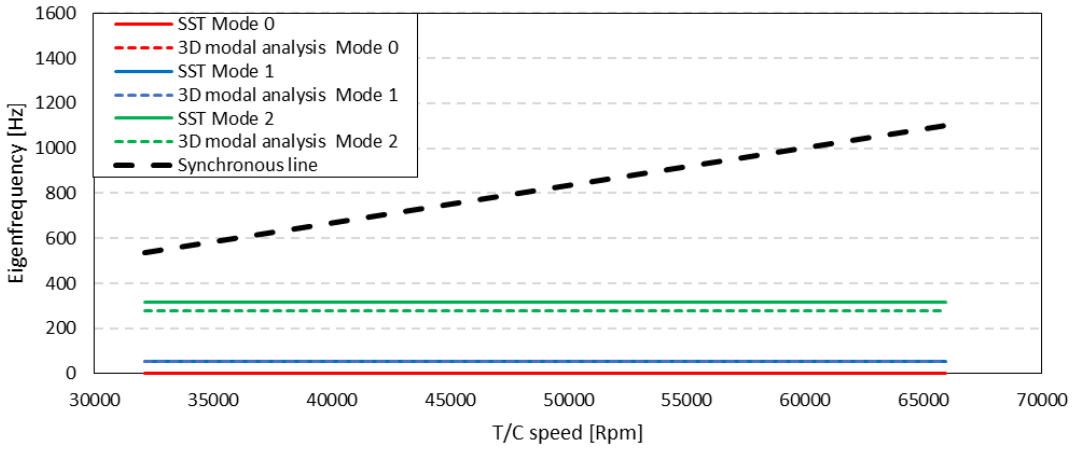

Figure 4-20: Simplified structural modal analysis Campbell diagram validation for modes 0,1,2.

Concerning the Campbell diagram modes selection, the modes, revealed by significantly higher magnitude, are grouped considering the symmetric ones of both compressor and turbine impellers. Specifically, the first mode corresponds to cylindrical gyroscopic effect while the second one corresponds to conical gyroscopic effect [Chatzisavvas et al. 2017].

The results, depicted in Figure 4-20, reveal a sufficient agreement between the developed model and the commercial one. Both modal models predict that none of the examined eigenfrequencies would cause any resonance operating cases, while all eigenfrequencies seem to be almost unchanged as the rotor speed varies. The reason is that the turbine and compressor have similar mass and inertia, while the shaft is splitted into three sub-shafts with equal mass and inertia each.

4.5 Modification of the centrifugal compressor

The CC meanline model, presented in the Chapter 3 is basically a single zone meanline model. In contrast to a three zone meanline model (eg. Stuart et al. (2017), (2018)), the basic disadvantage of the current one is its inability to calculate the impact of impeller outlet blade length in recirculation and active flow region generation and the volute losses due to 3D effect, which increase as the inlet width increases significantly.

For this work, the single zone approach is selected as more appropriate, as the development of a three zone model requires a series of CFD simulations for calculating the relationship between flow coefficient, specific speed and aerodynamic blockage.

1D compressor design processes, utilizing single zone meanline models, usually lead to both large impeller outlet blade length and volute inlet width with intensive 3D effects that are perceived only with 3D CFD analysis.

For overcoming this issue, an impeller outlet blade length restriction is developed. To elaborate further, using a number(13) of compressor measured

geometries, provided by T/C company[1], the compressor outlet to inlet area ratio is calculated as a function of design flow coefficient, assuming that specific speed does not affect the aerodynamic blockage. A correlation is established as shown in Figure 4-21.

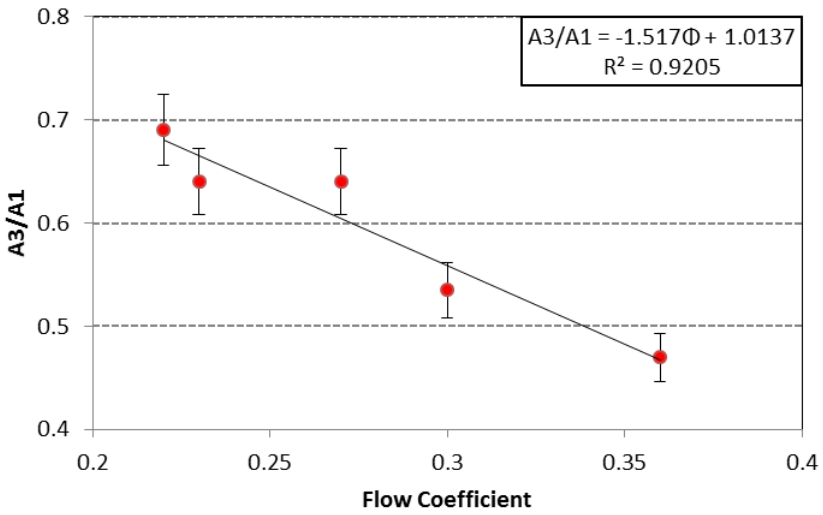

Figure 4-21: A3/A1 as a function of flow coefficient.

The negative trend is evident in accordance to Stuart et al. (2018). Thus, the following constraint,

$$\left|\frac{A_3}{A_1} - (-1.51\,\Phi + 1.0137)\right| \leq 5\% \tag{4.108}$$

is implemented into the optimization procedure.

4.6 3D centrifugal compressor design process

The 3D design process follows an optimization procedure, redesigning the compressor, using the preliminary design geometry as a starting point. For the impeller, the initial 3D geometry is generated from the 1D to 3D transformation tool, presented in the section 4.4.

For the 3D optimization process, an in-house utility function is developed, with the aim to run specific sub-processes in the background, such as flow domain meshing and flow domain modeling, in order to automate the compressor CFD performance prediction. Figure 4-22 shows the vaneless diffuser compressor 3D model, integrated into the optimizer.

[1] www.turbomed.gr

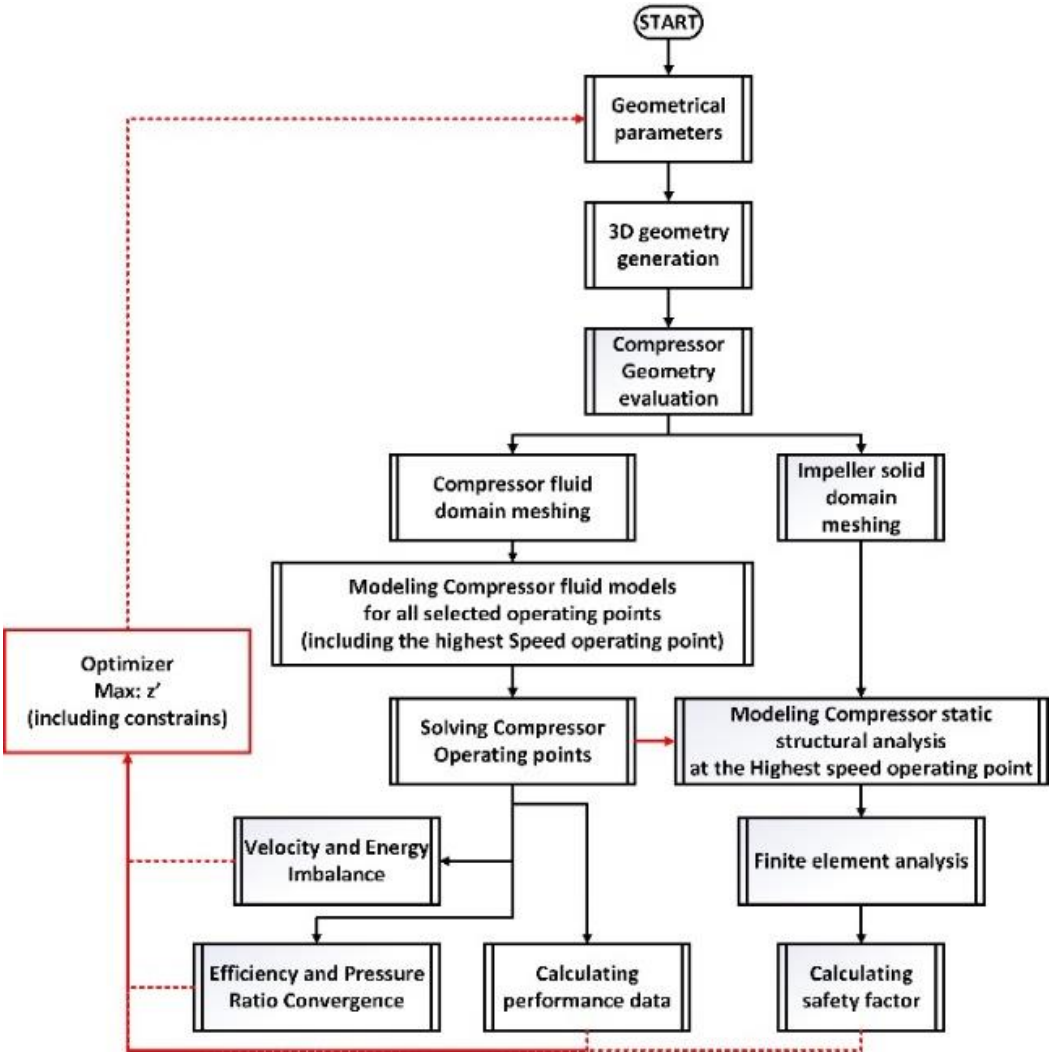

Figure 4-22: Compressor 3D design process overall flow chart.

In each optimization cycle, using dimensional geometrical variables, a 3D geometry is generated for each component (impeller, vaneless diffuser and volute). Regarding both the impeller and volute geometry, they are transformed in a proper CAD form[1]. All sub-domains (impeller, vaneless diffuser and volute) are then meshed. Note that the sub utility function which is aimed to replace the meshing GUI has as input the given meshing properties (mesh size, expansion rate, etc.). Then, the compressor fluid domain is created, by assembling the individual components. The boundary conditions, the fluid properties and the relative to stationary interface connection are set for each operating point, including the one with the highest load. After a solution is reached, the software calculates the given by CFD performance conditions in outlet (pressure ratio, efficiency, power) and transforms them to a form that the optimizer can read, while checking if the solution is converged.

[1] Impeller: ANSYS blade gen
Volute: ANSYS Design modeler

The in-house utility function treats the simulation sub-tools as black box software. Thus, each sub-tool can be easily replaced with both in-house and commercial tools (CFD solver, FEA solver, meshing, etc.).

Then, the main and the splitter blade solid domains are generated. A 3D static structural analysis is then performed, using the highest load CFD results and imposing them to the blades as a load. Thus, the safety factor is estimated, in order to check the structural integrity of each solution.

The optimization method, used in the 3D design process, is also user defined, similar to the preliminary design process. For this study, the commercial optimization tool[1] evolutionary algorithm, based on Rechenberg (1989) and Schwefel (1993) works, is selected, as it is extremely flexible with black–box software. Concerning the initial geometry, it is generated by coupling the preliminary design and the 1D to 3D transformation processes.

Regarding the compressor optimization variables, the ones that correspond to the impeller are separated into two groups, a graphic representation of which is depicted in Figure 4-10. The group A consists of the blade shape variables while the group B consists of the meridional plane dimensional geometrical variables.

- Group A: $\beta_{hub,1,}$ $\beta_{hub,b}$, $\beta_{hub,3}$, $\beta_{tip,1}$, $\beta_{tip,a}$, $\beta_{tip,b}$, $\beta_{tip,3}$, $t_{hub,}$, $t_{hub,}$, $t_{hub,3}$, $t_{tip,1}$, $t_{tip,a}$, $t_{tip,3}$
- Group B: Z, $R_{hub,1}$, $R_{hub,\,a}$, $R_{hub,3}$, R_4, $R_{tip,1}$, $R_{tip,\,a}$, $R_{tip,3}$, $X_{hub,a}$, $X_{hub,3}$, $X_{tip,a}$, $X_{tip,3}$

Concerning variable ranges, all blade angle parameters can vary from 0^o to 90^o, while the blade thickness ones vary from user defined lower limit(CNC milling machine limit) to +20% of initial geometry thickness. About the rest of the impeller variables, they vary from -20% to +20% of the initial geometry ones.

[1] Isight & SIMULIATM Execution Engine - Dassault Systèmes®." [Online]. Available: https://www.3ds.com/products-services/simulia/products/isight-simulia-execution-engine/

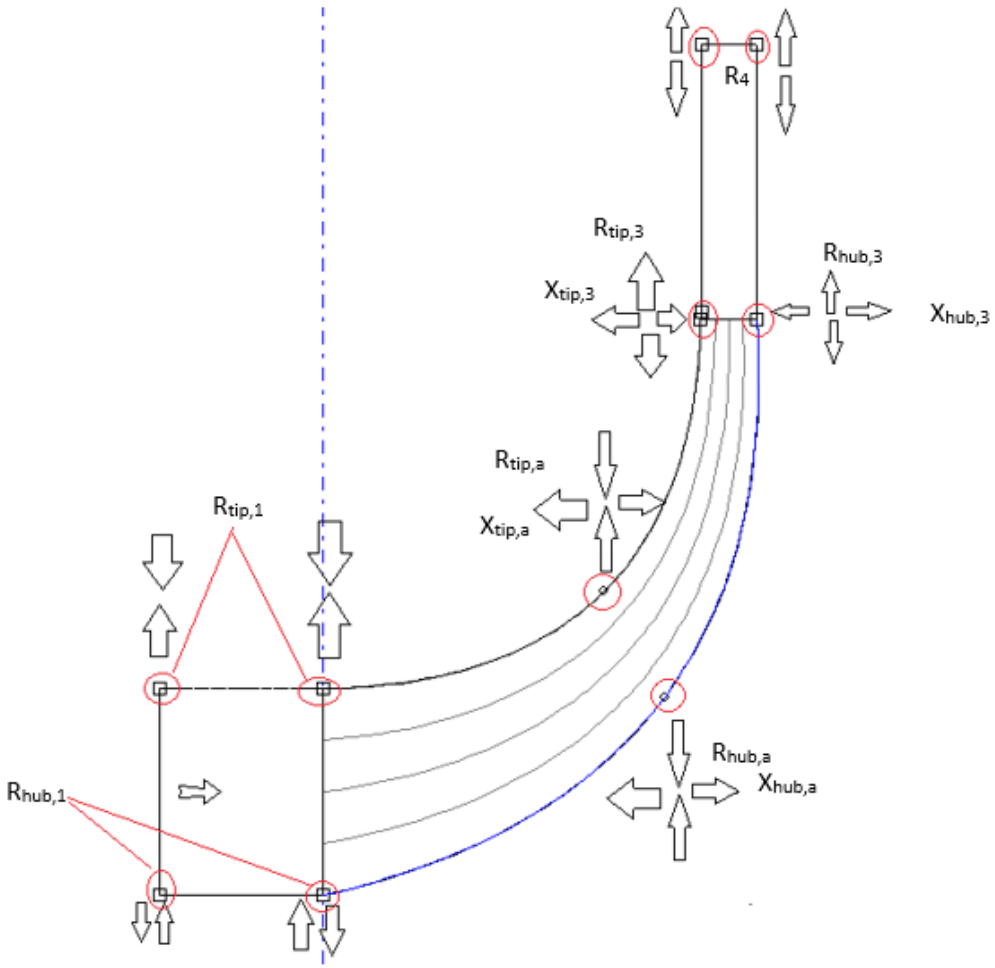

(a)

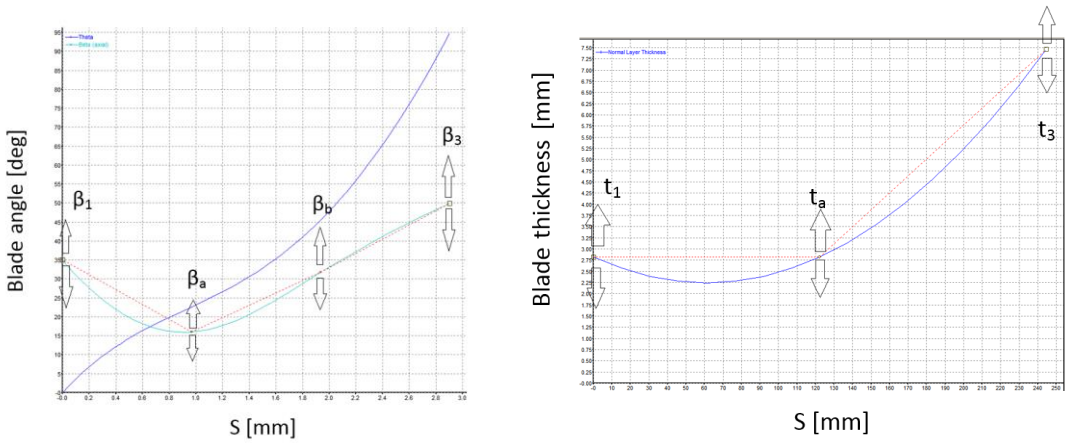

(b)

Figure 4-23: Compressor optimization variables: **(a):** Group A **(b)** Group B.

Volute variables consist of the inlet radius and the elliptical parameters (b/a) in every 45° cross sections(Figure 4-24). The outlet(360°) cross section is set as circular.

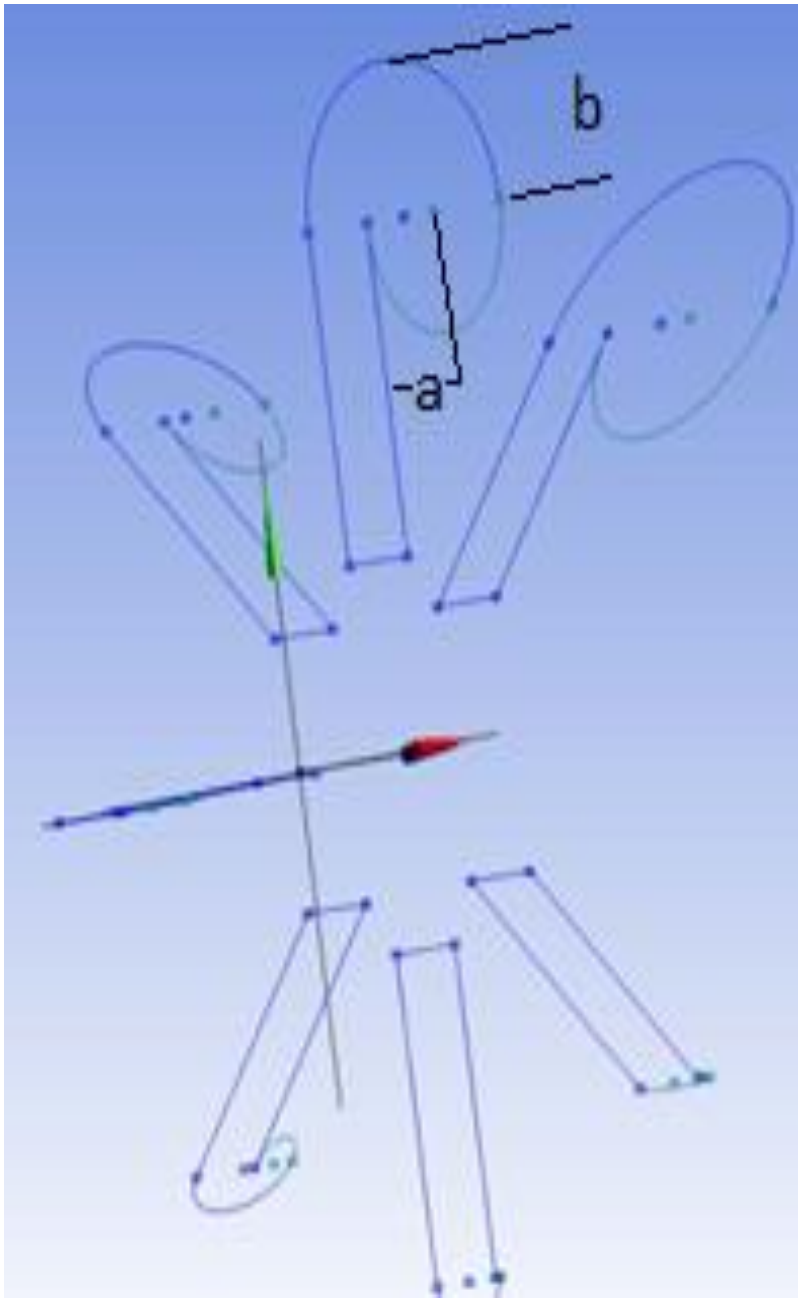

Figure 4-24: Semi external volute cross sections.

As the computational resources are limited to a 4 core 16GB RAM workstation, one optimization cycle last about 3.5 hours.

4.6.1 Centrifugal compressor CFD flow model

Regarding the simulation software, the fluid properties and the flow model, they are described in section 3.7.2.

Concerning the timescale of the pseudo-transient solution method, a physical timescale(dt) is selected,

$$dt = \left[\frac{0.1}{\omega_{imp}}, \frac{10}{\omega_{imp}}\right] \tag{4.109}$$

where ω_{imp} is the impeller angular velocity in [rad/s]. The physical timescale is suggested to be dynamically changed during CFD solving from lower to upper bound, in order to ensure reasonable convergence speed(under 300 second level iterations[1]) while avoids possible startup fatal solver errors due to unstable effects. [ANSYS Inc. 2011]

4.6.2 Centrifugal compressor CFD boundary conditions

The CFD analysis requires a connection between the rotating(impeller) and stationary domains(volute). There is an interface connecting the two domains(impeller with diffuser-volute), so when a change occurs in one domain it would be transferred to the other.

For this analysis, the frozen rotor model is utilized. This model, which is also known as multiple reference frame (MRF) model, treats the flow from one component to the next by changing the frame of reference across the interface, while keeping the relative orientation of the components fixed. The position of the mesh elements does not change between the two interfaces. The frozen rotor model produces a steady-state solution at each time instant, taking into consideration the two frames interaction, but the phenomena, varying with time, are neglected.

Regarding the impeller domain, a single impeller passage domain is modelled in order to reduce the computation time as the flow can be assumed to periodic. Since the impeller is treated as a single blade passage domain while the volute as fully 360° one, the solver is unable to calculate automatically the change in the sector size on either side (known as pitch change) based on the area ratio of the sides of the interface, especially in the current case where the change in the sector size on either side of the interface is huge. Thus, the pitch change is selected as user-defined and is expressed as:

$$pitch\ change\ value = \frac{1}{Z_{FB,imp}} \tag{4.110}$$

where $Z_{FB,imp}$ is the impeller full blade number(main and splitter blades).

[1] In ANSYS CFX there are two levels of iterations. The first level is the linear solver, which is solving the linear equations in matrix form, utilizing multigrid solver. These iterations are invisible. The second level captures the non-linear nature of the Navier Stokes equations. These iterations are visible.

As for the CFD boundary conditions, all walls are modeled as no-slip wall boundaries, apart from the shroud wall, which is modeled as a counter-rotating wall. Additionally, rotational periodic interfaces are used on the outer sides of the impeller blade passage.

The unavoidable tip clearance between the blade tip and the casing shroud, plays an important role on the performance and characteristics of a compressor, thus, interfaces are also set up within the tip clearance region. Considering the thermal conditions for the wall boundaries, these are adiabatic.

The impeller inlet is set as subsonic inlet boundary. For the inlet boundary, the total temperature, total pressure and flow direction are specified. The total temperature is 288.15 K, the total pressure is 1 atm and the inlet flow direction is axial.

The inlet turbulence intensity(I) is set equal to 5%, as given in eq. (3.306). Considering outlet boundary conditions, mass flow rate is imposed. The centrifugal compressor flow domain is depicted in Figure 4-25. Concerning the CFD convergence criteria, they are:

- Velocity and Energy RMS residuals $<=10^{-5}$
- Velocity and Energy imbalance <0.1% (Used to ensure that compressor is operates stably)
- Compressor pressure ratio and efficiency deviation from the average ones, calculated from the past 50 iterations) have to be lower than a tolerance value.

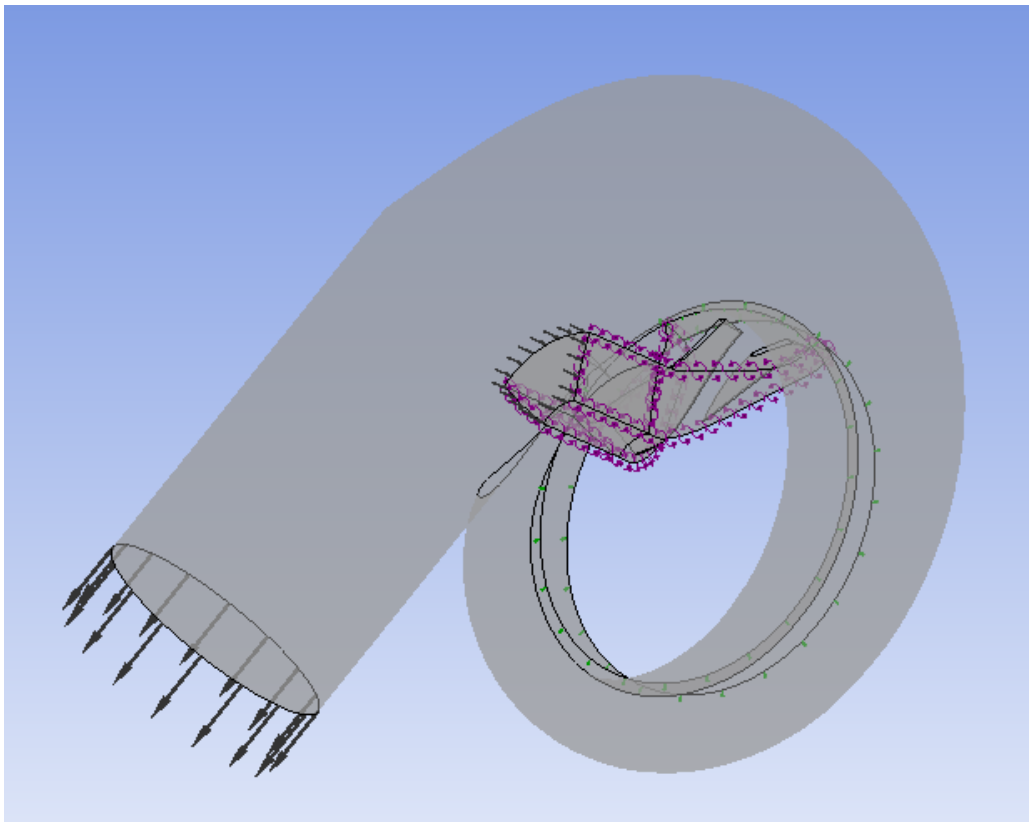

Figure 4-25: Centrifugal compressor flow domain[1].

4.6.3 Centrifugal compressor mesh generation

Regarding the CC mesh generation, it is performed separately for both impeller and diffuser-volute domains. For meshing volute, the multi-zone method is applied, providing automatic decomposition of the body geometry into mapped and free regions. An description is placed in section 3.7.4.

Considering the impeller mesh generation(Figure 4-26), a turbomachinery oriented mesh-generation tool[1], included in the current CFD package, is utilized. This meshing tool has a large degree of autonomy, which leads to a less time-consuming meshing.

The grid is divided into different structured blocks that act as a framework for the positioning of the mesh. The blocks are positioned by default to achieve the desired grid conditions. Each topology block handles the details of the topology surrounding a blade. Each block contains a specific number of mesh elements. The mesh elements vary in size across each of the topology blocks to achieve a smooth transition between blocks. The smooth transition is achieved by node biasing, which also helps reduce the number of mesh elements. 'ATM Optimized' topology method is also employed.

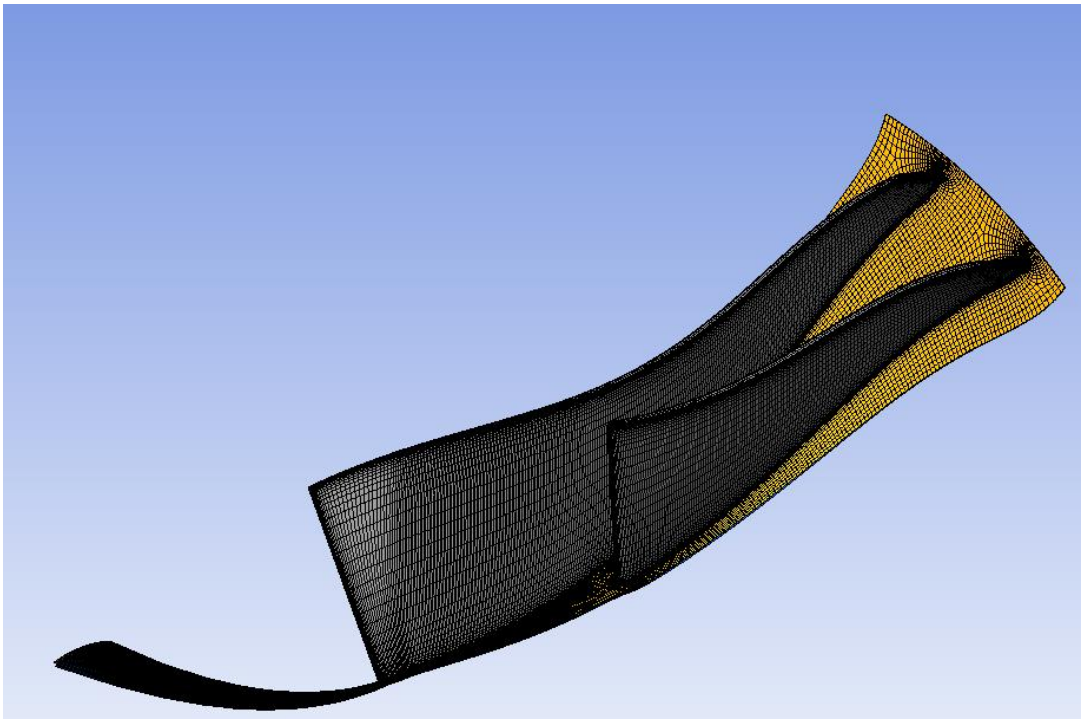

Figure 4-26: Impeller 3D mesh.

For meshing the tip clearance region in the impeller domain(Figure 4-27), the match expansion at blade tip method is employed. With this method, the clearance region grid is automatically adjusted based on the entire impeller mesh size.

[1] https://www.ansys.com/products/fluids/ansys-turbogrid

Concluding, the impeller mesh size is approximately 2 million nodes while volute mesh size of about 1.6 million nodes achieving a maximum y^+ value of the first nodes off the wall about 2.6 and 2.1 respectively. Both mesh sizes result from mesh independent study. The impeller mesh independent study is depicted in Figure 4-28 while the volute one is presented in chapter 3.

Both components y^+ values are lower than five, which ensures according to the CFD software manual that the CFD model captures the laminar and transitional boundary layers correctly. [ANSYS Inc. 2011]

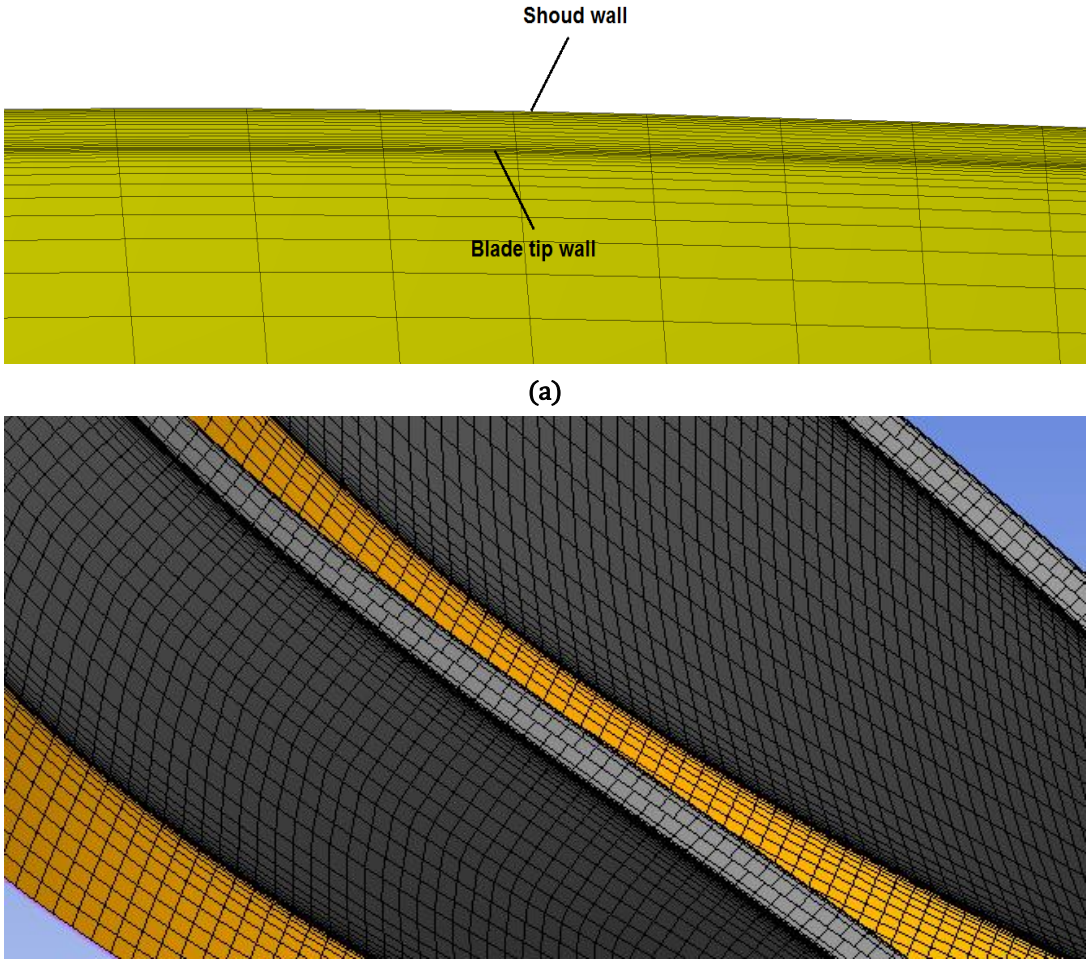

Figure 4-27: Impeller mesh in: **(a)** periodic surface in clearance region **(b)** tip surface.

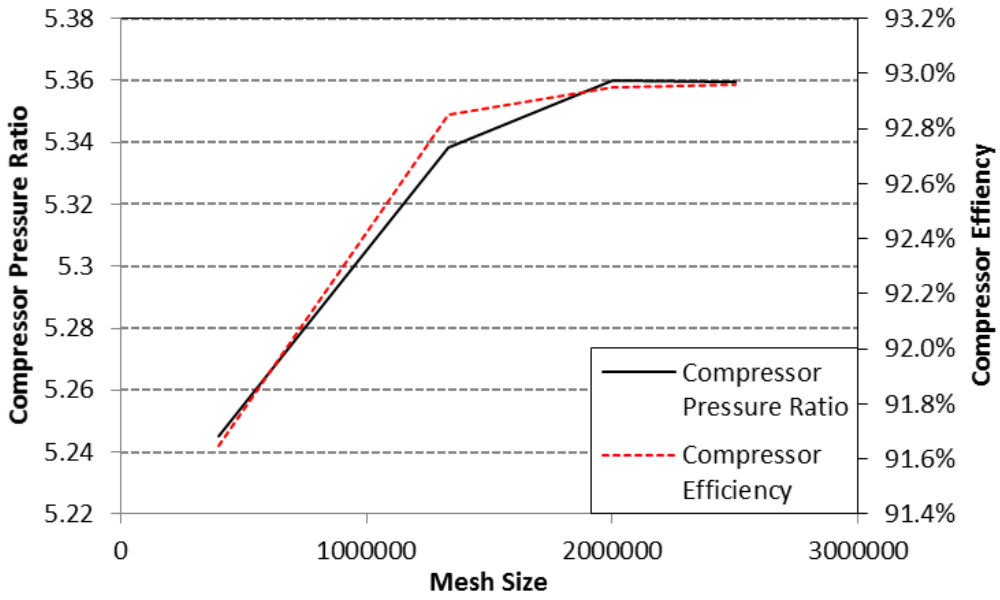

Figure 4-28: Impeller mesh independency study.

4.6.4 Centrifugal compressor CFD model validation

Concerning CFD model setup validation, the NASA B30-D2 (Figure 4-29) vaneless diffuser centrifugal compressor is selected [Medic et al. 2014].

Figure 4-29: NASA B30-D2 Impeller 3D geometry. (Medic et al. 2014).

The validation study is limited to impeller and vaneless diffuser as there is no available volute geometry. This geometry corresponds to a transonic compressor, which was studied as both vaned and vaneless diffuser with a NASA in-house CFD code[Medic et al. 2014]. Between them, the vaneless diffuser compressor is chosen as more relative to the current work. The maximum error between the only available efficiency curve and the CFD simulation results is less than 0.5%. The comparison is shown in Figure 4-30.

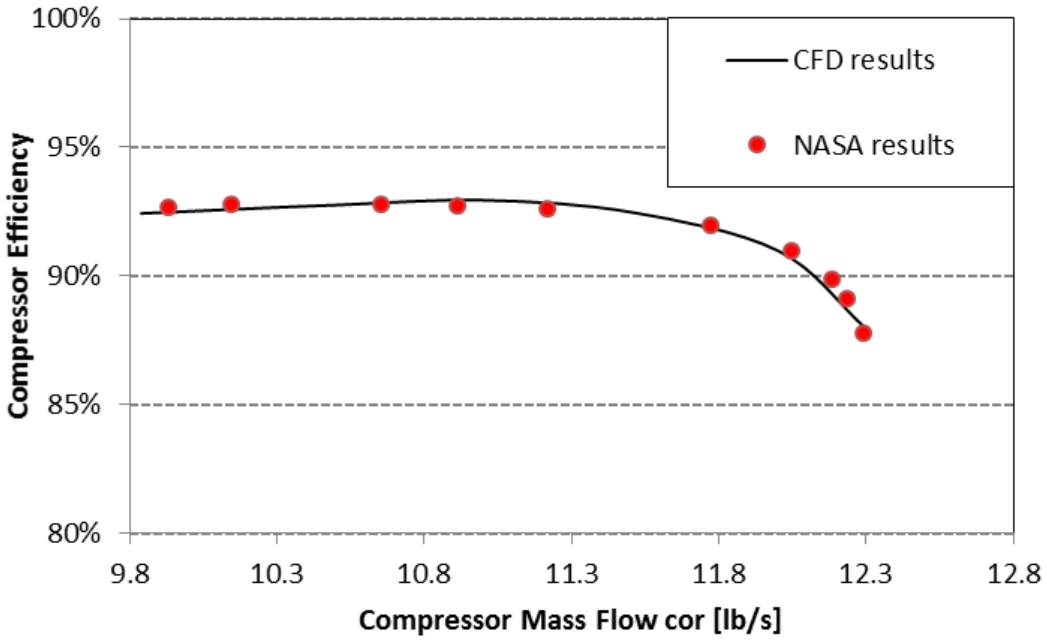

Figure 4-30: CFD compressor model validation. (Medic et al. 2014)

4.7 Summary and Discussion

In this chapter, the automated T/C design process was presented. It basically provides a design solution which is characterized by bothstructural integrity and matching quality with the entire T/Ced diesel engine system and its manufacturability.

A weighted single-objective optimization procedure is followed, in order to design a turbo-component or a T/C to match the entire system in an improved way, while ensuring its static and modal structural integrity.

Taking advantage from the usage of dimensionless parameters as optimization variables with defined ranges, it was shown that it can provide a more general and automated design process, since it does not require neither the optimization variables ranges nor the initial geometry to be redefined for different T/C scales, using the certified shop trials data as the only inputs.

Focusing on the dimensionless variables usage, the preprocessor philosophy, its correlations and the coupling with the meanline model were also presented.

For ensuring the static and the modal structural integrity, a simplified structural analysis tool was developed, that integrates a 1D to 3D transformation sub-tool which, in turn, allows the calculation of the required blade mass, center of mass, and the area moment of inertia.

Finally, a 3D high fidelity design procedure was presented, utilizing commercial 3D CFD and FEA tools, which is limited to vaneless diffuser CC design. Taking advantage from the coupling with the preliminary design tool, the detailed design does not rely on an initial 3D geometry either, which in many cases is not even available.

4.8 References

Alexiou, A., Aretakis, N., Kolias, I. and Mathioudakis, K.,. (2021). Novel Aero-Engine Multi-Disciplinary Preliminary Design Optimization Framework Accounting for Dynamic System Operation and Aircraft Mission Performance. Aerospace / MDPI, 8(2), 49.

Ansys, Inc. (2011) ANSYS CFX-Solver Theory Guide. Canonsburg, PA 15317.

Aungier, R. H. (2005). TurbineAerodynamics Axial Flow And Radial Inflow Turbine Design And Analysis. ASME PRESS, New York.

Aungier, R.H. (2000). Centrifugal Compressors, A Strategy for Aerodynamic Design and Analysis. ASME PRESS.

Ceyrowsky, T., A. Hildebrandt & Schwarze, R. (2018). Numerical investigation of the circumferential pressure distortion induced by a centrifugal compressor's external volute. Proceeding of ASME Turbo Expo, GT 2018-75919 Oslo, Norway.

Chatzisavvas, I., Nowald, G., Schweizer, B. and Koutsovasilis, P. (2017). Experimental and Numerical Investigations of Turbocharger Rotors on Full-Floating Ring Bearings With Circumferential Oil-Groove. Proceeding of ASME Turbo Expo, Charlotte, North Carolina, USA.

Goudas, A. (2019). Design and Modeling of Printed-Circuit Heat Exhangers and Centrifugal Compressors for Supercritical Carbon Dioxide Power Cycles. PhD Thesis, AUTH.

Japikse, D. (1996). Centrifugal Compressor Design and Performane. *3rd ed., Concepts ETI Inc.: Wilder,TN, USA, pp. 2.26–2.81.*

Japikse, D. and Baines, N. C. . (1997). *Introduction to Turbomachinery.* Concepts ETI Inc and Oxford University Press.

Li P. Y., Chu-Wei Gu, C. W., and Song, Y. (2015). *A New Optimization Method for Centrifugal Compressors based on 1D Calculations and Analyses.* MDPI Energies, Volume 8, pp 4317-4334.

Medic G., Sharma, O. P. ,Jongwook, J., Hardin, L. W., McCormick, D. C., Cousins, W. T., Lurie, E. A., Shabbir, A. , Holley,B. M., and Van Slooten, P. R. (2014.). *High Efficiency Centrifugal Compressor for Rotorcraft Applications.* NASA/CR—2014-218114/REV1. NASA Langley Research Center, Hampton, Virginia.

Nguyen-Schäfer, H.,. (2015). *Rotordynamics of Automotive Turbochargers.* Spinger International Publishing, Second Edition.

Person, J.,. (2015). 1D Turbine Design Tool Validation and Loss Model Comparison: Performance Prediction of a 1-stage Turbine at Different Pressure Ratios. https://www.diva-portal.org/smash/get/diva2:878059/FULLTEXT01.pdf

Rechenberg, I.,. (1989). *Evolution Strategy: Nature's Way of Optimization.* Springer-Verlag, Berlin.

Schaber, R., C. Salpingidou and H. Klingels. (2019). From interdisciplinary propulsion system parameter studies to initial module design - an integrated approach for conceptual design. ISABE-24040.

Schwefel, H. P.,. (August 1993). *Evolution and Optimum Seeking: The Sixth Generation.* John Wiley & Sons, Inc.605 Third Ave. New York, NYUnited States.

Shettigar, V. O., Pesiridis, A.,. (2014). Material Selection for variable geometry turbine nozzle for gasoline engine application. *Proceeding of ASME Turbo Expo 2014, GT2014-27119, June 16-20, 2014, Dusseldorf, Germany.* doi:https://doi.org/10.1115/GT2014-27119

Stuart, C.,Spence, S.,Filsinger, D., Starke A. and Kim, S. I. (June 26 - 30 , 2017.). *Characterising the influence of impeller exti recirculation on Centrifugal Compressor work input.* Proceeding of ASME. GT2017-63047. Charlotte, NC, USA.

Stuart, C., Spence, S., Filsinger, D., Starke, A. and Kim S. (2018) A three-zone modelling approach for centrifugal compressor slip factor prediction." Proceeding of ASME Turbo Expo. GT2018-75324. Oslo, Norway, June 11-15.

Tang, S., Peng, M., Xia, G., Wang, G. and Zhou, C.,. (2019). *Optimization design for supercritical carbon dioxide compressor based on simulated annealing algorithm.* Elsevier,Annals of Nuclear Energy 140(5):107107.

Wasserbauer, C. A., Kofskey, M. G. and Nusbaum, W. J. (1966). *Cold performance evaluation of a 4.59-inch Radial-Inflow Turbine designed for a Brayton-cycle space power system.* NASA TN D-3260, Lewis Research Center, Cleveland Ohio.

Wiesner, F.J. (1967). *A Review of Slip Factors for Centrifugal Impellers.* ASME Journal of Eng. Power Vol 89: pp. 558–572.

Chapter

5 Automatic Turbocharger Retrofit process

In the current chapter, an automatic T/C retrofit process is presented. All T/C retrofit options are analyzed, including all available turbo-components examination processes and criteria in order to select the one that best matches the entire engine system, aiming to retain or improve the diesel engine efficiency.

A retrofit process that relies on the engineer's personal judgment may not be optimal and thus a T/Ced diesel engine unnecessary degradation may occur. With the use of an automated process as the one presented here, it is guaranteed that the best retrofit solution will be provided. Additionally, the automation of such a process will improve greatly the productivity of T/C manufacturers by decreasing the time spent in tasks such as, searching for available components, matching, analyzing and re-designing a new one.

5.1 General description

The process provides an automatic T/C retrofit solution, by examining all turbo-components (compressors and turbines) available in a data base. It selects the one that best matches the entire engine system, aiming at retaining or improving the diesel engine original efficiency, certified during shop trials. Basically, it sorts all available turbo-components, the technical specifications of which are stored in a database, according to the matching quality(section 3.8) and the calculated overall performance. Additionally, a capability of checking specific turbo-components as retrofitting parts is provided, leading to a high computational cost reduction, if specific original T/C component (e.g. turbine) is available.

In case that the best fitted T/C does not fully satisfy the matching criteria, the process also integrates a flow trimming sub-tool for compressor or turbine that adapts the T/C performance in order to satisfy the matching requirements. During a retrofit procedure, four options are analyzed, aiming to guide the T/C manufacturer in opting for the most suitable one, based on system matching-

performance and manufacturing economic analysis. Regarding the retrofitting options, they are the followings:

- Option 1: T/C component (Compressor or Turbine) retrofit, using the corresponding available turbo-components.
- Option 2: Entire T/C retrofit, using available compressor and turbine pairs.
- Option 3: T/C component re-design (compressor or turbine optimization).
- Option 4: Entire T/C re-design (compressor and turbine combined optimization).

For making the T/C retrofit process fully automated, the current process, taking advantage from the T/Ced diesel engine simulation process(Chapter 3), utilizes 1D meanline models for calculating turbomachinery components maps and a fully coupled process for integration with the turbomachinery components and the diesel engine.

5.2 Turbo-component retrofit

The turbo-component retrofit process refers to a component (e.g. compressor) replacement, while the other turbo-component (e.g. turbine) is retained. The new component is chosen from the inventory of available ones based on its performance characteristics, aiming to provide the best choice among those. The current option is the one with the lowest process cost as only one component is replaced. Figure 5-1 depicts the option 1 retrofit process.

Specifically, it calculates the overall T/Ced diesel engine fuel consumption and matching quality for each available turbo-component. Then, sorts them based on their fuel consumption and their matching quality. In case a turbo-component does not satisfy the matching criteria(section 3.8), it is excluded from the results sorted list, as an infeasible solution.

The average diesel engine fuel consumption is calculated as follows:

$$\dot{m}_{fuel} = \frac{\sum hr_i \, \dot{m}_{fuel,i}}{\sum hr_i} \tag{5.1}$$

where i is the diesel engine operating points and hr_i the corresponding operating hours.

Concerning the structural integrity, both the static and the modal structural analysis should be carried out. It is assumed that each turbo-component, having been part of a commercial T/C, it is designed to be structurally safe from both static and modal analysis perspective. Assuming that the T/C maximum speed is close to design speed, then the retrofitted T/C static structural integrity is automatically ensured. However, this assumption cannot be applied from a modal analysis perspective, due to different turbo-components coupling. Thus, a

simplified modal analysis is performed, extensively described in section 4.4, ensuring the retrofit solution structural modal integrity.

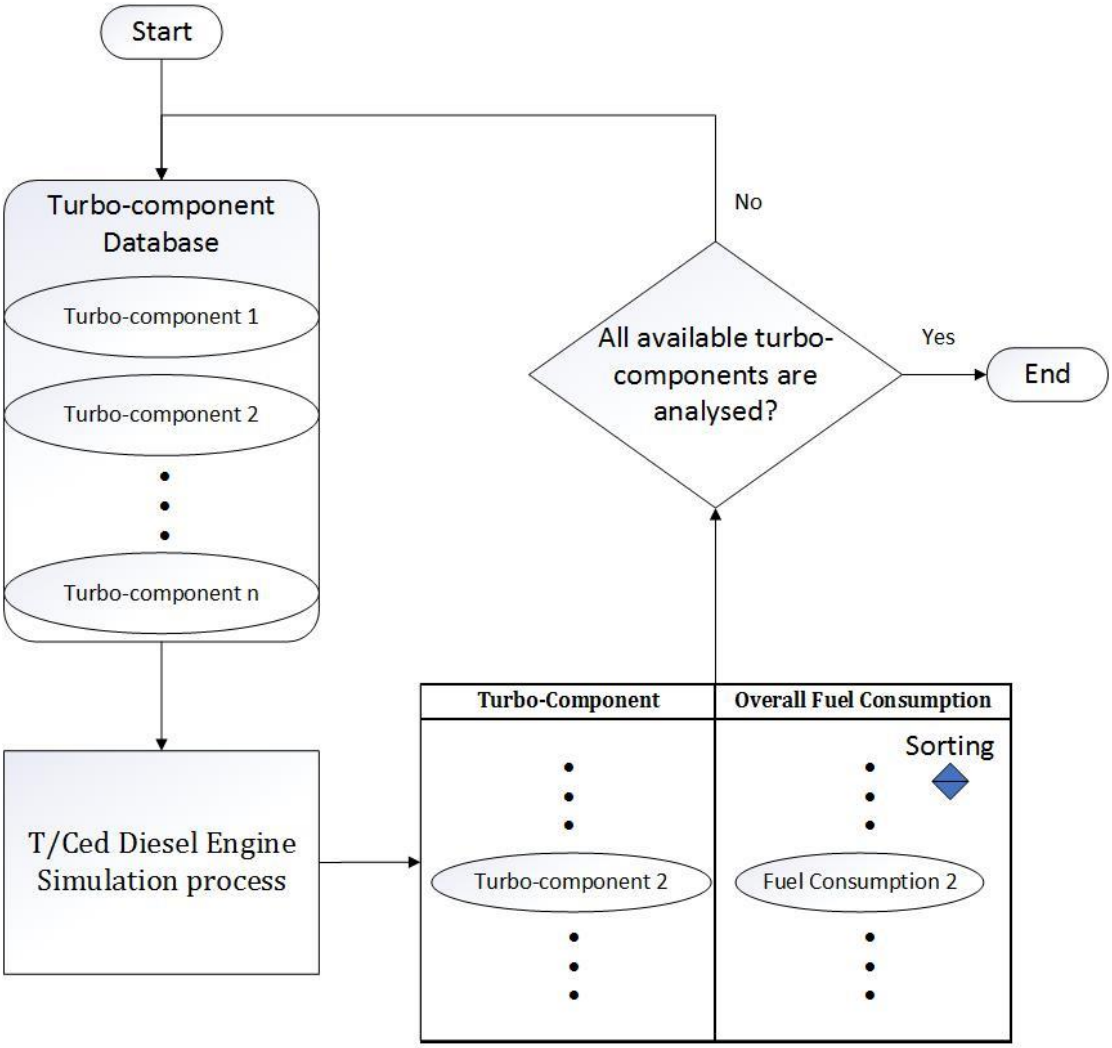

Figure 5-1: T/C Turbo-component retrofit.

5.3 Entire turbocharger retrofit

Considering the entire T/C retrofit process, both turbo-components are replaced with available ones. The process chooses the best fitted turbo-component pairs, according to the overall fuel consumption, while ensuring matching quality and structural integrity. The Figure 5-2 depicts the option 2 retrofit process, where the overall diesel engine fuel consumption is calculated based on equation (5.1) and the constraints are the same with the ones used in option 1.

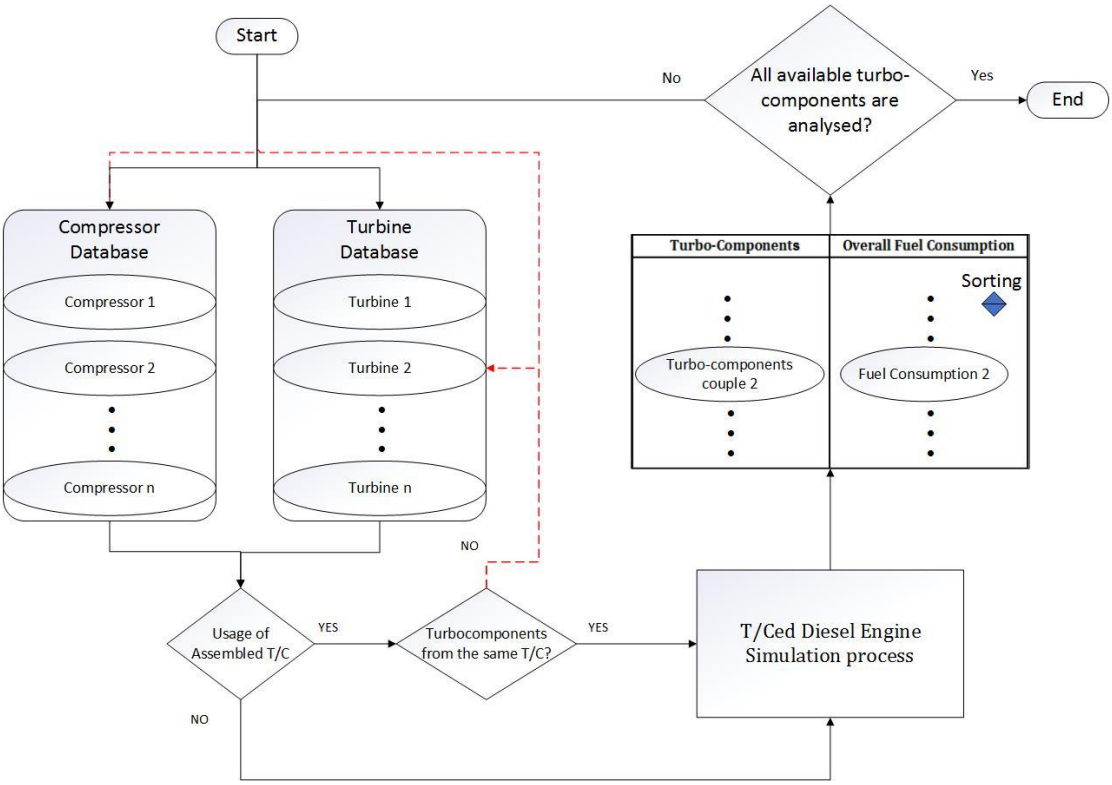

Figure 5-2: Entire T/C retrofit.

5.4 Available turbo-components data base

The available turbo-components data-base, developed in this PhD thesis, includes 13 different T/C geometries, provided by a T/C manufacturing company[1]. These geometries are used as input in the compressor and turbine meanline models, in order to generate the corresponding performance maps.

Concerning the data base portfolio(Figure 5-3), it comprises single stage turbochargers, capable of satisfying mass flow rates between 0.61 kg/s to 2.5 kg/s, hence allowing a flexible retrofit for a given engine application with defined engine power range.

Finally, each time a new turbo-component performance prediction is performed, automatically its geometry and its performance map are both inserted to the database.

[1] www.turbomed.gr

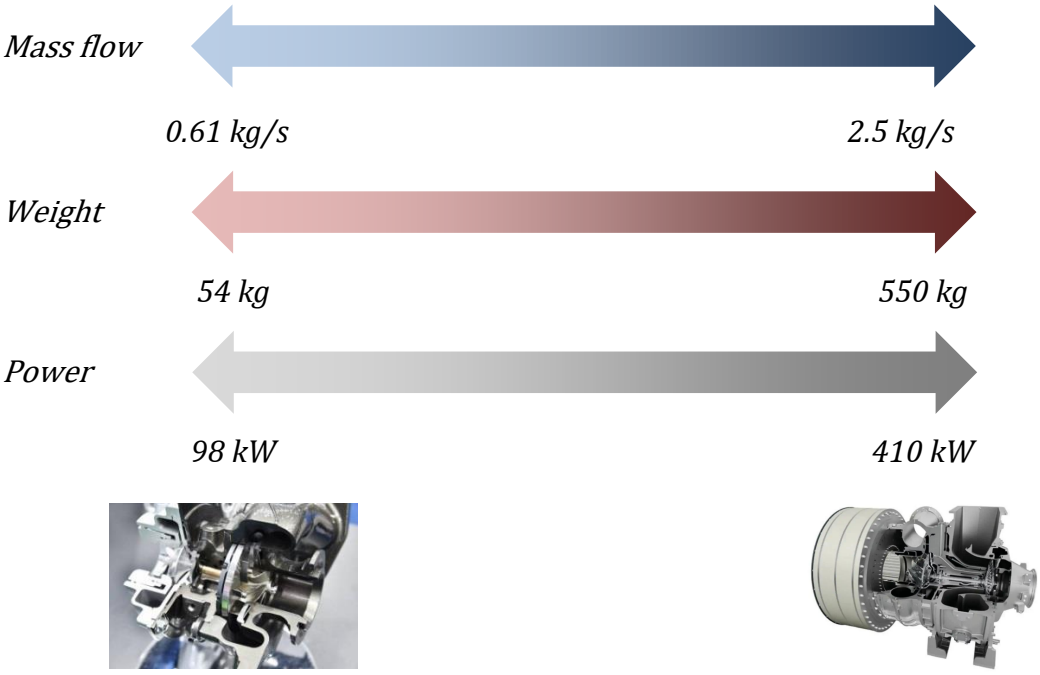

Figure 5-3: Database T/C mass flow and weight range.

5.5 Trimming sub-tool process

In case the best-retrofitted T/C does not fully satisfy the matching criteria, a trimming process can be performed for compressor or turbine, in order to adapt the performance map to satisfy the matching quality and the stable operation requirements. According to Swain and Engeda (2014) there are 2 trimming approaches, the flow (Figure 5-4a) and axial (Figure 5-5a) trimming.

The flow trimming reduces mass flow while maintaining both pressure ratio and efficiency as shown in Figure 5-4, where both the impeller head coefficient and its isentropic efficiency against flow coefficient are predicted for each defined flow trim. In this figure, the flow coefficient for each trimmed impeller is normalized by the choked flow coefficient. As Swain and Engeda (2014) point out, the relative flow range (that is, the stall margin) actually increases with flow trimming.

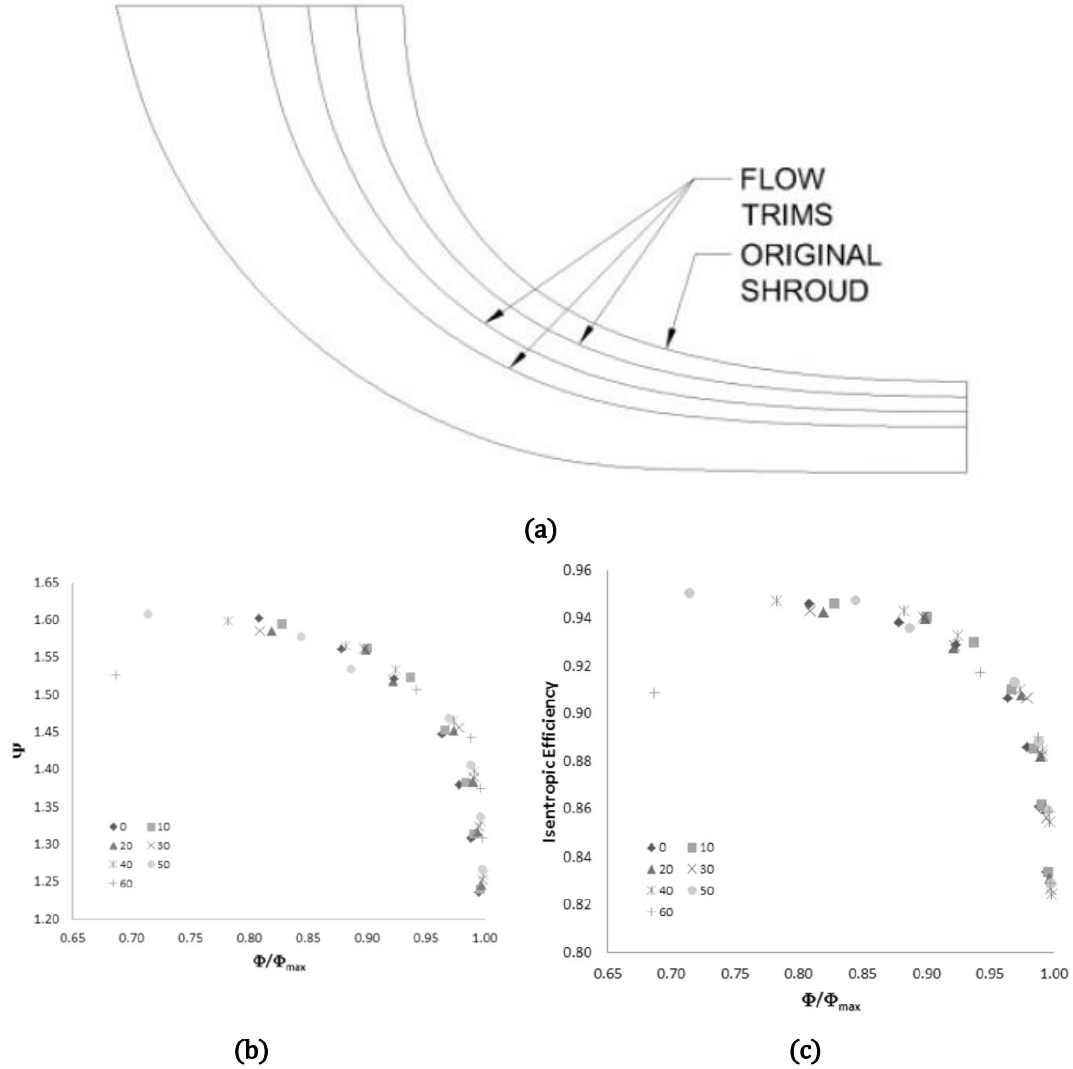

Figure 5-4: Flow-trimmed impeller: **(a):** Meridional trim profile **(b)** Head coefficient against flow coefficient ratio **(c)** Isentropic efficiency against flow coefficient ratio. [Swain and Engeda (2014)]

According to Rodgers (2001), the impeller flow trimming is limited to a range of specific speeds between 0.5 and 1.2. A later study by Zhang et al. (2010) showed that an impeller with a baseline specific speed of 0.06 was flow trimmed to 75% of its original blade height and found that flow trimming could be applied to low specific speed impellers but recommended that trimming be limited to 50% of the baseline blade height. So, the proper percentage of blade trimming depends on the baseline impeller geometry.

Regarding the axial trimming process, it reduces pressure ratio without adversely affecting the flow range or impeller efficiency as depicted in Figure 5-5, where both the impeller head coefficient and its isentropic efficiency against flow coefficient are predicted for each defined axial trim. Basically, with this mechanism, the pressure ratio is reduced in the passage, leading to higher throughflow velocity. According to Swain and Engeda (2014), the axial trimming is limited at some point by the reduction of the choked flow rate, which in the

Swain and Engeda (2014) case, presented in Figure 5-5b, is the 60% trim. This reduction in choked flow is due to the fact that reducing the passage area in the radial portion of the passage moved the choke point from the inlet to the passage.

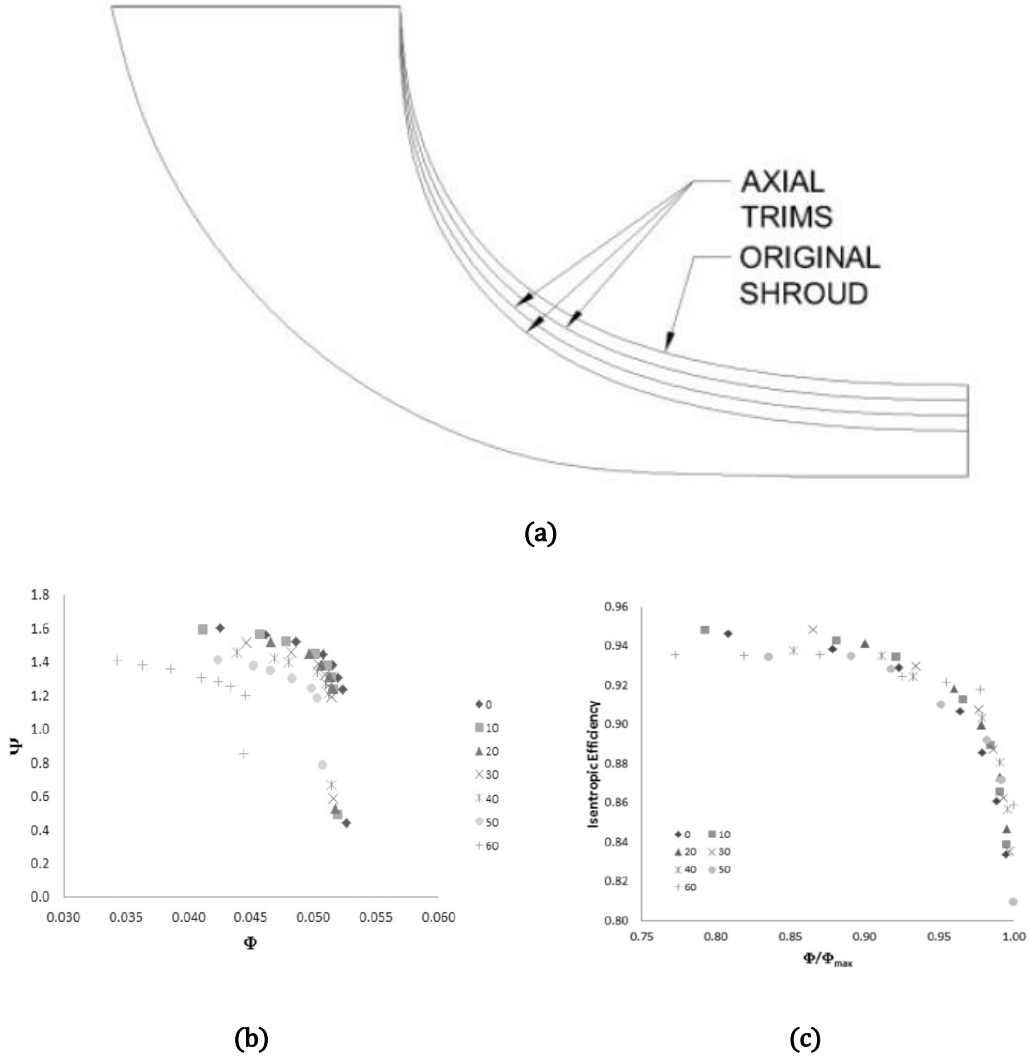

Figure 5-5: Axially-trimmed impeller: **(a):** Meridional trim profile **(b)** Head coefficient against flow coefficient ratio **(c)** Isentropic efficiency against flow coefficient ratio. [Swain and Engeda (2014)]

5.6 Summary and Discussion

In this chapter, an automatic T/C retrofit process was presented. Utilizing the T/Ced diesel engine simulation process, it examines all turbo-components (compressors and turbines) available in a data-base, in order to select the one that best matches the entire engine system, aiming at retaining or improving the diesel engine original efficiency, certified during shop trials.

Basically, it sorts the available turbo-components, the technical specifications of which are stored in a database, according to the matching quality and the calculated overall performance. Additionally, a capability of checking specific turbo-components as retrofitting parts is provided, leading to a high computational cost reduction, if specific original T/C component (e.g. turbine) is available.

Also, a manual trimming sub-tool is integrated, in order to adapt the T/C performance, in case that there is no available retrofit solution that can fully satisfy the engine operation requirements.

5.7 References

Rodgers, C. (2001). *Centrifugal compressor blade trimming for a range of flows.* In Proceedings of ASME Turbo Expo 2001-GT-0316, V001T03A020; 7 pages, New Orleans, Louisiana.

Swain, D. and Engeda, A. (2014). *Effect of Impeller blade trimming on the performance of a 5,5:1 pressure ratio centrifugal compressor.* IMechE, Part A Journal of Power and Energy Vol 228 (2014): pp. 878–888.

Zhang, D., DiLiberti, J. L., and Cave, M. (2010). A CFD study on a base and a flow-trimmed low specific speed centrifugal compresor. In Proceedings of the ASME 2010 International Mechanical Engineering Congress & Exposition.

Chapter

6 Application case A: Turbocharger Retrofit and Redesign

The T/C design and retrofitting processes presented in the previous chapters are applied in a retrofitting case study, where all theretrofitting options presented in Chapter 5 are analyzed. Considering the diesel engine, a T/Ced 5-cylinder 4-stroke diesel auxiliary engine is selected for this test case, the technical specifications of which, including its certified shop trials, are extensivly described in section 3.8.

In the first and second option, a T/C retrofitting is carried out, examining all available turbo-components.

In the third option, a compressor designing is performed, following a weighted single-objective optimization procedure, in order to provide an improved retrofitting solution, aiming to at least reconstituting the original diesel engine performance, while ensuring compressor structural integrity. Taking advantage from the usage of dimensionless parameters as optimization variables with defined ranges, a more general and automated design process is provided since it does not require neither the optimization variables ranges nor the initial geometry to be redefined for different T/C scales, utilizing existing shop trials data as the only inputs.

In the fourth option, similarly to option 3, a weighted single-objective optimization procedure is employed to design both the compressor and the turbine to match the entire T/Ced system in an improved way. The optimization process focuses on engine fuel consumption reduction for the engine range of operation, while ensuring appropriate matching between the turbomachinery components and the diesel engine. The structural integrity (static-modal) for both turbo-components is ensured by using a simplified structural and modal analysis. Additionally, volute surrogate loss models, trained with CFD data, are also provided for both CC and RT as option, allowing for a more detailed design process. The process produces four T/C (compressor and turbine) improved 1D geometries (if it is possible), of different possible T/C configurations, namely vaneless diffuser centrifugal compressor – axial turbine, vaned diffuser centrifugal compressor – axial turbine, vaneless diffuser centrifugal compressor

– radial turbine, vaned diffuser centrifugal compressor – radial turbine. This way the combination that gives the best improvement in the diesel engine operation is identified.

Finally, a techno-economical assessment is carried out, analyzing all four retrofit options in order to propose the most profitable one.

6.1 A turbocharger retrofitting with selected turbo-components

A T/C retrofitting with selected turbo-components is carried out, aiming to guide the T/C manufacturer in opting for the most suitable one. The selection is accomplished by sorting the available turbo-components, the technical specifications of which are stored in a database(section 5.4), according to the matching quality(section 3.8) and the calculated overall performance eq. (5.1) .

In the current section, the replacement of both a T/C component and entire T/C is studied.

6.1.1 Option 1: Compressor retrofit

In the first option, a retrofit process is performed by choosing a compressor individually, while retaining the original turbine. The retrofitted compressor operating line is presented in Figure 6-1, showing the matching quality with the entire diesel engine system.

A 0.8% increase in SFC at nominal operational point is also noticed (Figure 6-2). Also, comparing both original turbine operating lines before(Figure 3-43) and after retrofit(Figure 6-2), it can be seen that the line lays in lower efficiency areas after retrofit, hence contributing to the engine SFC increase.

Considering the significant T/C speed drop(about 12%), it is caused due to the higher capacity CC(higher pressure ratio) usage, shown in Table 6-1, combined with the turbine efficiency reduction.

The retrofitted compressor is chosen from the inventory of available compressors, which already exists and have their corresponding performance characteristics. The process makes the best choice among those, but even the most suitable one is not perfectly fitted for the given diesel engine.

Table 6-1: Geometrical parameters change between baseline and retrofitted compressors.

Parameter	Change
$R_{hub,1}$	27%
$R_{tip,1}$	2%
R_3	11%
R_4	14%
Main Blades	-1

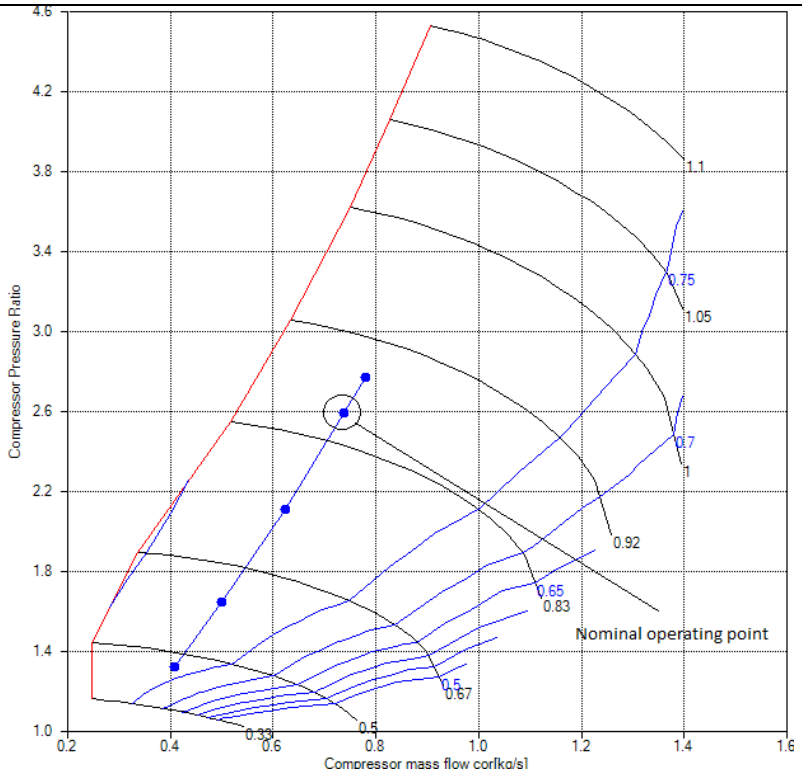

(a)

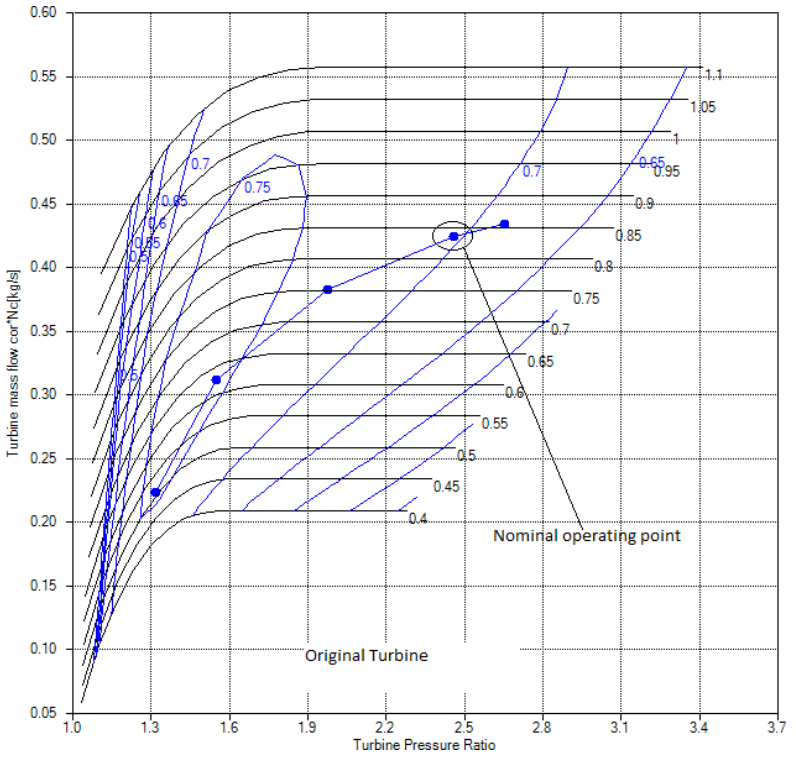

(b)

Figure 6-1: Retrofitted map and operating line (Option 1): **(a)** Compressor **(b)** Turbine.

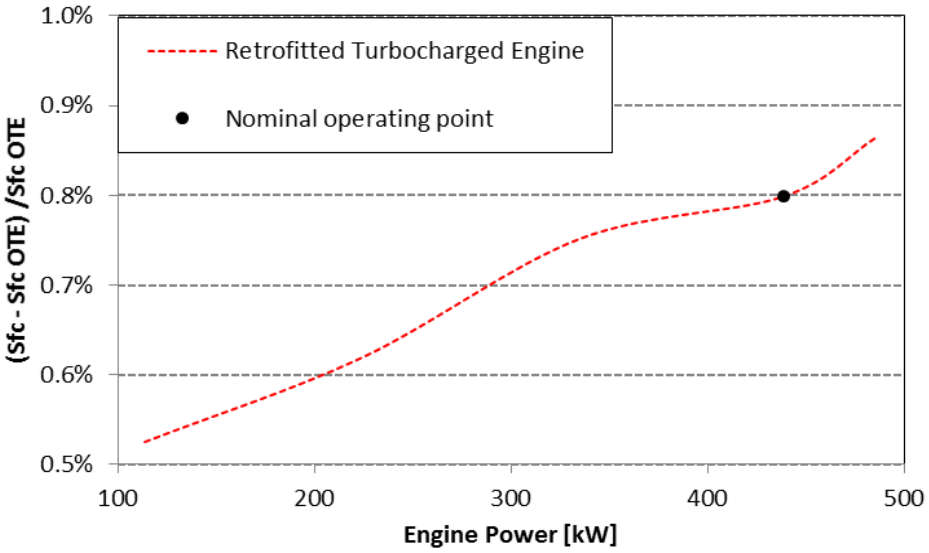

Figure 6-2: SFC change for retrofitted compressor.

For further demonstrating the process capabilities, the flow trimming process, presented in section 5.5, is applied in the retrofitted compressor. This process, by cutting the compressor blade tip, moves the stall line away from the operating line. This process capability is applied in case that compressor operates close to stall line.

The performance maps for trimmed compressors by 5 and 10% along with T/C operating line are shown in Figure 6-3. Both trimmed compressors ensure the T/C stable operation and the matching quality between compressor and the entire diesel engine system.

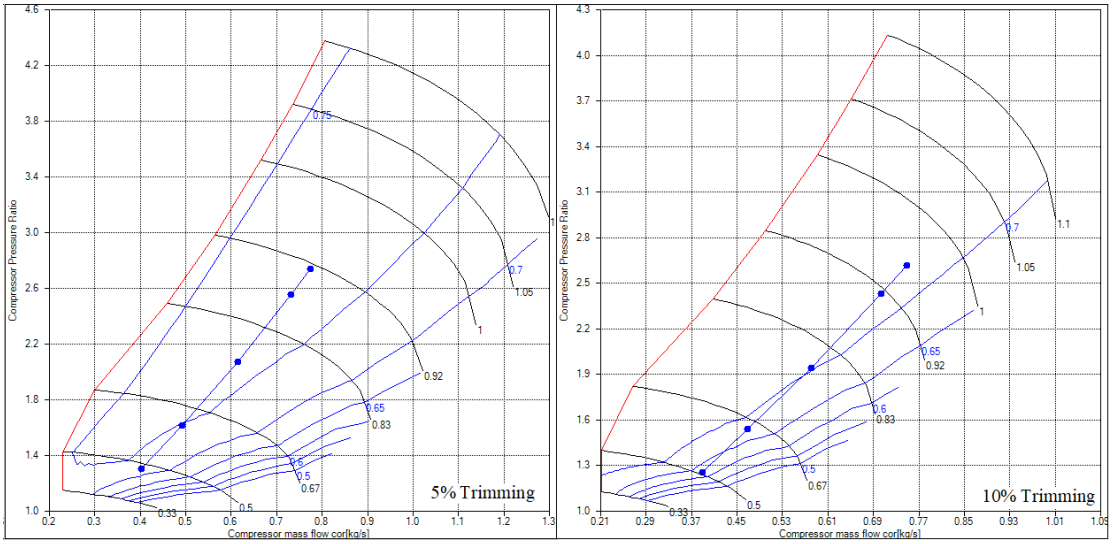

Figure 6-3: Trimmed compressor performance maps and operating lines.

The trimmed compressor by 5% is considered more appropriate because the specific fuel consumption increase is negligible compared to the 10%, as

Figure 6-4 shows. Additionally, the T/C maximum speed is slightly higher by 5%, although having a maximum speed lower than design speed, hence not working in over-speed conditions.

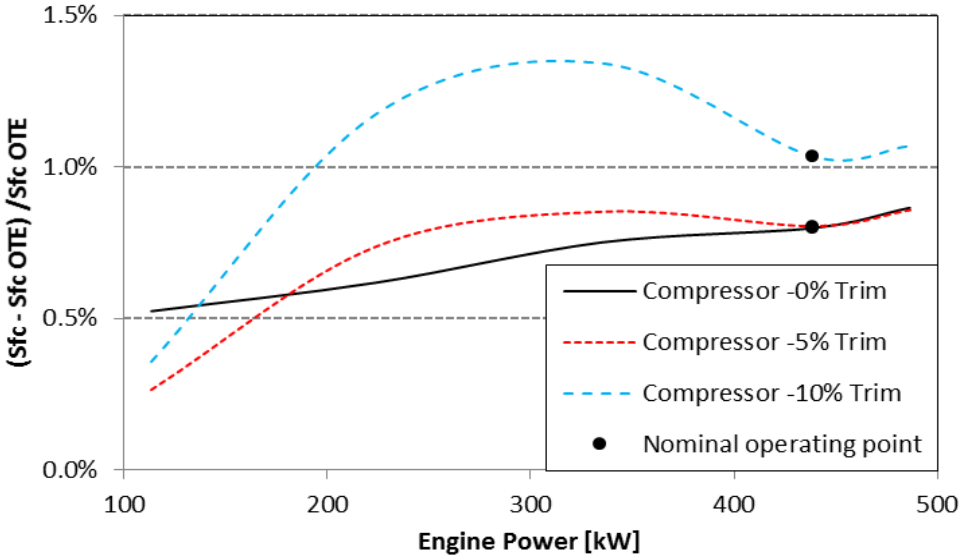

Figure 6-4: SFC change for trimmed compressors retrofit.

6.1.2 Option 2: Entire turbocharger retrofit

In the second option, a retrofit process is carried out using available compressor and turbine. The best fitted T/C is the one that consists of the compressor, chosen in option 1.

The T/C speed does not exceed the nominal value, hence decreasing the chance of bearing failure due to over-speed. However, due to the turbine replacement, the maximum T/C speed increases about 11.37% (Figure 6-1 and Figure 6-6). Regarding the turbine comparison between both the baseline and the retrofitted one, they both have similar impeller geometry(Figure 6-5). Although, the vaned nozzle existence in the retrofitted one justifies its more efficient operation.

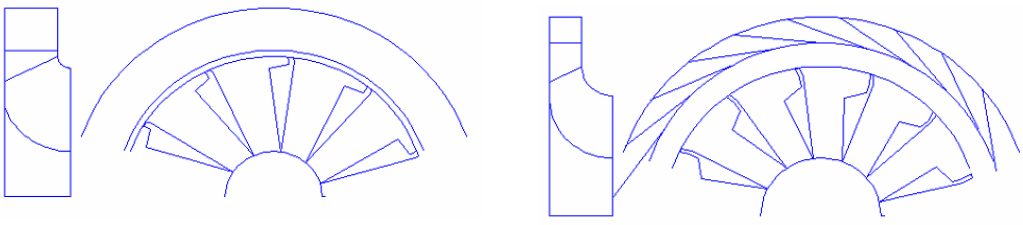

Figure 6-5: Turbine geometry: **(a):** Baseline **(b)** Retrofitted

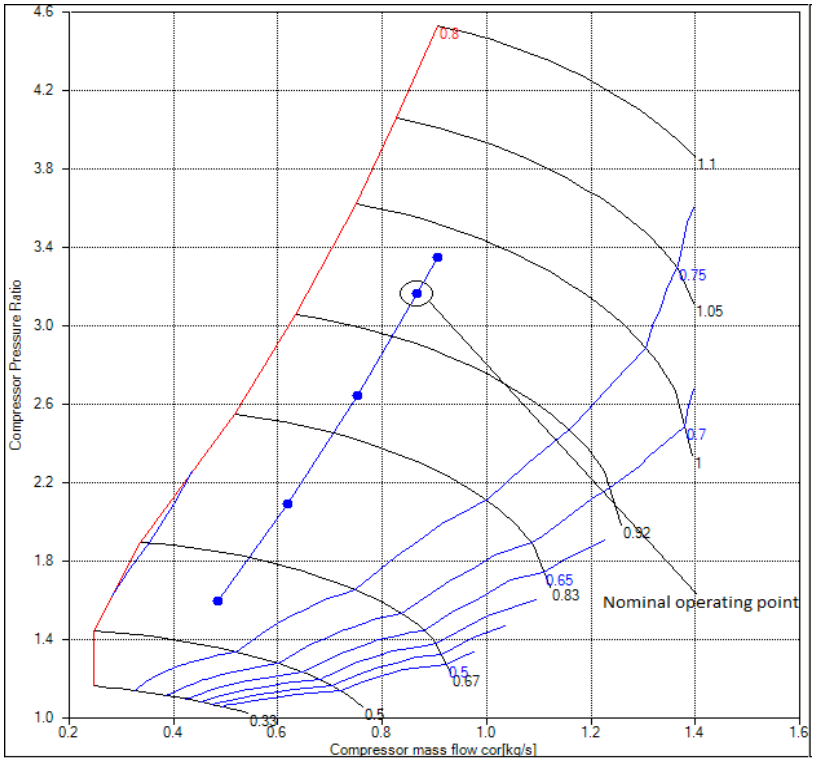

(a)

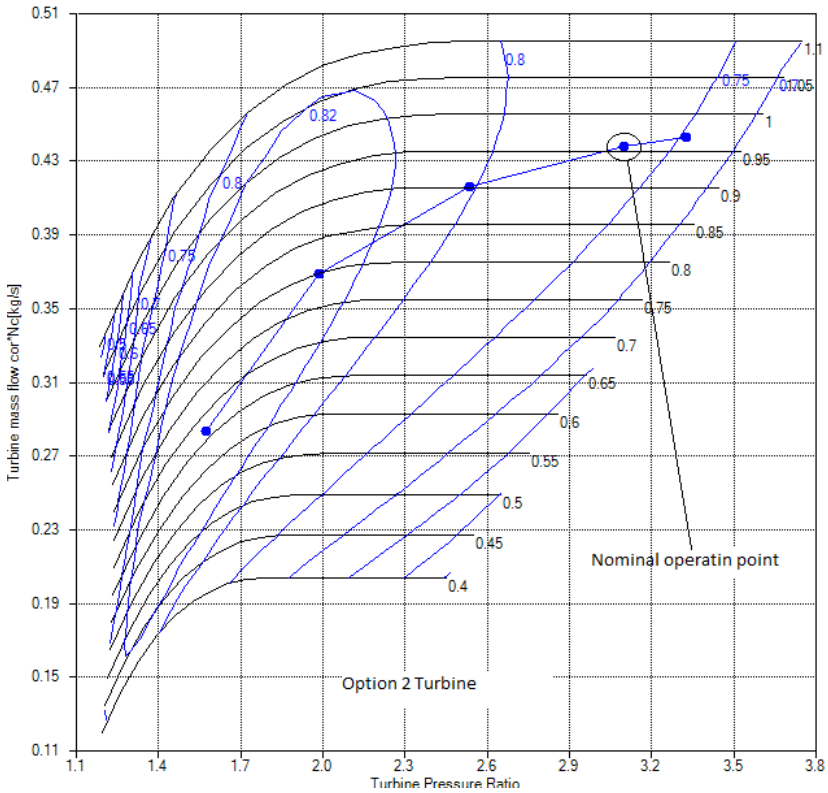

(b)

Figure 6-6: Retrofitted map and operating line (Option 2): **(a)** Compressor **(b)** Turbine.

For the SFC line, a slight increase in nominal operating point about 0.27% is shown in Figure 6-7.

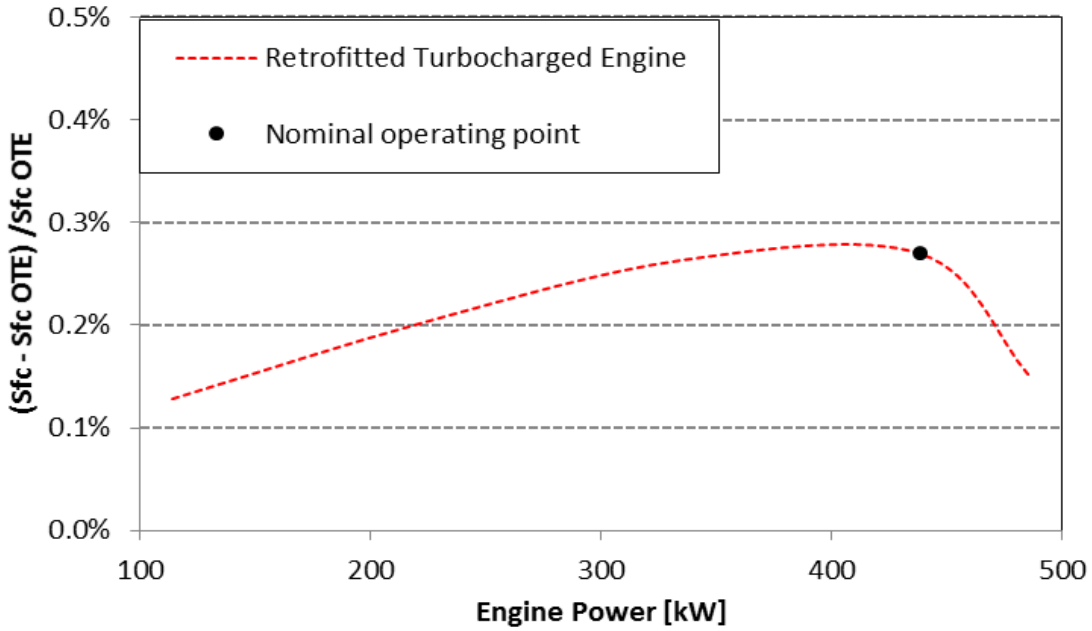

Figure 6-7: SFC change for entire T/C retrofit.

Concluding, the current option provides a slightly better retrofitting solution (Figure 6-2 and Figure 6-7), having lower specific fuel consumption in comparison to Option 1. However, it should be noted that the replacement of entire T/C, instead of the compressor, increases the process cost, hence making Option 2 less attractive.

6.1.3 Structural Integrity analysis

During the retrofit process, it is important to ensure that the solution is structurally safe. It is assumed that each turbo-component, having been part of a commercial T/C, it is designed to be structurally safe from both static and modal analysis perspective. Due to the fact that in both retrofit options, the maximum T/C speed is close to the nominal one, their static structural integrity is automatically ensured. Although, this assumption is not met from a modal analysis perspective, due to the change in the turbo-component pair, hence requiring a modal analysis verification.

According to the results, provided by the simplified modal analysis tool(section 4.4.4), both retrofit solutions operate stably with underdamped behavior. Analyzing the Campbell Diagram, depicted in Figure 6-8, both retrofit solutions have similar behavior due to their similar size. Also having acceptable distance from the synchronous speed, the resonance avoidance is ensured.

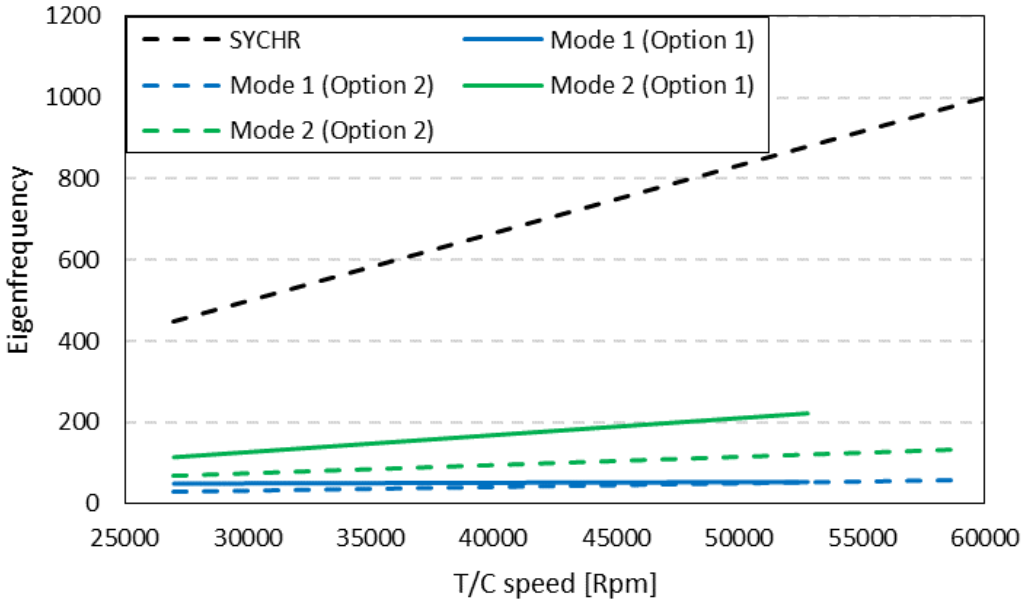

Figure 6-8: Option 1 and 2 Campbell Diagram.

6.2 Turbocharger compressor re-design(Option 3)

For option 3, it is assumed that the engine operates at 50% and 75% load, with equal operation time for each load. For presentation purposes, it is assumed for compressor redesign process that there is no available diesel engine model. Thus, the optimization objective function can be expressed as:

$$max: z' = 0.5\ \eta_{cmp,50} + \ 0.5\ \eta_{cmp,75} \qquad (6.1)$$

As nominal point, the one which corresponds to 75% engine load is chosen. The highest speed operating point is the one which corresponds to 110% engine load. Finally, the impeller material is chosen to be Aluminum Alloy 7075 T651.

6.2.1 Turbocharger compressor preliminary design analysis

The compressor mass flow, speed and power are used as the basic input data, available from shop trials. In particular, default parameters values are used for optimization process initialization.

With T/Ced diesel engine performance analysis being carried out, the improved compressor operation is predicted. The T/C operating line on the compressor performance map is presented in Figure 6-9. The design process provides a CC with a 1.99% and 1.59% efficiency increase in 50% and 75% engine load, respectively (Figure 6-10).

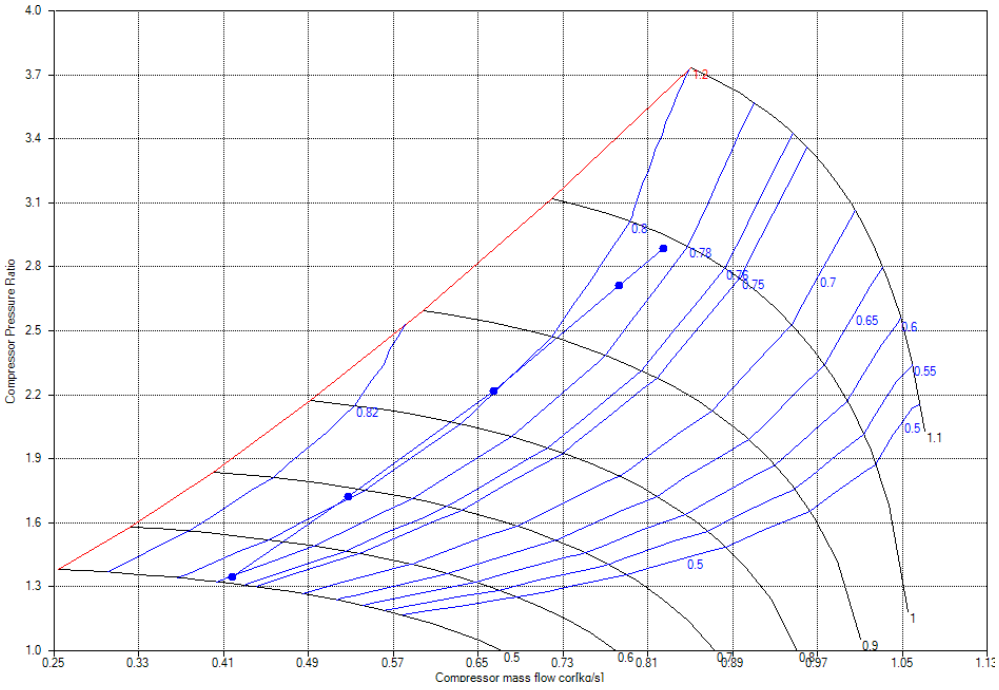

Figure 6-9: 1D improved compressor map and operating line.

Regarding the specific fuel consumption, a 0.24% decrease in 50% and 0.31% in 75% engine load is noticed (Figure 6-10), leading to an overall 0.27% fuel consumption reduction. It is obtained that even with this efficiency increase, the SFC seems to slightly decrease, showing the importance of the entire T/C redesign.

Finally, as T/C is an auxiliary part of the diesel engine, its redesign, even with this efficiency increase, cannot affect significantly the engine fuel consumption without integrating diesel engine re-tuning (valve timing, injection timing, etc.) in design process.

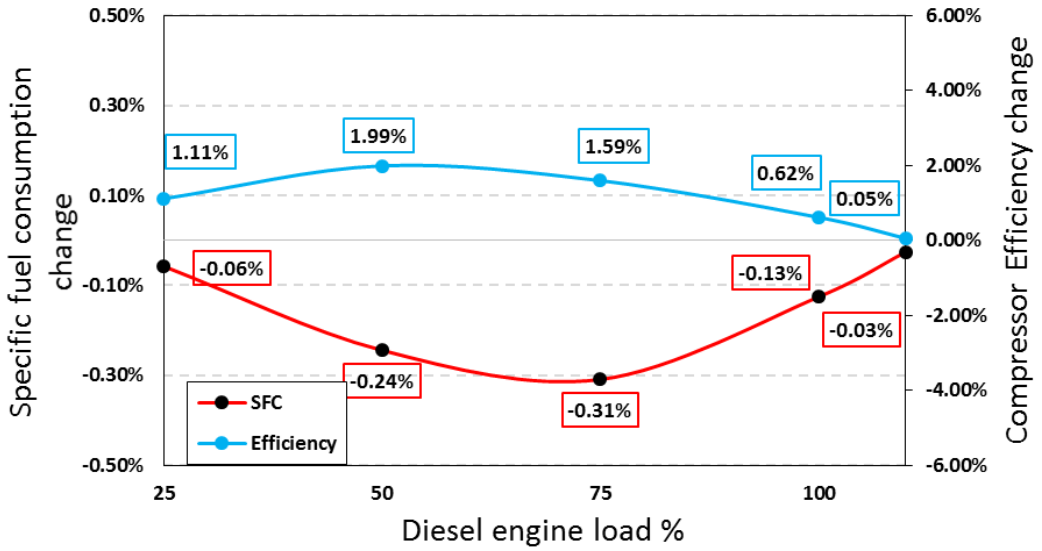

Figure 6-10: Diesel SFC and compressor efficiency change between 1D improved and baseline compressor.

The simplified structural analysis shows that the new compressor achieves a safety factor of about 1.25, while the turbo-spool(re-designed compressor and original turbine pair) operates stably(underdamped behavior) avoiding resonance(Figure 6-11), hence ensuring compressor structural integrity.

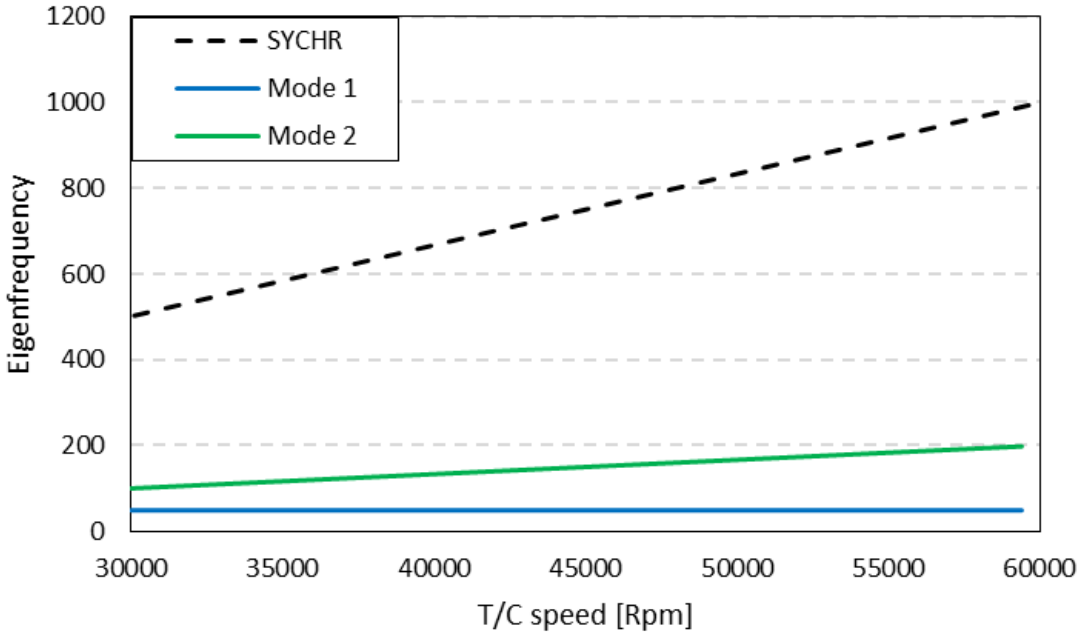

Figure 6-11: T/C with re-designed compressor (Option 3) Campbell Diagram.

The T/C design process scope is either to provide an initial 3D geometry to the high-fidelity 3D design process or a fast reliable solution. The generated 3D geometry from the 1D design of the present test case is shown in Figure 6-12. For stall margin, the limit is calculated based on the CFD velocity and energy imbalance parameter (<0.1%), which describes the fluid domain flow steadiness.

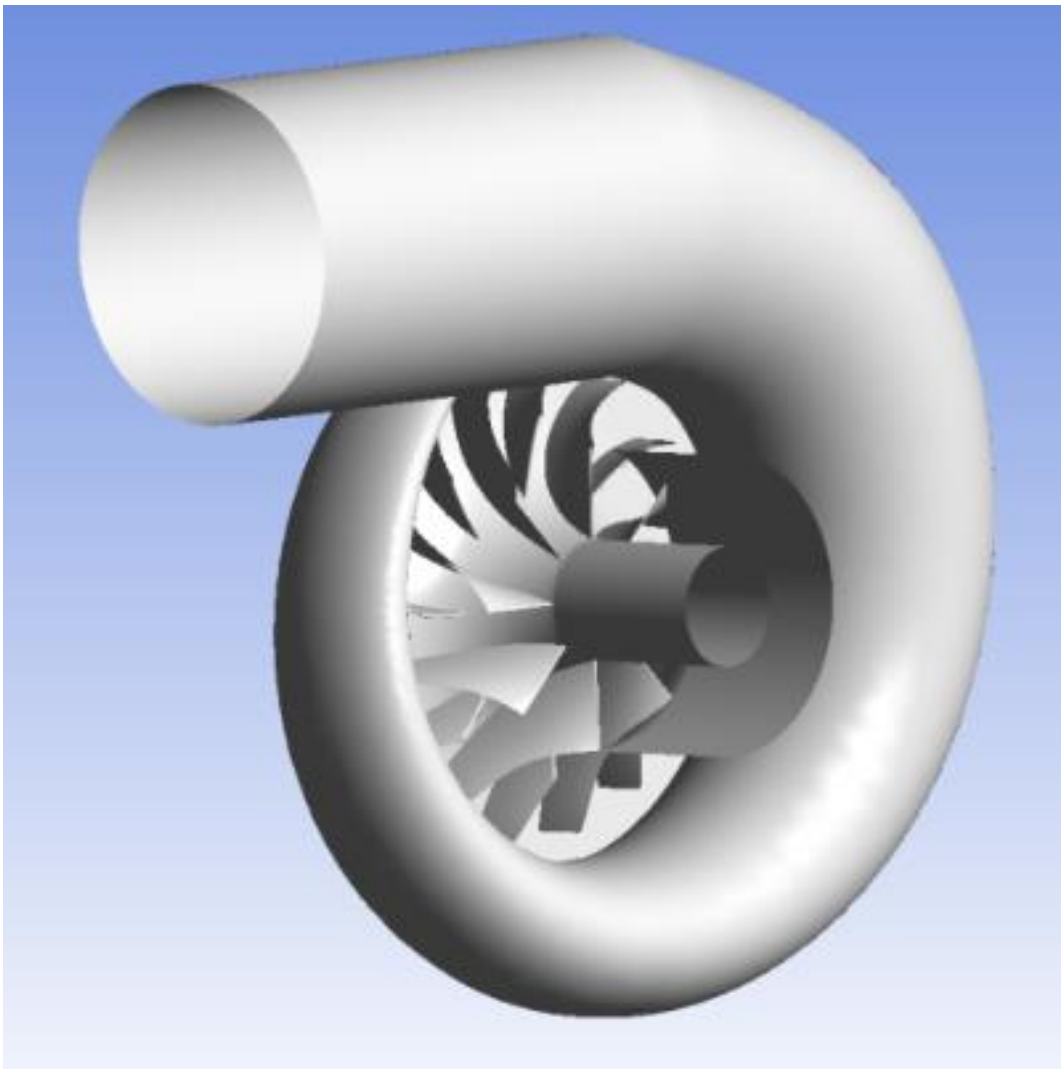

Figure 6-12: 3D geometry generated from the 1D design process

For evaluating the 1D design process, a CFD compressor map is generated(1 day simulation run, utilizing a 4 core 16GB RAM workstation) and combined with the T/Ced diesel engine simulation process. The CFD compressor map and the operating line are depicted in Figure 6-13.

According to the compressor operating results (Figure 6-14), the design process provides a CC with a 0.86% at 50% and 0.07% efficiency increase at 75% load. For specific fuel consumption, a 0.08% at 50% and 0.01% increase at 75% engine load. Also, based on FEA results, the preliminary designed 3D compressor achieves a safety factor about 1.33, ensuring structural integrity.

Concluding, the design process is capable of providing a 3D compressor geometry, which reconstitutes (slightly improve) the original compressor performance, considering that it is not a time consuming process, requiring low computational resources. Additionally, the operating line lies on lower efficiency area showing that if turbine was included in design process, more efficient operation could be succeeded.

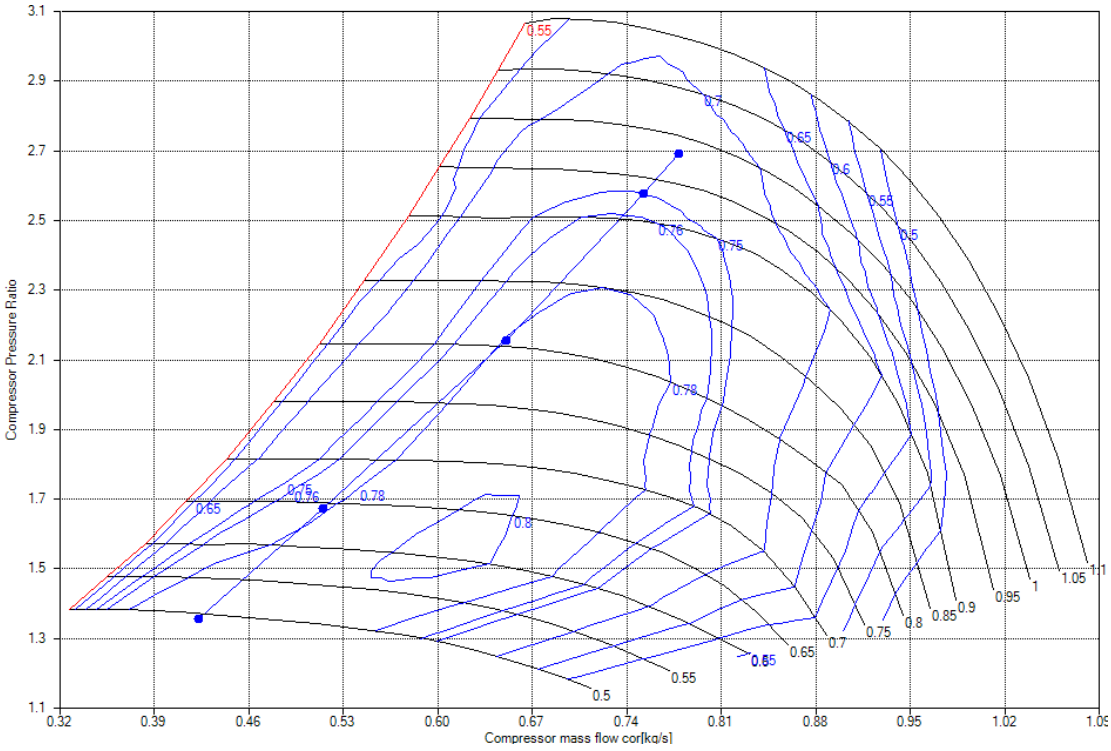

Figure 6-13: CFD compressor map (1D optimization) and operating line.

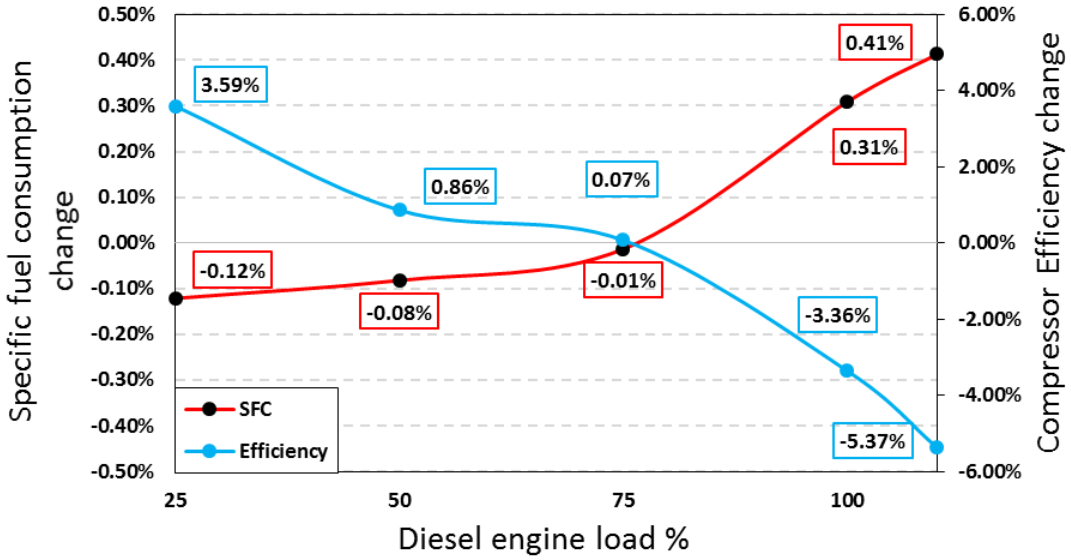

Figure 6-14: Diesel SFC and compressor efficiency change between 3D compressor (1D optimization) and baseline compressor.

6.2.2 Evaluation of Modified Centrifugal Compressor Single Zone Model

As mentioned in Chapter 4, eq. (4.108) is implemented into the process, in order to avoid compressor geometry solutions with large outlet blade height (b_3) and volute inlet width (b_4). For evaluating this correlation, the aforementioned design process is repeated without the usage of this correlation. The CFD compressor map is depicted in Figure 6-15.

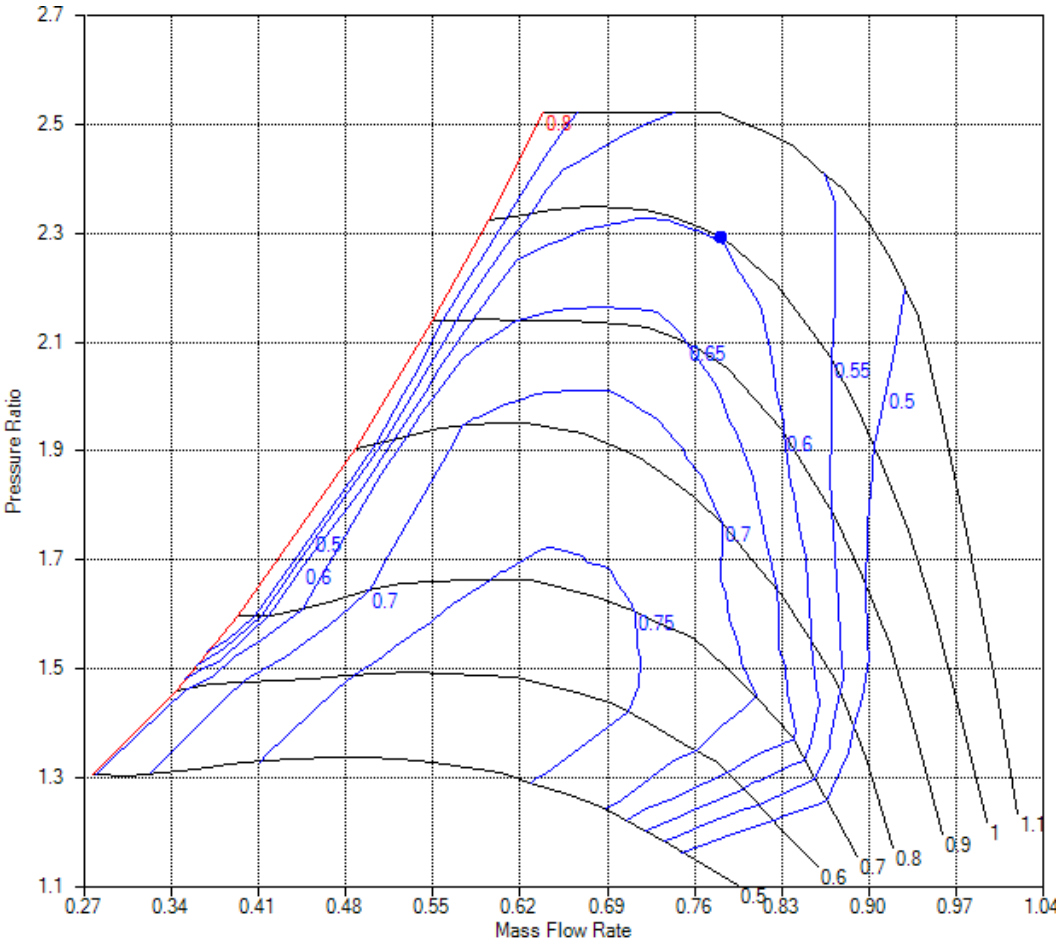

Figure 6-15: CFD compressor map (1D Optimization without the empirical correlation)

The comparison of both preliminary designed compressor CFD maps (Figure 6-13 and Figure 6-15) shows the significant reduction in compressor efficiency indicating the importance of this constraint during 1D optimization.

This comparison also shows that the highest difference is located in blade height/diffuser width, with an increase about 27.3%. This increase leads to both intensive impeller recirculation(negative velocities close to impeller exducer shroud region) and volute 3D effects, as depicted in Figure 6-16 and Figure 6-17, respectively.

These phenomena cannot be observed when using a meanline compressor model, hence showing the importance of including such a correlation in 1D optimization.

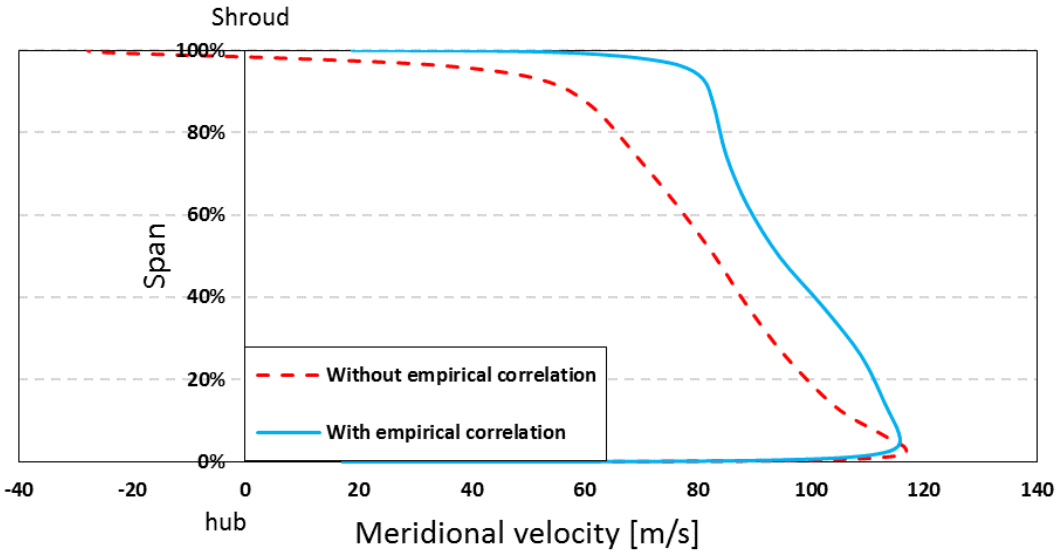

Figure 6-16: Mass average impeller exducer meridional velocity across span

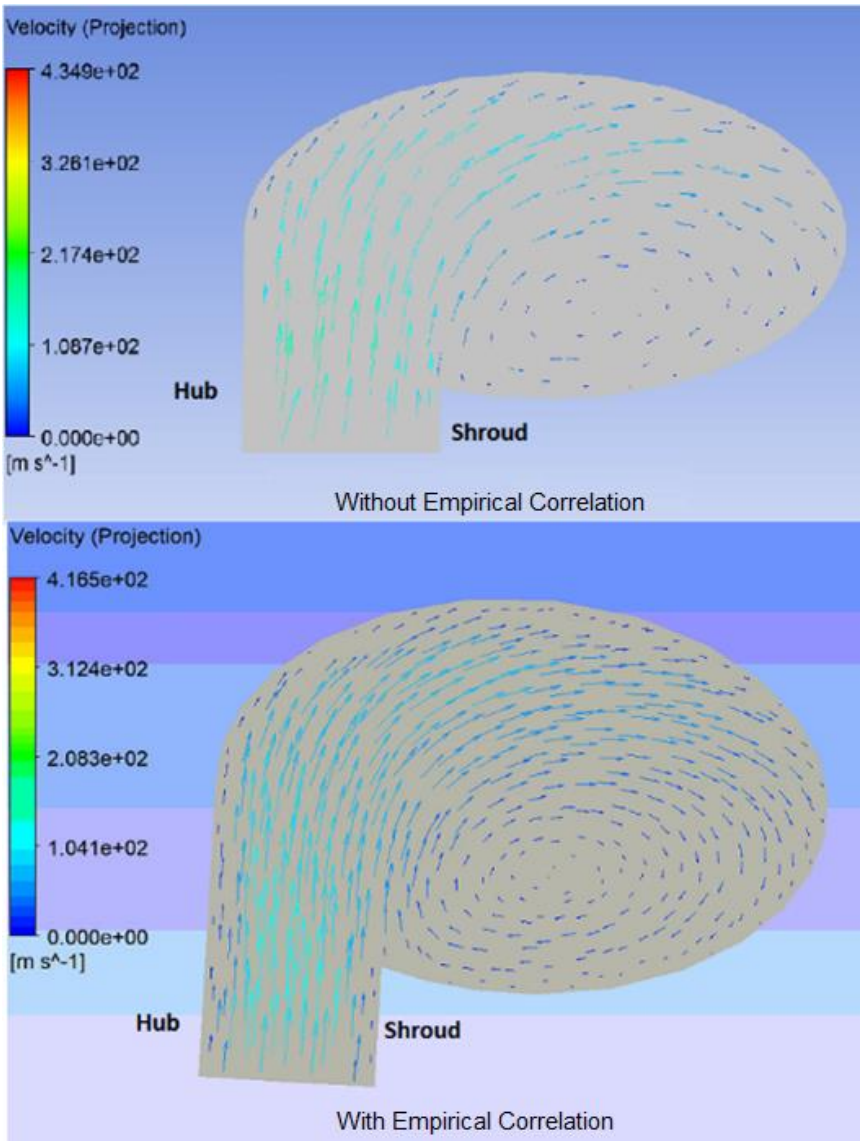

Figure 6-17: Volute 45º cross section velocity vectors projection

6.2.3 3D compressor design

Having as initial geometry the 3D one, generated by the preliminary design procedure (Figure 6-12), a CFD optimization is carried out. The optimization process lasted about 4 months due to the limited computational resources(4-core 16GB RAM workstation). The designed compressor 3D geometry is shown in Figure 6-18, including the flow pattern at 75% engine load.

Figure 6-19 depicts the CFD generated map and the operating line for the detailed designed compressor (CFD optimization). The efficiency is about 79.8% and 80.5% for 50% and 75% engine load respectively. According to the FEA results, the optimized compressor achieves a safety factor of 1.35, ensuring compressor structural integrity. Due to the lack of a fully 3D original turbine geometry, it is chosen not to perform a high-fidelity modal analysis with 3D Modal, assuming that the simplified modal analysis is sufficient.

According to Figure 6-20, the 3D optimization provides a compressor with a 2.08% efficiency increase in 75% engine load and 1.50% in 50% engine load. For specific fuel consumption, a 0.26% decrease in 50% and 0.44% in 75% engine load is noticed, leading to a total of 0.34% fuel consumption decrease.

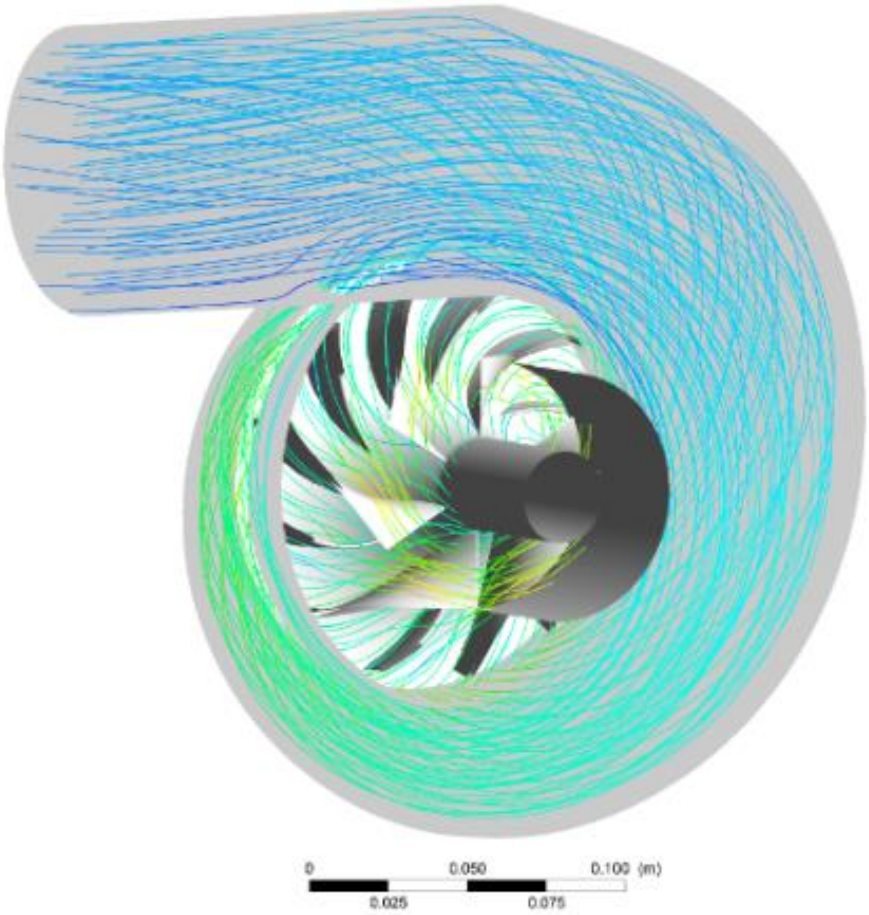

Figure 6-18: Compressor 3D geometry(CFD Optimization) and flow pattern at 75% engine load.

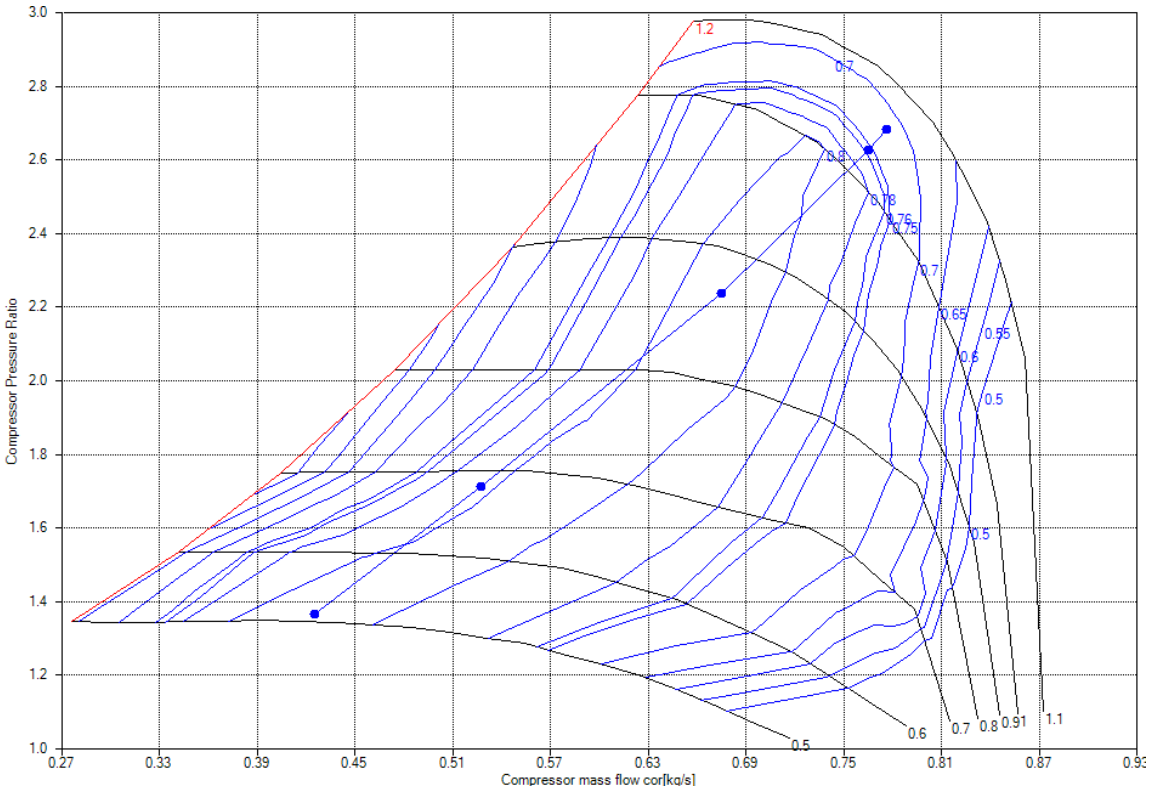

Figure 6-19: CFD compressor map (CFD Optimization) and operating line.

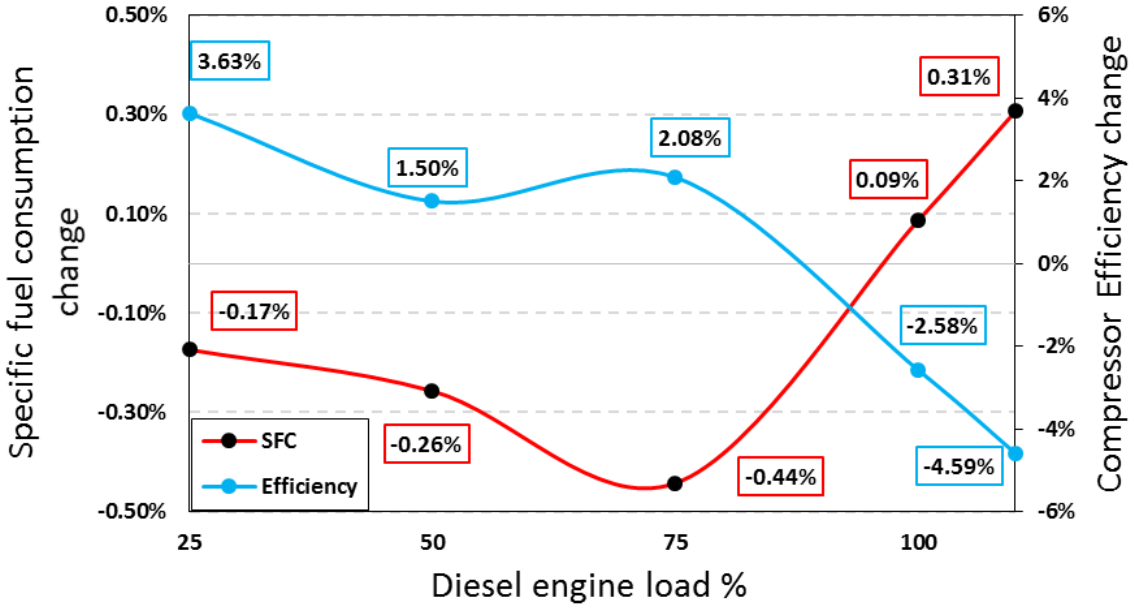

Figure 6-20: Diesel SFC and compressor efficiency change between 3D compressor (CFD Optimization) and baseline compressor.

At this point, it is useful to compare the 3D geometries that correspond to the preliminary and high-fidelity design processes.

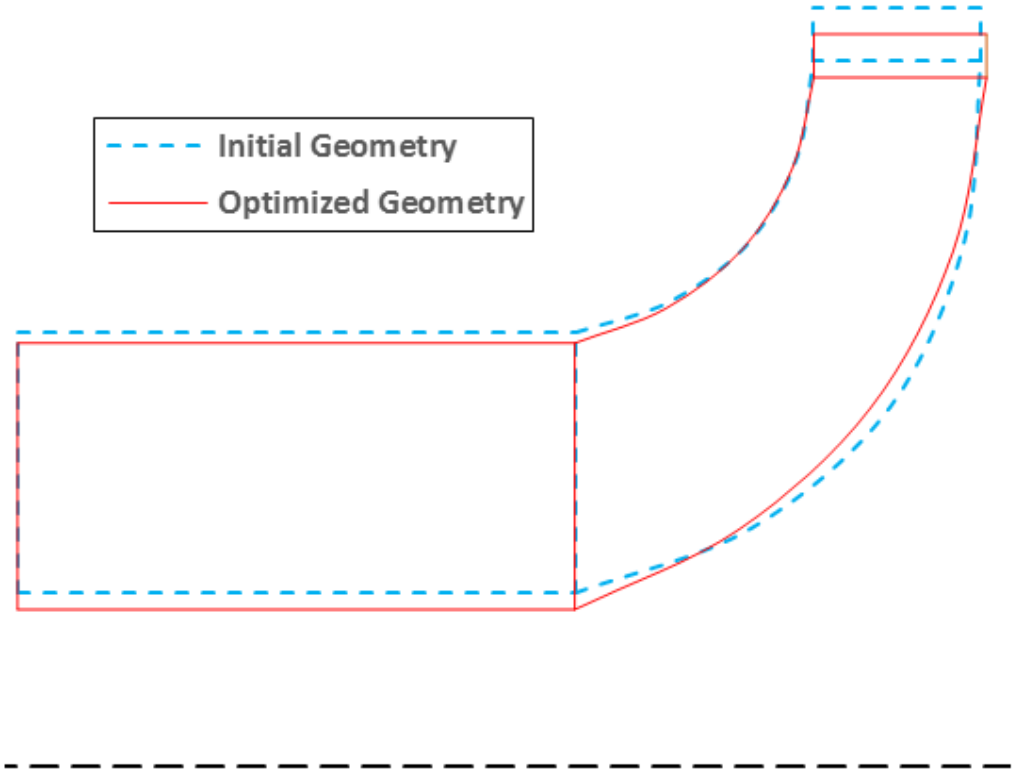

Figure 6-21: 1D and CFD optimization 3D impeller geometry meridional view

The 3D designed CC geometry shows variation in blade shape as seen by the blade angle and thickness change (Figure 6-22) in contrast to the meridional geometry (Figure 6-21) which is close to the 3D geometry, generated by the preliminary design part.

Concerning the volute geometry comparison between both preliminary and high fidelity design solutions, a 2.23% reduction in R4 and a 2.93% increase in R_{vol} are noticed. Also, the elliptical parameter changes between preliminary and high-fidelity 3D designed volute is depicted in Figure 6-23.

Concerning efficiency increase resulting from CFD optimization, Figure 6-24 depicts the flow patterns in impeller and volute, where the most significant flow pattern improvement is observed.

For the impeller, the 3D design process enhances the flow close to shroud by significantly reducing the wake flow region. In volute flow, both circumferential velocity (parallel to meridional and cross section plain) is enhanced, leading to smoother flow into the volute component reducing losses due to 3D effects.

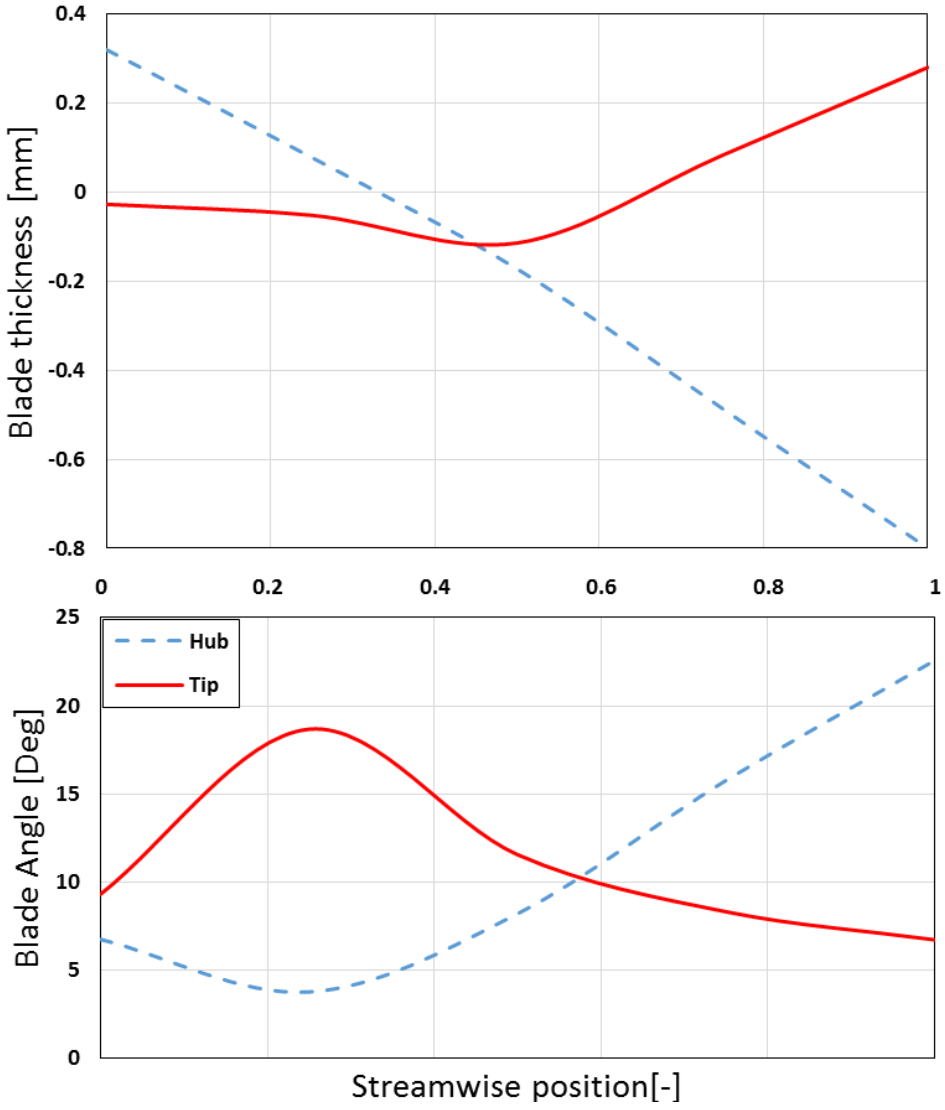

Figure 6-22: 1D and CFD optimization blade angle and thickness across streamwise

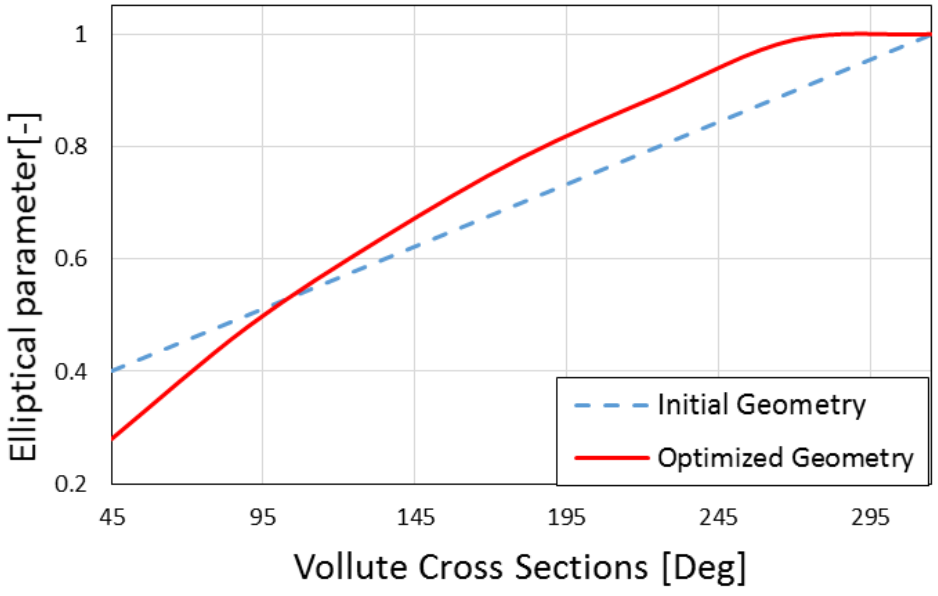

Figure 6-23: 1D and CFD optimization 3D volute elliptical parameters

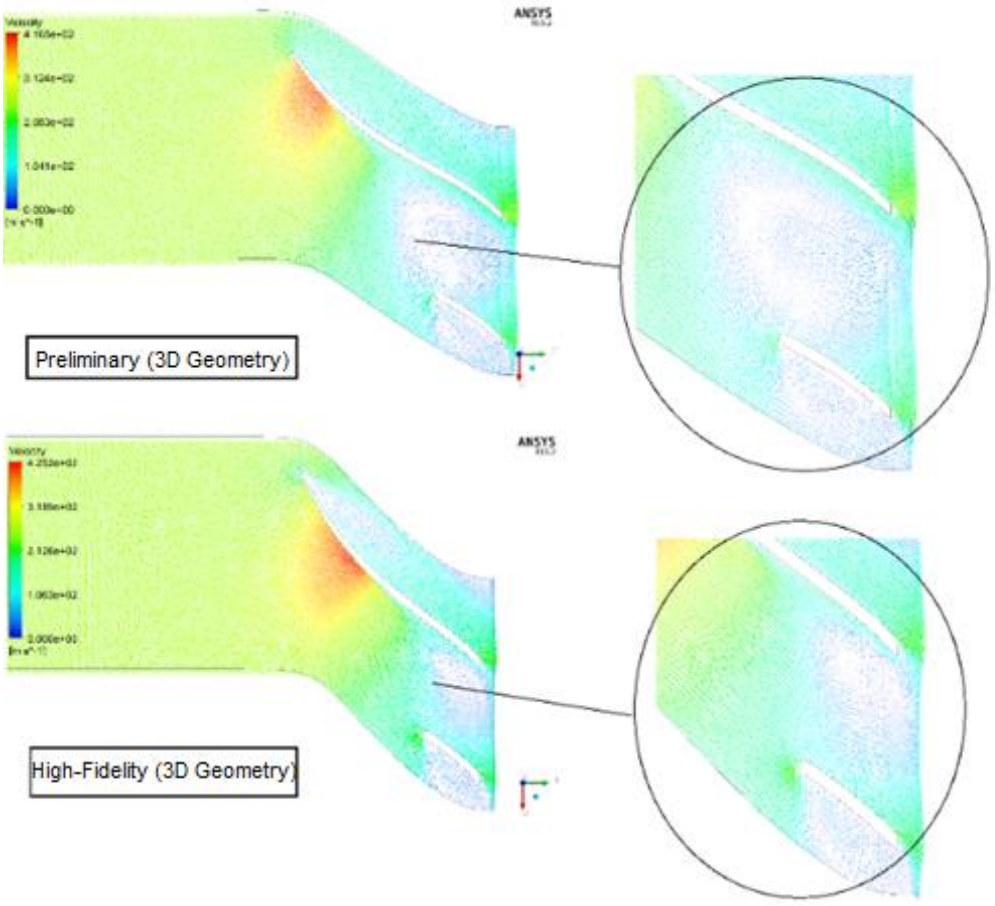

(a)

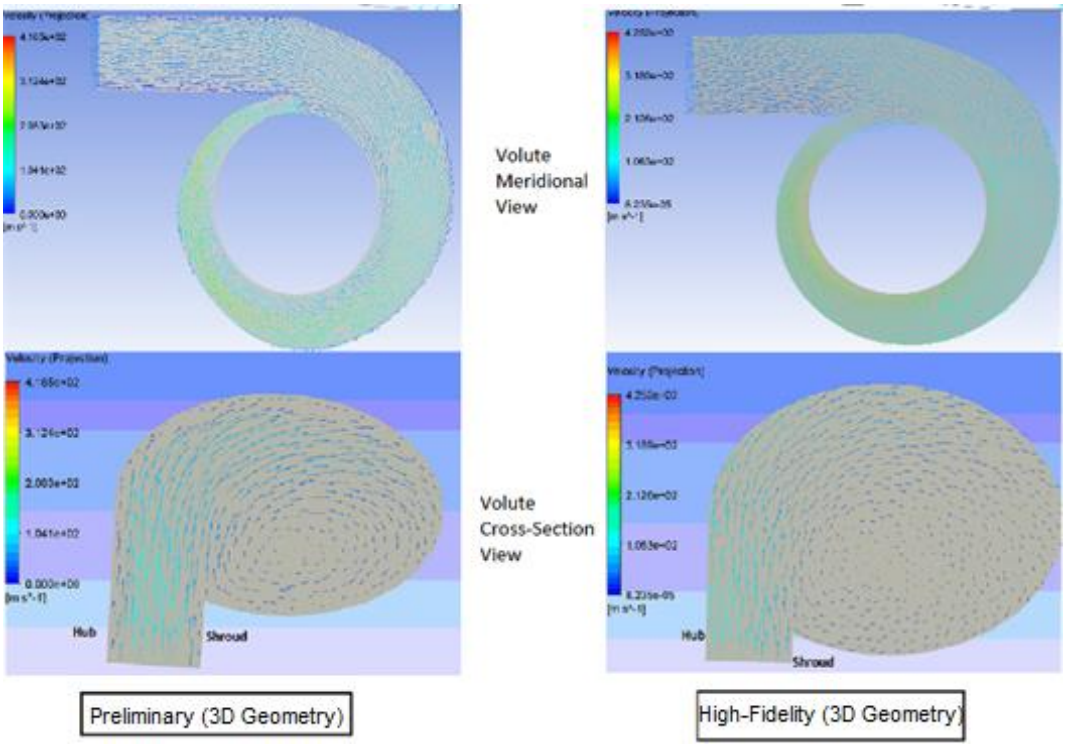

(b)

Figure 6-24: 1D and CFD optimization 3D flow pattern at 75% engine load: **(a)** Impeller tip blade to blade **(b)** Volute.

Table 6-2 shows that both improved compressor geometries, generated by both preliminary and high fidelity design processes, have a size close to the baseline one, hence validating the right operation of both design processes, knowing that initialization is based on default values.

Table 6-2: Geometrical parameters change between baseline and designed compressors.

Parameter	Preliminary Solution	High fidelity Solution
$R_{hub,1}$	10.1%	0.5%
$R_{tip,1}$	-17.5%	-20.4%
R_3	-4.2%	-6.8%
R_4	1.2%	-2.3%
R_5	-3.9%	-1.6%
R_{vol}	-9.5%	-12.7%
$\beta_{hub,1}$	-65.6%	-25.1%
$\beta_{tip,1}$	31.4%	40.5%
β_3	-12.9%	22.3%
b_3	24.2%	33.2%
Main Blades	-1	-1
Splitter Blades	-1	-1

6.3 Entire Turbocharger re-design(Option 4)

For option 4, it is assumed that there is available diesel engine model. The engine operates at 25%, 50%, 75% 100% and 110% load, with an operating time equal to 1.25%, 47.5%, 47.5% 2.5% and 1.25% of annual operation respectively. Thus, the optimization objective function can be expressed as:

$$min: z = 0.0125\dot{m}_{fuel,25} + 0.475\dot{m}_{fuel,50} + 0.475\dot{m}_{fuel,75} + 0.025\dot{m}_{fuel,100} + 0.0125\dot{m}_{fuel,110} \quad (6.2)$$

As nominal point is chosen the one which corresponds to 50% engine load. The highest speed operating point is the one which corresponds to 110% engine load. Finally, CC, AT and RT materials are chosen to be Aluminum Alloy 7075 T651, Nimonic Alloy 81 and Stainless steel 304 respectively. In this section, all four possible T/C configurations are examined in order to choose the best fitted configuration for the best reconstitution. Then, configuration A (vnless CC-RT) is compared with the one which is designed, integrating the volute surrogate loss models in the design process.

6.3.1 Turbocharger Vaneless Centrifugal Compressor–Radial Turbine (Configiguration A)

With T/Ced diesel engine performance analysis being carried out, the designed T/C operation is calculated. The T/C operating lines on turbo-components performance maps are presented in Figure 6-25

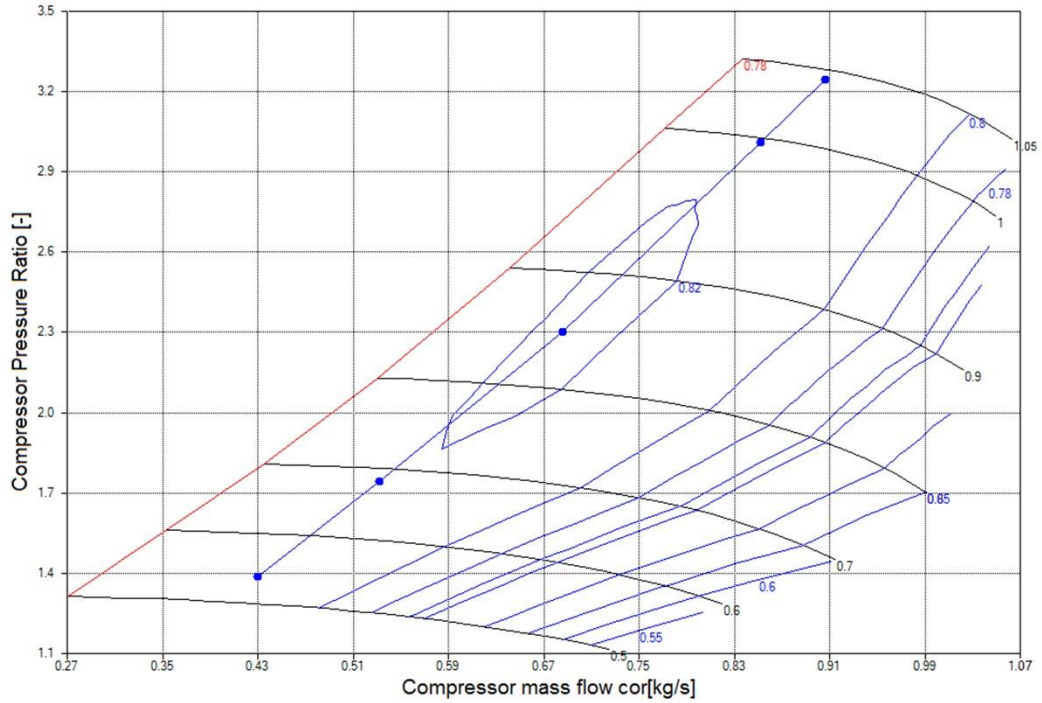

(a)

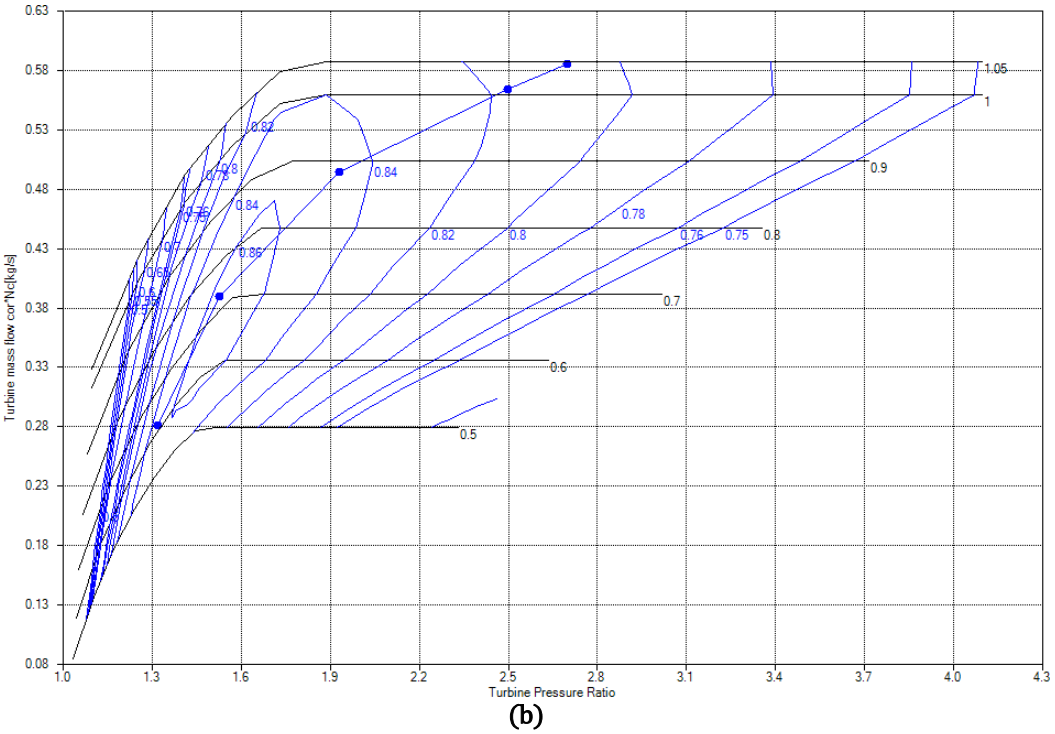

(b)

Figure 6-25: 1D designed T/C maps and operating lines: **(a)** vnlss diffuser CC **(b)** RT.

The design process provides a compressor with an efficiency increase from 3.19% to 4.78% and a turbine with a an efficiency increase from 8.61% to 11.08. For fuel consumption, a decrease from 0.167% to 0.416% is noticed, shown in Figure 6-26, leading to an overall reduction by 0.401% according to eq. (6.2).

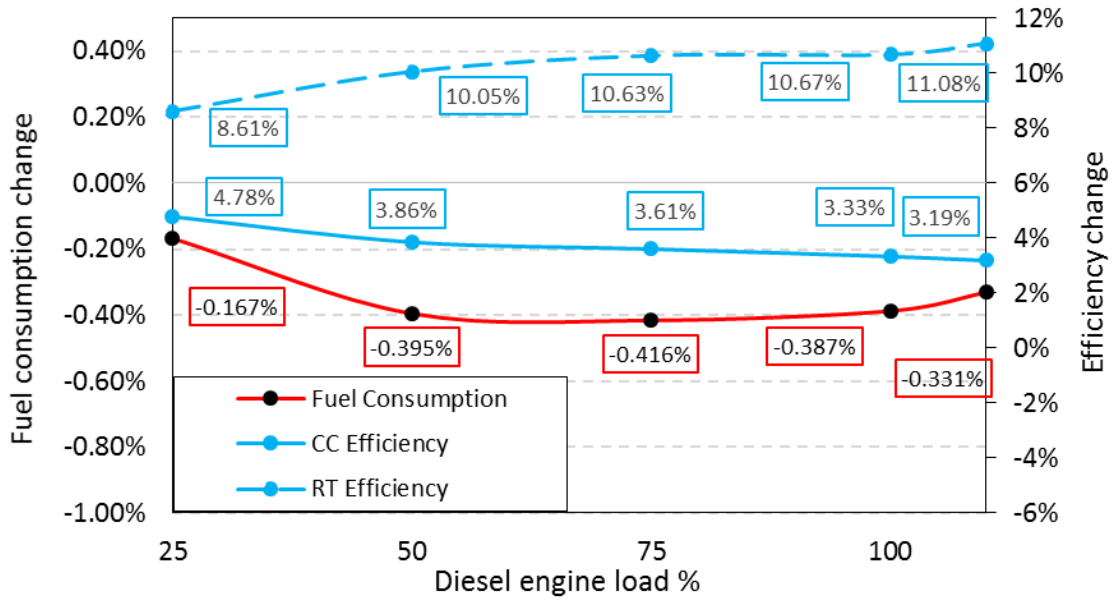

Figure 6-26: Diesel fuel consumption and turbo-components efficiency change between 1D improved and baseline T/C (Vnless Diffuser CC – RT).

Similar to the compressor design process, even with this efficiency increase, the fuel consumption seems to slightly decrease, showing the small impact of T/C in the overall diesel engine performance, as it is an auxiliary part.

Concerning T/C structural integrity, the results from simplified static and modal analysis, show that the T/C achieves structural integrity(Table 6-3), while avoiding resonance operation Figure 6-27.

Table 6-3: 1D improved T/C(Vnless Diffuser CC – RT) static and modal analysis results.

Vnless Diffuser CC-RT		
	Compressor	Turbine
Safety factor	1.32	1.62
Stability	Stable	
Behavior	Underdamped	
Max Decay	-58.17	

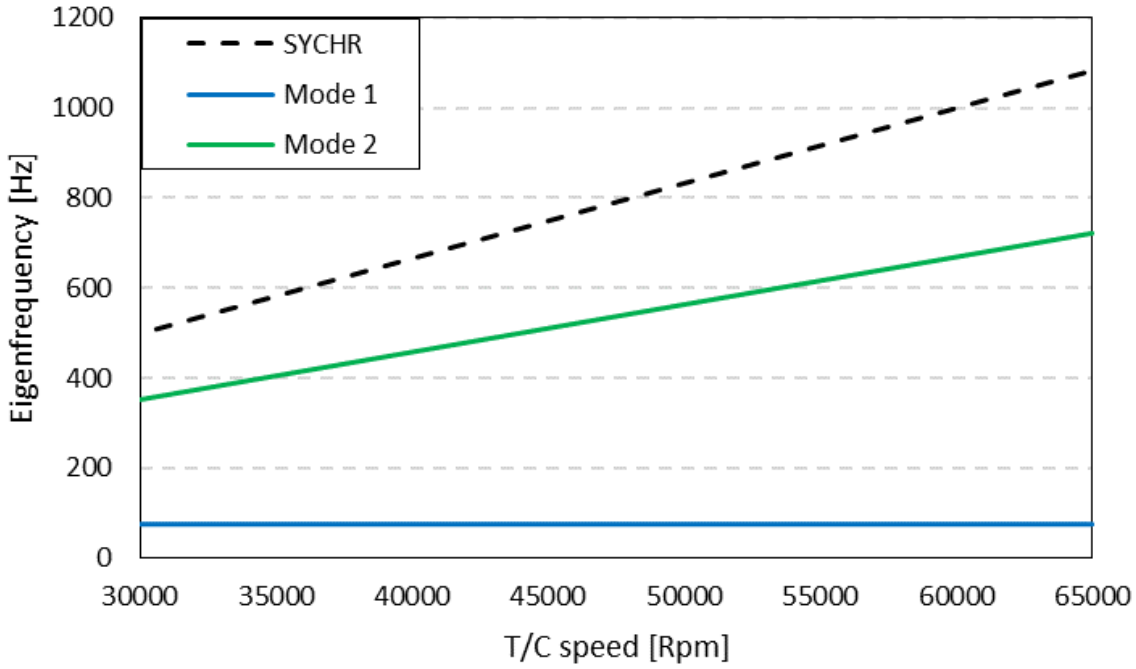

Figure 6-27: 1D improved T/C(Vnless Diffuser CC – RT) modal analysis.

6.3.2 Modified Turbocharger Vaneless Centrifugal Compressor – Radial Turbine (Configuration A')

Having set the CFD based surrogate volute loss models, the configuration A design process is repeated in order to evaluate how the new models affects the designed geometry. With T/Ced diesel engine performance analysis being carried out for configuration A', the new T/C operation is calculated. The T/C operating line on both compressor and turbine performance maps are presented in Figure 6-28. The design process provides a T/C compressor with an efficiency increase from 1.97% to 5.92% and a T/C turbine with 5.61% to 9.88% efficiency increase. For fuel consumption a decrease from 0.168% to 0.395% is noticed, shown in Figure 6-29, leading to an overall reduction by 0.356% according to eq. (6.2).

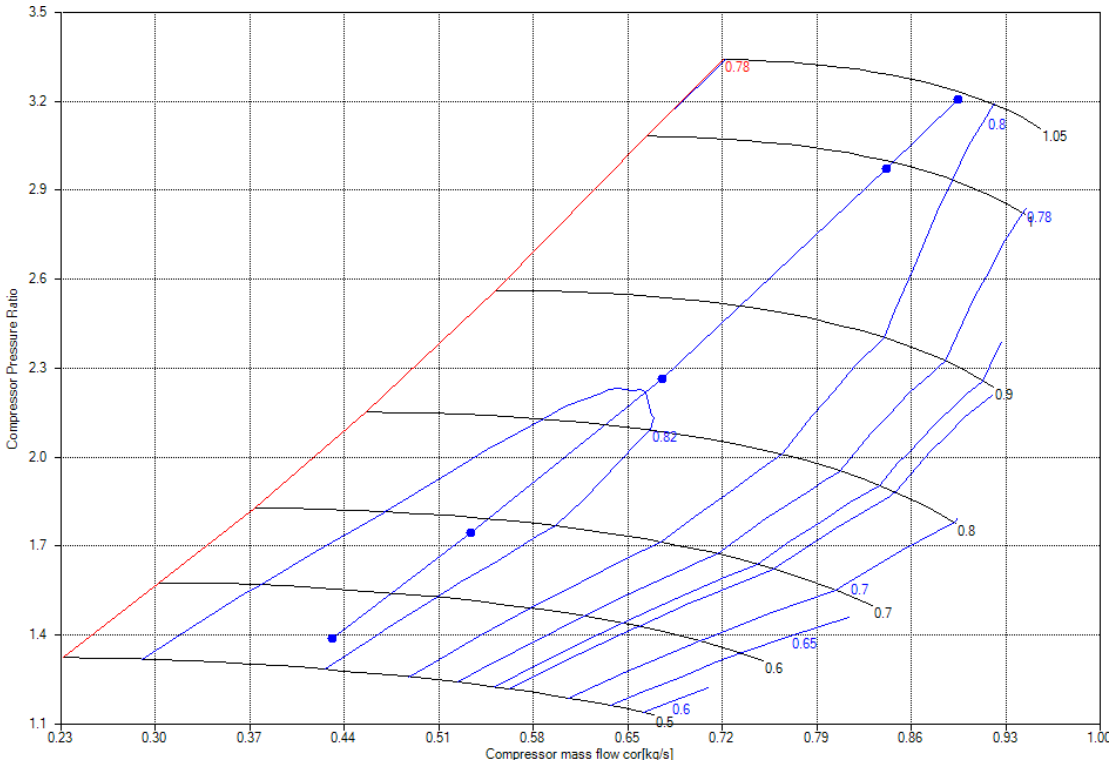

(a)

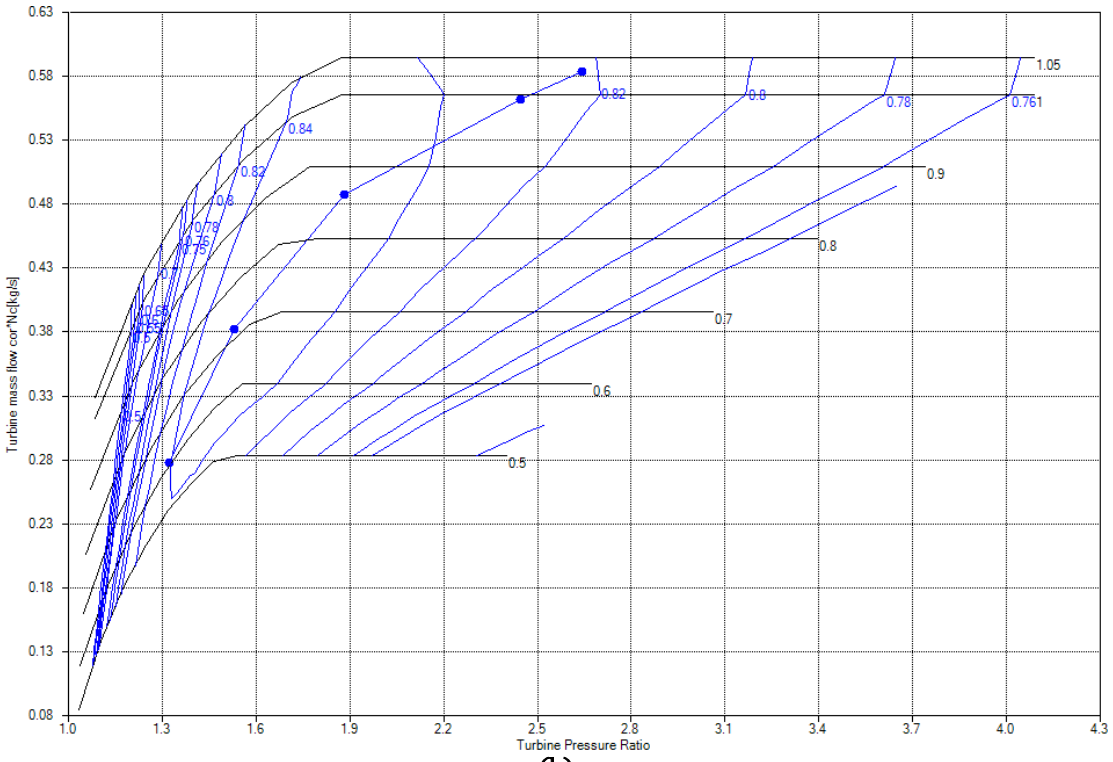

(b)

Figure 6-28: 1D improved T/C maps and operating lines (CFD based Volutes): **(a)** Vnless diffuser CC **(b)** RT.

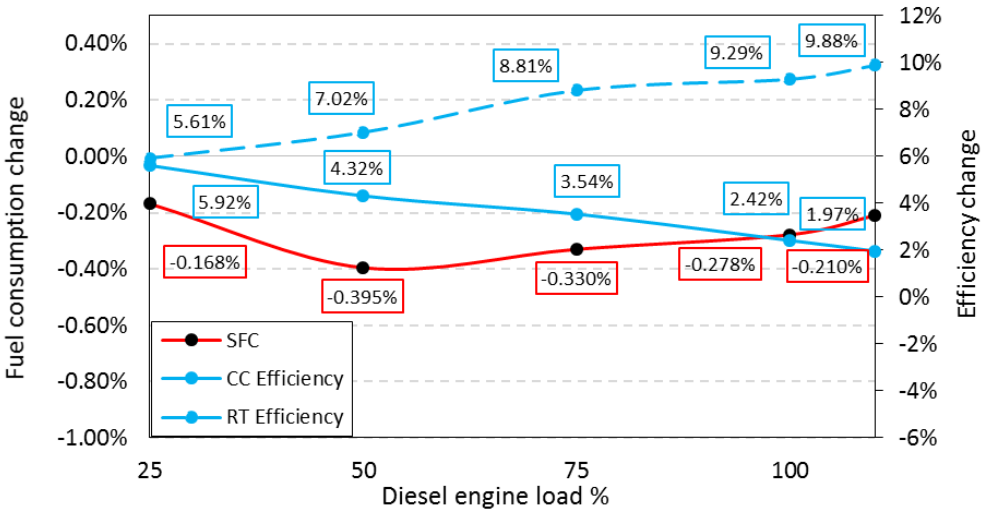

Figure 6-29: Diesel fuel consumption and turbo-component efficiency change between 1D improved and baseline T/C. (CFD based Vnd Diffuser CC – RT)

The results from simplified static and modal analysis, show that the T/C is also structurally safe with similar results(safety factor, decay rate, Campbell diagram Figure 6-30) with the ones presented in section 6.3.1. It is obtained that both the static and the modal analyses provide similar results due to similar sizes of both compressor and turbine impellers.

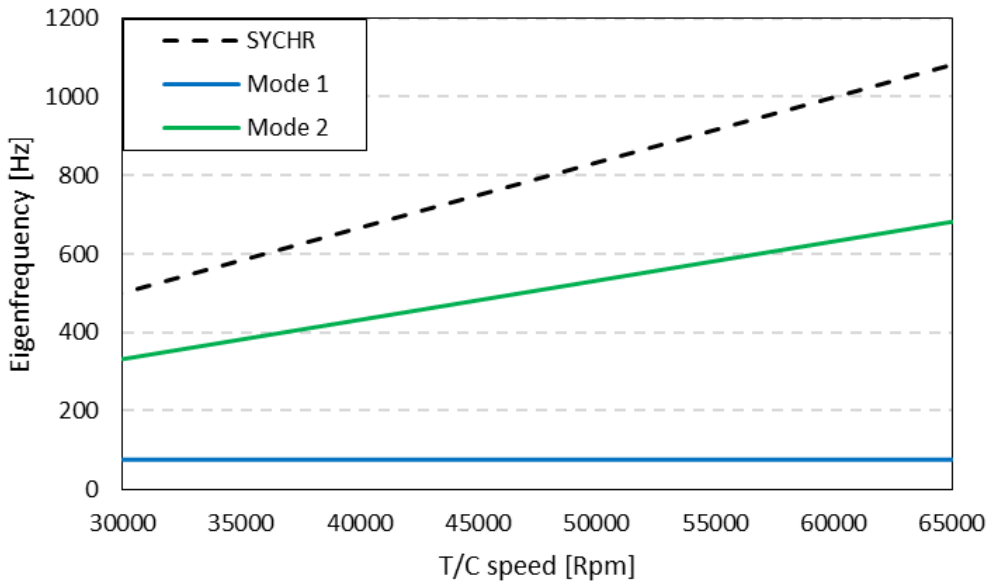

Figure 6-30: 1D improved T/C (CFD based Vnless Diffuser CC – RT) modal analysis.

Comparing both configuration A and A' geometries (Figure 6-31), it can be seen that they have similar size as expected. The overall fuel consumption increases in the CFD-based surrogate volute loss case due to the additional secondary losses. Although, in case of the compressor, a slight increase is noticed, verifying that equation (4.108) prevent compressor geometry solutions

with intensive volute 3D effects. Additionally, a diffuser channel width decrease is noticed. This reduction is due to the ability of the CFD based model to calculate the volute secondary losses, depends on the channel width and can be seen from the increase in deviation of both loss models curves in low mass flow (low Mach numbers) in the Chapter 3.

Concerning RT volute geometry comparison, an aspect ratio increase is noticed. This increase is due to the CFD based model flow angle underestimation in comparison with the conventional one. Specifically, for achieving a specific absolute Mach number, the CFD-based one requires higher outlet radial velocity which can be accomplished by increasing volute aspect ratio.

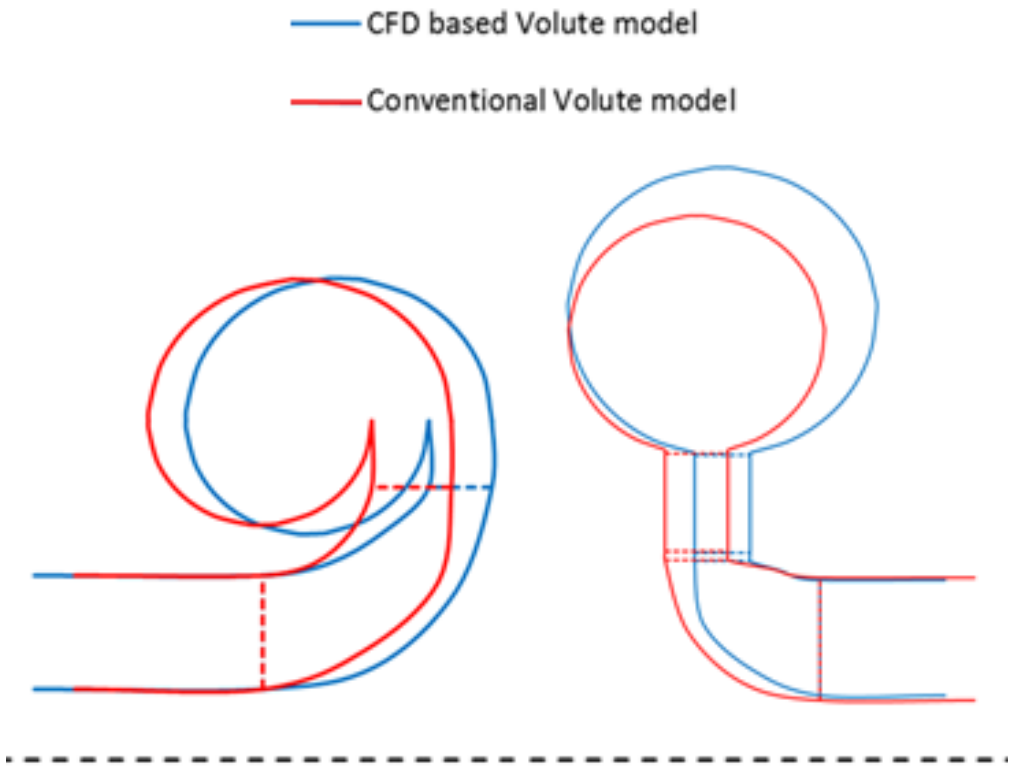

Figure 6-31: 1D design T/C geometry(meridional view) comparison between CFD based and conventional volute model.

6.3.3 Turbocharger Vaned Diffuser Centrifugal Compressor – Radial Turbine (Configuration B)

With T/Ced diesel engine performance analysis being carried out for configuration B, the improved T/C operation is calculated. The T/C operating line on both compressor and turbine performance maps are presented in Figure 6-32

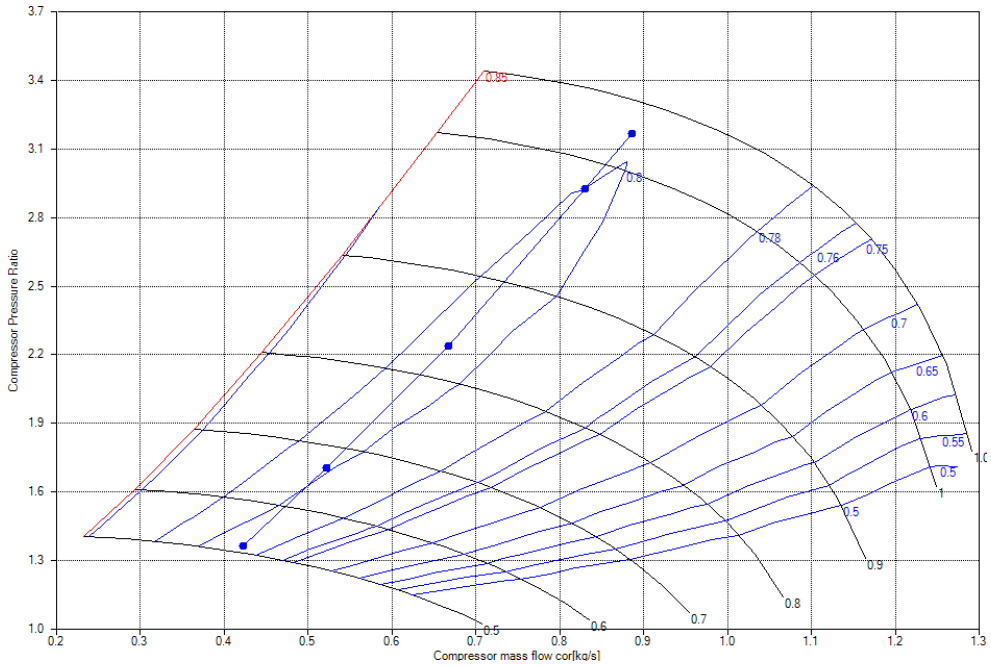

(a)

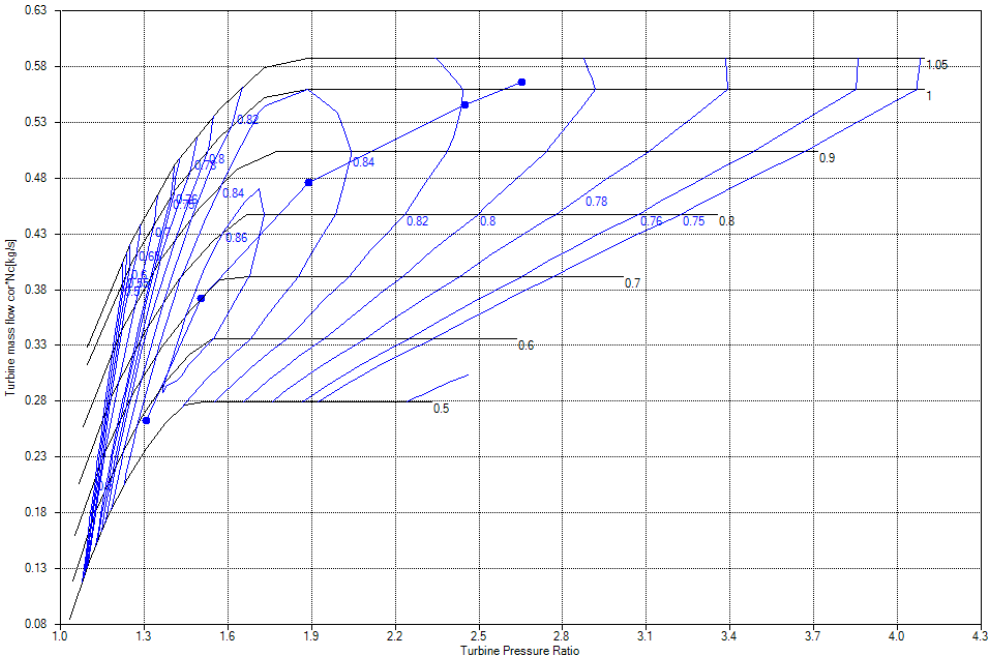

(b)

Figure 6-32: 1D improved T/C maps and operating lines: **(a)** vnd diffuser CC **(b)** RT.

The design process provides a compressor with a 1.36% to 2.27% efficiency increase and a turbine with a 9.12% to 11.28% efficiency increase as depicted in Figure 6-33. For fuel consumption a decrease from 0.064% to 0.238% is noticed, shown in Figure 6-33, leading to an overall reduction by 0.288% according to eq. (6.2).

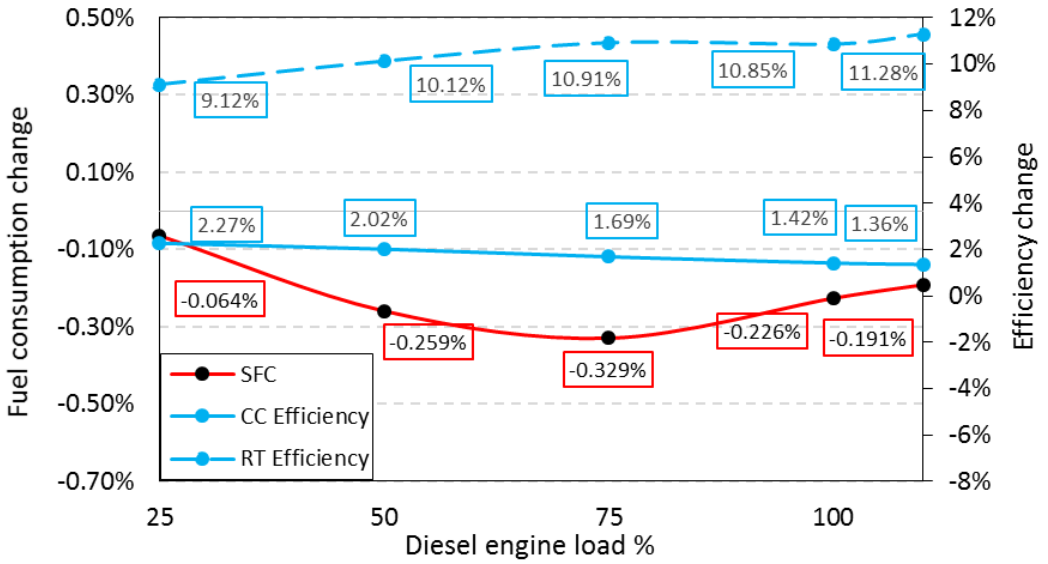

Figure 6-33: Diesel fuel consumption and turbo-components efficiency change between 1D improved and baseline T/C. (Vnd Diffuser CC – RT)

Similar to the configuration A design, the fuel consumption seems to slightly decrease, showing the small impact of T/C in the overall diesel engine performance. Regarding the T/C structural integrity, the results from the simplified analysis, shows that the T/C is structurally safe with similar results(safety factor, decay rate, Campbell diagram Figure 6-34) with the ones presented in section 6.3.1.

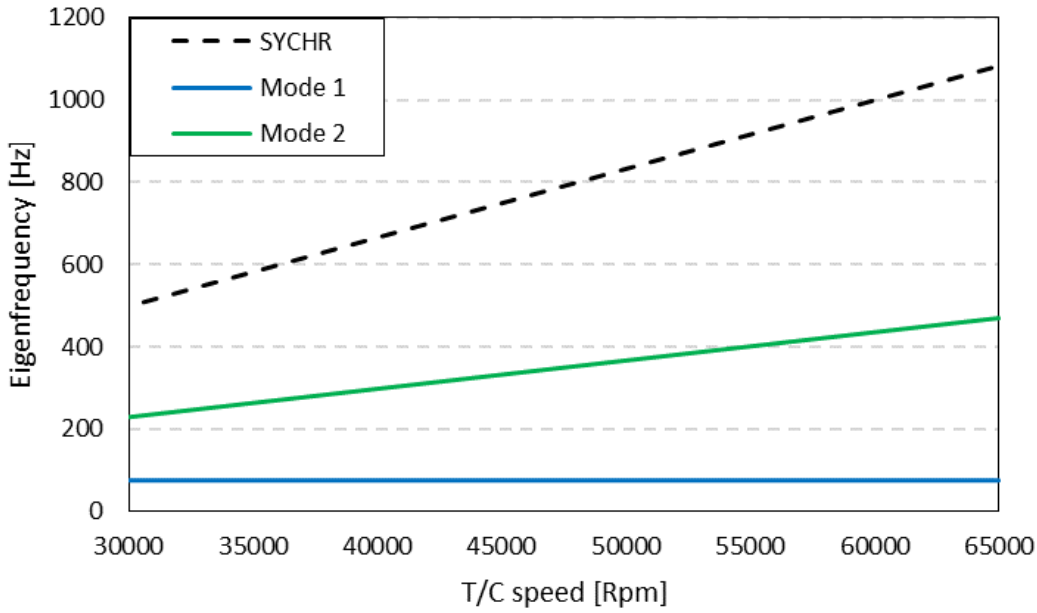

Figure 6-34: 1D optimization T/C(Vnd Diffuser CC – RT) modal analysis.

6.3.4 Turbocharger Vaned/Vaneless Centrifugal Compressor – Axial Turbine (Configuration C & D)

For both configurations the design process is unable to find a feasible Turbine design solution able to match the entire engine system. The current engine requires a T/C with specific speed about 1.2. According to Figure 6-35, published by Japikse and Baines (1997), for such specific speed value the Radial Turbine usage is un-avoidable as axial turbine is inefficient. For such T/Ced Diesel Engine, the T/C configurations C and D are inadequate.

Figure 6-35 validates the entire design process as both Configuration A and B radial turbine reach a maximum efficiency about 86% which is expected according to Japikse and Baines (1997). For further axial turbine design interpretation see Appendix.

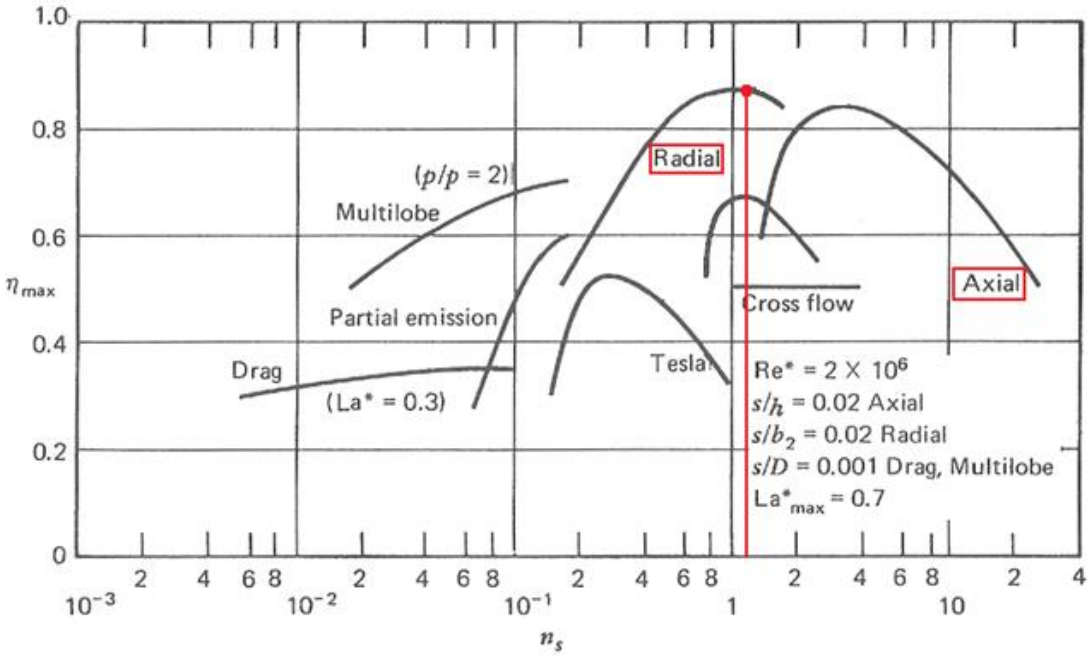

Figure 6-35: Turbine Efficiency-Specific speed depending on its type. [Japikse and Baines, 1997]

6.3.5 Choosing the best fitted Turbocharger

In this part of the test case, all four possible T/C configurations are evaluated by performing a multi-point design process for diesel engine reconstitution. According to the results axial turbine T/C are proven to be insufficient for this T/Ced diesel engine as was expected according to Japikse and Baines (1997). For this reason both configuration A and B are compared with the aim to choose the most efficient T/C.

According to Figure 6-36, it can be seen that the entire T/C re-designing provides higher fuel consumption reduction compared with the T/C compressor one, presented in the previous section(6.3). As for the best configuration, it is the vaneless Diffuser CC- Radial Turbine (Configuration A) which according to public literature is commonly used for similar size auxiliary engines.

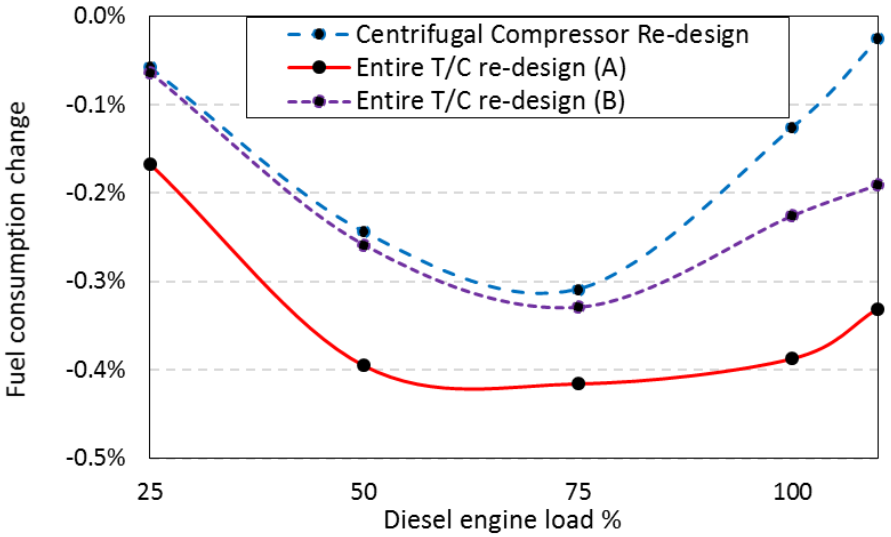

Figure 6-36: Diesel fuel consumption change for CC and entire T/C re-design.

According to the comparison of configuration A and B (Figure 6-36 and Figure 6-37), by adding a vaned diffuser in a compressor component:

- For a narrow range of off-design operation around the nominal point the flow is better driven to the volute, hence reducing its loss coefficient.
- Extra losses are added due to vanes.

Thus, for the current T/C requirements, the volute loss benefit is lower, compared to the extra losses due to vane placement in the diffuser, leading to a more efficient vaneless diffuser CC than the vaned one. The process is also evaluated, considering that the baseline T/C is a vaneless diffuser.

Concluding, the best fitted T/C is the vaneless Diffuser CC- Radial Turbine one (Configuration A), as it provides both the lowest fuel consumption and the lowest purchase cost.

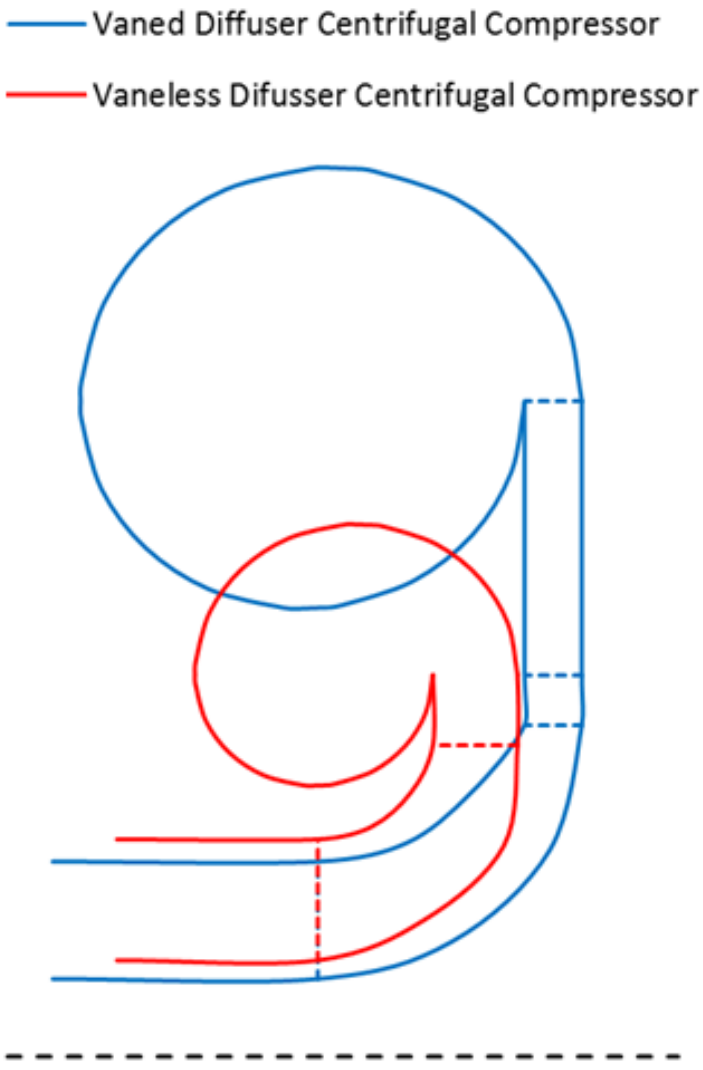

Figure 6-37: 1D design T/C geometry(meridional view) comparison between Vaned and Vaneless diffuser CC.

6.4 Retrofit Techno-economic assessment

The techno-economic assessment is an important part of the retrofit-design analysis, as analyzes the economic performance of all aforemention retrofit options, in order to guide the T/C manufacturing company which option should select.

Using indicative costs about T/C purchase and manufacturing, Figure 6-38 shows the payback period for each option. Fuel costs typical at the period of writing this PhD thesis have been employed as marine diesel fuel cost (bunker) varies and data for different fuels and locations are published daily[1].

For the retrofit process economic scenario, it is assumed that the marine company takes a loan with an indicative annual interest rate equal to (2.3%)[2],

[1]Ship & Bunker, News and inteligence for the marine fuels industry. www.shipandbunker.com
[2]https://data.worldbank.org/indicator

hence the interest rate parameter (r) is integrated in the profit function for the repayment period (0-t_0).

Considering the options 2 and 4, the entire T/C is replaced and redesigned, respectively. Thus, the baseline functional parts(entire baseline turbine, baseline bearings, etc.) can be sold. In that case, an indicative selling price reduction factor is also employed, as the baseline parts are sold as second hand ones.

According to the aforementioned assumptions, the profit for each retrofit option for both repayment and after repayment period is defined as:

$$P_{opti}(t) = \begin{cases} (TC_{opt1} - TC_{opti})(1+r)^t + (\dot{m}_{fuel,opt2} - \dot{m}_{fuel,opti})t & , \quad t \le t_0 \\ (\dot{m}_{fuel,opt2} - \dot{m}_{fuel,opti})(t - t_0) & , \quad t > t_0 \end{cases} \tag{6.3}$$

where the subscript i represent the corresponding option (2, 3 and 4). Concerning the fixed costs, they are also expressed as:

$$TC_{opt1} = C_{CC} \tag{6.4}$$

$$TC_{opt2} = C_{T/C} - (C_{T/C} - C_{CC})\,(1 - \chi_{T/C}) \tag{6.5}$$

$$TC_{opt3} = C_{red,CC} + C_{man,CC} \tag{6.6}$$

$$TC_{opt4} = C_{red,T/C} + C_{man,T/C} - (C_{T/C} - C_{CC})\,(1 - \chi_{T/C}) \tag{6.7}$$

Table 6-4: Turbocharger re-design additional cost in comparison with the market one.[1]

Turbocharger re-design additional cost(compared to market one)		
	Minimum additional cost	Maximum additional cost
T/C A1	$551.00	$609.00
T/C A2	$522.50	$577.50
T/C A3	$551.00	$609.00

According to a commercial sale site[2] and comparing T/C prices with those of T/C parts, it is concluded that the CC price is about the 26.97% of the T/C overall price. Also, a 7.51% and 19.45% of the overall CC price corresponds to impeller and volute components, respectively.

Table 6-5: Turbocharger purchase cost for both stock and used T/C.[5]

Turbocharger purchase cost for both stock and used T/C			
	New	Used	Reduction%
T/C B1	$542.64	$353.38	35%
T/C B2	$384.67	$283.18	26%
T/C B3	$659.83	$475.02	28%
T/C B4	$774.66	$468.00	40%

[1] https://www.buyautoparts.com/
[2] https://www.ebay.co.uk/

Thus, for this economic scenario and under the assumptions used, the payback periods for option 2, 3 and 4 are 7050h, 387h and 5159h, respectively.

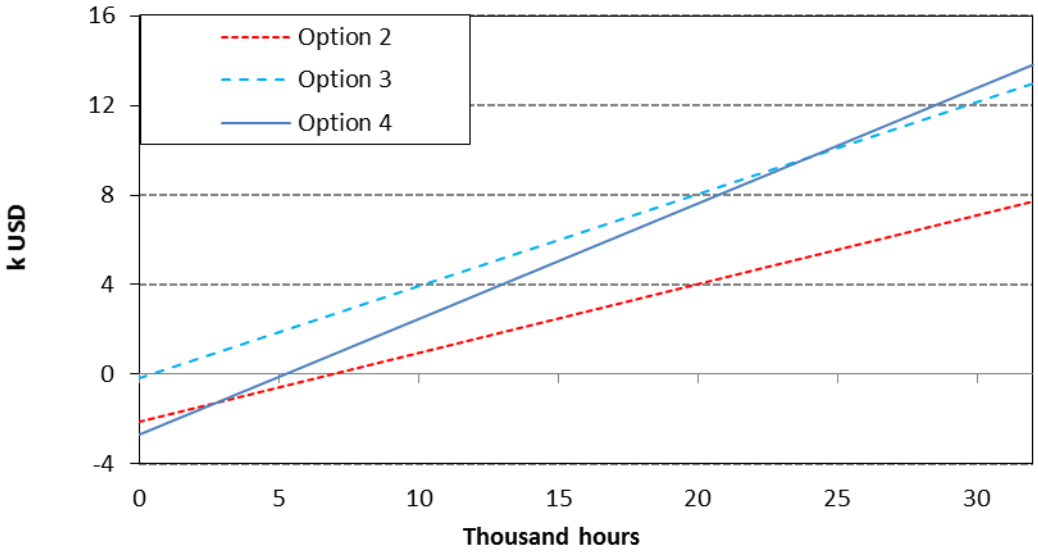

Figure 6-38: Estimated cumulative benefit in function of time of operation.

Concluding, according to the estimated cumulative benefit as function of time of operation(Figure 6-38), the option 3 provides the fastest payback period while the option 4 provides the highest long term profit.

In most cases, a T/C operation may not exceed the 3 years (24000h) due the harsh working conditions which lead to material failure, hence making the option 3 more suitable even if the option 4 provides higher long term profit.

6.5 Application test case summary and conclusions

The design-retrofit processes are applied in a retrofitting test case. First the first two retrofitting options are analyzed (compressor retrofit and entire T/C retrofit). In the first and second option a T/C retrofit is performed, using the corresponding available turbo-components. The solutions, that the processes provide, show that the initial performance cannot be achieved using off-the-self solutions, having a specific fuel consumption increase about 0.8% for option one and 0.27% for option two in nominal operation point. Both options solutions are structurally safe with similar modal behavior.

In next step, the processes are applied in a T/C Centrifugal Compressor design test case, aiming to cover the third retrofit option. Thus, a weighted single-objective optimization procedure is followed, redesigning it to match the entire engine system in an optimum way, while ensuring its structural integrity. Taking advantage from the usage of dimensionless parameters as optimization variables with defined range, a more general and automated design process is

provided since does not require both optimization variables ranges and initial geometry to be redefined for different T/C scale, using shop trials data as the only inputs.

The test case is separated in two parts. In the first part, taking advantage from the 1D to 3D transformation sub-tool, the preliminary design process provides both 1D and 3D geometry, showing that, apart from a preliminary design study, it can generate a fast operable and manufacturable compressor 3D geometry. In the second part, another optimization procedure is performed using CFD and FEA analysis. Utilizing the preliminary 3D compressor, the 3D design process does not rely on an initial 3D geometry, which in many cases is not available.

The results show that an improved retrofitting solution can be achieved, showing that the design process is reliable for fast compressor 3D design. Comparison of the both preliminary and high-fidelity sub-tools results shows that the user can reduce the design process computational time, by disabling impeller meridional geometrical optimization variables($R_{hub,a}$,$R_{hub,3}$,$R_{tip,1}$, etc.) and focusing only on the blade shape. Utilizing the high-fidelity sub-tool, the compressor is further improved, achieving an overall 1.75% efficiency increase and 0.34% diesel engine fuel consumption reduction.

The design process is applied also in an entire T/C design test case, aiming to cover the last (fourth) retrofit option. It examines all possible T/C configurations by applying a multi-point design process for optimal diesel engine reconstitution in each of them. The results indicate that the best configuration is the vaneless diffuser centrifugal compressor-radial turbine (Configuration A), achieving the higher fuel consumption decrease (0.401%), while ensuring stable operation and structural integrity.

The comparison between both configuration A and B design geometries indicates that both compressors have impellers of similar size. Also, with the vaned diffuser usage, the scroll volute size increase in order to reduce its losses taking advantage from the constant inlet flow angle (vaned diffuser). For such diesel engines the usage of T/C encompassing an axial turbine is infeasible.

Additionally, the study of how the new volute loss models affect the designed geometry, shows that both compressor volutes have similar aspect ratios, as both conventional and CFD based loss models have similar trends, while the CFD based Radial Turbine illustrates a higher aspect ratio, compared to the conventional one.

Finally, a techno-economical assessment is performed, studying all possible retrofit options. The results indicate that redesigning only the compressor, provides faster payback period, whereas redesigning the entire T/C provides higher long term profit.

6.6 References

Japikse, D. and Baines, N. C. . (1997). *Introduction to Turbomachinery.* Concepts ETI Inc and Oxford University Press.

Swain, D. and Engeda, A.,. (2014). Effect of Impeller blade trimming on the performance of a 5,5:1 pressure ratio centrifugal compressor. Imeche Journal of Power and Energy Vol 228 (2014): pp. 878–888.

Chapter

7 Application case B: Turbocharger fault effects on Diesel-engine performance

7.1 Turbocharger Fouling Assessment

The increasing need for marine engine system downsizing, combined with the harsh working conditions, leads to frequent engine components failure, especially for the T/C, making the fault effect simulation an important part of design or retrofitting process. Thus, the T/Ced diesel engine simulation process is applied in a fouling analysis for both T/C and Intercooler. The T/C components fouling simulation is materialized using physical consistent parameters such as roughness increase, rather than arbitrary mass flow, and efficiency reduction factors. In this way, the fault effect on the stall margin is obtained, thus the effect of faults on operability (usually neglected in 1D analysis to the author's knowledge) is assessed as well. Therefore, an alternative, lower fidelity, and time efficient option for studying the faults effect on the stall margin is provided, which otherwise is obtained using higher-fidelity, but time consuming CFD tools [Melino et al. 2011].

T/C fouling basically leads to inefficient operation and a shift of operating and stall margin. All compressors are susceptible to fouling as a result of the ingestion of air impurities that accumulate on and stick to gas path free surfaces, blades and shrouds, modifying airfoil geometry (Diakunchak 1992). Additionally, oil leaks from compressor seals and bearings mix with some of the ingested particles and deposit on the blade surfaces (Lakshminarasimha et al. 1994). The result will be the deterioration of airfoils aerodynamic behavior and reduction in flow area leading to the compressor and engine performance degradation. A typical fouled compressor impeller is depicted in Figure 7-1.

Turbine fouling is mainly depending on type and quality of the operating fuel as discussed by Meher-Homji (1987). When heavy fuel oil or crude oil is used, the turbine degradation is expected to be significant. Low melting point ashes, metals and unburned hydrocarbons can be aggregated in the turbine in the form of scale. The contaminants deposition will have an impact over blade, by changing the airfoil shape, the inlet angle and increasing the surface

roughness. These effects will result to the reducing of the airfoil throat area and apparently reducing the performance characteristics and the service life of the component. Also, especially in marine gas turbines, sulfidation may occur resulting in turbine corrosion. As a result, fouling rate increases, as discussed by Basendwah et al. (2006). A typical fouled vaned nozzle can be seen in Figure 7-2, where roughness increase is depicted.

Figure 7-1: Fouled Compressor Impeller.[1]

Figure 7-2: Fouled Turbine vaned nozzle[2].

[1] www.turbomed.gr
[2] https://maredu.hcg.gr

In the current fouling test case analysis, the study is limited to radial turbine T/C. Although, the presented procedure for studying the fouling effect in engine degradation is governed by the same principles with axial turbine T/Ced diesel engine. Since both T/C components may be fouled, five different fouling cases are simulated herein. The simulation is performed by altering the blade thickness and roughness accordingly, as presented in Table 3-11 and Table 7-2. The thickness change due to fouling is between 0.2 and 0.5 mm as proposed by Mezheritsky and Sudarev (1990) for a medium size T/C.

The results of fouling analysis are shown in Figure 7-1– Figure 7-5. As seen in Figure 7-1, compressor fouling causes the movement of the stall margin towards lower pressure ratios for high rotational speeds, hence reducing the compressor stable operation regime.

Table 7-1: Turbocharger Compressor fouling conditions.

Centrifugal Compressor			
Fouling condition	Blade thick. change[mm]	Blade thick. change [%]	Friction coef. change [%]
F1	+0.2	+21	+13
F2	+0.5	+54	+50
F3	-	-	-
F1-F3	+0.2	+21	+13
F2-F3	+0.5	+54	+50

Table 7-2: Turbocharger Turbine fouling conditions.

Radial Turbine			
Fouling condition	Nozzle thick. change [mm]	Nozzle thick. change [%]	Friction Coef. change [%]
F1	-	-	-
F2	-	-	-
F3	+0.5	-2.4	+37.5
F1-F3	+0.5	-2.4	+37.5
F2-F3	+0.5	-2.4	+37.5

Turbine fouling is mostly affecting the inlet mass flow and turbine efficiency hence reducing shaft horse power and increasing specific fuel consumption. As seen in Figure 7-4 the fifth simulated case (F2-F3), which is the most severe one, results to a shaft horse power reduction of 22% highlighting the effect that T/C components fouling can have on a T/Ced engine. For this reason, the original nominal power demand cannot be satisfied for this case.The effect of fouling on fuel consumption is considerably leading to a specific fuel increase by about 5% for the worst case, as depicted in Figure 7-5.

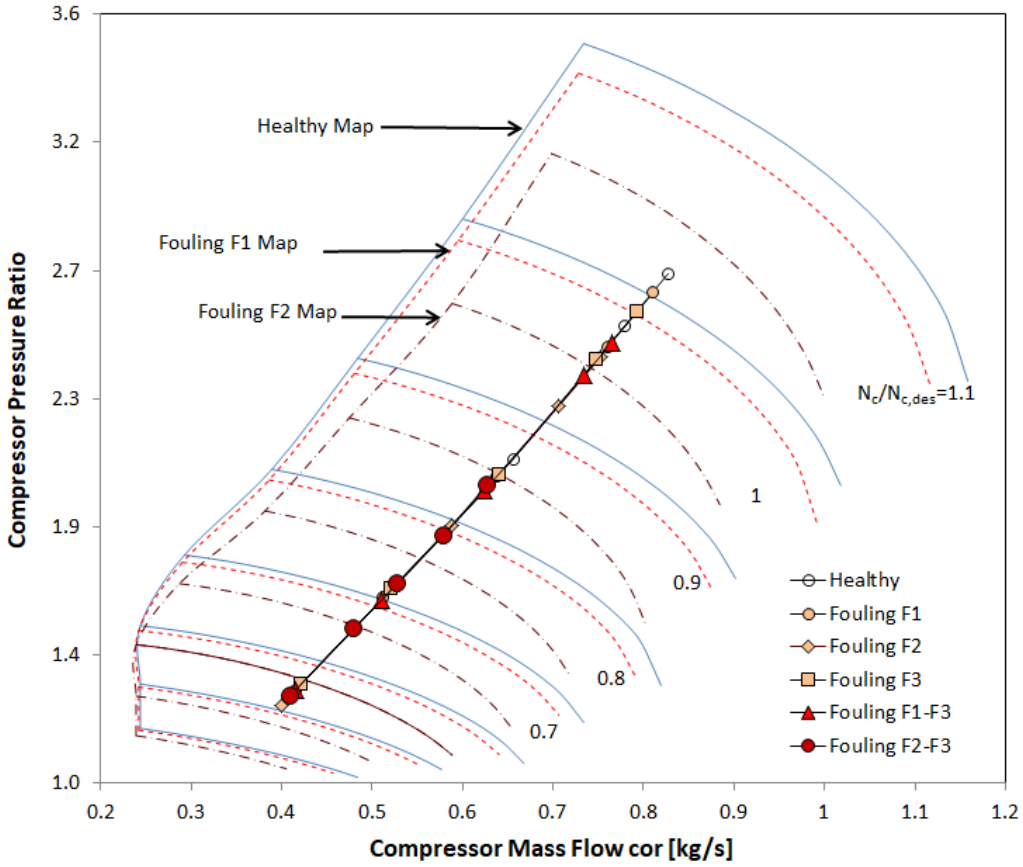

Figure 7-3: Compressor map and operating line change due to fouling.

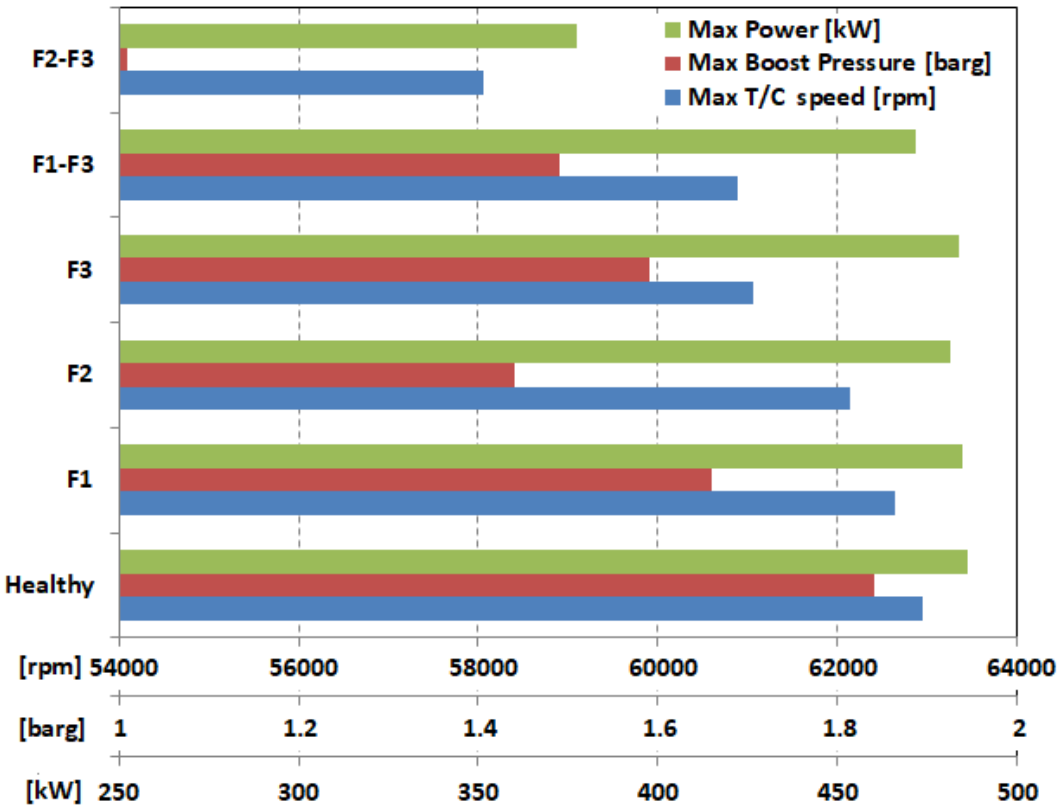

Figure 7-4: Engine power, boost pressure, and T/C speed variation due to fouling.

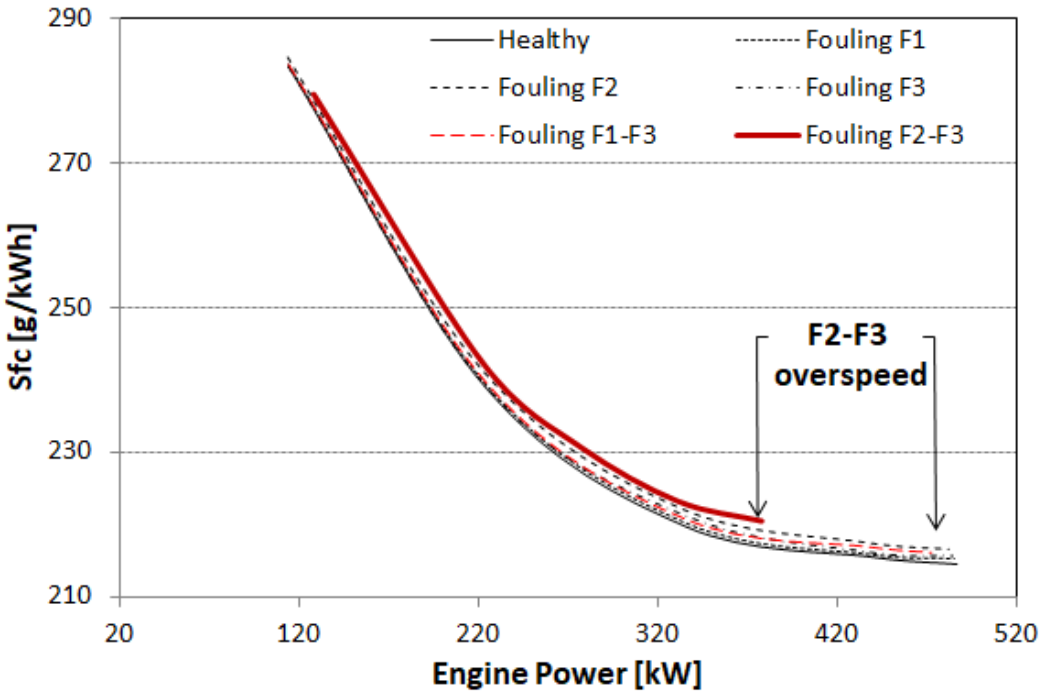

Figure 7-5: SFC variation due to fouling.

For further interpretation of the fouling analysis, an additional simulation is performed, with results presented in Table 7-3, highlighting the effect of fouling in engine performance degradation for constant engine speed and load. The demanded shaft power, used in this simulation, represents the fifth simulated case (F2-F3) maximum power, aiming to ensure that engine operates stably in all fouling conditions. It is observed that, as the fouling level increases, the fuel consumption increases in order to satisfy the demanded load. Also, boost pressure and T/C rotational speed reduction occurs due to compressor and turbine degradation. Finally, the system outlet temperature rises because of the turbine efficiency reduction.

Table 7-3: System operation dependence on fouling.

Fouling condition	Radial Turbine Specific shaft horse power (377 kW)				
	T/C rotational speed	Boost Pressure	$T_{trb,in}$	$T_{trb,out}$	SFC
F1	-0.9%	-10.0%	3%	4%	0.28%
F2	-2.0%	-22.2%	8%	12%	1.06%
F3	-2.2%	-6.2%	2%	4%	0.17%
F1-F3	-2.6%	-13.9%	5%	8%	0.61%
F2-F3	-3.7%	-26.1%	9%	15%	1.31%

7.2 Intercooler Fouling Assessment

The air density determines the maximum weight of fuel that can be effectively burned per working stroke in the cylinder. The increase in air density can be performed by decreasing the charged temperature leading to power increase. Intercooling is used for this purpose. In most cases, an intercooler consists of three channels.

- Air channel
- Brackish water channel
- Sea water channel

Brackish water drains heat energy from charged air through a finned tube exchanger, increasing its density. Next, this energy is transferred to sea water through a secondary exchanger. In order to perform the simulation of a fouled intercooler it was assumed that:

- Maximum fouling sea water resistance is 0.176 m^2K/kW (Kakac et al.2012)
- Maximum pressure drop increase is 0.29% due to fouling. (Gautam et al. 2017)

Using the heat exchanger fouling assumptions, clean cooler effectiveness to fouled cooler effectiveness ratio can be determined as follows:

$$\frac{\varepsilon_{\text{clean}}}{\varepsilon_{\text{fouled}}} = \frac{\frac{1}{U_{\text{clean}}} + R_f}{\frac{1}{U_{\text{clean}}}} \tag{7.1}$$

Calculating ε_{fouled} and using it, in T/Ced engine model, SFC, power and temperature changes can be calculated. Heat exchanger fouling leads to effectiveness reduction and pressure drop increase, hence, the air density before the manifold is decreased causing engine shaft power and efficiency reduction. The fuel consumption is increased by 1% as reported in Table 7-4, thus the heat exchanger fouling economic effect can become significant.

Table 7-4: Fouled intercooler parameters.

Condition	SFC[g/kWh]	$T_{trb,in}$[°C]	$T_{trb,out}$[°C]
Healthy	214.49	480	360
Fouled Intercooler	216.72 (+1.04%)	497 (+17°C)	381 (+21°C)

Additionally, exhaust gas temperature increases significant and the T/C operating line is moved towards stall (Figure 7-6), expected to affect T/C stable operation.

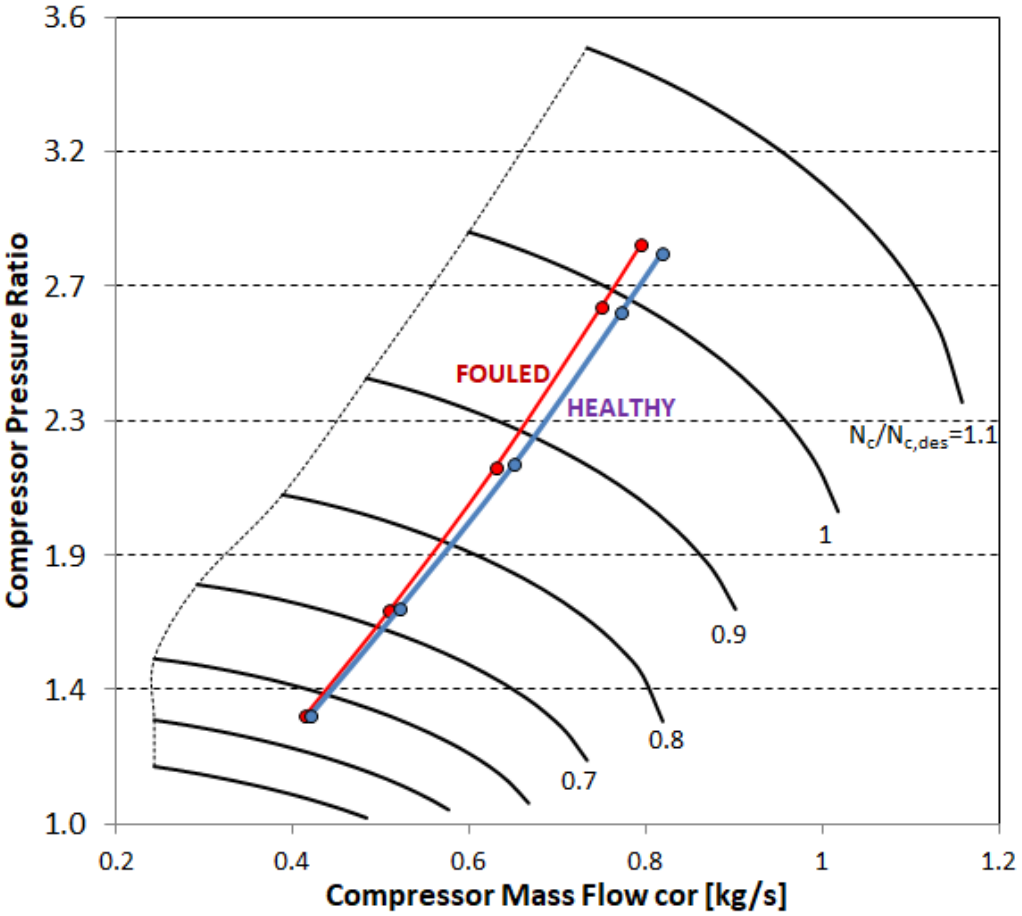

Figure 7-6: Operating line movement due to intercooler fouling.

The heat exchanger fouling rate depends on many parameters, including time. It is of interest to assess how the buildup of heat exchange fouling affects the overall T/Ced engine performance over time. The changes in pressure drop and resistance over time are evaluated according to the following and the values discussed, whereas time is assumed dimensionless, for expressing the relative change of performance parameters over time (Figure 7-7).

- Pressure drop reduction function against fouling resistance has parabolic form. (Gautam et al. 2017)
- Fouling resistance function against time has linear form. (Kakac et al.2012)

As seen in Figure 7-8 the SFC increase and the shaft power decrease are more profound during the first period of fouling. Over time, the fouling build up worsens degrading the overall performance but the degradation rate is expected to reduce over time.

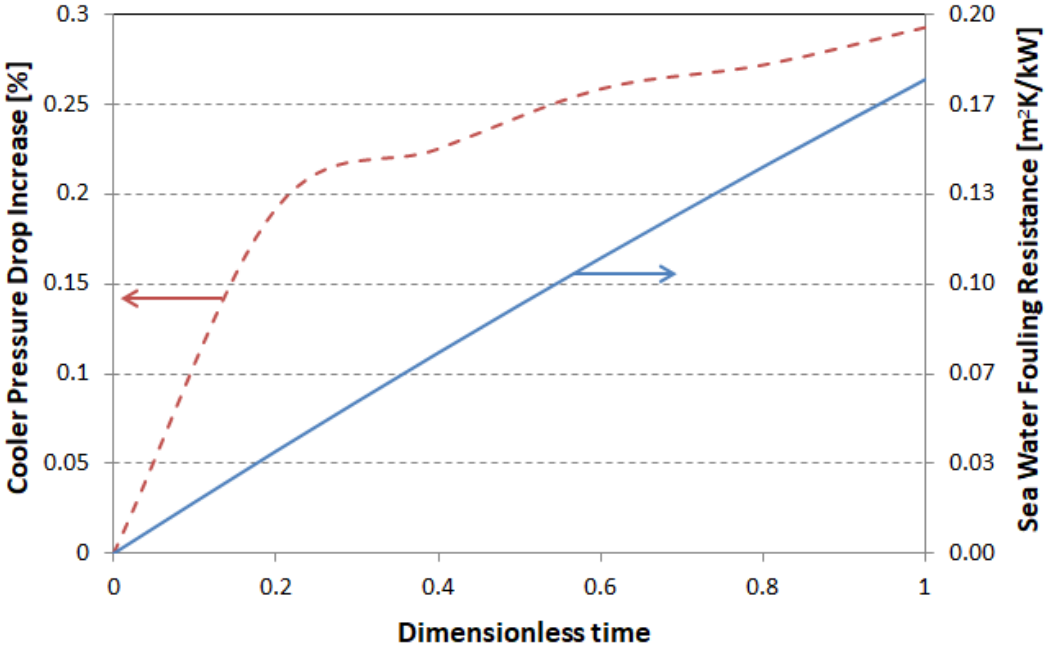

Figure 7-7: Intercooler fouling pressure drop and resistance against time.

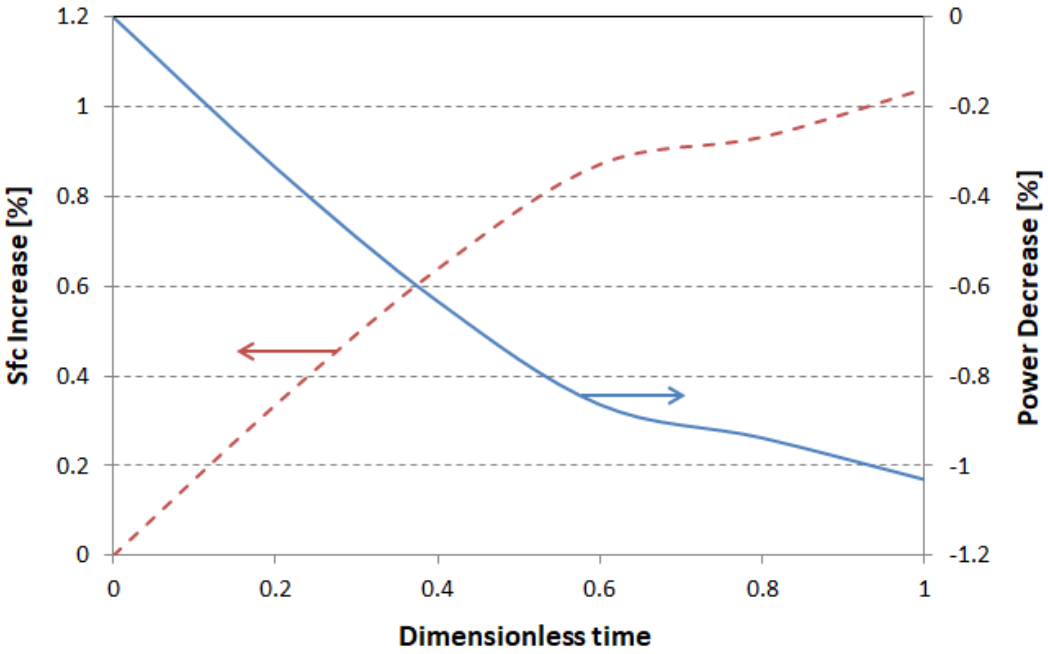

Figure 7-8: SFC and power change rate due to fouling.

7.3 Application test case summary and conclusions

In the fouling study test case, utilizing the T/Ced diesel engine simulation process, an overall system simulation and operation analysis is carried out assessing operability and performance parameters. Specific faults are simulated utilizing physical consistent parameters such as blade friction and thickness based on relevant literature data. Analysis results show a significant reduction in engine performance, especially in case of both turbo components being fouled, in contrast to the heat exchanger fouling. In more detail, the results indicate that:

Compressor fouling causes the movement of the stall line towards lower pressure ratios, hence reducing the compressor stable operation regime. Turbine fouling is mostly affecting the inlet mass flow and turbine efficiency reducing shaft horse power and increasing specific fuel consumption. As for the combination of compressor and turbine fouling, power may be reduced up to 22%, highlighting the effect that T/C components fouling can have on a T/Ced engine and leading to a 5% specific fuel consumption increase.

Heat exchanger fouling leads to effectiveness reduction and pressure drop increase, resulting, for the case examined herein, by 1% specific fuel consumption increase and by 1% power decrease, indicating that intercooler fouling may affect the engine life cycle cost. Additionally, the exhaust gas temperature increases significantly, an increase that is expected to affect the T/C bearings life. Also, the T/C operating line is moved towards stall line, increasing the possibility of working under unstable operation.

7.4 References

Basendwah, A., Pilidis, P. and Li, Y. G. (2006). *Turbine Off- Line Water Wash Optimization Approach for Power Generation.* Proceeding of ASME Turbo expo, Barcelona, Spain, GT2006-90244, pp. 65-76; 12 pages.

Diakunchak, I. S. (1992). Performance Deterioration in Industrial Gas Turbines. *ASME J. Eng. Gas Turbines Power, 114(2): 161-168*

Gautam K., Parmar, N. and Vyas, B. (2017). Effect of fouling on thermal and hydraulic parameter of Shell and Tube Heat Exchanger. *Student conference 2017, Czech Technical University, Prague, Czech Republic.*

Kakac, S., Liu H. and Pramuanjaroenkij A. . (2012). *Heat Exchangers.* CRC Press.

Lakshminarasimha A. N., Boyce, M. P. and Meher-Homji, C. B. . (1994). Modelling and Analysis of Gas Turbine Performance Detrerioration. *ASME J. Eng. Gas Turbines Power,, 116*, 46-52.

Meher-Homji, C. B . (1987). Compressor and Hot Section Fouling in Gas Turbines – Causes and Effects. *Proceedings of the 9th Industrial Energy Technology Conference.* Houston: Texas A&M University.

Mezheritsky A.D. and Sudarev, A.V. . (1990). The mechanism of fouling and the cleaning technique in application to flow parts of the power generation plant compressors. Proceeding of ASME Turbo Expo, Brussels, Belgium, 90-GT-103.

Chapter

8 Conclusions and Future Work

Integrated processes for T/C design and retrofitting were presented. These processes were developed with three modes of operation, providing a fully automated simulation, design and retrofit for T/Ced diesel engine.

The first mode provides a T/Ced diesel engine simulation option. With such an application, capable to simulate the system operation over its whole envelope, T/C matching quality and diesel engine operation improvement studies or T/Ced diesel engine fouling analysis can be performed.

In the design mode, a multi-point optimization process is employed, aiming to provide a fast and reliable turbo-component or the entire T/C design solution based on T/Ced diesel engine range of operation. The optimization process focuses on engine fuel consumption reduction in the engine's range of operation, while ensuring appropriate matching between turbomachinery components and the diesel engine. Both turbo-components structural integrity is ensured by performing simplified static and modal analysis. Dimensionless parameters are used as optimization variables, for both compressor and turbine, providing a more general and automated design process since it does not require both optimization variables ranges and initial geometry to be redefined for different T/C scale. Additionally, the surrogate volute loss models, trained with CFD simulated data, are also provided for both centrifugal compressor and radial turbine as option, allowing for a more detailed design process. The process produces four improved T/C (compressor and turbine) (if it is possible), of different possible configurations, namely vaneless diffuser centrifugal compressor – axial turbine, vaned diffuser centrifugal compressor – axial turbine, vaneless diffuser centrifugal compressor – radial turbine, vaned diffuser centrifugal compressor – radial turbine. The combination that gives the best improvement to the diesel engine operation is identified. For the centrifugal compressor design, a high fidelity design option is provided as well by performing a CFD compressor multi-point design optimization process, producing an optimized 3D compressor geometry. It complies with the T/Ced diesel engine range of operation, while structural integrity is ensured by Finite Element analysis.

In the retrofit mode, all available turbo-components are examined, in order to select the one that best matches the entire engine system, aiming to retain or

improve the diesel engine efficiency, while ensuring chosen turbo spool dynamic structural integrity .

8.1 Application test cases conclusions

Applying the integrated processes in several test cases, the conclusions are the following:

1. T/C retrofitting with selected turbo-components test case:
    - With the mass usage of the processes proposed here, it is guaranteed that the retrofit process, will provide the best retrofit solution, avoiding unnecessary fuel consumption and operating cost increase. Also, their usage will increase the productivity of T/C manufacturers, decreasing the time, spending in tasks such as, searching for available T/C, matching, analyzing and designing a new compressor.
    - Due to the limited number of available turbo-components, the initial performance cannot be achieved using off-the-self solutions, having a specific fuel consumption increase, compared to the baseline T/C. In that case, a T/C component or T/C redesigning is suggested for reconstituting the initial performance.
2. T/C compressor re-design test case:
    - An improved retrofitting solution can be achieved by redesigning the T/C compressor.
    - The comparison between both preliminary and high fidelity 3D designed geometries shows that the user can reduce the 3D design process computational time, by disregarding impeller meridional geometrical optimization variables($R_{hub,\ a}$, $R_{hub,3}$,$R_{tip,1}$, etc.) and focusing only on blade shape geometry parameters.
3. Entire T/C re-design test case:
    - The results indicate that best configuration is the vaneless diffuser centrifugal compressor-radial turbine, achieving the higher fuel consumption decrease, while operation is stable and structurally safe.
    - The comparison of both vaneless and vaned diffuser compressor designed geometries indicates that both compressors have similar size impellers. With the vaned diffuser, the scroll volute size increases in order to reduce its losses, taking advantage from the constant inlet flow angle (vaned diffuser).
    - The comparison between conventional and surrogate volute loss models in terms of the T/C design solution indicates that:
        i. Compressor volutes have similar aspect ratio as both models have similar trends.

ii. The turbine volute surrogate model leads to geometry with higher aspect ratio, compared to the conventional one, as the latter under-estimates the outlet flow angle.

- The design process provides a more efficient T/C, compared to both baseline and compressor redesigned T/C.

4. T/C and Intercooler fouling assessment test case:
   - Compressor fouling causes the displacement of the stall line towards lower pressure ratios, hence reducing the compressor stable operation regime.
   - Turbine fouling is mostly affecting the inlet mass flow and turbine efficiency reducing shaft power and increasing specific fuel consumption.
5. Intercooler fouling assessment test case:
   - Intercooler fouling leads to effectiveness reduction and pressure drop increase, resulting to specific fuel consumption increase and power decrease.
   - The exhaust gas temperature increases significantly, affecting the T/C bearings life.
   - The T/C operating line is moved towards the stall margin increasing the chance of working under unstable operation.

8.2 Contributions to Science and Technology

The most important results from this thesis that can be considered as novel are the following:

- The T/C design is performed in engine system level, including all possible configurations.
- Structural integrity is ensured, by integrating a simplified structural static and modal analysis.
- Multi-point design analysis based on T/Ced diesel engine operating line.
- 1D Optimization with dimensionless parameters as variables:
  a. General and automated design process by using dimensionless optimization variables instead of dimensional ones.
  b. No need of redefining both the variables ranges and initial geometry for different T/C scale, hence providing a more general and automated design process.
  c. Can be used in any turbomachinery design application, with zero or minor adjustments.
- Simplified structural analysis (static analysis):
  a. Can be used from any turbomachinery meanline code
  b. Does not require as input entire blade shape but inlet and outlet blade angle and thickness, as blade geometry is automatically generated via a blade transformation technique. This technique follows a

turbomachinery sub-component blade angle/thickness adaptation approach based on known 3D geometries.
   c. Ensures geometry structural integrity

- Simplified structural analysis (modal analysis):
  a. Can be used from any turbomachinery meanline code
  b. Ensures geometry structural integrity
  c. Provides more accurate results compared to similar studies by having more degrees of freedom and including the gyroscopic effect.
- Centrifugal compressor and radial turbine CFD-based surrogate volute models development.
  a. Can be used by centrifugal compressor and radial turbine meanline models.
  b. Accuracy improvement compared to the conventional meanline loss models.
  c. Overcomes the loss prediction problem due to 3D effects.
- 1D T/C component fouling simulation process:
  a. Usage of physically consistent parameters such as roughness increase rather than arbitrary mass flow, and efficiency reduction factors, hence providing the fault effect on the stall margin.
  b. Provides an alternative, lower fidelity, and time efficient option for studying the faults effect on the stall margin, which usually is obtained using higher-fidelity, but time consuming CFD tools.
- Study of the intercooler fouling effect on the T/Ced diesel engine degradation and compressor stall margin.
- Processes modification:
  a. Turbo-components meanline loss models can be easily modified without affecting the entire process operation.
  b. Surrogate volute loss models can be further trained or re-trained, by replacing the corresponding loss coefficient parameters files.
  c. Diesel engine model can be easily replaced without affecting the entire process functionality as it is treated as a black box software.
  d. Each 3D compressor design sub-tool can be easily replaced with both in-house and commercial tools (CFD solver, FEA solver, meshing, etc.) as the design process treats them as a black box software.
  e. Optimization tool can be easily replaced as all design sub-tools are coupled via a “Driver” tool, developed within the python environment.

8.3 Future Work

The following processes extensions are suggested:

- Engine Model:

    a. Replacing of the single-zone diesel engine model by a more detailed phenomenological one ,coupled with detailed modeling for NOx emissions from diesel engine, whereas CO2 emissions will be directly calculated by the fuel consumption.
    b. Development of a filling emptying engine model may be consindered, allowing to study the whole system operation for pulse turbocharging and how it affects stable operation regime.
- T/C model:
    a. Physics-informed machine learning(CFD or Measurements-based) models development for each T/C turbo-component.
    b. Electric engine model development: e-turbochargers analysis
- Extending the high fidelity design process for all turbo-components.
- Modal Analysis:
    a. More detailed compressor/turbine impeller moment of inertia and mass.
    b. Compressor/Turbine impeller modal analysis as elastic body

8.4 List of publications

1. Ntonas K, Aretakis N, Roumeliotis I, Pariotis E, Paraskevopoulos Y & Zannis Y (2020) Integrated simulation framework for assessing turbocharger fault effects on diesel-engine performance and operability, Journal of Energy Engineering, 146 (4) Article No. 04020023.
2. Ntonas, K., Aretakis, N. , Roumeliotis, I. and Mathioudakis, K., "A Marine Turbocharger Retrofitting Platform," ASME Journal of Engineering for Gas Turbines and Power, 142 (11) Article No. GTP-20-1402/111008.(Also Proceeding of ASME Turbo Expo. GT2020-14643. Virtual, Online, September 21-25), 2020.
3. Ntonas, K., Aretakis. N,. Mathioudakis, K., "A Marine Turbocharger Compressor Multi-point 3D Design optimization tool.," Proceeding of ASME Turbo Expo 2021, GT2021-59518, Virtual Conference, June 7-11., 2021..
4. Ntonas, K., Aretakis. N,. Mathioudakis, K.," 1D Multi-point Marine Turbocharger design, for optimal performance reconstitution". Proc IMechE, Part A: Journal of Power and Energy, 2022. (Under review)

APPENDIX: Axial Turbine Design Application

The design process is applied in an axial turbine design study for demonstration purposes. For further verifying the design process, the axial turbine validation test case, presented by Person (2015), is redesign aiming to improve the initial performance. In the current section, a design approach is presented, assuming fixing mean radius turbine.

Axial Turbine design strategy

In the current design case, a multi-point axial turbine design is performed aiming to maximize the overall turbine efficiency. The nominal point corresponds to 100% of baseline turbine nominal speed [Person 2015] while both 60% and 80% are selected as base points.

All selected design points are depicted in Figure A 1,while the objective function can be expressed as:

$$max: z' = \frac{\eta_{trb,60} + \eta_{trb,80} + \eta_{trb,100}}{3} \quad \text{(A.1)}$$

The constraints are extensively described in the design process section. The design process is performed, having the hub and tip radius parameters fixed and equal to the baseline values, presented by Person (2015)

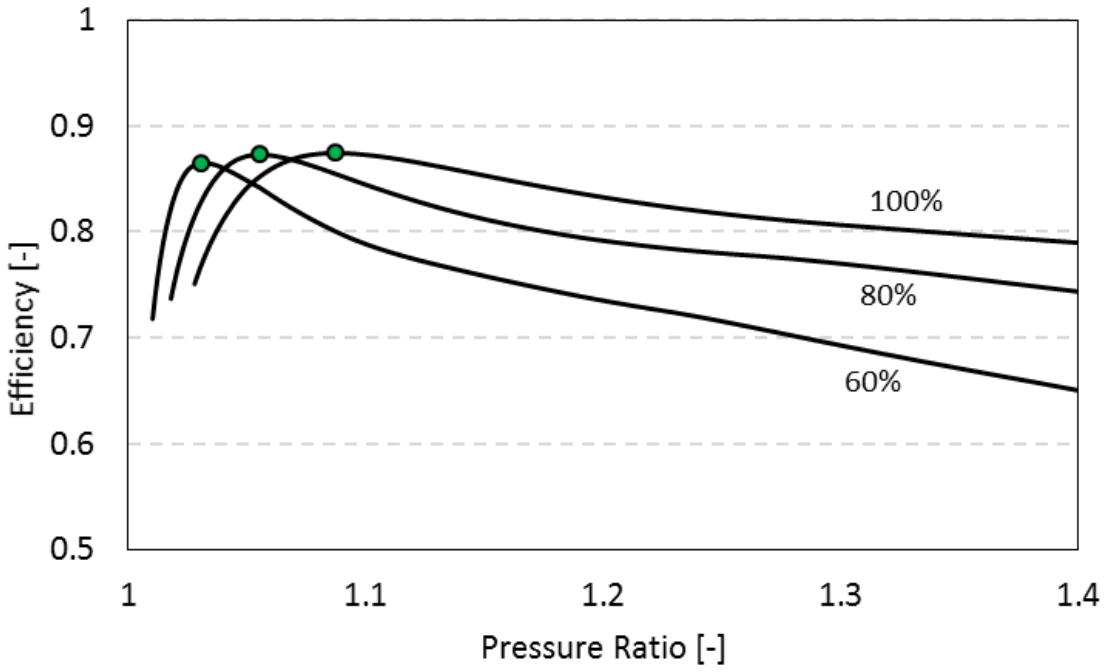

Figure A 1: Turbine selected design points.

The performance comparison, depicted in Figure A 2 and Figure A 3, indicates that the baseline turbine performance is reconstituted/slightly improved (0.8% overall efficiency increase).

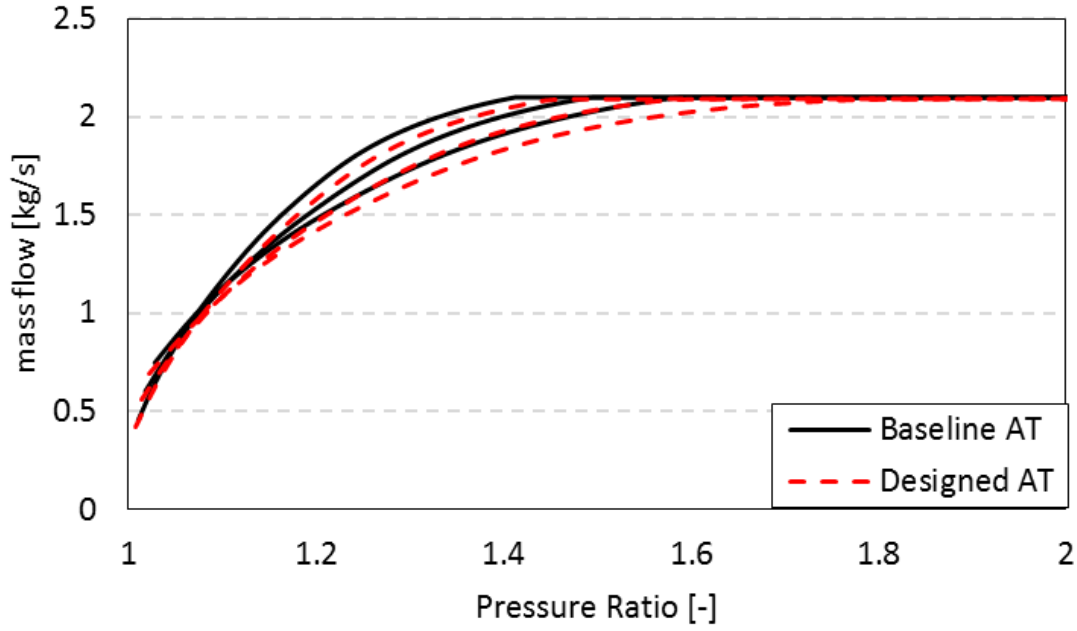

Figure A 2: Turbine mass flow against pressure ratio.

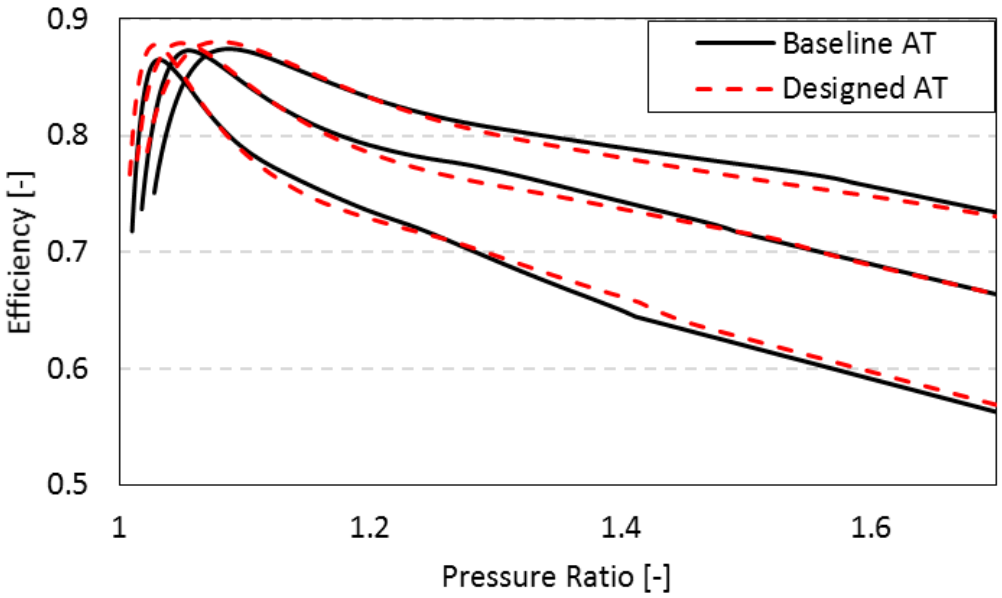

Figure A 3: Turbine efficiency against pressure ratio.

According to the geometry comparison in meridional view for both baseline and design turbine (Figure A 4), for increasing the overall efficiency, the process drives the design solution to slightly higher chord length, while the blade height across streamwise is retained.

Figure A 4: Meridional view geometry comparison.

Concerning the blade variables, Table A 1 shows a small change in blades shape.

Table A 1: Baseline and Design turbines basic geometrical parameters change.

Axial Turbine			
Stator			
Parameter	Value	Parameter	Value
c	5.89%	$\beta_{b,2}$	-0.03%
e	-9.59%	t_{max}/c	0.77%
Rotor			
Parameter	Value	Parameter	Value
$\beta_{b,1}$	-8.37%	$\beta_{b,2}$	8.62%
e	20.20%	t_{max}/c	-16.14%
c	9.70%		

References

Person, J.,. (2015). 1D Turbine Design Tool Validation and Loss Model Comparison: Performance Prediction of a 1-stage Turbine at Different Pressure Ratios, Master of Science Thesis, KTH, School of Industrial Engineering and Management Energy Technology.